Pankaj Tambe
Peter Huang
Suyog Jhavar *Editors*

Advances in Mechanical Engineering and Material Science

Select Proceedings of ICAMEMS 2023

Springer

Lecture Notes in Mechanical Engineering

Lecture Notes in Mechanical Engineering (LNME) publishes the latest developments in Mechanical Engineering—quickly, informally and with high quality. Original research reported in proceedings and post-proceedings represents the core of LNME. Volumes published in LNME embrace all aspects, subfields and new challenges of mechanical engineering. Topics in the series include:

- Engineering Design
- Machinery and Machine Elements
- Mechanical Structures and Stress Analysis
- Automotive Engineering
- Engine Technology
- Aerospace Technology and Astronautics
- Nanotechnology and Microengineering
- Control, Robotics, Mechatronics
- MEMS
- Theoretical and Applied Mechanics
- Dynamical Systems, Control
- Fluid Mechanics
- Engineering Thermodynamics, Heat and Mass Transfer
- Manufacturing
- Precision Engineering, Instrumentation, Measurement
- Materials Engineering
- Tribology and Surface Technology

To submit a proposal or request further information, please contact the Springer Editor of your location:

Europe, USA, Africa: Leontina Di Cecco at Leontina.dicecco@springer.com
China: Ella Zhang at ella.zhang@springer.com
India: Priya Vyas at priya.vyas@springer.com
Rest of Asia, Australia, New Zealand: Swati Meherishi
at swati.meherishi@springer.com

Indexed by SCOPUS, EI Compendex, and INSPEC.

All books published in the series are evaluated by Web of Science for the Conference Proceedings Citation Index (CPCI).

To submit a proposal for a monograph, please check our Springer Tracts in Mechanical Engineering at https://link.springer.com/bookseries/11693.

Pankaj Tambe · Peter Huang · Suyog Jhavar
Editors

Advances in Mechanical Engineering and Material Science

Select Proceedings of ICAMEMS 2023

Springer

Editors
Pankaj Tambe
School of Mechanical Engineering (SMEC)
VIT-AP University
Amaravati, Andhra Pradesh, India

Peter Huang
Department of Mechanical Engineering
Binghamton University
Binghamton, NY, USA

Suyog Jhavar
School of Mechanical Engineering (SMEC)
VIT-AP University
Amaravati, Andhra Pradesh, India

Paper in this product is recyclable.

Contents

About the Editors

Dr. Pankaj Tambe received his B.E. degree from Nagpur University, Nagpur, in 2002, M.Tech. degree from Motilal Nehru National Institute of Technology (MNNIT) Allahabad in 2005, and his Ph.D. degree from the Indian Institute of Technology, Bombay, (IIT-B) in 2010. He is Professor at the School of Mechanical Engineering, VIT-AP University, Andhra Pradesh, India. He is Active Researcher with research interest in Polymer Processing, Interface and Interphases of Composite Materials. The applications of his research are in aerospace structures, interiors of automobiles, EMI shielding packaging and high K-dielectric materials. He is Editorial Board Member of Composite Interfaces, Taylor & Francis, UK.

Dr. Peter Huang is Associate Professor and Director of Undergraduate Studies in mechanical engineering in the Watson College of Engineering and Applied Science at Binghamton University. He received his B.A. degree in physics from Cornell University, M.Sc. and Ph.D. degrees in engineering from Brown University, and postdoctoral training in biomedical engineering at Tufts University. Dr. Huang's research interests encompass the broad areas of fluid mechanics and mass transport in biomedical applications. His research group specializes in experimental microfluidics, optical diagnostics, and computational modeling, with ongoing projects in understanding the mechanobiology of heart valve calcification, modeling perivascular amyloid transport and cerebral amyloid angiopathy, and electrospray-based targeted printing. His research has been funded by the National Science Foundation and National Institutes of Health. Dr. Huang has taught fluid dynamics and transport phenomena at both the undergraduate and graduate levels since 2008 and was a recipient of the 2019 SUNY Chancellor's Award of Excellence in Teaching. He currently serves as Chairperson of the Watson College Undergraduate Studies Committee, Member of the Binghamton University Health Sciences Transdisciplinary Area of Excellence Steering Committee, Member of the Binghamton University Human Subject Research Review Committee (IRB), and Member of the Institutional Review Board of United Health Services Hospitals at Binghamton, New York.

Dr. Suyog Jhavar is Associate Professor at the School of Mechanical Engineering at Vellore Institute of Technology-AP (VIT-AP University). He is among the first few researchers who has received Ph.D. in Metal Additive Manufacturing in India. He received Ph.D. from IIT-Indore, in 2014 and M.Tech. in welding engineering from IIT-Roorkee in 2010. During his Ph.D. research, he integrated a welding heat source with an indigenously designed wire deposition system to develop a novel metallic additive manufacturing system. The results obtained were very promising and published in international scientific literature of repute and highly cited. His expertise includes designing of AM machine tool and architecture along with parametric, metallurgical and mechanical characterization of parts processed through AM route. His expertise also entails mathematical modeling and prediction of deposition profile for quality improvement in the 3D printed components.

Design Modelling for Commercial/Pilot-Scale Circulating Fluidized Bed Combustion (CFBC) Boiler

S. Naga Kishore, T. Venkateswara Rao, and M. L. S. Deva Kumar

Abstract Two biggest problems in present Indian pulverized coal combustion (PCC) power plants are that large capacity of PCC plants has reached retirement due to age limit and huge coal import from outside countries. Increasing the utilization of circulating fluidized bed combustion (CFBC) technology in India is the best solution for renovating old PCC boilers to extend their life to 20–25 years and reducing coal import by increasing the utilization of local low-grade coals in effective manner. Even though CFBC technology is economically sound, technically feasible and environmentally friendly than PCC technology, CFBC technology utilization in India is still in the nascent stage. To increase the utilization of CFBC technology in India, more design models are needed to come out on Indian low-grade fuels such as Indian lignite and high ash coal for predicting thermal and environmental performance, analysing design and optimizing processes in operation at wider range of operating parameters. In this paper, a CFBC boiler design modelling which is developed by programming code of visual basics for applications (VBA) software is explained. To check the accuracy, the design methodology is applied to validate the practical data of different CFBC units on various aspects such as thermal performance model (boiler efficiency, flow rates), hydrodynamic model (solids volume fraction), heat transfer model (water wall heat transfer coefficient) and sulphur capture model (SO_2 emissions). The design procedure which is applied for validation process gives satisfactory results on different aspects, and the qualitative agreement is found between predicted values and actual measurements.

Keywords CFBC · Boiler · Design · Performance · Heat transfer · Emissions

S. Naga Kishore (✉) · M. L. S. Deva Kumar
Department of ME, JNT University College of Engineering, Anantapur, India
e-mail: nagakishore.surisetty@gmail.com

T. Venkateswara Rao
Department of ME, DBS Institute of Technology, Kavali, India

Nomenclature

A	Boiler element cross-sectional area (m^2).
a	Decay coefficient ($-$).
ASH	Weight fraction of ash in fuel ($-$).
C_{SO}	Concentration of SO$_2$ emissions below secondary air introduction (kmol/m^3).
$C_{SO2(H)}$	Concentration of SO$_2$ emissions at furnace exit (kmol/m^3).
E_{sor}	Sulphur capture efficiency (%).
E_c	Cyclone efficiency (%).
EA	Excess air (%).
f_c	Weight fraction of unreacted sorbent in bed solids.
H	Furnace height (m).
H_i	Height of point of injection of secondary air (m).
H_f	Height of furnace above secondary air level (m).
h_{tot}, h_b	Heat transfer coefficient of water wall and back-pass elements (W/m^2 K).
h_i, h_o	Inside and outside heat transfer coefficients (W/m^2 K).
K	Reaction rate of sulphation (m^3/kmol.s).
k_w	Tube wall thermal conductivity (W/mK).
LMTD	Log mean temperature difference.
m_c	Coal feed rate (kg/s).
m_s	Steam flow rate (t/h).
$m_{s,RH}$	Reheater steam flow rate (t/h).
m_{sor}	Limestone feed rate (kg/s).
P_{RH}	Reheater pressure (MPa).
P_{SHO}	Final superheater outlet pressure (MPa).
PA/SA	Ratio of primary air (%)/secondary air (%).
Q	Element heat duty (kW).
S	Sulphur mass fraction in coal ($-$).
T_b	Average bed temperature (°C)
T_{RHI}	Reheater inlet temperature (°C).
T_{RHO}	Reheater outlet temperature (°C).
T_{SHO}	Final superheater outlet temperature (°C).
T_{FW}	Feed water temperature (°C).
T_w	Wall temperature (°C).
U	Superficial gas velocity (m/s).
X_{CaCO3}	Weight fraction of calcium carbonate in limestone.
x_w	Tube wall thickness (m).

Greek Letters

ρ_{avg}	Average bed density (kg/m^3).
η_b	Boiler efficiency (%).
ε	Voidage at given section ($-$).
ε_a	Voidage at secondary air injection ($-$).
ε_{avg}	Average bed voidage ($-$).
ε_e	Voidage at the exit of furnace ($-$).
ε_s	Solid volume fraction at given section ($-$).
φ	Proportionality constant in pore plugging time ($-$).
δ_{max}	Maximum extent of sulphation ($-$).

1 Introduction

At present, electricity shortage of coal fired plants in India is based on two big problems such as rise of imported coal prices and retirement of huge capacity [1, 2]. Many coal fired plants (PCC plants) in India were installed in between 1960 and 1975. A number of PCC plants having capacity of 22,716 MW are ready to stop working due to retirement condition [2, 3]. A total of 9824.3 MW was retired during the period of 2017–2022 [4]. As a result, there is an immediate need for installing more new power plants and revamping old PCC boilers to extend their life up to 20–25 years in India to meet demand. For old PCC boilers, CFBC technology is a better alternative to renovate with less cost, to improve local coal utilization and to reduce cost at similar environmental performance compared to traditional PCC technology [5].

The coal quantity in million tonnes (MT) which is imported from neighbouring countries has been increasing every year. It is noticed that the value of imported coal from neighbouring countries was reached to 208.933 MT for the year 2021–22 [6]. The amount of money spent for this imported coal was 2,287,418.46 million Rupees which is 97.15% more than previous year 2020–21 (in value 1,160,240.54 million Rupees) [6]. To reduce this huge cost of coal import from other countries, CFBC technology is an essential alternative which supports to burn local low-grade fuels effectively [5].

Though CFBC technology is economically sound, technically feasible and environmentally friendly than PCC technology, CFBC technology usage in India is still in the developing stage [5]. To encourage more utilization of CFBC technology in India, new design models on CFBC boilers must be introduced for analysing new designs, optimizing processes in operation and predicting thermal and environmental performances. In the design modelling of CFB boiler, the input data such as operating steam parameters, fuel and limestone analysis, solid properties and operating bed data are needed [7, 8]. Some of the authors developed design models of commercial/ pilot-scale CFB boilers on different capacities through different ways.

Greenfield Research Inc. (GRI) developed an expert system (CFBCAD) in the year 1999 for designing CFB boiler with the input parameters mentioned above in the collaboration with Daltech, Dalhousie University [9]. The procedure followed in this system is convenient to make possible for designers. Several authors tried this procedure manually (directly and with slight changes) to check design and performance under different operating conditions and achieved favourable results with lesser error in the validation of practical data. Some of the works [8, 10–13] which explained and used the expert system design procedure of CFB boiler in elaborated mathematical way are explained below with the proper input data.

Cen et al. [10] used manual mathematical procedure which was mentioned in expert system [9] for 62 MW to predict design and performance and got reasonable agreement in validating expert system results. Kim and Choi [11] discussed and compared the design and performance of six different capacities (2 MW, 75 tph, 200 MW, 340 MW, 460 MW and 600 MW) of practical operated CFBC boilers in detail. In this work, authors selected plants having three configurations of CFB loop (design without EHE, design with EHE and design with pant leg) and explained element heat duty based on its surface area in each boiler. The design steps to be followed for furnace and standard industry proportions to be taken for cyclone design were proposed. Kim et al. [12, 13] concentrated only heat exchangers to predict performance of 2 and 300 MW at varying loads in mathematical way for which they proposed a design methodology.

In this work, the results are predicted by design modelling of VBA programming code for different aspects (thermal performance, hydrodynamics, heat transfer model and sulphur capture) of pilot and commercial-scale CFBC boilers at the same operating bed parameters and compared with practical results. The model procedure applied for validation process gives satisfactory results on different aspects, and the reasonable agreement is found between designed and actual measurements.

2 Modelling of CFBC Boiler Design

The good design of CFB boiler should always maintain efficient energy transformation with minimum impact on environment under all operating conditions. But it may be difficult to implement. If the design reaches a degree with which all targets (maximum thermal efficiency, minimum emissions and amount of solid waste) are reached, the design can be treated as better design. Additionally, to that manufacturers also see minimum operating and capital cost. Still, many aspects of design in the CFB boiler are based on rule of thumb [8].

A traditional algorithmic program is performed a stepwise arithmetic operation in visual basic for applications (VBA) software with MS Excel as host application. The design software covers heat exchangers circuit and gas-particle loop such as furnace, recirculation system and back-pass. Initially, boiler configuration is first fixed out depending on boiler capacity, and later input data are selected.

Table 1 Key equations used in program to determine design parameters

Parameter/model	Equation	References
Boiler efficiency (η_b)	$\eta_b = 100 - \text{total heat losses in } \% \cdots (1)$	[8]
The solid volume fraction (ε_s)	$\varepsilon_s = 1 - \varepsilon \cdots (2)$	[14]
Axial voidage (ε)	$\varepsilon = \varepsilon_e - (\varepsilon_e - \varepsilon_a) \exp\left[-a(H - H_i)\right] \cdots (3)$	[15]
Water wall heat transfer coefficient (h_{tot})	$h_{tot} = 5\rho_{avg}^{0.391} \times T_b^{0.408} \quad \cdots (4)$	[16]
Overall heat transfer coefficient (h$_b$)	$\frac{1}{h_b} = \frac{1}{h_i} + \frac{x_w}{k_w} + \frac{1}{h_o} \cdots (5)$	[17]
Surface area of boiler elements (A)	$A = \frac{Q}{h_b(\text{LMTD})} = \frac{Q}{h_f(T_b - T_w)} \cdots (6)$	[8]
SO$_2$ concentration at the exit, (C$_{SO2}$(H))	$E_{sor} = 1 - \frac{C_{SO_2}(H)}{C_{S0}} =$ $1 - \exp\left[\frac{-KX_{CaCO_3} f_c}{100U} \rho_{avg} H_f\right] \cdots (7)$	[8]
Sulphur capture model	$\frac{m_{sor}}{m_c} =$ $\frac{3.12 \, E_{sor} \, \rho_{avg} \, H_f \, S - 100\varphi U(\text{ASH}) E_c \ln(1 - E_{sor})}{E_c \left[\delta_{max} X_{CaCO_3} \rho_{avg} H_f + 100\varphi U \ln(1 - E_{sor})\right]} \cdots (8)$	[8]

The current design program is suitable for making design of CFBC boiler having external recirculation hot cyclone configuration with normal lower furnace. The program analyses two design types. They are boiler with reheater facility and boiler without reheater facility in which user can choose the heat transfer surface layout based on capacity.

The key equations included in program for determining design parameters are shown in Table 1. From the previous works [8, 10–14], the steps to be followed in this program for design model of CFBC boiler are shown in flowchart Fig. 1.

It is laborious to take any decision and execute a compromise for standard algorithm software. For the VBA program used in this work, the designer needs to interfere and stop the program for confirmation of results at intermediate steps. Based on current results, the designer gives next decisions to complete further calculations. The program for this work is not deigned with automated decision making, and it is needed to take decisions manually by the designer.

2.1 Design Model Input

Input required for the design model is fuel and sorbent composition, steam cycle (operating steam data) and bed data (bed temperature, primary and secondary air ratio, excess air percentage, fluidization velocity, Ca/S ratio, particle mean diameter and desulphurization efficiency). Physical properties of coal and gas, physical constants,
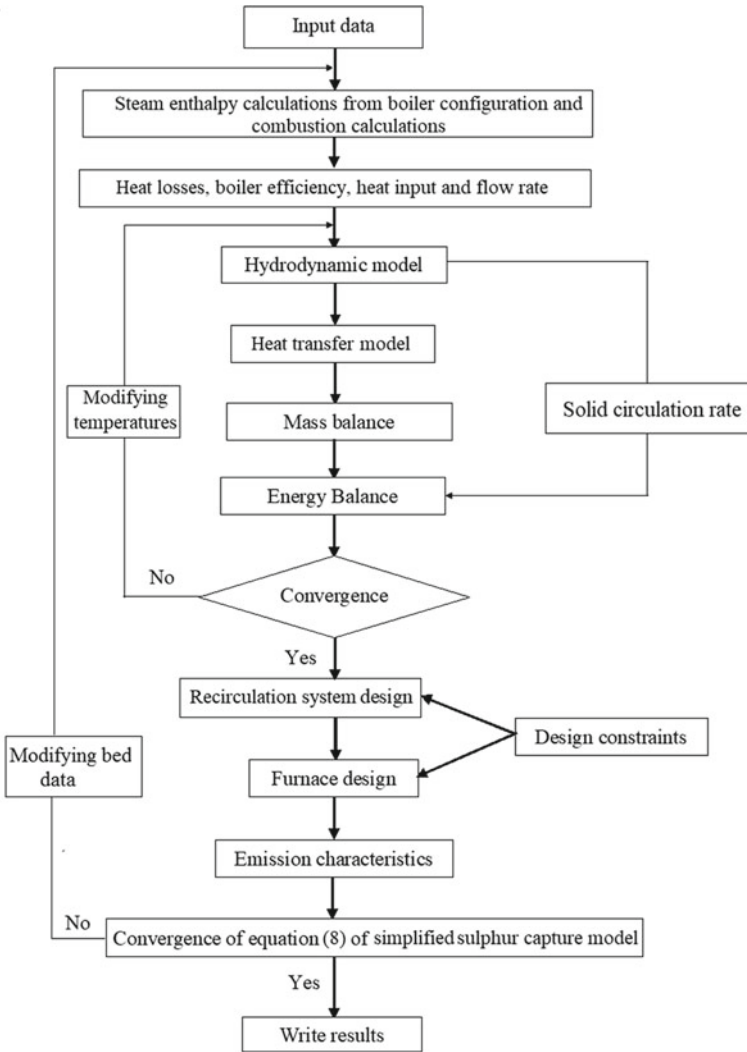
Fig. 1 Flowchart of procedure followed in VBA program for design of CFBC boiler

some default parameters to determine surface area of heating elements, steam tables and industry accepted/default values are incorporated in the program.

A number of tables are involved in this work for steam properties at different pressures and temperatures and air/gas/coal properties at different temperatures. Sometimes, data in the tables do not match with discrete values. In such a case, properties are determined by interpolation method.

2.2 Validation

Experimental data are essential for analysing predicted design in validation. The experimental results on laboratory/bench-scale units are considered in most cases for validating predicted data. But, the model prediction becomes more reliable if experimental data of commercial units are properly available. Hence, care is taken for model validation in the selection of commercial plants which have necessary input data along with experimental results in the published literature. Availability of complete bed data of input is a big problem for commercial plants in published literature. In case of absence of data in published literature, the range of operating bed data which is used successfully in commercial operations of CFBC units was taken for model calculations, and they are given in Table 2.

Care is taken in case of absence of data that solid properties of respective fuel for program are taken from the plants located with similar capacity and nearer to the validation plants. For absence of data, the $CaCO_3$ in limestone is considered as 90% for validation plant.

3 Results and Discussion

The design methodology explained in Fig. 1 was used to be validated with the actual measured data available in the published literature of different capacities of CFBC boilers. The present program is suitable only for external recirculation configurations. The validation was applied to different aspects of design such as thermal performance (boiler efficiency, fuel and limestone feed rates), hydrodynamic parameter (solid volume fraction), water wall heat transfer coefficient and SO_2 emissions of plant.

Table 2 Bed data range for model calculations in case of absence of data

Parameter	Value (or) range [References]
Primary and secondary air ratio (−)	40:60–60:40 [8]
Superficial gas velocity (m/s)	2–12 [18]
Ca/s ratio (−)	2–14 [19]
Sulphur capture efficiency (%)	75–95 [17]
Constant in pore plugging time	0.0977–0.0367 [8]
Mean particle diameter (mm)	0.2–1.5 [18]
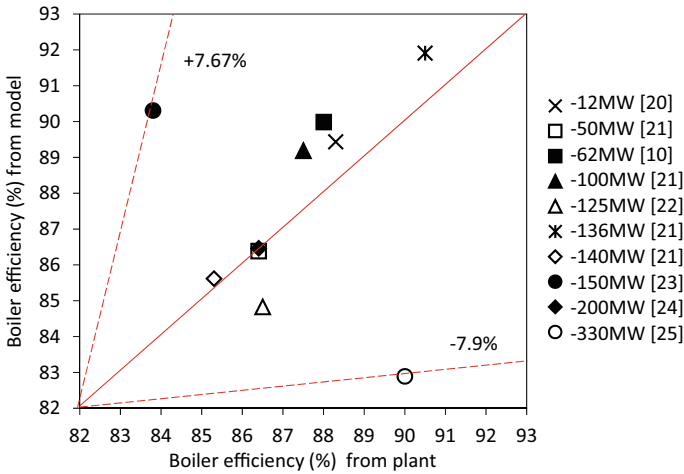
Fig. 2 Validation of boiler efficiency (%) of CFBC boilers with different capacities

3.1 *Thermal Performance*

3.1.1 Boiler Efficiency

Typical validation results of boiler efficiency for different CFBC units are shown in Fig. 2. The boiler efficiency of different plants was investigated by the VBA design model with the required input data (coal and limestone data, operating steam data and bed data) which were taken from the published literature of respective plants as mentioned in Appendix Table I. The heating values of fuel samples were estimated from the equations based on coal constituents for the model calculations, and these values were slightly deviated with heating values of published data. The model results were close to plant data, and the average error ranged between $+7.67\%$ and -7.9%.

3.1.2 Feed Rate

Figures 3 and 4 show the relation between calculated and measured data of fuel and limestone feed rates (kg/s) for different CFBC units. The input data used for model calculations are mentioned in Appendix Table I. The model values of fuel rate were reached nearer to measured data, and the maximum error was not crossed $+15.14\%$. Similarly, model results have given fair agreement with measured results for limestone feed rate, and the maximum error was identified within the limits of $+11.09\%$.

Fig. 3 Validation of fuel feed rate (kg/s) of CFBC boilers with different capacities
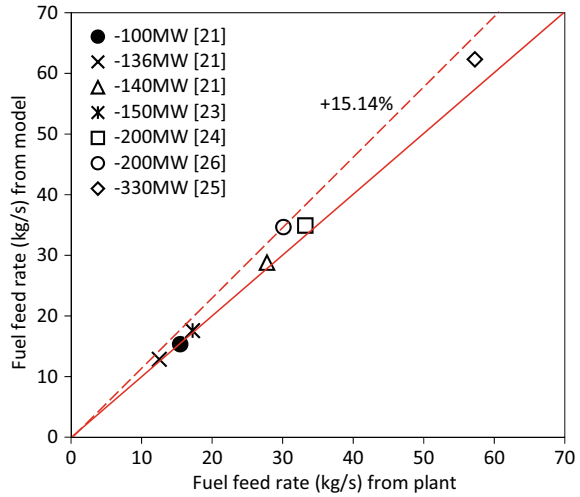
Fig. 4 Validation of limestone feed rate (kg/s) of CFBC boilers with different capacities
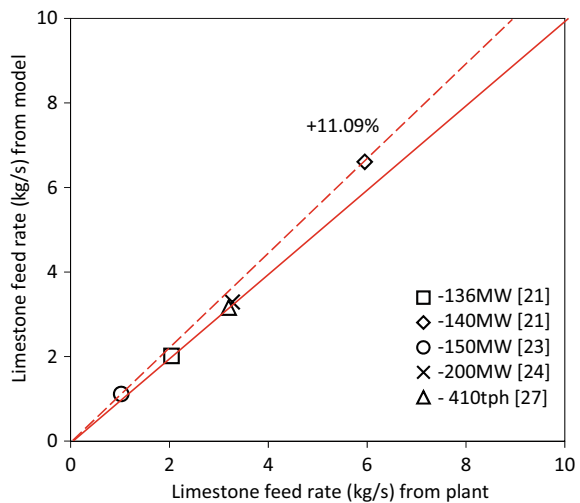
3.2 Hydrodynamics

The comparison of solids volume fraction between predicted results of model and plant values is explained below for two CFBC units. The predicted values were determined using Eqs. (2) and (3) as shown in Table I, and bed data used for solid volume fraction are shown in Appendix Table II. The model values were estimated for same furnace heights which were mentioned in the published literature.
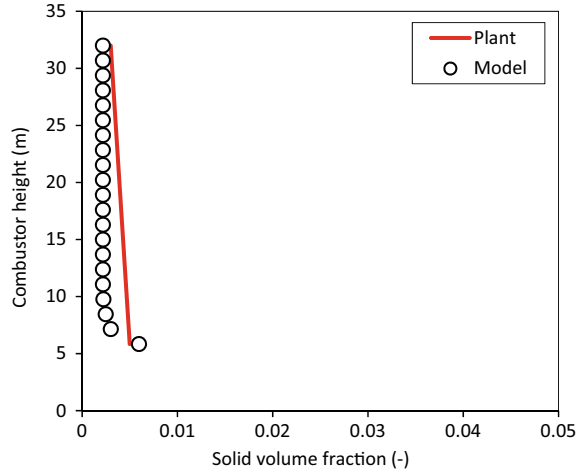
The measured profile of solids volume fraction for 200 MW Tonguea CFBC boiler [26] is shown in Fig. 5. The program is designed to determine solid volume fraction for only furnace zone in the plant. Because, no boiler element is placed in CFBC loop except upper furnace. The model results were very close to plant data from the stage of introduction of secondary air. The satisfactory agreement between model and plant data was obtained, and the relative deviation in upper furnace was measured as 40.5%.

Figure 6 explains the solids volume fraction (%) in axial way between predicted values by model and plant data of 200 MW CFB riser from Sun et al. [28]. The plant data of solids volume fraction were measured by using pressure drop and distance of two pressure sensor points. The lower furnace end was assumed as position of secondary air injection, and minimum solids circulation rate was considered for predicting model results due to unavailability of data. The predicted profile was validated at six positions (5.2, 12.1, 17.7, 24, 27.4 and 30.5 m) from the end of lower furnace and obtained exponential manner. The model value was deviated with maximum error 55.2% at 12.1 m height in the furnace due to inaccurate values of decay factor, solids circulation rate, voidages at point of inflexion and furnace exit. The average error was obtained as 19.63%.

3.3 Heat Transfer Coefficient

The water wall heat transfer coefficient was estimated using Eq. (4) for different commercial/pilot-scale boilers (12 MW [20], 150 MW [23], 2 MW [12], 465 tph (135 MW) [29], 65 tph [30, 31] and 50 MW [32]). The bed data of these boilers used for model prediction are displayed in Appendix Table III. For model calculations, heat transfer coefficient was investigated at same furnace height which is available
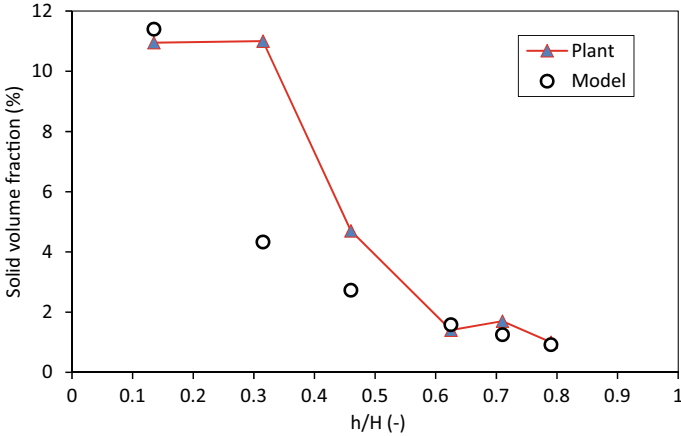
Fig. 6 Comparison of solid volume fraction with plant data of 200 MW CFBC boiler from Sun et al. [28]

Fig. 7 Validation of heat transfer coefficient of water wall for different capacities of CFBC boilers
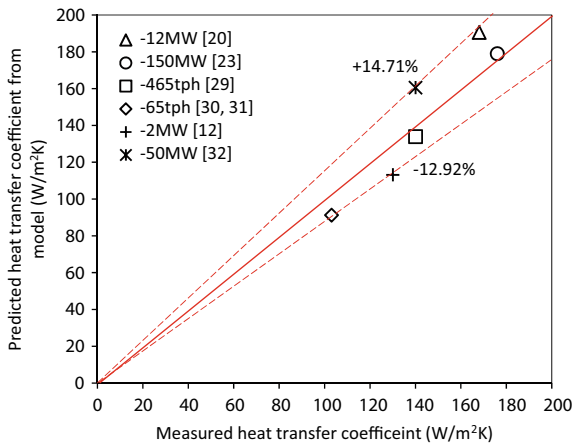
in actual plant. Fair relationship as shown in Fig. 7 was observed between measured and predicted results. The deviation was located between + 14.71% and − 12.92%.

3.4 SO_2 Emissions

The bed reference data of CFBC plants (125 MW [22], 330 MW [25], 75 tph [33], 220 tph [34], 2 MW [35] and 12 MW [20, 36]) for sulphur capture mentioned by different works are shown in Appendix Table IV. SO_2 emissions of these CFBC units were predicted by Eq. (7). The model calculations were performed at same Ca/S

ratio, bed temperature and sulphur capture efficiency followed in actual plants. Table 3 represents a typical validation of SO_2 emissions for different CFBC boilers. In case of unavailability of Ca/S ratio for model calculations of 75 tph CFBC boiler, the Ca/S ratio was considered as '2' where Eq. (8) was verified. In case of unavailability of sulphur capture efficiency (E_{sor}) for model calculations of 330 MW CFBC boiler, E_{sor} was taken as 77% where Eq. (8) was verified.

It was also noticed in 125 MW CFBC boiler model calculations that the sulphur capture model was verified at fluidization velocity as 6 m/s which is slightly higher than published value (5 m/s). But, the value 6 m/s is also safe limit for avoiding erosion problems in furnace [8]. Hence fluidization velocity as 6 m/s was considered for model calculations. For SO_2 emissions, qualitative agreement is found between actual and model results. The maximum deviation placed between -25.3% and $+17.8\%$ is shown in Table 3.

4 Conclusions

The motto of this work was to encourage CFBC technology for constructing new boilers and for renovating and revamping old PC fired boilers in India by promoting a design model methodology developed in visual basics for applications (VBA) program. Design modelling was applied on various aspects (thermal performance, hydrodynamics, heat transfer coefficient and SO_2 emissions) of CFBC boilers having different capacities for checking modelling accuracy. A qualitative agreement was found between model results and actual data from the all aspects in the validation. The design modelling used in the present work can be recommended strongly for analysing new designs, identifying optimum values, evaluating thermal performance and SO_2 emissions. The conclusions which were noticed from deign modelling applied on various aspects are given below.

- Boiler efficiency was predicted using model for different commercial and pilot-scale CFBC boilers. The predicted values were fitted well with plant data. Ten plants with different capacities were taken for boiler efficiency in which the error deviation ranged in between $+7.67\%$ and -7.9%. The average error was identified as 0.268%.
- Good relation was obtained between measured and calculated results in flow rates (fuel and limestone feed rate). Fuel feed rate was investigated with model procedure for seven commercial units and validated with plant data. The error deviation for fuel feed rate was identified within the limits of $+15.14\%$, and average error is 6.39%. Similarly, limestone feed rate was predicted for five CFBC boilers and validated with actual data of the plant. The maximum error crossed $+11.09\%$, and average error was obtained as 8.54%.

Table 3 Validation of SO_2 emissions at 100% load for different capacities of CFBC boilers

References	S (%)	Capacity	Plant value			Model value			Error in emissions (%)
			Ca/S ratio (−)	E_{sor} (%)	SO_2 emissions	Ca/S ratio (−)	E_{sor} (%)	SO_2 emissions	
Gauvillé et al. [22]	0.92	125 MW	< 2.5	92.5	330 mg/Nm³	2.4	92.5	259.6 mg/Nm³	− 21.21
Sun et al. [25]	0.62	330 MW	2.3	N/A	390 mg/m³	2.3	77	387.44 mg/m³	− 0.656
Gu et al. [33]	0.27	75 tph	> 1	97	35 mg/Nm³	2	97	31.34 mg/Nm³	− 10.45
Lu et al. [34]	1.18	220 tph	2.33	90	< 250 ppm	2.33	90	186.658 ppm	− 25.3
Han et al. [35]	0.25	2 MW	6.5	75	100 ppm	6.5	75	117.815 ppm	17.8
Wang et al. [20]	0.85	12 MW	3	N/A	160 ppm	3	90	134.289 ppm	− 16.06
Wang et al. [36]									

S—sulphur content in coal, E_{sor}—sulphur capture efficiency, N/A—not available

- The model results of solid volume fraction for voidage were investigated with empirical model and compared with actual data. Reasonable agreement was found between plant and model data. The average error not crossed 30%.
- The water wall heat transfer coefficient predictions of different CFBC boilers were fitted very close to experimental data. Maximum error was obtained in the limits of $+14.71\%$ and -12.92%.
- The simplified sulphur capture method was used in the design model of CFBC boiler for investigating SO_2 emissions. The model results have shown good relation in measured SO_2 emissions of different CFBC plants. Good agreement was found between model and plant results, and average error not crossed -9.5%.

Appendix

See Table I.
See Table II.
See Table III.
See Table 1V.

The error in case of validation is measured by the following equation:

$$\text{error } (\%) = \frac{\text{Predicted value} - \text{Measured value}}{\text{Measured value}} \times 100$$

Table I Steam, fuel and bed data of different CFBC units predicting boiler efficiency and flow rates

CFBC boiler	12 MW	50 MW	62 MW	100 MW	125 MW	136 MW	140 MW	150 MW	200 MW	330 MW	200 MW	410 tph
Reference	[20]	[21]	[10]	[21]	[22]	[21]	[21]	[23]	[24]	[25]	[26]	[27]
Ultimate analysis of coal												
Carbon (%)	63.01	49.6	63.39	55.12	29.08	80.5	35.0	59.15	49.6	40.68	52.9	59.9
Hydrogen (%)	3.59	1.0	3.88	2.52	1.95	2.25	3.0	4.19	1.0	2.66	0.3	2.91
Oxygen (%)	6.23	1.5	6.51	3.39	4.58	0.5	12.02	8.61	1.5	4.32	3.7	2.49
Nitrogen (%)	1.15	0.5	1.13	0.87	0.32	1.0	3.42	1.22	0.5	0.69	0.2	0.71
Sulphur (%)	0.85	1.4	0.78	1.63	0.92	6.10	0.66	3.63	1.4	0.62	0.6	3.12
Ash (%)	23.74	36.0	21.62	29.14	30.15	0.4	37.0	14.3	36.0	45.03	39.1	22.16
Moisture (%)	1.43	10.0	2.7	7.33	33	9.25	8.9	8.9	10.0	6	3.3	8.71
Steam parameters												
m_s (t/h)	73	2/30	75	410	367	453.6	428.4	476.28	670	1025	693	410
T_{SHO} (°C)	450	510	450	540	540	540	543	540	545	543	541	540
P_{SHO} (MPa)	3.82	9.8	3.82	9.8	13.3	10.8	14.5	13.2	13.8	18.6	17.3	9.8
$m_{s, RH}$ (t/h)	–	–	–	–	338	383.2	384.5	432	N/A	929	541	–
T_{RHO} (°C)	–	–	–	–	540	540	540	540	545	543	541	–
Steam parameters												
T_{RHI} (°C)	–	–	–	–	N/A	343	344	343	340	340	342.8	–
P_{RH} (MPa)	–	–	–	–	3	2.72	4.27	3.3	3.7	4.49	3.9	–
T_{FW} (°C)	105	230	150	220	242	238	252	237	230	259	244	220
Bed data												
EA (%)	20	20	20	20	20	20	20	15	25	20	N/A	N/A
PA/SA	60/40	N/A	60/40	N/A	40/60	N/A	N/A	N/A	65/35	60/40	62/38	60/40

(continued)

Table I (continued)

CFBC boiler	12 MW	50 MW	62 MW	100 MW	125 MW	136 MW	140 MW	150 MW	200 MW	330 MW	200 MW	410 tph
Reference	[20]	[21]	[10]	[21]	[22]	[21]	[21]	[23]	[24]	[25]	[26]	[27]
Ca/S ratio	3	2.1	N/A	2.2	< 2.5	2.3	1.6	N/A	2	2.3	1.5–3.0	N/A
E_{sor} (%)	N/A	90	90	90	92.5	95	55	N/A	90	N/A	N/A	> 90

m_s—steam flow rate, T_{SHO}—temperature of final superheater outlet, P_{SHO}—final superheater outlet pressure, $m_{s, RH}$—reheater steam flow rate, T_{RHO}—reheater outlet temperature, T_{RHI}—reheater inlet temperature, P_{RH}—reheater pressure, T_{FW}—feed water temperature, PA/SA—primary air (%)/secondary air (%), EA—excess air, E_{sor}—sulphur capture efficiency, N/A—not available

Table II Bed data used to predict solids volume fraction profile of commercial CFBC boilers at 100% load

References	Capacity	Furnace dimensions (area × height) (m² × m)	d_{50} (mm)	Coal density (kg/m³)	Furnace exit temperature (°C)	Superficial gas velocity (m/s)	Decay factor (−)
Lee et al. [26]	200 MW	19 × 7 × 32	0.332	2200	925	4.6	1.1957
Sun et al. [28]	200 MW	22.7 × 7.2 × 38.2	1.5	N/A	930	N/A	N/A

d_{50}—mean particle diameter, N/A—Not available

Table III Bed data used to predict water wall heat transfer coefficient of different commercial/pilot-scale CFBC boilers at 100% load

References	Capacity	Furnace dimensions (area × height) (m² × m)	Excess air (%)	Ca/S ratio (—)	PA/SA (—)	d_{50} (mm)	ρ_p (kg/m³)	G_S (kg/m²s)	T_b (°C)	U_o (m/s)
Kim et al. [12]	2 MW	1.2 × 2.4 × 214	20	4.66	80/20	0.3	2600	7.5	870	4.8
Wang et al. [20]	12 MW	2.45 × 5.45 × 21	20	3	60/40	1.22	2400	3.56	930	N/A
Basu and Halder [23]	150 MW	N/A × N/A × 45	15	N/A	N/A	N/A	N/A	10	871	5.6
Yu et al. [29]	465 tph	6.6 × 13.1 × 38	41	2	60/40	0.332	N/A	5.79	885	5.9
Han et al. [30]	65 tph	4.737 × 4.855 × 17	N/A	5.32	60/40	2.69	2100	7	800–950	5
Qing et al. [31]										
Ni and Li [32]	50 MW	N/A × N/A × 27	20	0	60/40	N/A	N/A	N/A	925	N/A

PA/SA—ratio of primary air to secondary air, d_{50}—mean particle diameter, ρ_p—solid particle density, G_S—solids flux, T_b—Average bed temperature, U_o—superficial gas velocity, N/A—not available

Table IV Bed data used to predict SO_2 emissions different commercial/pilot-scale CFBC boilers at 100% load

References	Capacity	S (%)	Furnace dimensions (area × height) (m^2 × m)	Ca/S ratio (−)	T_b (°C)	E_{sor} (%)	U_o (m/s)
Gauvillé et al. [22]	125 MW	0.92	8.6 × 11 × 33	< 2.5	850–860	92.5	5
Sun et al. [25]	330 MW	0.62	N/A	2.3	900	N/A	< 5.4
Gu et al. [33]	75 tph	0.27	3.23 × 7.23 × 21.5	> 1	810	97	5
Lu et al. [34]	220 tph	1.18	21.4 × 20.7 × 30	2.33	890	90	N/A
Han et al. [35]	2 MW	0.25	1.2 × 2.4 × 14	6.5	900	75	4.8
Wang et al. [20] and Wang et al. [36]	12 MW	0.85	2.45 × 5.45 × 21	3	925	N/A	N/A

S—sulphur content in fuel, T_b—bed temperature at furnace exit, E_{sor}—sulphur capture efficiency, U_o—Superficial gas velocity, N/A—not available

References

1. Coal shortage: Will your electricity bill go up? Times of India (2021/10/13) https://timesofindia.indiatimes.com/business/india-business/coal-shortage-will-your-electricity-bill-go-up/articleshow/86984085.cms. Last accessed 2022/09/11
2. Central Electricity Authority (2020) CEA annual report 2019–2020. Ministry of Power, Government of India
3. Central Electricity Authority (2021) Executive summary on power sector. Ministry of Power, Government of India
4. Central Electricity Authority (2022) CEA annual report 2021–2022. Ministry of Power, Government of India
5. Lockwood T (2013) Techno-economic analysis of PC versus CFB combustion technology. IEA Clean Coal Centre
6. Provisional Coal Statistics 2021–22, Coal Controller's Organisation, Ministry of Coal, Government of India (2022)
7. Batu A (2008) Investigation of combustion characteristics of indigenous lignite in A 150 KWT circulating fluidized bed combustor. Ph.D. Thesis, The Middle East Technical University
8. Basu P (2015) Circulating fluidized bed boilers-design, operation and maintenance. Springer, Switzerland
9. Basu P, Dutta A, Miller L (2003) An intelligent tool for evaluating bids for circulating fluidized bed boilers. In: Proceedings of 17th international conference on fluidized bed combustion, May 18–21, Jacksonville, Florida, USA, Paper no FBC2003-153, pp 113–116
10. Cen K, Basu P, Cheng L, Fang M-X, Luo Z-Y (2001) Design and performance verification of a 62-MWt CFB boiler. J Eng Gas Turbines Power 123:240–245
11. Kim T, Choi S (2011) Comparative evaluation of thermal design parameters of different sizes of circulating fluidized bed boiler. J Korean Soc Combust 16(4):16–22

12. Kim T, Choi S, Hyun H-S (2014) Performance prediction of a circulating fluidized bed boiler by heat exchangers block simulation at varying load conditions. Proc IMechE Part A: J Power Energy 228(1):17–32
13. Kim T, Choi S, Kim J-S (2015) Performance prediction of a large-scale circulating fluidized bed boiler by heat exchangers block simulation. Proc IMechE Part A: J Power Energy 229(3):298–308
14. Ozkan M (2010) Simulation of circulating fluidized bed combustors firing indigenous lignite. Thesis of Master of Science, Middle East Technical University
15. Kunii D, Levenspiel O (1991) Flow modeling of fast fluidized beds. In: Basu P, Hasatani M, Horio M (eds) Proceedings of circulating fluidized bed technology III, Pergamon Press, Oxford pp 91–98
16. Dutta A, Basu P (2002) Overall heat transfer to water-walls and wing walls of commercial circulating fluidized bed boilers. J Inst Energy 75:85–90
17. Basu P (2006) Combustion and gasification in fluidized beds. Taylor & Francis group, New York
18. John RG, Hsiaotao B, Mohammad G (2003) Circulating fluidized beds. Chapter 19, Handbook of fluidization and fluid particle systems, Marcel Dekker
19. Nowak W, Mirek P (2013) Circulating fluidized bed combustion. Woodhead Publishing Limited, pp 701–764
20. Wang Q, Luo Z, Li X, Fang M, Ni M, Cen K (1999) A mathematical model for a circulating fluidized bed (CFB) boiler. Energy 24:633–653
21. Kavidass S, Walker DJ, Nortan Jr Gs (1999) IR-CFB Repowering: A cost effective option for older PC fired boilers. Power-Gen International 99, BR-1687a, November 30-December 2, New Orleans, Louisiana, USA
22. Gauvillé P, Foucher J-C, Moreau D (2012) Achievable combustion efficiency with ALSTOM CFB boilers for burning discarded coal. J South Afr Inst Min Metall 112(6):437–447
23. Basu P, Halder PK (1989) A new concept for operation of a pulverized coal fired boiler using circulating fluidized bed firing. J Eng Gas Turbines Power 111:626–630
24. Belin F, Bolumen AG, Walker DJ, Babichev LA, Levin MM, Volkovitskaya PI (1996) 200 MW CFB boiler burning High-Ash Anthracite. In: Power-Gen international'96, BR-1629, December 4–6, Orlando, Florida, U.S.A
25. Sun X, Jiang M, Yu L, Zhang Y, Shi Z, Wang F, Zhang M, Huang Z (2013) Research and design of 330 MW circulating fluidized bed boiler. In: Cleaner combustion and sustainable world, Qi H, Zhao B (eds). Springer-Verlag, Berlin Heidelberg and Tsinghua University Press, pp 623–627
26. Lee J-M, Kim J-S, Kim J-J (2003) Evaluation of the 200 MWe Tonghae CFB boiler performance with cyclone modification. Energy 28:575–589
27. Yang C, Gou X (2006) Dynamic modeling and simulation of a 410 t/h Pyroflow CFB boiler. Comput Chem Eng 31:21–31
28. Sun YK, Lu QG, Bao SL, Na YJ, Gao ZY, Gu JS, Shao GZ, Shen YG, Wang HG (2011) Commercial operation test and performance analysis of a 200 MWe super-high-pressure circulating fluidized bed boiler. Ind Eng Chem Res 50:3517–3523
29. Wang Y, Lu J, Yang H, Zhao X, Yue G (2005) Measurement of heat transfer in a 465t/h circulating fluidized bed boiler. In: Proceedings of 18th international conference on fluidized bed combustion, FBC2005-78050, New York, ASME
30. Han X, Jiang X, Wang H, Cui Z (2006) Study on design of Huadian oil shale-fired circulating fluidized bed boiler. Fuel Process Technol 87:289–295
31. Qing W, Bai J, Zhao L, Sun B, Liu H (2008) Validity of an expert system for oil shale-fired CFB boiler design and performance analysis. Oil shale 25(4):400–411
32. Ni W, Li Z (1994) Modelling and simulation of the 50 MWe CFBC boiler. J Therm Sci 3(4):267–272
33. Gu J, Yang H, Li C, Lyu J (2017) Design and operation of a MSW and STRAW co-firing CFB boiler. In: Proceedings of 12th international conference on fluidized bed technology CFB-12, Centre of Energy, AGH University of Science and Technology Krakow, Poland, pp 1057–1063

34. Lu J, Zhang J, Zhang H, Liu Q, Yue G (2007) Performance evaluation of a 220t/h CFB boiler with water-cooled square cyclones. Fuel Process Technol 88:129–135
35. Han K, Hyun J, Choi W, Lee J (2009) A study of co-combustion characteristics of North Korean Anthracite and Bituminous Coal in 2 MWe CFBC Power Plant. Korean Chem Eng Res 47(5):580–586
36. Wang Q, Luo Z, Ni M, Cen K (2002) Model prediction of the operating behaviour of a circulating fluidized bed boiler. J Zhejiang Univ Sci 3:251–257

On the Critical Role of Surface Tension in Film Condensation onto a Horizontal Cylinder

Uttam Kumar Kar ⓘ **, Sayantan Sengupta** ⓘ **, and Shantanu Pramanik** ⓘ

Abstract   We explore the subtle role of surface tension on condensate drainage onto a horizontal cylinder. Our study considers a subcooled cylindrical surface exposed to a pool of saturated water vapour. The condensate film flow is assumed to be steady and laminar. We appropriately reduce the Navier–stokes equations in the cylindrical coordinate system invoking certain assumptions and build a simplified mathematical theory. We model the effects of surface tension by the well-known Laplace formula. We have used the temperature- dependent thermos-physical properties of liquid water for generalisation. The Reynolds' correlation is used to predict the viscosity of the liquid water. The model governing equations are solved for a suitable set of boundary conditions by the Runge–Kutta method. It is observed that the role of surface tension is predominant near the bottom of the cylinder, whereas it is reasonably weak in the upper part of the cylinder. We found that the film dynamics strongly depend on the cylinder radius. Furthermore, we develop correlations for predicting the local and average Nusselt number, which would be useful for engineering applications.

Keywords Mathematical modelling · Film condensation · Surface tension · Subcooling

1   Introduction

Film condensation has been studied extensively for its diverse applications in thermal power stations, chemical plants, refrigerators, air conditioners, and industrial cooling devices. We study free convective film condensation of saturated vapour over a horizontal cylinder, as shown in Fig. 1. Unlike the case of condensation onto a flat plate [1], the varying curvature of the condensate surface and non-uniform gravity field come into play here. Among many analyses on this subject area, the pioneering work was presented by Sparrow and Gregg [2], excluding the effect of surface tension.

U. K. Kar · S. Sengupta (✉) · S. Pramanik
National Institute of Technology, Durgapur, West Bengal 713209, India
e-mail: sayantan.sengupta@me.nitdgp.ac.in
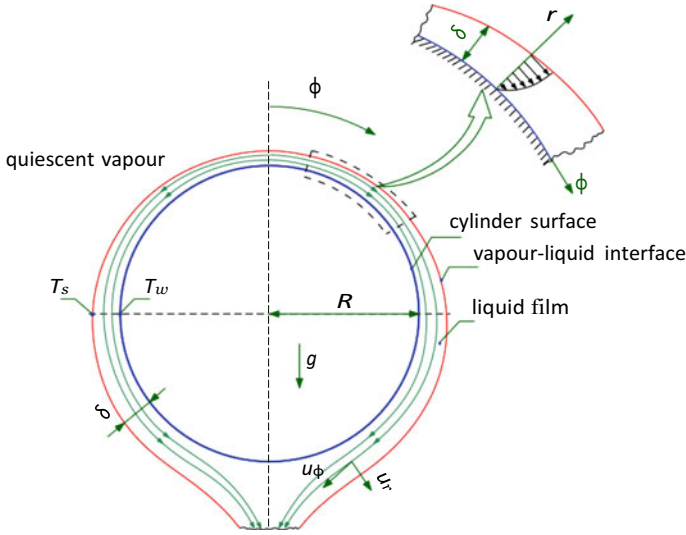
Fig. 1 Schematic representation of the condensate film forms over the outer surface of subcooled metallic tube submerged in a quiescent vapour bath

Later, Krupiczka [3] projected the importance of surface tension for film condensation occurring on wires and small-diameter tubes. An extension of Krupiczka's theoretical study is found in [4] for forced convection condensation. For forced convective cases, numerical simulations [5, 6] were performed to elucidate the dynamics of the liquid film as well as the vapour layer; experiments [7] were performed to study the condensation performance. Subsequently, the researchers experimentally investigated the effect of vapour superheating [8] and the presence of non-condensable gases [9] on condensation performance. The present study solely considers the case of free convection condensation, for which the cylinder rests at a quiescent vapour pool. We propose a mathematical model considering surface tension while neglecting the inertial terms of the Navier–Stokes equations. For the sake of generalisation, the temperature-dependent thermos-physical properties of liquid water are taken into account.

2 Mathematical Model

The present study addresses the critical role of surface tension on a dynamic condensing film forms around a circular cylinder. In this regard, we consider a subcooled cylindrical surface ($T_{\rm w}$) submerged in quiescent saturated water vapour ($T_{\rm s}$). The surrounding vapour close to the cold surface condenses onto the surface as tiny droplets by exchanging latent enthalpy (ΔH). A continuous film forms over the curved surface as the process reaches the steady state. Here, the falling film

grows in the radial direction due to continuous entrainment of vapour mass across the interface. Figure 1 describes a steady-state picture of the process considered in this study. We establish a simple mathematical model based on a few assumptions without much sacrificing the physics of thin-film flow.

We assume the condensate flow as steady, laminar, and incompressible. The density of the vapour (ρ_v) is much less compared to the density of the liquid (ρ_l), and as the surrounding vapour is quiescent, the effect of interfacial shear is neglected. We also consider the boundary layer theory assumptions for the analysis of the film dynamics, thus, ignored the cross stream pressure variation inside the liquid film. Again, the temperature variation across the film is assumed to be linear, and thermal equilibrium is preserved at the liquid–vapour interface as the vapour is dry saturated. The thermos-physical properties of both liquid and vapour phases are constant, except the liquid's viscosity varies exponentially with temperature [10].

2.1 Model Equations and Boundary Conditions

Here, we introduce the conservation equations and boundary conditions in their simplified form, implementing the above assumptions. Therefore, conservation equations of mass, momentum, and energy are presented in cylindrical coordinate system one after another. The conservation equation for mass in two-dimensional form can be written as

$$\frac{\partial u_\phi}{R \partial_\phi} + \frac{\partial u_r}{\partial r} = 0, \tag{1}$$

where R is the radius of the tube and u_ϕ and u_r are the tangential and radial velocities of the liquid at a point, respectively. In the absence of inertia terms, the ϕ-momentum equation will be

$$\nu_l \frac{\partial^2 u_\phi}{\partial r^2} + g \sin\phi - \frac{1}{\rho R} \frac{\partial p}{\partial \phi} = 0, \tag{2}$$

where ρ is the density of the liquid, g is the acceleration due to gravity, p is the static pressure, and ν_l is the kinematic viscosity of the liquid. If the pressure gradient ($\partial p/\partial\phi$) is caused by surface tension force [3] only, then

$$\frac{\partial p}{\partial \phi} \equiv -\frac{\sigma}{R^2} \frac{d\delta}{d\phi}. \tag{3}$$

Now, substituting the above expression, Eq. (2) transforms into the following form:

$$\nu\iota\frac{\partial^2 u_\phi}{\partial r^2} + g\sin\phi + \frac{\sigma}{\rho R^3}\frac{d\delta}{d\phi} = 0, \tag{4}$$

where σ is the surface tension and δ represents the film thickness. Again, to predict effect of viscosity on film dynamics accurately, the temperature dependence of kinematic viscosity of water (ν_l) satisfactorily correlated as $\nu_l = \nu_0\, e^{-aT}$, where $\nu_0 = 0.00006$ and $a = 0.015$ [10, 11]. Then, introducing the linear temperature distribution the kinematic viscosity of water varies radially across the film as $\nu_l = \alpha e^{-\beta r}$, where $\alpha = \nu_0 e^{-aT_W}$ and $\beta = a\Delta T/\delta$. Therefore, the ϕ-momentum equation reduces to

$$\frac{\partial^2 u_\phi}{\partial r^2} = -\frac{1}{\alpha}\left[g\sin\phi + \frac{\sigma}{\rho R^3}\frac{d\delta}{d\phi}\right]e^{\beta r}. \tag{5}$$

As the thickness of the condensing film is very thin, the latent heat released by the saturated vapour is transported to the tube wall by conduction across the film. Therefore, the energy conservation equation can be written as:

$$\delta\frac{d}{Rd\phi}\left[\int_0^\delta u_\phi dr\right] = \frac{\lambda}{\rho}\frac{(T_s - T_w)}{\Delta H}, \tag{6}$$

where λ is the thermal conductivity of the liquid.

Integrating Eq. (5) twice and applying the following boundary conditions:

$$\text{at}\quad r = \delta,\quad \frac{\partial u_\phi}{\partial r} = 0 \tag{7}$$

$$\text{at}\quad r = 0,\ u_\phi = 0 \tag{8}$$

we obtain the distribution of u_ϕ across the film as follows:

where

$$u_\phi(r) = \frac{C}{\beta^2}\left[e^{\beta r} - \beta e^{\beta\delta}r - 1\right], \tag{9}$$

$$C = -\frac{1}{\alpha}\left[g\sin\phi + \frac{\sigma}{\rho r^3}\frac{d\delta}{d\phi}\right] = f(\phi)\ \text{only}. \tag{10}$$

Having achieved the velocity profile given by Eq. (9), we have solved the differential–integral form the energy Eq. (6) which reduces to the following form:

$$\delta^4\left\{\cos\phi + \frac{We}{R}\frac{d^2\delta}{d\phi^2}\right\} + 3\delta^3\left\{\sin\phi\frac{d\delta}{d\phi} + \frac{We}{R}\left(\frac{d\delta}{d\phi}\right)^2\right\} = \frac{1}{C_5}\frac{\alpha^2 R}{g}\frac{Ja}{\Pr_{l,0}}e^{aT_w}, \tag{11}$$

Table 1 Expressions of dimensionless numbers appearing in Eq. (12)

Dimensionless number	Symbol	Definition
Weber number	We	$\frac{\sigma}{\rho g R^2}$
Jacob number	Ja	$\frac{c_P(T_s - T_w)}{\Delta H}$
Prandtl number	$\mathrm{Pr}_{l,0}$	$\frac{\alpha \rho c_P}{\lambda}$

where

$$C_5 = \left\{ \frac{\int 1}{C_3^3} - \frac{C_4}{C_3^3} + \frac{1}{C_3^2} + \frac{C_4}{2C_3} \right\}^{\int} \tag{12}$$

$C_3 = a\Delta T$ and $C_4 = e^{a\Delta T}$. Table 1 describes the expressions of dimensionless numbers appearing in Eq. (12).

2.2 Dimensionless Model Equations and Initial Conditions

Here, we assume a suitable scale $\delta_s \equiv (\alpha^2 R/g)^{1/4}$ to non-dimensionalise the film thickness δ. Therefore, the expression for non-dimensional film thickness became:

$$\delta^* = \frac{\delta}{\delta_s}. \tag{13}$$

Accordingly, dimensionless form of Eq. (11) can be written as

$$(\delta^*)^4 \left\{ \int \cos\phi + \delta_s \frac{We}{r} \frac{d^2\delta^*}{d\phi^2} \right\}^{\int} + 3\,(\delta^*)^3 \left\{ \int \sin\phi \frac{d\delta^*}{d\phi} + \delta_s \frac{We}{r} \left(\frac{d\delta^*}{d\phi} \right)^2 \right\}^{\int} = \frac{1}{C_5} \frac{Ja}{Pr_{l,0}} e^{a\,Tw}. \tag{14}$$

Now, we define the dimensionless groups appearing in Eq. (13) as follows:

$$Q_1 = \frac{1}{C_5} \frac{Ja}{\mathrm{Pr}_{l,0}} e^{aT_w}, \tag{15}$$

and,

$$Q_2 = \frac{1}{\left\{ \frac{1}{4}We\ R^{-\frac{3}{4}} \sqrt[4]{\frac{\alpha^2}{g}} \right\}^{\int}} = \frac{1}{\left\{ \frac{1}{4}We^{\frac{11}{8}} N_p^{\frac{3}{8}} \right\}^{\int}} \tag{16}$$

where,

$$N_p = \left(\frac{\rho g^{\frac{1}{3}} \alpha^{\frac{4}{3}}}{\sigma} \right)^{\int}. \tag{17}$$

We define this dimensionless parameter (N_{p}) as property number since it is a combination of hydrodynamic properties of a fluid. Accordingly, Eq. (14) reduces to

$$\frac{d^2\delta^*}{d\phi^2} = \left\{ Q_1 - (\delta^*)^4 \cos\phi - 3\,(\delta^*)^3\,\sin\phi\,\frac{d\delta^*}{d\phi} - \frac{3}{Q_2}(\delta^*)^3 \left(\frac{d\delta^*}{d\phi}\right)^2 \right\} Q_2\,(\delta^*)^{-4}. \tag{18}$$

The required initial condition to solve dimensionless governing Eq. (18) numerically is $(\delta^*)_{\phi=0}$ and $(d\delta^*/d\phi)_{\phi=0}$. The second initial condition directly comes from the symmetry of the problem at $\phi = 0$ as

$$\frac{d\delta^*}{d\phi} = \frac{d\delta}{d\phi} = 0 \quad \text{at } \phi = 0. \tag{19}$$

Again, the variation of film thickness is assumed to be linear in the neighbourhood of $\phi \to 0$; therefore, $(d^2\delta^*/d\phi^2)_{\phi=0} = 0$. Now, applying the above assumption to Eq. (18) gives us the first initial condition as

$$\delta^* = \sqrt[4]{Q_1} \quad \text{at } \phi = 0. \tag{20}$$

Integration of Eq. (18) subject to initial conditions (19) and (20) gives normalised film thickness δ^* as a function of ϕ and the dimensionless groups Q_1 and Q_2.

3 Heat Transfer Analysis

Furthermore, the heat transfer performance of the system can be justified based on the optimum value of average heat transfer coefficient (h_{m}) comparing with the expenditure of cooling effort. The local and average heat transfer coefficients, h_ϕ and h_{m}, can be evaluated using the following technique [1]:

The peripheral distribution of dimensional film thickness $(\delta_{\phi,Q})$ can be evaluated using Eq. (13) as

$$\delta_{\phi,Q} = \delta^*\delta_{\mathrm{s}} = \frac{1}{C_{\phi,Q}}\left(\frac{\alpha^2 R}{g}\right)^{\frac{1}{4}}. \tag{21}$$

Therefore, the expression of local heat transfer coefficient (h_ϕ) will be

$$h_\phi = \frac{\lambda}{\delta_{\phi,Q}} = C_{\phi,Q}\,\lambda\left(\frac{g}{\alpha^2 R}\right)^{\frac{1}{4}}, \tag{22}$$

and the average heat transfer coefficient (h_{m}) can be evaluated as

$$h_{\mathrm{m}} = \overline{C}_{\phi,Q}\,\lambda \left(\frac{\int g}{\alpha^2 R}\right)^{\frac{1}{4}},\tag{23}$$

where

$$\overline{C}_{\phi,Q} = \frac{1}{(\phi_2 - \phi_1)} \int_{\phi_1}^{\phi_2} C_{\phi,Q}\,\mathrm{d}\phi.\tag{24}$$

The local Nusselt number can be expressed as:

$$\mathrm{Nu} = \frac{h_\phi \delta_{\mathrm{s}}}{\lambda},\tag{25}$$

if we use 'δ_{s}' as the length scale.

Therefore, the local Nusselt number will be:

$$\mathrm{Nu} = \frac{C_{\phi,Q}\lambda}{\lambda}\left(\frac{\int g}{\alpha^2 r}\right)^{\frac{1}{4}}\delta_{\mathrm{s}} = C_{\phi,Q},\tag{26}$$

and the average Nusselt number will be,

$$\mathrm{Nu}_{\mathrm{m}} = \frac{h_{\mathrm{m}}\delta_{\mathrm{s}}}{\lambda} = \overline{C}_{\phi,Q}.\tag{27}$$

4 Discussion

This section analyses the change in the peripheral distribution of dimensionless film thickness over tube surface for various circumstances. The condensation process occurs in a non-uniform gravity field; besides the body force, the influence of surface tension and viscous force is considered here. In this context, we have examined the effect subcooling and surface tension force on the condensation process by varying the Ja and We, respectively. Additionally, we have commented on the heat transfer characteristics of the condensing surface.

It is evident from the geometry of the condensing surface (see Fig. 1) that the tangential component of body force ($g \sin \phi$) starts increasing from its minimum at $\phi = 0$ and becomes maximum at $\phi = \pi/2$, then again starts decreasing and reaches to its minimum at $\phi = \pi$. Therefore, one can expect a trend of decrease in film thickness up to $\phi = \pi$ as the fluid particles accelerate in this zone. However, the actual phenomenon is different because the combined effect of wall shear and momentum exchange between the condensing mass and the liquid film reduces the kinetic energy of the fluid particle downstream. Figure 2 shows that for Ja = 0.0093, the dimensionless film thickness (δ^*) increases very slowly up to $\phi = 2.0$, then

Fig. 2 Peripheral
distribution of the
dimensionless film thickness
(δ^*) for different values of
Jacob number (Ja) [at We $=$
0.01695]
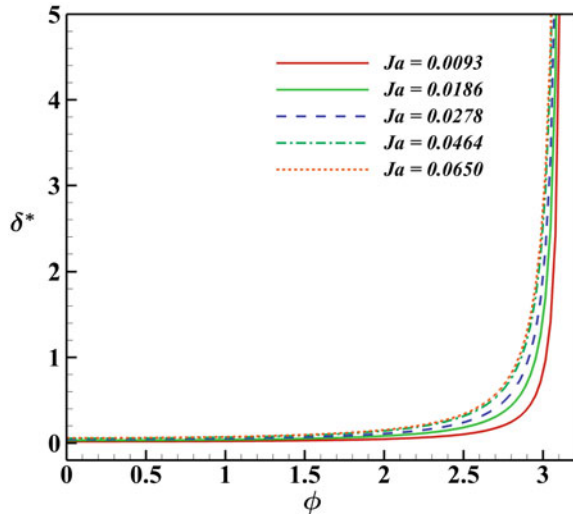
increases gradually up to $\phi = 3.0$ after that jumps to a higher value suddenly which
may be due to the dripping effect. After crossing the maximum body force point ($\phi =
\pi$), the fluid particles start to decelerate and cause a rapid increase in film thickness
as shown in Fig. 2. The gravity force balances the viscous force in the upper part
of the cylinder. However, due to the rapid increase in curvature, the surface tension
force starts to neutralise the viscous force, and the effect of gravity vanishes as fluid
particles reaches $\phi = \pi$.

We have altered the values of Ja to verify the effect of subcooling on the
film dynamics; thus, Jacob's number is varied from 0.0093 to 0.0650. Figure 2
depicts that as we increase the subcooling effect, the average thickness of the film
$\delta_{avg}^* \equiv (1/\phi) \int \delta^* d\phi$ increases up to Ja $= 0.0186$. However, the effect is more signif-
icant in the ϕ lower part of the cylinder. Further increase in Ja causes overlapping
of the curves, which indicates that $\delta_{a}^*{}_{vg}$ becomes independent of Ja. An increase
in subcooling effort increases the rate of condensation; therefore, a limiting value
of $\delta_{a}^*{}_{vg}$ indicates the faster condensate drainage where liquid inertia will play an
important role. As we have neglected the effect of inertia in our mathematical model,
therefore, further increase in Ja cannot predict the physics accurately. For this reason,
we restrict the case study up to Ja $= 0.0650$.

Again, to examine the effect of surface tension force on the film dynamics, we
varied the Weber number (We) from 0.1060 to 6.7818, keeping the Ja fixed to Ja
$= 0.0650$. Figure 3 shows that instead of increasing the We, the distribution of
dimensionless film thickness (δ^*) is almost identical for all We in the upper part
of the cylinder. However, δ^* distribution is distinguishable in the lower part of the
cylinder as the effect of We is significant in this zone. At higher values of We ($=
6.7818$), the pressure gradient due to the surface tension becomes dominant and
drives the condensate downwards; hence, growth of δ^* is not rapid in the lower part
of the cylinder. Moreover, the viscous effects start to overtake the favourable pressure

Fig. 3 Variation of the
dimensionless film thickness
(δ^*) for various values of
Weber number (*We*) [at Ja =
0.0650]
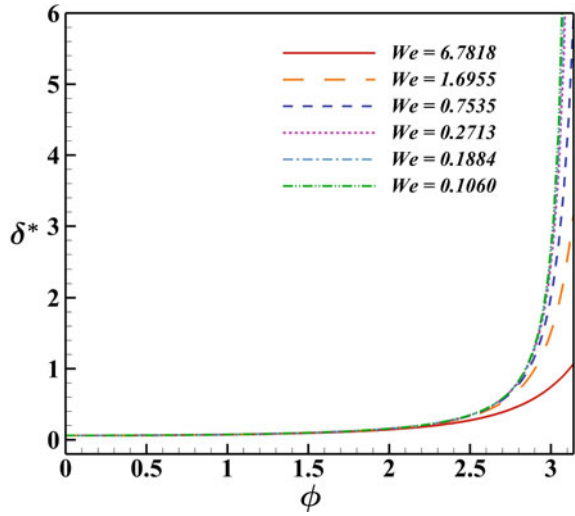
gradient manifested by the surface tension force as We and cause a rapid growth in
the condensing film. Figure 3 also depicts that for We < 0.1884, the distribution of
δ^* became independent of We. The expression of the average Nusselt number (Nu$_m$)
described in Eq. (27) plays an important role to predict the heat transfer performance
of the surface. Equation (27) shows that Nu$_m$ is inversely proportional to $(\delta_a^*{}_{vg})^{1/4}$.
Therefore, the characteristics of film thickness variation decide the heat transfer
performance of the surface: the lower the film thickness, the higher will be the heat
transfer across the film. More heat can be conducted across the condensing film if the
thickness is small because the liquid film blanket acts as a barrier to the heat transfer
process.

5 Conclusion

In this study, we attempt to explore the role of surface tension on the condensa-
tion process occurring in a non-uniform body force (gravity) field. Therefore, we
have considered a horizontal circular cylinder whose outer surface was exposed
to saturated water vapour. The thickness of the tube wall is assumed to be negli-
gible and maintained at constant temperature. The fluid flow encapsulating the
condensing film has modelled considering assumptions of boundary layer theory.
The temperature dependence of liquid viscosity is incorporated in the model, while
other thermos-physical properties of the condensate remain constant.

The effect of subcooling on the condensation process has been studied by altering
the Jacob number (Ja). Results reveal that after reaching a critical value of Ja, the
overall thickness of the film ceases to increase. Again, the investigation of Weber
number (We) variation shows that influence of surface tension force is dominant for

higher values of We (= 6.7818), and the effect is localised in the lower part of the cylinder. For comparatively lower values of We (= 0.1060), the surface tension effect is insignificant.

Equation (27) provides the expression of average Nusselt number (Nu_m) which decides the thermal performance of the system. Analysis shows that Nu_m is inversely proportional to the average dimensionless film thickness ($\delta_a^*{}_{vg}$). Therefore, more heat can be transferred across the tube wall if the average film thickness is low.

In this article, we have neglected the effect of liquid inertia; however, our study reveals that a similar work with higher rate of subcooling (Ja > 0.0650) can only be performed if inertia effect is considered.

References

1. Nusselt W (1916) Die oberflhenkondensation des wasserdampfes. Z Ver Dtsch Ing 60(27):541–546
2. Sparrow E, Gregg J (1959) A boundary-layer treatment of laminar-film condensation. ASME J Heat Transfer 81:13–17
3. Krupiczka R (1985) Effect of surface tension on laminar film condensation on a horizontal cylinder. Chem Eng Process 19(4):199–203
4. Jacobi A, Goldschmidt V (1989) The effect of surface tension variation on filmwise condensation and heat transfer on a cylinder in cross flow. Int J Heat Mass Transfer 32(8):1483–1490
5. Saleh EA, Ormiston SJ (2016) A sharp-interface elliptic two-phase numerical model of laminar film condensation on a horizontal tube. Int J Heat Mass Transfer 102:1169–1179
6. Zhang J, Li W, Minkowycz W (2016) Numerical simulation of condensation for r410a at varying saturation temperatures in mini/micro tubes. Numer Heat Transf A 69(5):464–478
7. Fouda A, Wasel M, Hamed A, Zeidan ESB, Elattar H (2015) Investigation of the condensation process of moist air around horizontal pipe. Int J Therm Sci 90:38–52
8. Zhao Z, Li Y, Wang L, Zhu K, Xie F (2015) Experimental study on film condensation of superheated vapour on a horizontal tube. Exp Therm Fluid Sci 61:153–162
9. Tang G, Hu H, Zhuang Z, Tao W (2012) Film condensation heat transfer on a horizontal tube in presence of a noncondensable gas. Appl Therm Eng 36:414–425
10. Reynolds O (1885) On the theory of lubrication and its application to Mr. Beauchamp tower's experiments, including an experimental determination of the viscosity of olive oil. Phil Trans Roy Soc 1:157
11. Kar UK, Sengupta S, Pramanik S (2022) Dynamics of condensate film in the vicinity of a pulling vapor stream. Phys Fluids 34(12):123611

Artificial Roughness-Aided Performance Improvement of a Solar Chimney Power Plant: A Numerical Investigation of Conjugate Heat Transfer

Avishek Mukherjee, Sayantan Sengupta, Uttam Kumar Kar, and Achintya Kumar Pramanick

Abstract A solar chimney power plant (SCPP), consisting of four essential components: a chimney, a collector, a turbine and an energy storage layer, is a typical kind of thermal power plant that converts solar radiation into electricity using natural convection. The collector is the most important part of an SCPP, where the air is heated up due to solar radiation. The heated air finds its path through the chimney, resting vertically at the central portion of the collector. Thus, a better collector design always ensures greater effective buoyancy, considered as the driving mechanism of the turbine. Here, we utilize artificial roughness elements either at the roof or at the ground of the collector to enhance the effective heat transfer and, thereby, the net buoyancy. We consider rectangular roughness elements, the height varying from 4 to 25 mm. The parametric study is performed by computational fluid dynamic (CFD) simulations incorporating conjugate heat transfer effects. The fluid and solid domains of the SCPP are resolved separately in the simulations by solving the Navier–Stokes equations and the Laplace equation, respectively. The standard k–ε model resolves the turbulence within the fluid domain. Finally, we obtain that the ground roughness yields better performance than the roof roughness. The maximum overall performance is achieved at a ground roughness height of 11 mm.

Keywords Solar chimney · Artificial roughness · Turbulence · Natural convection · Performance

A. Mukherjee · S. Sengupta (✉) · U. K. Kar · A. K. Pramanick
Department of Mechanical Engineering, National Institute of Technology, Durgapur, W.B 713209, India
e-mail: sayantan.sengupta@me.nitdgp.ac.in

1 Introduction

In the current situation, energy is the backbone of any country's socioeconomic development. An ever-increasing population and good living standards necessitate limitless energy resources to meet expanding energy demand. Non-renewable energy supplies (fossil fuels) are finite and are overused; hence, they must be limited. Similarly, extensive fossil fuel consumption has badly contaminated our environment, putting life on our planet in jeopardy. This overall circumstance needs technological improvements in generating clean and sustainable energy. The solar chimney power plant (SCPP) will have an excellent possibility for large-scale conversion of solar radiation energy. An SCPP is a thermal power plant that converts solar radiation into electricity. The collector, wind turbine and chimney are the three basic components of a traditional SCPP. In our setup, a semi-transparent collector constructed of soda lime glass (3 mm thick) covers the ground area. The collector's ground, acting here as an energy storage layer, is made of steel (2 mm thick). A PVC chimney is positioned at the centre of the collector. The size of the computational domain is kept fixed throughout the study, i.e., the chimney radius is 0.1 m, and chimney height is 2 m, the collector radius is 1.5 m, and the gap between the ground and roof of the collector is kept as 0.06 m.

The collector's operation can be explained from the knowledge of radiation heat transfer. Short-wavelength solar radiation can easily pass through the semi-transparent collector's roof before being absorbed by the ground, raising the temperature of the ground surface. The radiation emitted from the ground surface is in the long-wavelength region [1], which is why it cannot pass through the collector's roof. As a result, thermal energy is trapped inside the collector leading to a rise in air temperature within the collector space. This phenomenon is known as the greenhouse effect. The density of the air inside the collector is reduced as it warms, and then, due to the density difference, a constant updraft is produced. Thus, the air is pumped by the chimney as a result of the net upward buoyancy force. A wind turbine is placed inside the chimney to transform the kinetic energy of the fluid stream into shaft power, which is finally converted into electricity by using a generator. Of many variables controlling the efficiency of an SCPP, such as the chimney geometry, collector geometry, geographical location (latitude, longitude) and meteorological conditions, we focus on the most sensitive one, which is the collector geometry.

Natural convection through energy-producing devices is not that old that has gained popularity in a few decades. The wind tower, Trombe wall and solar chimney are passive devices operating under natural convection. In 1982, a prototype of SCPP with a nominal output capacity of 50 kW was built in Manzanares, Spain, and tested for seven years [2–4]. However, the efficiency of the SCPP could have been higher. Later, research is performed to improve the overall performance of an SCPP by several geometrical modifications. In the present study, we implement artificial roughness to modify the collector's profile, resulting in increased buoyancy aiming to improve the overall performance of an SCPP. Rectangular roughness elements are placed either on the ground or on the roof of the collector. The impact

of such geometrical modifications is examined in CFD simulations performed over a range of roughness heights. Literature shows some prior studies on the effect of roof roughness [5] and ground roughness [6] on the performance of an SCPP. Here, we are interested in doing a comparative study to examine which artificial roughness performs better than the other. To our knowledge, no such comparative study has been conducted thus far.

2 Method of CFD Simulations

To describe the buoyant airflow inside the SCPP, we assume steady, 2D axisymmetric and incompressible turbulence. The material properties are shown in Table 1. The fluid and solid domains of the SCPP are resolved separately in the simulations by solving the Navier–Stokes equations and the Laplace equation, respectively. The Boussinesq approximation is used to simulate the body force term [7]. The turbulence within the fluid domain is resolved by the standard k-ε model, where $C_{1\epsilon} = 1.44, C_{2\epsilon} = 1.92$ and $\sigma_\epsilon = 1.3, \sigma_k = 1$. The turbulent viscosity μ_t varies spatially and is modelled by $\rho C_\mu \frac{k^2}{\epsilon}$, where $C_\mu = 0.090$. Simulations are executed by a CFD software Ansys Fluent [8]. Coupled algorithm with second-order discretization techniques is employed. The scaled residuals for convergence requirements are set as 10^{-6}.

2.1 Geometric Details and Boundary Conditions

Figure 1 shows the schematic of the current setup, geometrical dimensions, meshes and boundary conditions. The symbols c, G, h, H, p, r and R denote the clearance distance from the axis, the gap between the roof and ground, roughness height,

Table 1 Properties of working fluid and solid materials

Material properties	Steel	PVC	Soda lime glass
Density in (kg/m^3)	8030	1380	2500
Sp. heat transfer coefficient (W/m^2 K)	502.48	1100	870
Thermal conductivity in (W/mK)	16.27	0.18	1.06
Fluid properties	*Air*		
Density in (kg/m^3)	1.1414		
Sp. heat transfer coefficient (W/m^2 K)	1007.24		
Viscosity (kg/m s)	0.0000187		
Thermal conductivity in (W/mK)	0.02674		
Thermal expansion (1/K)	0.003268		

chimney height, roughness pitch, chimney radius, collector radius and roughness width, respectively. Simulations are run over a range of roughness heights. A uniform heat flux of 800 W/m² [9], equivalent to total solar thermal energy absorption at the energy storage layer, is imposed at the ground plate (absorber). The ambient temperature is constant (306 K). The outer surface of the collector's roof is a transparent isothermal wall with a fixed temperature same as the ambient. The chimney wall is insulated, on which heat flux is zero. The pressure outlet and the pressure inlet boundary conditions, respectively, model the outlet and inlet of the system. At the inlet and outlet, the turbulent inlet intensity and turbulent viscosity ratios are kept at 3.7% and 10, respectively.
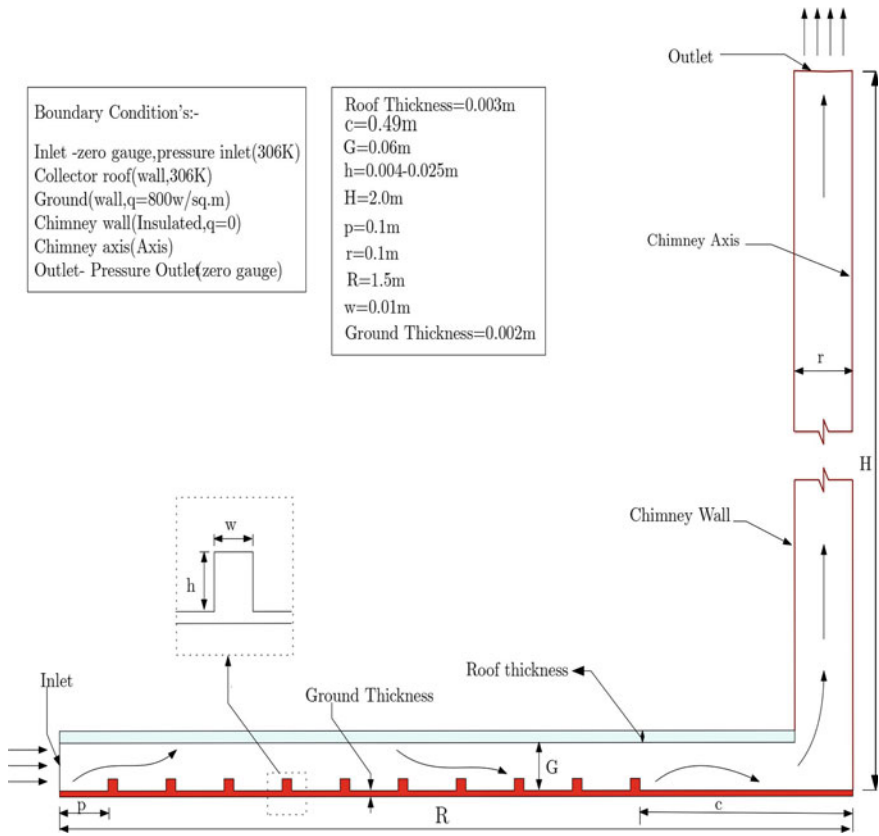
Fig. 1 Schematic representation of the computational domain and boundary condition

2.2 Grid Independence Test and Validation

We perform grid independence tests with several grid distributions to ensure that the computational results are independent of mesh elements' size. Figure 2 depicts the variation in the average temperature within the collector space for five distinct cell layouts. The findings show that the collector temperature close to the inlet is nearly the same for all grid distributions. However, the maximum temperature differs by 0.2 °C as the number of cells changes from 551,000 to 928,000. We consider the distribution corresponding to 640,000 cells as the optimum one without sacrificing accuracy. The present numerical model and the adapted CFD techniques are upheld by the experimental and numerical results of Kasaeian et al. [9]. Figure 3 compares the average roof temperature obtained in the present study with the results of Kasaeian et al. [9].

3 Results and Discussion

We run CFD simulations considering a 2D axisymmetric geometry for both the fluid and solid domains. We evaluate the impact of roughness elements on conjugate heat transfer and fluid flow characteristics. By adjusting the h value (4–25 mm), the influences of collector ground and roof roughness are examined separately. Purposefully, we have undertaken the friction factor (f) formulation from Bernardes et al. [10]; and thermal performance (j) and overall thermal performance (λ) are estimated by Kurian et al. [11].

The friction factor is estimated as:

Fig. 2 Results of grid independence test showing collector's centreline temperature versus radius
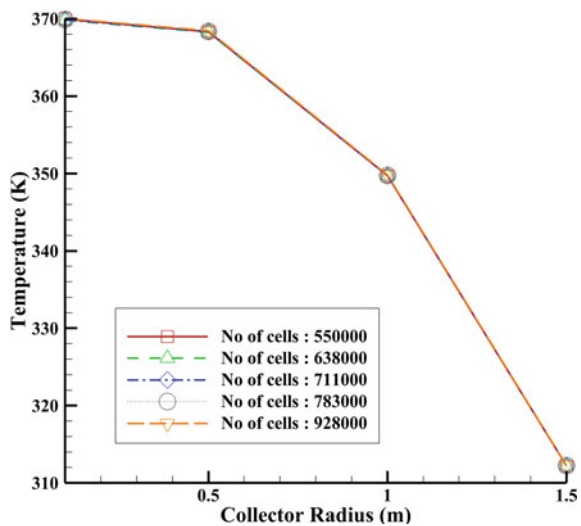
Fig. 3 Validating the present CFD method with the experimental and numerical data of Ref. [9]
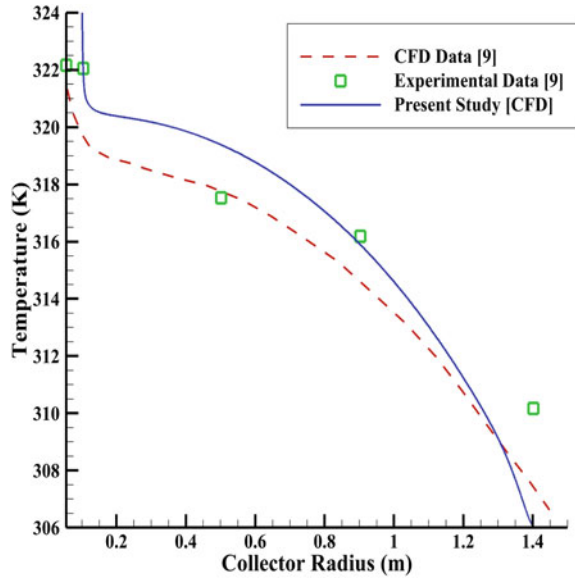
$$f = \left(\frac{\tau_{\text{ground}} + \tau_{\text{roof}}}{\rho * u_{\text{mean}}^2} \right) \qquad (1)$$

Thermal performance is estimated as:

$$j = \text{St} * (\text{Pr})^{\frac{2}{3}} \qquad (2)$$

Overall thermal performance is estimated as:

$$\lambda = \left(\frac{j}{f} \right) \qquad (3)$$

3.1 Contours of Various Parameters

First, we illustrate the flow features at the central portion of the SCPP, where the chimney is located. Figure 4c shows the streamlines in the chimney, in the central zone of the collector and at their junction. It is interesting to note how the streamlines alter radially inward to vertically upward. Near the collector wall, the streamlines are radially inward, whereas they are vertically upward within the chimney space. The marked change occurs at the base of the chimney, near the junction of the chimney and the collector. Figure 4a displays the contours of temperature in the chimney space. It is observed that temperature rises radially inward but decreases when fluid
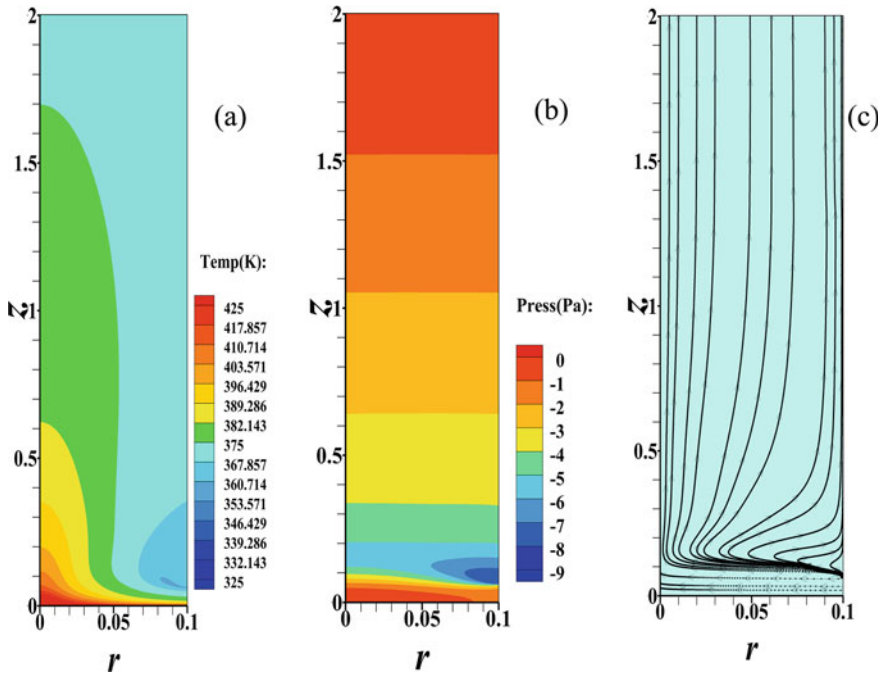
Fig. 4 Streamlines and contours inside chimney **a** temperature (T); **b** static pressure (p); **c** streamlines; in the presence of ground roughness ($h = 0.011$ m)

convects vertically upward. Figures 4b and 5a together exhibit how pressure rises with a corresponding fall of axial velocity towards the chimney exit. The radial velocity contours (Fig. 5b) and the streamlines (Fig. 4c) near the chimney base indicate the separation and reversal of radial flow. The adverse pressure gradient at the central zone of SCPP, illustrated in Fig. 4b, causes the flow separation. The streamline bending (Fig. 4c) is indicative of the radial flow reversal.

The contours of velocity and temperature within the collector for two different types of roughness (ground and roof) are shown in Figs. 6 and 7. The radial velocity is predominant of the two velocity components, viz. radial and axial. It is expected that the magnitude of area-average radial velocity should increase in the radially inward direction to satisfy the requirement of mass conservation since the flow area monotonically decreases in this direction. The contours of radial velocity (Figs. 6a and 7a) corroborate this conclusion. However, locally this conclusion may be violated. For example, near the roughness elements, the flow is separated due to obstruction, and some radial momentum is converted to axial momentum (as exhibited in Figs. 6b and 7b). Owing to such transformation, the axial velocity would be of the order of the radial velocity, and the expected trend may be violated. However, the local evolution of the axial component brings forth a rise in turbulent kinetic energy. Consequently, good cross-stream mixing occurs, as reflected in the thermal boundary layers shown

Fig. 5 Contours in chimney:
a axial velocity (w), **b** radial
velocity (u) for ground
roughness $h = 0.011$ m
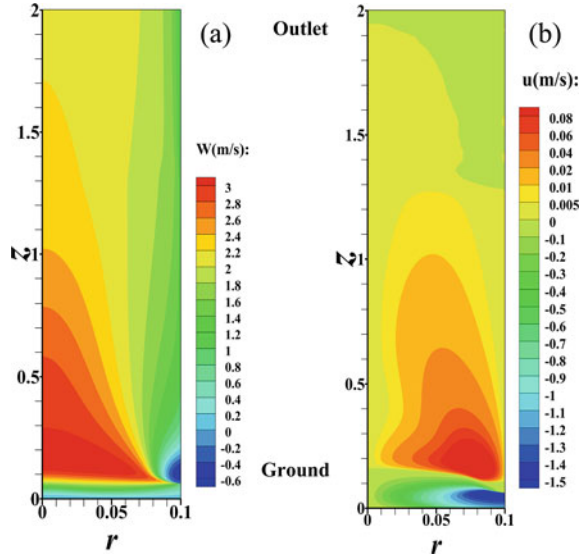
in Figs. 6c and 7c. This additional cross-stream mixing may increase the collector's
performance if the streamwise advection is not disturbed too much.

3.2 Performance Analysis

Figures 8 and 9 reveal two distinct characteristics of performance improvement by
reversing the placement of artificial roughness elements. Figure 8 depicts that the
friction factor (f) first decreases with an increase in h and then increases beyond h
$= 0.011$ m. The increase in f is more rapid in the presence of roof roughness than
ground roughness; the overall trend is that roof roughness yields a more significant
pressure loss than ground roughness. The advantage of ground roughness compared
to roof roughness is also reflected in the average trend of the thermal performance
parameter (j). Thus, ground roughness provides better overall thermal performance
(λ) than roof roughness (Fig. 9). We observe that the graphs of λ versus h exhibit a
peak attained at $h = 0.011$ m for the case of ground roughness and at $h = 0.01$ m for
roof roughness.

 We investigate further to understand the reason why ground roughness offers
better performance characteristics than roof roughness. Figure 10 shows the velocity
vectors close to the roughness elements. The vector arrows near the centreline of the
collector are almost parallel to the direction of the radial inflow. However, the vector
arrows near the roughness elements alter their arrangements significantly due to the
evolution of a cross-stream flow. This cross-stream secondary flow generates vortices
behind the roughness elements, which improves mixing within the thermal boundary
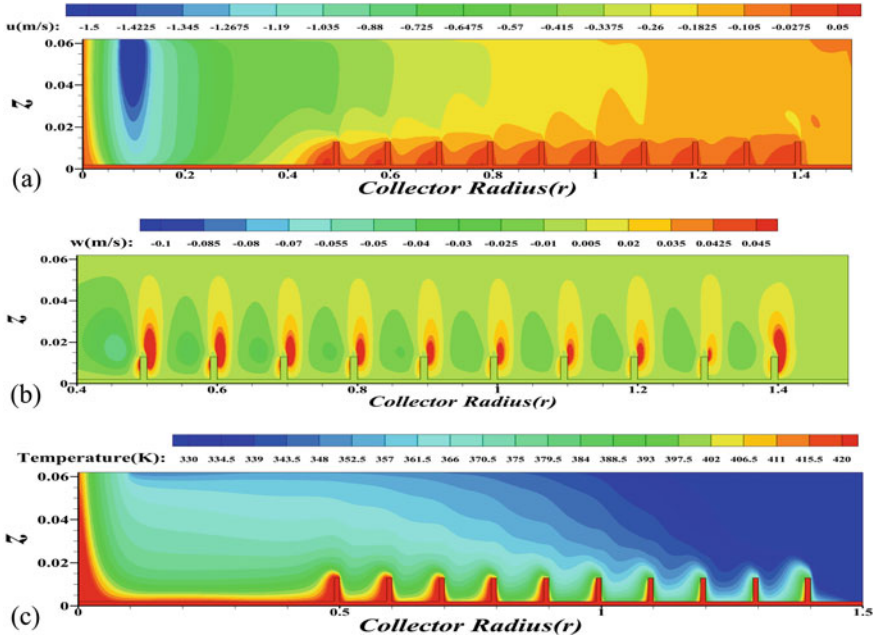
Fig. 6 Contours within collector space: **a** radial velocity (u), **b** axial velocity (w), **c** temperature (T) in the presence of ground roughness, $h = 0.01$ m

layer. It is observed that the temperature gradient near the ground roughness elements is considerably higher than the roof roughness elements. Accordingly, the potential of thermal mixing would be higher in case of ground roughness.
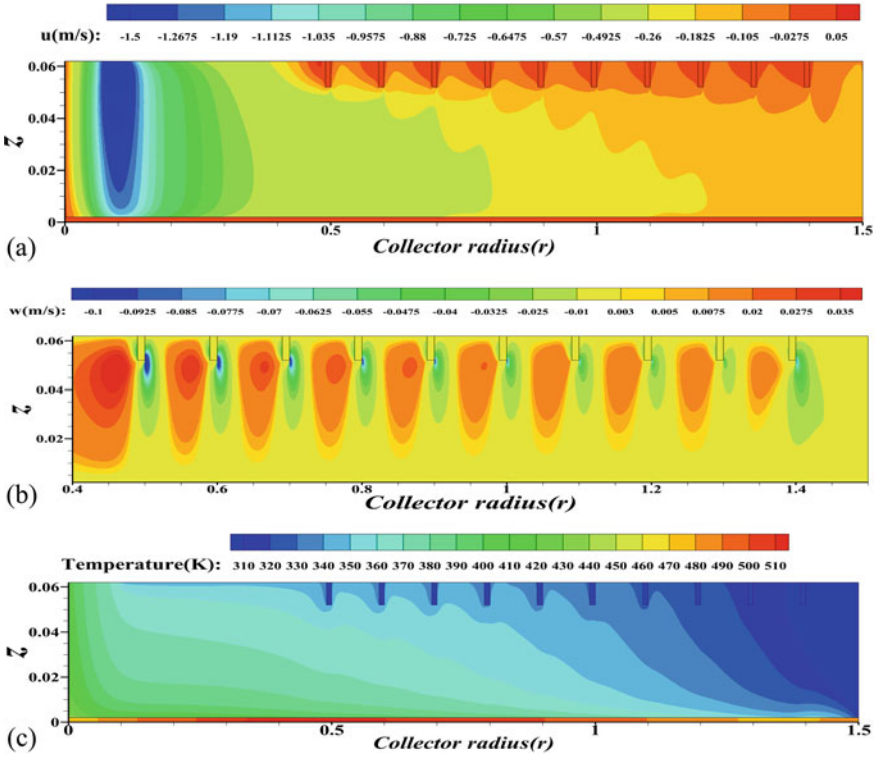
Fig. 7 Contours within collector space: **a** Radial velocity (u), **b** axial velocity (w), **c** temperature (T) in the presence of roof roughness, $h = 0.01$ m
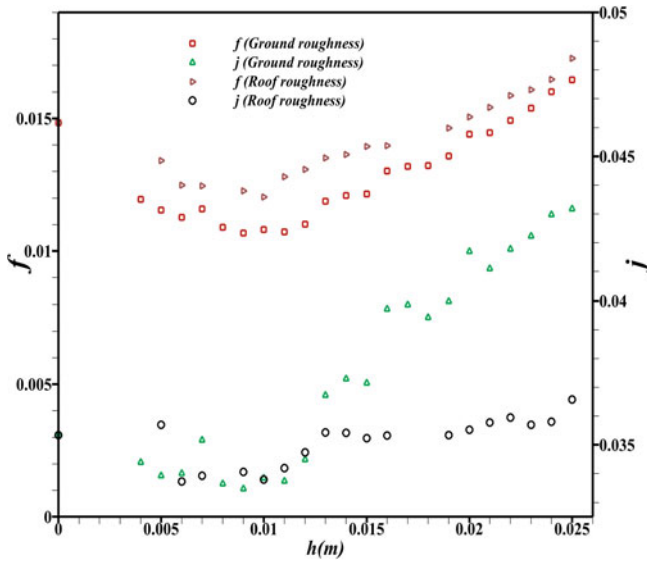
Fig. 8 Effect of roughness height (h) on the variation of friction factor (f) and thermal performance (j)

Fig. 9 Effect of roughness height (h) on the variation of overall thermal performance (λ)
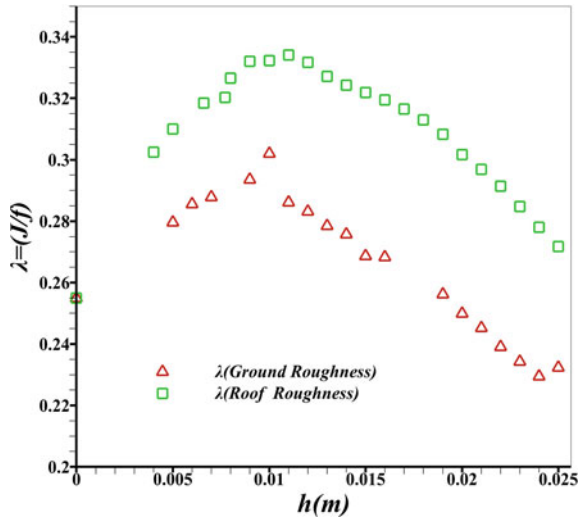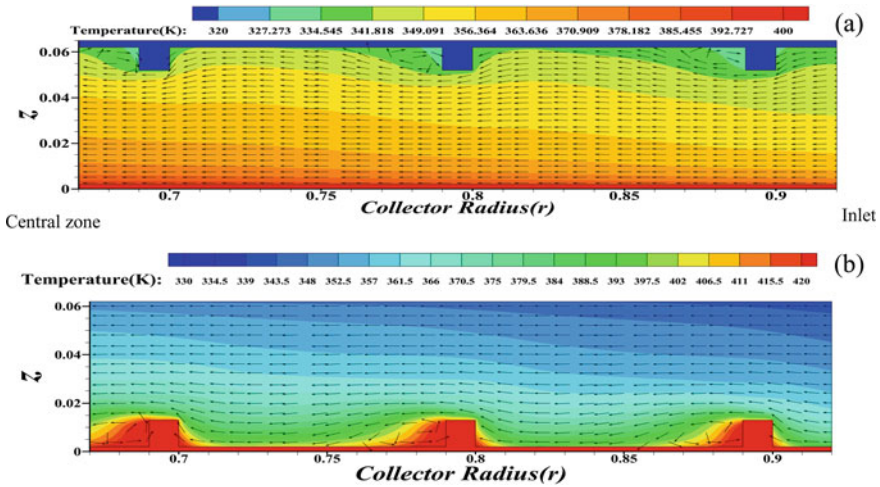
Fig. 10 Velocity vectors and temperature variations within the thermal boundary layer in the presence of roughness elements **a** roof roughness **b** ground roughness ($h = 0.01$ m)

4 Conclusion

A solar chimney power plant (SCPP) comprises four cardinal elements: chimney, collector, turbine and energy storage layer. The collector collects solar radiation to heat the inside air, which rises into the chimney located at the centre of the collector. The current study assesses the possibility of improving an SCPP's overall performance by proposing a better design of collector that offers a greater effective buoyancy, the motive force for an SCPP. Two sets of computational fluid dynamic (CFD) simulations are performed by considering artificial roughness elements at the collector's ground and roof, respectively. We have implemented the conjugate heat transfer (CHT) in our CFD modelling. The conduction equation in the solid domain and Navier–Stokes equations in the fluid domain are solved simultaneously in CHT. At the ground's lower surface, a steady heat flow of 800 w/m^2 is applied to replace an equivalent amount of solar radiation. The standard k–ϵ model predicts the turbulence in the fluid domain. We conducted a parametric study by gradually increasing the height of the roughness elements (4–25 mm), keeping the pitch (0.1 m) and width (0.01 m) unchanged. In our study, the effect of artificial roughness on the roof or ground is assessed separately on the overall thermal performance, friction factor and thermal performance of the SCPP. The computational results reveal that the system's thermal performance peaks around the roughness height of 0.01 m. Further, the ground roughness is more effective for enhancing the performance of SCPP. We have demonstrated that apart from streamwise convection, cross-stream convection also occurs due to roughness. The cross-stream convection attributes thermal mixing within the thermal boundary layer. Our thermo-fluid-dynamic analysis indicates that the potential of thermal mixing is higher for the ground roughness.

References

1. Gholamalizadeh E, Chung JD, A parametric study of a pilot solar chimney power plant using CFD. IEEE Access, pp 63366–63374. https://doi.org/10.1109/ACCESS.2018.2875411
2. Haaf W, Friedrich K, Mayr G, Schlaich J (1983) Solar chimneys part I: principle and construction of the pilot plant in Manzanares. Int J Solar Energy 2:3–20
3. Najm OA, Shaaban S (2018) Numerical investigation and optimization of the solar chimney collector performance and power density. Energy Convers Manage 168:150–161
4. Jamali S, Yari M, Mahmoudi SMS (2018) Enhanced power generation through cooling a semi-transparent PV power plant with a solar chimney. Energy Convers Manage 175:227–235
5. Fallah SH, Valipour MS (2019) Evaluation of solar chimney power plant performance: the effect of artificial roughness of collector. Sol Energy 188:175–184
6. Elwekeel FNM, Abdala AMM, Rahman MM (2019) Effects of novel collector roof on solar chimney power plant performance. J Sol Energy Eng 141:031004
7. Ayadi A, Driss Z, Bouabidi A, Nasraoui H, Bsisa M, Abid MS (2018) A computational and an experimental study on the effect of the chimney height on the thermal characteristics of a solar chimney power plant. Proc Inst Mech Eng, Part E: J Process Mech Eng 232:503–516
8. Fluent ANSYS (2011) Fluent 14.0 user's guide. Ansys Fluent Inc.
9. Kasaeian A, Ghalamchi M, Ghalamchi M (2014) Simulation and optimization of geometric parameters of a solar chimney in Tehran. Energy Convers Manage 83:28–34
10. dos Santos Bernardes MA (2003) Symmetric sink flow and heat transfer between two parallel disks 36959:649–655
11. Kurian R, Balaji C, Venkateshan SP (2016) Experimental investigation of convective heat transfer in a vertical channel with brass wire mesh blocks. Int J Therm Sci 99:170–179

Effect of Wind Shear Profile on Broadband Noise Emissions from Wind Turbines Blades Under Neutral Atmospheric Conditions

Vasishta Bhargava Nukala and Chinmaya Prasad Padhy

Abstract The size of utility-scale wind power plants and number of installations are increasing constantly due to growing demand for wind power and to combat climate change. One of key issues posed with large size turbines is longer blades with higher blade tip speeds which generate higher aerodynamic noise levels and cause deleterious health effects such as annoyance and stress for inhabitants near turbines. In this paper, the effect of log-law and power law wind shear profiles on the sound power level is investigated when turbines operate in neutral atmospheric boundary layer conditions. Brooks et al. [1] and Moriarty & Migliore [2] models have been implemented for predicting turbulent boundary layer trailing edge noise and inflow broadband noise levels from blades of 2 MW wind turbine. Results demonstrate that using power law exponent range of 0.05–0.2, inflow noise increased by 2–5 dB for entire frequency spectra, while trailing edge noise increased by 2 dB for $f < 1$ kHz. With log-law profile, the trailing edge noise showed a change of 10 dB while for inflow noise showed change up to 5 dB when surface roughness varied from 0.01 to 0.1. The overall noise levels predicted by both models using power and log-law have been validated with measured data of GE 1.5sle and Siemens SWT turbines at wind speed of 11 m/s. It was found that overall noise levels obtained using power law agreed with experiment data within 2 dBA, while log-law predictions deviate by 4–7 dBA for $f < 1$ kHz and within 1 dBA for $f > 1$ kHz in the frequency spectra.

V. B. Nukala (✉) · C. P. Padhy
Department of Mechanical Engineering, School of Technology, GITAM (Deemed to be) University, Hyderabad, Telangana, India
e-mail: vnukala@gitam.in

1 Introduction

In the recent past, research on wind turbine noise emissions has extensively progressed due to its significant effects on long-term public health living near the wind farms. As wind power plants continue to grow at a faster rate due to advancement of manufacturing technologies, turbines of large size have longer blades and higher tip speed has the potential to produce higher noise emissions in surrounding areas. Even though noise exposure from aircraft and road traffic dominates community noise levels, perception and annoyance of wind turbine noise among inhabitants is high and becomes stronger due to non-acoustical factors (e.g., time of day or night) during specific environmental conditions. Therefore, use of noise evaluation criteria based on perception and annoyance is required during design and assessment of wind turbine systems for social acceptance. Wind turbines operate in surface atmospheric boundary layer (ABL) conditions in which temperature effects such as inversion and lapse influence changes to the turbulence intensity and wind shear experienced by the neighboring turbines in the wind park which lead to lower power production and increased noise emissions. For wind turbines, two major aerodynamic noise sources are airfoil self-noise from moving blades and turbulent inflow noise due to atmospheric turbulence patterns. In the past, several researchers have proposed different methods for predicting airfoil self-noise mechanisms for airfoils and wind turbines. Reference [3] implemented validation methodology based on rapid distortion anisotropic turbulent velocity spectrum for predicting turbulent inflow noise from thin airfoils. Figure 1 shows a typical topographic structure of a land-based wind turbine and its influence on the velocity profiles experienced by turbines. The stability pattern of velocity profiles within ABL is essential to estimate not only the mechanical and aerodynamic loads on the turbine but also to predict the acoustic emissions. [4, 5] studied the influence of atmospheric stability patterns on the measured sound pressure levels from utility-scale wind farms located in Netherlands and found that noise data collected during day, evening and night times varied by a difference of 5 dB. A further investigation on microphone screen-induced noise and background noise levels from the field measurements was conducted to verify the influence of microphone screen diameter and location on measured sound pressure level. Numerous studies on noise emissions from wind turbines have been conducted to find the potential sources of airfoil self-noise as well as from the interaction of moving blades with tower wake flow in various operating conditions. Particularly, [4–7] suggested quasi-empirical models for trailing edge and inflow turbulence noise emissions like those in helicopters. However, improved inflow and trailing edge models were developed by [1, 2, 4, 5] based on the quasi-empirical expressions to the sound pressure level. These models were initially derived for thin airfoils with finite span and varying chord lengths and relied on several assumptions related to turbulent flow parameters which include turbulence intensity, length scale, boundary layer displacement thickness, flow angle of attack and mean flow velocity to predict sound pressure. The long-range sound propagation effects in atmosphere were done to investigate the noise
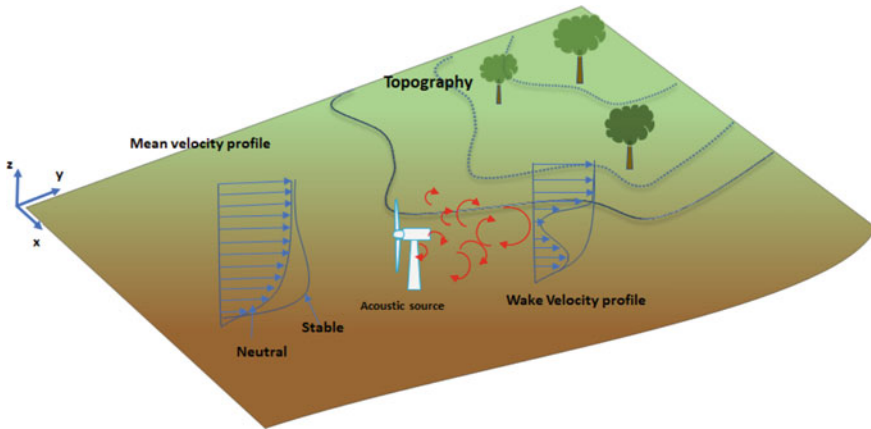
Fig. 1 Sketch of wind turbine operating environment in topographic conditions

levels produced from arrays of wind turbines operating in complex terrain conditions. High fidelity and improved noise prediction models have also been proposed for full scale and prototype wind turbines operating in different wind shear and atmospheric turbulence conditions [4–11]. Additionally, fundamental concepts to predict the amplitude modulation of trailing edge aerodynamic noise taken during measurements in a wind farm by [4, 5, 12–14] are reviewed. The influence of blade tower wake interaction on the leading-edge impulsive noise source caused due to unsteady flow over the downwind rotor blades was discussed, and active control methods to mitigate the low-frequency broadband noise were also proposed. In this paper, the influence of wind shear profiles on the sound emissions is investigated using BPM and Moriarty models for a utility-scale 2 MW wind turbine. Power and log-law profiles are implemented for varying wind shear exponents, surface roughness lengths (indicative of terrain roughness) at mean hub height velocity of 11 m/ s. Results for 1/3rd octave A-weighted overall sound power level (OASPL) L_{wA} are compared for both velocity profiles and compared to measured data of GE-1.5sle and Siemens SWT wind turbines.

2 Methods

In this section, quasi-empirical methods proposed by [1, 2] are discussed. These methods can predict the turbulent inflow and trailing edge self-noise from blades utilizing the turbulence velocity spectra and boundary layer properties. Figure 2 illustrates the turbulent inflow and aerodynamic self-noise generation mechanisms from a rotating wind turbine blade. Primary source of noise occurs from trailing edge of blade during operation due to turbulent boundary layer flow on blade surface having a finite impedance. This type of noise can vary in intensity depending on flow angle of
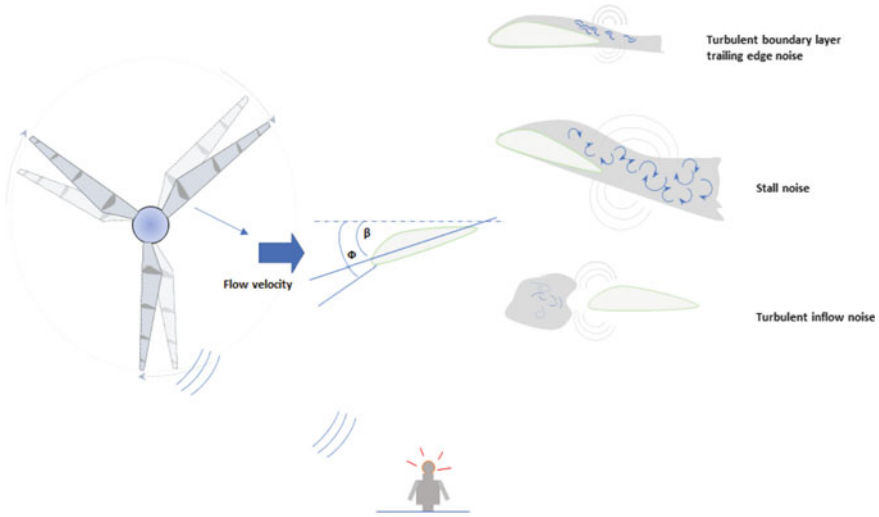
Fig. 2 Illustration of types of noise sources from a wind turbine rotor and noise perceived by receiver (adapted from [8])

attack, mean velocity and receiver positions relative to moving source in rotor plane. However, the strength of turbulent inflow noise has been found to be dependent on large-scale turbulent eddies size in incoming flow comparable to leading-edge curvature of blade. It also varies with turbulence intensity in the atmospheric boundary layer.

2.1 Inflow Noise Model

The turbulent inflow noise model proposed by [2] has been implemented in the present study. This model uses low-frequency directivity factor and characterizes low- and high-frequency noise levels in the SPL spectra. To include the turbulence characteristics in the noise prediction model, it uses the low-frequency correction factor which is derived from the Amiet's experiments on thin airfoil [2]. The SPL for turbulence induced noise can be evaluated using Eqs. (1)–(4)

$$\mathrm{SPL}_{in} = \mathrm{SPL}_H + 10 \cdot \log\left[\frac{\mathrm{LFC}}{1 + \mathrm{LFC}}\right] \tag{1}$$

$$\mathrm{SPL}_H = 10 \cdot \log\left[\frac{\rho^2 c^2 l L}{2r^2} M^3 u^2 I^2 \frac{K^3}{\left(1 + K^2\right)^{\frac{7}{3}}} D_L\right] + 78.4 \tag{2}$$

$$\mathrm{LFC} = 10 S^2 \mathrm{M} K^2 \beta^{-2} \tag{3}$$

$$S^2 = \left(\frac{2\pi K}{\beta^2} + \left(1 + 2.4 \frac{K}{\beta^2} \right)^{-1} \right)^{-1} \qquad (4)$$

where $\beta = \sqrt{1 - M^2}$ and $K = \frac{\pi f c}{U}$ and LFC is factor involving the aero-acoustic sears transfer function, S, which varies with acoustic wave number K. L is the span length of airfoil source, I is the turbulence intensity, l is the integral length scale parameters, and r is the total or effective distance position of microphone from turbine. To take account of compressibility effects of turbulent flows on generation of acoustic field, it also considers the Prandtl-Glauert compressibility criterion as function of Mach number, M, and given by β. D_L is the low-frequency directivity function expressed in terms of observer angles in the rotor and azimuthal planes respectively

2.2 BPM Trailing Edge Noise Model

Reference [1] developed model for airfoil self-noise mechanisms based on wind tunnel experiment data obtained for series of test data of thin symmetric airfoils with chord length ranging from 2.5 to 60 cm. NACA0012 airfoil was chosen and modeled as half infinite flat plate structure. The empirical-derived expressions for far field sound pressure level constitute geometry properties of airfoils and boundary layer parameters such as boundary layer thickness, in terms of chord and AOA. Also, a directivity function was included to analyze the effect of sound field radiation close to source. Furthermore, in this model, the SPL is predicted using the logarithmic scaling of boundary layer variables, predominantly displacement thickness δ^*, Mach number M, high-frequency directivity function D_h, effective distance between microphone and turbine r_e, blade span length L and spectral shape functions A and B that depend on the Strouhal number, St. Also, the sound pressure levels vary with fifth power of local velocity or free stream Mach number, M^5, and with chord Reynolds number, Re_c. The broadband spectrum of acoustic pressure is divided into three components, viz. pressure side source which uses directional expression and appears dominant in high-frequency region, and suction side source exhibits peak toward low-frequency part of spectrums. Both the sources are found to vary negligibly with angle of attack (AOA). The stall separation noise is critical to AOA and produces peaks at high positive values of AOA. This noise source reduces to compact dipole and uses low-frequency directivity function. The flow separation noise also occurs for high positive AOA for which high-frequency directivity is used. The three noise sources are added logarithmically along the individual blade segments to obtain resultant overall SPL. The empirical equations involved to evaluate the SPL are given by Eqs. (5)–(8)

$$SPL_p = 10. \log \left[\frac{\delta_p^* M^5 L \overline{D_h}}{r_e^2} \right] + A \left[\frac{St_p}{St_1} \right] + [K_1 - 3] + \Delta K_1 \qquad (5)$$

$$\text{SPL}_s = 10.\log\left[\frac{\delta_s^* M^5 L \overline{D_h}}{r_e^2}\right] + A\left[\frac{St_s}{St_1}\right] + [K_1 - 3] \tag{6}$$

$$\text{SPL}_\alpha = 10.\log\left[\frac{\delta_s^* M^5 L \overline{D_h}}{r_e^2}\right] + B\left[\frac{St_s}{St_2}\right] + K_2 \tag{7}$$

$$\text{SPL}_{\text{Total}} = \sum_{i=1}^{N} 10.\log\left[10^{\frac{\text{SPL}_i}{10}}\right] \tag{8}$$

The log-law and power law for wind shear profiles have been defined by Eqs. (9) and (10) given in [4]

$$\frac{U(z)}{U(z_r)} = ln\left(\frac{\frac{z}{z_0}}{\frac{z_r}{z_0}}\right) \tag{9}$$

$$\frac{U(z)}{U(z_r)} = \left(\frac{z}{z_r}\right)^\alpha \tag{10}$$

where z is the surface roughness height in m, z_0 is the standard or reference roughness height, z_r is the roughness height at r m above the ground, U is the wind velocity at given height in m/s, and α is the wind shear exponent.

3 Results

Table 1 shows the turbine specifications for assessment of overall sound power level. The [1, 2] noise models have been implemented using MATLAB software. The turbine parameters are given as key inputs to blade element momentum method to evaluate aerodynamic flow field data and coupled to noise solver for prediction of noise. The receiver (microphone) distance is fixed at 120 m downwind direction from source and at height of 0.2 m above ground. It must be noted that the atmospheric propagation effects such as absorption (from air or ground), scattering and refraction (caused due to wind and temperature gradients) around obstacles are not considered in quasi-empirical models. To account for these effects on assessment of overall sound power level (OASPL), IEC 61400-11 standard for acoustic emission measurements criteria has been considered which deducts 6 dB for the attenuation of sound due to geometric spreading and the above factors. Geometric spherical spreading has been included which considers turbine as dipole point source operating in a homogenous neutral atmosphere condition. Figure 3 illustrates the velocity profiles as function of height above ground computed using log-law and power law at free stream velocity of 11 m/s at shear exponent of 0.1 and surface roughness length of 0.05 (representative of plain grass land). Figure 4a, b demonstrate the comparison of 1/3rd octave frequency

Table 1 Design variables for 2 MW turbine

Parameter	Value
Cone	0°
Tilt	~ 3°
Tower height	~ 80 m
Length of blade	~ 37 m
Rotor speed	~ 17 RPM
Maximum twist	~ 13°
Maximum chord	~ 3.22 m
Orientation	Upwind
No of blades	Three
Rated power	2 MW

spectra of turbulent inflow noise computed using [2] model by implementing log-law and power law wind shear profiles. Figure 5a, b illustrate the trailing edge noise computed using the [1] model at mean wind speed of 11 m/s. A comparison of results from log-law and power law profiles for wind shear reveals that effect of surface roughness on trailing edge noise from blades influences entire frequency spectra increasing the SPL by 4-6dBA.

On the other hand, for increasing wind shear exponents, the change in SPL values is found significant for frequencies, $f < 1$ kHz. For high-frequency broadband components, $f > 1$ kHz, the changes to SPL values remain insignificant. It can be noted that trailing edge noise is produced significantly from rotor blades during the down-wind direction of rotation in rotor plane [2, 4, 6, 7, 9, 10, 12, 15]. This broadband phenomenon is perceived as *swish* by observer in rotor plane and propagates in far field as result of amplitude modulation of sound waves at blade passing frequencies

Fig. 3 Comparison of wind shear profile obtained from power and log-law distributions at mean wind speed of 11 m/s using wind shear exponent (α) of 0.1 and surface roughness (z_0) of 0.05 m
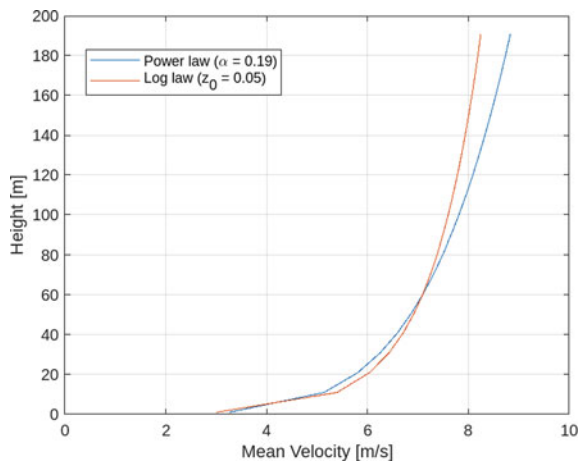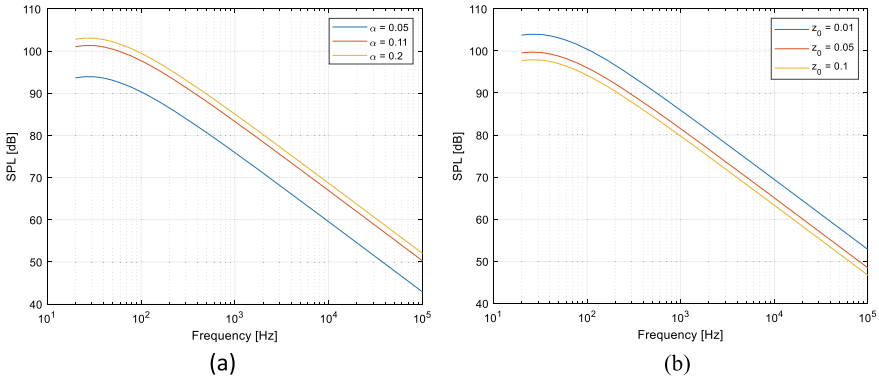
Fig. 4 Comparison of turbulent inflow noise level (L_w) from a 2 MW wind turbine **a** for different wind shear exponents using power law, **b** for different surface roughness values using log-law
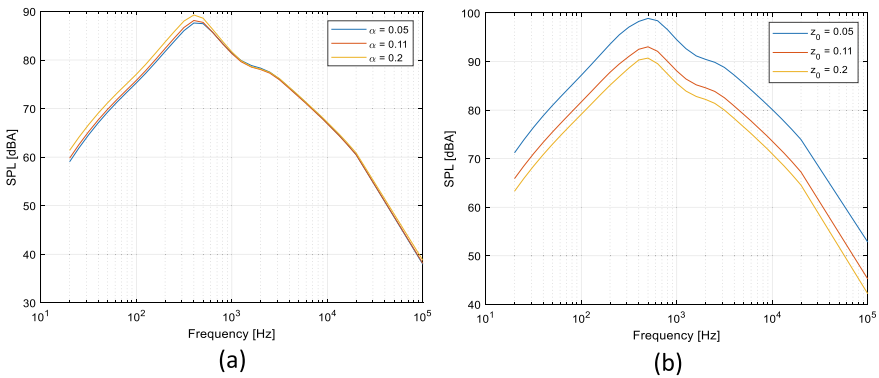
Fig. 5 Comparison of TBL-TEN level for 2 MW machine **a** for different wind shear exponents using power law **b** for different surface roughness values using log-law

(BPF). Figure 6 shows the validation of overall sound power level considering the broadband turbulent inflow and trailing edge noise components.

4 Conclusions

The present study investigated the effect of wind shear profiles using power and log-law on aerodynamic noise generation for 2 MW wind turbine in neutral atmospheric condition. The turbulent inflow noise model outputs have shown that when both wind shear exponents, surface roughness lengths are varied from a range 0.01 to 0.2, the noise levels are increased by ~ 2–8 dB keeping other factors constant. The Brooks et al. [1] model for turbulent boundary layer trailing edge noise is a very good

Fig. 6 Comparison of overall A-weighted L_{wA} (OASPL) from a 2 MW machine obtained using power law and log-law distribution with measured data of GE-1.5sle, Siemens 2.3 MW 95, Siemens 2.3 MW 101 and Siemens 2.3 MW 93 turbines
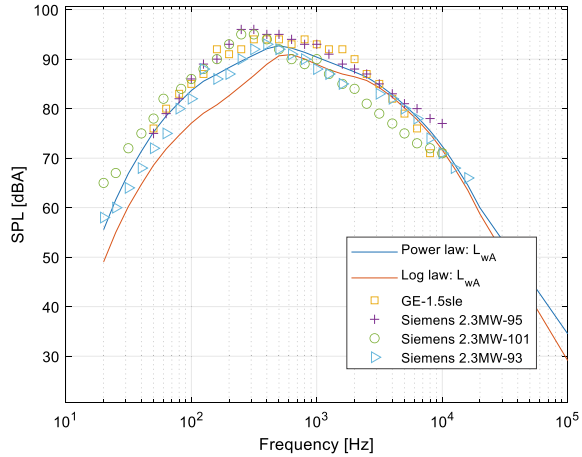
predictor in the high-frequency region of SPL spectra and showed good agreement with experiment data. The trailing edge and turbulent inflow noise models have demonstrated good accuracy for predicting overall sound power level however, wind shear profile based on power law agreed more closely with experiment data than log-law profile in low-frequency region of sound spectrum and thus more realistic.

References

1. Brooks TF, Pope DS, Marcolini MA (1989) Airfoil self noise and prediction. NASA Reference Publication 1218 (1989). Available from: https://ntrs.nasa.gov/archive/nasa/casi.ntrs.nasa.gov/19890016302.pdf
2. Moriarty P, Migliore P (2003) Semi empirical aero-acoustic noise prediction code for wind turbines [Technical report]. Available from: http://citeseerx.ist.psu.edu/viewdoc/download?doi=10.1.1.197.1153&rep=rep1&type=pdf
3. Faria MA, Saab Jr, JY, Rodriguez S, Pimenta MM (2020) A rapid distortion theory based aerofoil turbulent inflow noise prediction method. J Braz Soc Mech Sci Eng 42(397):1–9
4. Van den Berg (2006) The sound of high winds: effect of atmospheric stability on wind turbine sound and microphone noise, Doctoral Thesis, University of Gronningen, Netherlands
5. Van den Berg (2013) Wind turbine noise: an overview of acoustical performance and effects on residence. In: Proceedings of acoustics, Victor harbor, Australia
6. Hubbard HH, Shephard KP (1991) Aeroacoustics of large wind turbines. J Acoust Soc Am 6(89):2495–2508
7. Grosveld FW (1985) Prediction of broadband noise from horizontal axis wind turbines. J Propul Power 4(1):292–299
8. Shen WZ, Zhu WZ, Barlas E, Li Y (2019) Advanced flow, and noise simulation method for wind farm assessment in complex terrain. J Renew Energy 143:1812–1825. https://doi.org/10.1016/j.renene.2019.05.140
9. Oerlemans S, Lopez MB (2005) Acoustics array measurements on a full-scale wind turbine. In: 11th AIAA/CEAS aeroacoustics conference, Monterey, California. https://doi.org/10.2514/6.2005-2963

10. Doolan C, Moreau DJ, Arcondoulis E, Albarracin C (2012) Trailing edge noise production, prediction and control. N Z Acoust 3(25):22–29
11. Cotte B, Tian Y (2016) Wind turbine noise modeling based on Amiet's theory: effects of wind shear and atmospheric turbulence. Acta Acust Acust 4(102):626–639
12. Dragn D, Emmanuelli A, Colas J, Stevens RJAM, Blanc-Benon P (2022) Effect of a 2D hill on the propagation of wind turbine noise, AIAA, vol 2923. https://doi.org/10.2514/6.2022-2923
13. Bresciani APC, Maillard J, De Santana LD (2022) Perceptual evaluation of wind turbine noise. In: 16th congress francais d' Acoustique, Marseille, France, 2022
14. Ray ML, Rogers AlL, McGowan JG (2014) Analysis of wind shear models and trends in different terrains, Renewable Energy Research Laboratory, University of Massachusetts, Amherst, USA
15. Merino-Martinez R, Pieren R, Schaffer B (2021) Holistic approach to wind turbine noise: from blade trailing edge modifications to annoyance estimation. Renew Sustain Energy Rev 148. https://doi.org/10.1016/j.rser.2021.111285

Effect of Magnetic Field on Couette Flow in a Fluid-Saturated Porous-Filled Duct Under the Local Thermal Non-equilibrium with Viscous Dissipation

Nitish Gupta and D. Bhargavi

Abstract In our present analysis, we explore the impact of the magnetic field on the Couette flow occurring within a duct that contains a porous material. This investigation incorporates considerations of viscous dissipation and local thermal non-equilibrium (LTNE). The lower plate experiences movement and is exposed to isoflux boundary conditions, whereas the upper plate remains stationary and adiabatic. To describe the one-directional flow within the porous region, we utilize the Darcy–Brinkman (DB) model. The investigations also aim to quantify the effects of the Hartmann number (M_W), thermal conductivity ratio (κ), Brinkman number (Br_W), and Biot number (Bi_W) on enhancing heat transfer. Analytical solutions are derived for the governing equations, providing fully developed profiles of Nusselt numbers and dimensionless temperatures for both the fluid and solid phases. In the Couette flow model, the presence of a magnetic field impacts the temperature distribution in both phases. Furthermore, irrespective of the Hartmann number (M_W) in the Couette flow, the temperature in the solid phase is consistently higher than that in the fluid phase, thereby confirming the existence of local thermal non-equilibrium (LTNE).

Keywords Porous media · Couette flow · Brinkman number · Hartmann number · LTNE model

1 Introduction

Extensive research has been conducted on fundamental transport phenomena in porous media, primarily employing the local thermal equilibrium (LTE) assumption. This hypothesis, first demonstrated by Vafai and Tien [1], considers the fluid and

---

N. Gupta · D. Bhargavi (✉)

Department of Mathematics, National Institute of Technology Warangal, Warangal 506004, India

e-mail: bhargavi@nitw.ac.in

solid-matrix phases to be in a state of LTE and has been widely studied for convective transport in porous media. However, practical engineering problems have shown that the LTE hypothesis often fails, as highlighted by many authors [2–6]. In contrast to the local thermal equilibrium (LTE) model, Nield and Bejan [7] proposed the concept of local thermal non-equilibrium (LTNE) in the temperature equation. This approach considers temperature variations between the fluid phase (FP) and solid phase (SP), allowing for an interphase temperature difference. Yi et al. [8] investigated the impact of LTNE in parallel plate geometry using both linear and nonlinear flow models. Notably, Virto et al. [9] and Dehghan et al. [10] have presented innovative studies that explore various scenarios where LTNE is considered. Furthermore, several authors, including Tin et al. [11], Torabi et al. [12], and Buonomo et al. [13], have discussed the inclusion of viscous dissipation within the LTNE model.

When one surface moves tangentially in relation to the other, it creates a flow of viscous fluid known as Couette flow and discussed by Nakayama [14]. Pantokratoras [15] examined the behavior of flow in the Couette flow model. Existing literature, including works by Pantokratoras [15], Nakayama [14], and Kuznetsov [16] show that investigations of Couette flow in porous media often neglect viscous dissipation. On the other hand, relevant research by Kaurangini and Jha [17] and Jha and Odengle [18] assumes the local thermal equilibrium (LTE) model. Kuznetsov [16] conducted a detailed study on heat transfer in porous channels, considering both fully and partially filled configurations, with a focus on Couette flow. Baig et al. [19] recently examined the impact of Couette flow in a microchannel under local thermal equilibrium (LTE) conditions. On the other hand, Chen et al. [20] utilized the local thermal non-equilibrium (LTNE) model in their investigation, although magnetic field parameters were not taken into account. They concluded that the impact of LTNE is amplified under severe circumstances.

This paper focuses on investigating the influence of the magnetic field on Couette flow in a saturated porous material, utilizing the local thermal non-equilibrium (LTNE) model. The fluid flow through the porous media is described by the Darcy–Brinkman model (DB model). The magnetic field is applied perpendicular to the flow direction. Analytical expressions for the temperatures in the fluid phase (FP) and solid phase (SF) are derived, along with fully developed Nusselt numbers (FDNM).

2   Problem Formulation

In Fig. 1, the problem geometry depicts a channel with parallel plates. The notation T^*_e represents the fluid entering the channel at a constant temperature, while W represents the separation distance between the plates. In the current setup, the upper wall remains stationary and adiabatic while the lower wall of the channel is subjected to a constant wall heat flux (q) and is moving with a velocity of u_0. The flow is assumed to be unidirectional, laminar, steady, and incompressible. Additionally, the porous medium is assumed to be homogeneous and isotropic. Transverse to the flow direction, a magnetic field is applied. In the LTNE, there are porous and fluid areas.
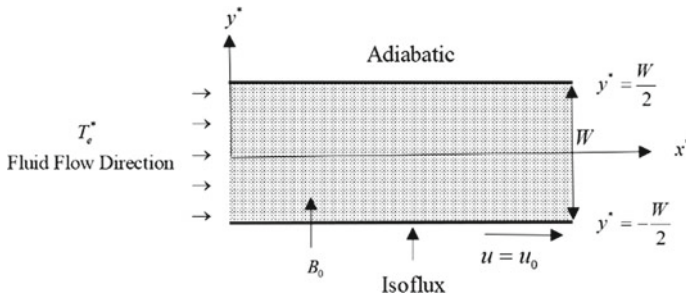
Fig. 1 Problem geometry

It is presumed that the flow field is a thermal field that is both completely formed and still evolving. Axial conduction is minimal, as is heat production. The thermophysical properties remain constant. The government equations are rendered dimensionless by utilizing the following set of dimensionless variables.

$$\xi^* = x^*/(Pe)W, \ \ \eta = y^*/W, \ \ U = u/u_0,$$
$$\theta_{\mathrm{f}}^* = \frac{k_{\mathrm{s,eff}}\left(T_{\mathrm{f}}^* - T_{\mathrm{w}}^*\right)}{qW}, \ \ \theta_{\mathrm{s}}^* = \frac{k_{\mathrm{s,eff}}\left(T_{\mathrm{s}}^* - T_{\mathrm{w}}^*\right)}{qW} \tag{1}$$

where the letters s, f, and w stand for solid phase (SP), fluid phase (FP), and wall. T^* stands for temperature in dimensional form. Also, the Peclet number and thermal conductivity in the SF are given by Pe and $k_{\mathrm{s, \ eff}}$, respectively.

In Eq. (1), the dimensionless coordinates are denoted by ξ^* and η. The symbols θ^* and U represent the dimensionless temperature and velocity, respectively.

Equation (2) represents the momentum equation for fluid flow through a porous medium by incorporating the Brinkman–extended Darcy equation and utilizing the dimensionless variables described in Eq. (1).

$$\frac{1}{\varepsilon}\frac{\mathrm{d}^2 U}{\mathrm{d}\eta^2} - \left(\frac{1}{Da_{\mathrm{W}}} + M_{\mathrm{W}}^2\right)U = 0 \tag{2}$$

The Darcy number, the Hartmann number, and ε value of being given in Eq. (2) by Da_{W}, M_{W}, and ε, respectively.

$$Da_{\mathrm{W}} = K/W^2, \ \ M_{\mathrm{W}} = \sqrt{\sigma B_0^2 W^2/\mu_{\mathrm{f}}}, \ \ \varepsilon = \mu/\mu_{\mathrm{eff}} \tag{3}$$

The hydrodynamics boundary conditions are

$$U\left(\frac{1}{2}\right) = 0, \ \ \text{and} \ \ U\left(-\frac{1}{2}\right) = 1 \tag{4}$$

The analytical solution expression of Eq. (2) using the condition is given in Eq. (4).

$$U(\eta) = \coth\left[\sqrt{\left(\frac{\varepsilon}{Da_W} + \varepsilon M_W^2\right)}\right]\left\{\sinh\left[\left(\frac{1}{2} - \frac{\eta}{2}\right)\sqrt{\left(\frac{\varepsilon}{Da_W} + \varepsilon M_W^2\right)}\right]\right\} \quad (5)$$

The above expression in the absence of M_W is presented in Chen et al. [20].

Dimensionless forms of thermal energy equations for SP and FP (LTNE model) are given by

$$\frac{\partial^2 \theta_s^*}{\partial \eta^2} - \mathrm{Bi_W}\left(\theta_s^* - \theta_f^*\right) = 0 \quad (6)$$

$$k_1 U(\eta)\frac{\partial \theta_f^*}{\partial \xi^*} = \frac{\partial^2 \theta_f^*}{\partial \eta^2} + \mathrm{Bi_W}\,\kappa\left(\theta_s^* - \theta_f^*\right) + \kappa \mathrm{Br_W}\left[\frac{U^2}{Da_W} + \frac{1}{\varepsilon}\left(\frac{dU}{d\eta}\right)^2\right] \quad (7)$$

In Eqs. (6) and (7), $\mathrm{Bi_W}$, $\mathrm{Br_W}$ denote the Biot number, and Brinkman number, respectively; however, the theoretical definitions for ε, k_1, and κ are given in the literature by Gupta and Bhargavi [21] and it can be defined as,

$$\mathrm{Bi_W} = a_{sf}h_{sf}W^2\big/k_{se}, \ \mathrm{Br_W} = \mu_f u_{ref}^2 W\big/qK, \ k_1 = k_f\big/k_{fe}, \ \kappa = k_{se}\big/k_{fe} \quad (8)$$

In Eq. (7), $\partial\theta_f^*\big/\partial\xi^*$ is constant as we are taking constant heat flux at the moving plate and can be calculated by the processor given in the literature [10].

Thermal boundary conditions (Refs. [19, 20]) are given as follows:

$$\frac{\partial\theta_f^*}{\partial\eta} = 0, \ \frac{\partial\theta_s^*}{\partial\eta} = 0 \text{ at } \eta = \frac{1}{2} \text{ and } \theta_f^* = 0, \ \theta_s^* = 0 \text{ at } \eta = -\frac{1}{2} \quad (9)$$

The contribution of viscous dissipation is expressed as

$$\mathrm{IH} = \mathrm{Br_W}U^2 \text{ and } \mathrm{FH} = Br_W Da_W\left(dU\big/d\eta\right)^2, \quad (10)$$

where IH and FH are the internal heating and frictional heating.

3 Analytical Expression for Temperature Field

The coupled systems of Eqs. (6) and (7) solve by decoupling the system and using Eq. (5) along with the boundary conditions (Eq. 9).

Fluid Phase:

$$
\theta_f^*(\eta) = \frac{e^{-\sqrt{2\kappa Bi}}\left\{\begin{array}{l} -32\varepsilon\sqrt{\kappa Bi}A_2^2 A_3\left\{\left\{\begin{array}{l}\sqrt{Bi}\left(e^{\sqrt{2\kappa Bi}}+e^{3\sqrt{2\kappa Bi}}\right)(1+2\eta)\\ +2\sqrt{2}e^{4B_1}\sinh[(1+2\eta)B_1]\end{array}\right\}A_2+1\right\}\\ +16\varepsilon Bi\sqrt{\kappa}e^{\sqrt{2\kappa Bi}}A_3 B_2 B_5\left\{\begin{array}{l}\kappa Bi(1+2\eta)A_2\\ +\sinh[(1-2\eta)A_2]B_4\end{array}\right\}\\ -8\sqrt{\kappa}e^{\sqrt{2\kappa Bi}}(1+\kappa Bi)B_2 B_7+\sqrt{\kappa}e^{\sqrt{2\kappa Bi}}B_2 B_3 Br\\ \left\{\begin{array}{l}B_5\left[2(BiK(2\eta-3)(1+2\eta)-4)A_2^2 A_6+B_8\right]\\ -\kappa Bi\cosh[2(1-2\eta)A_2]A_5 B_6\end{array}\right\}\\ -8\sqrt{\kappa}\left[e^{(5-2\eta)B_1}+e^{(3+2\eta)B_1}\right]\left\{B_7+Br A_2^2 B_3\left[B_8-A_6 B_5\right]\right\}\end{array}\right\}}{64\varepsilon\sqrt{\kappa Bi}A_2^2 B_2 B_3 B_5}
\tag{11}
$$

Solid Phase:

$$
\theta_s^*(\eta) = \frac{e^{-\sqrt{2\kappa Bi}}\left\{\begin{array}{l}8\sqrt{\kappa}A_2^2\left[\begin{array}{l}e^{(5-2\eta)B_1}\\ +e^{(3+2\eta)B_1}\end{array}\right]\left\{\begin{array}{l}Br B_3\left[\kappa Bi\cosh[4A_2]A_5-A_6 B_5\right]\\ -4\varepsilon Bi A_3 B_5\sinh[2A_2]\end{array}\right\}\\ +16\varepsilon\sqrt{Bi}A_3 B_5\left\{\begin{array}{l}4\sqrt{2}e^{4B_1}\sinh[(1+2\eta)B_1]A_2^3\\ +\sqrt{\kappa Bi}e^{\sqrt{2\kappa Bi}}B_2\left\{\begin{array}{l}\kappa Bi\sinh[(1-2\eta)A_2]\\ +B_3\left[\begin{array}{l}(1+2\eta)A_2\\ -\sinh[2A_2]\end{array}\right]\end{array}\right\}\end{array}\right\}\\ +2Br\sqrt{\kappa}e^{2\sqrt{2\kappa Bi}}B_3\cosh\left[\sqrt{2\kappa Bi}\right]\\ \left\{\begin{array}{l}A_2^2 A_6 B_5\left[\begin{array}{l}8+2\kappa Bi(2\eta-3)(1+2\eta)\\ +\kappa Bi\cosh[4A_2]A_5\end{array}\right]\\ -\kappa^2 Bi^2 A_5\cosh[2(1-2\eta)A_2]\end{array}\right\}\end{array}\right\}}{64\varepsilon\sqrt{\kappa}Bi A_2^2 B_2 B_3 B_5}
\tag{12}
$$

4 Fully Developed Nusselt Number (FDNM)

The formulation of FDNM Nu_{FD} at $\eta = -1/2$ is given by

$$
Nu_{FD} = -1\big/\kappa\left[\theta_{mf}^*\right]
\tag{13}
$$

In Eq. (13), θ_{mf}^* is evaluated by

$$
\theta_{mf}^* = \int_{-1/2}^{1/2}\left[U(\eta)\theta_f^*(\eta)\right]d\eta
\tag{14}
$$

Expression of FDNM is calculated by Eq. (13), by using Eqs. (11) and (14).

$$
\text{Nu}_{\text{FD}}
$$

$$
= \frac{\left\{48\sinh[A_2]^2\left\{\begin{matrix}-8e^{4B_1}B_1\left[\varepsilon 4\sqrt{2\text{Bi}}A_2^3A_3 - \sqrt{\kappa}\sinh[2B_1]C_1\right]\\ -\text{Bi}\sqrt{\kappa}e^{\sqrt{2\kappa\text{Bi}}}C_{10}\end{matrix}\right\}\right\}}{\left\{\begin{matrix}192\varepsilon\sqrt{\text{Bi}}\sinh[A_2]^2A_2A_3 + 96\varepsilon\text{Bi}\sqrt{\kappa}e^{3\sqrt{2\kappa\text{Bi}}}(\sinh[2A_2]-2A_2)A_2A_3\\ +48\varepsilon\text{Bi}\sqrt{\kappa}e^{\sqrt{2\kappa\text{Bi}}}A_3B_2B_4B_5\\ +\dfrac{24e^{2B_1}}{B_1^2-A_2^2}\left\{\begin{matrix}\sqrt{\kappa}e^{4B_1}\cosh[2A_2]A_2\left\{\text{Br}A_2^2B_3\left[A_6B_5-B_8\right]-B_7\right\}\\ +2e^{2B_1}\left(4\sqrt{2}\varepsilon\sqrt{\text{Bi}}A_2^3A_3C_7 - \sqrt{\kappa}C_1C_8\right) - \sqrt{\kappa}\cosh[2A_2]A_2C_1\end{matrix}\right\}\\ +\dfrac{e^{\sqrt{2\kappa\text{Bi}}}\sqrt{\kappa}\left[B_2(\text{Bi}C_3 - 3\sinh[A_2]C_9) - 24A_2C_5\right]}{A_2}\end{matrix}\right\}} \tag{15}
$$

A_I, $I = 1, 2, 3, 4$, and 5, B_J, $J = 1, 2, \dots, 8$, and C_K, $K = 1, 2, \dots, 10$ appearing in Eqs. (11), (12), and (15) are the constants and given in Appendix.

5   Results and Discussion

5.1   *Temperature Field*

Figure 2 provides visual aids for the discussion of the temperature field by displaying the viscous dissipation fluctuation with the Hartmann number values (M_W). The profile given in Fig. 2 shows that the values of internal heating (IH) and frictional heating (FH) are attained maximum at the lower wall which is the moving wall and the minimum value reaches the upper wall which is fixed. As M_W increases, values of IH and FH increase. Moreover, for a large value of Br_W, the values of IH and FH increase.

To understand the effect of M_W, Br_W, Bi_W, and κ on θ_f^* and θ_s^*, the plots are given at $\text{Da}_W = 0.05$ in this section. Figures 3 and 5 are given for the fluid phase and Figs. 4 and 6 are given for the solid phase. From Figs. 3a and 4a, as M_W increases from 0.5 to 4.5, the magnitude of temperatures in both phases increases. Additionally, as Br_W increases ($\text{Br}_W = 0.1$ to 0.5), the magnitude of θ_f^* as well as for θ_s^* decreases.

As Bi_W increases ($\text{Bi}_W = 10$ to 100), the magnitude of θ_f^* is increasing and this increase at low Br_W is more. This result is given in the literature [8, 10]. Plots given in Figs. 5 and 6 indicate the effect of ratio κ on temperature magnitude, θ_f^* and θ_s^*. For each Br_W, the temperature in both phases increases with the increase in ratio κ.

From Figs. 3, 4, 5 and 6, one can notice that with the increase of Brinkman number, Br_W, temperature magnitude in both phases increases. Additionally, $\theta_s^* > \theta_f^*$ which validate the LTNE impact on the problem. Also, this property can see in many literatures [10, 22].
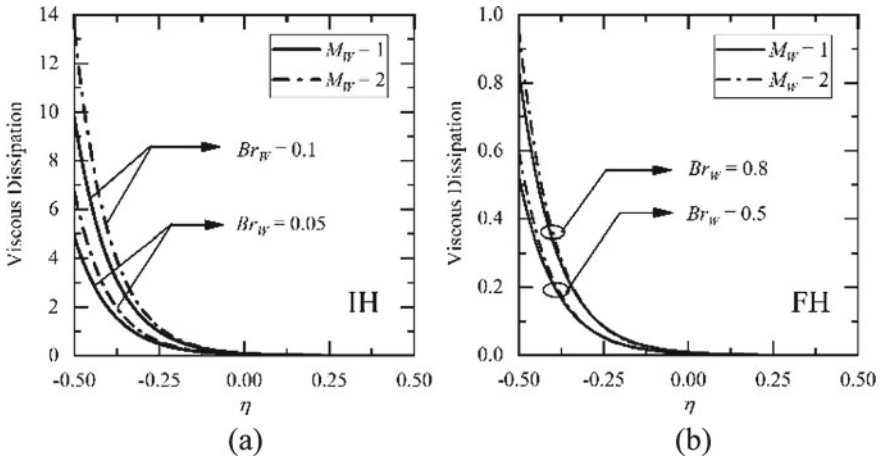
Fig. 2 Mutations in dissipation functions with η at $\mathrm{Da_W}$ for **a** IH, and **b** FH

Fig. 3 Change in θ_f^* for distinct values of $\mathrm{M_W}$ at $\mathrm{Da_W} = 0.05$, $\kappa = 1$, $\mathrm{Br_W} = 0.1$, 0.5 for **a** $\mathrm{Bi_W} = 10$, and **b** $\mathrm{Bi_W} = 100$
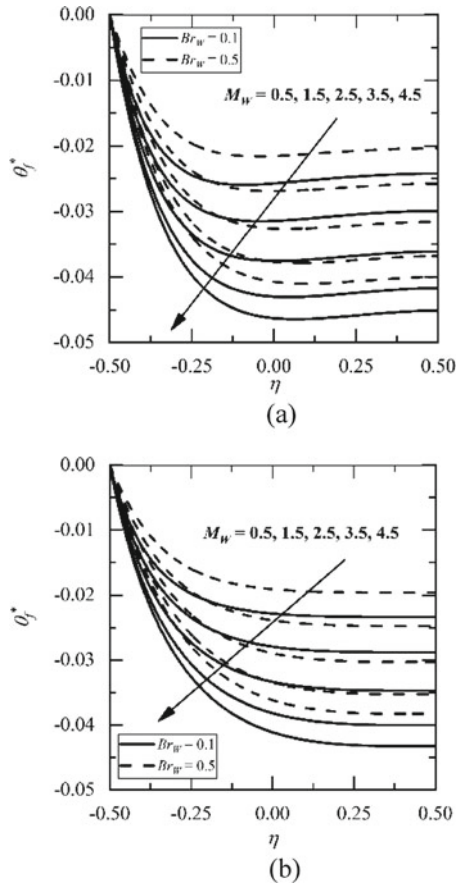
Fig. 4 Change in θ_s^* for distinct values of M_W at $Da_W = 0.05$, $\kappa = 1$, $Br_W = 0.1, 0.5$ for **a** $Bi_W = 10$, and **b** $Bi_W = 100$

(a)

(b)
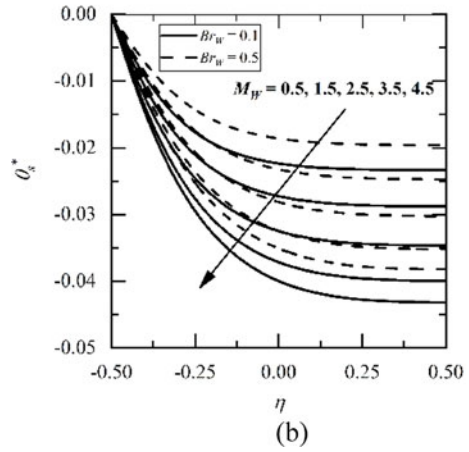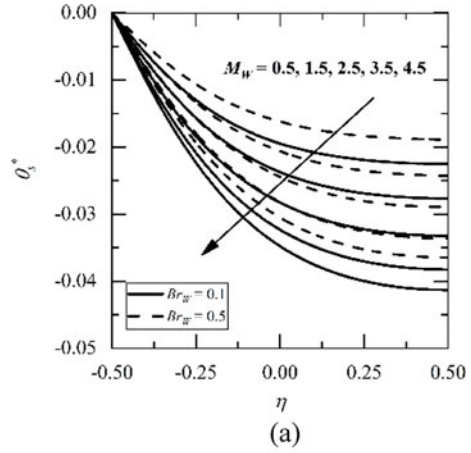
Fig. 5 Change in θ_f^* for distinct values of κ, at $M_W = 2$, $Da_W = 0.05$ for $Br_W = 0.1, 0.5$
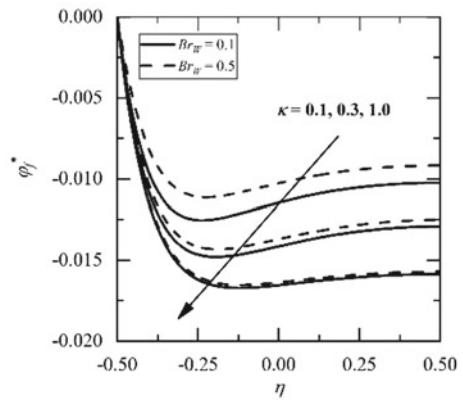
Fig. 6 Change in θ_s^* for distinct values of κ, at $M_W = 2$, $Da_W = 0.05$ for $Br_W = 0.1, 0.5$
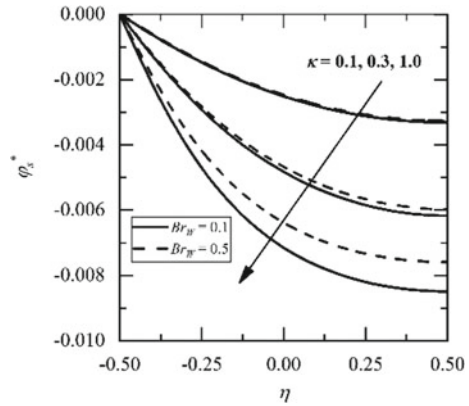
5.2 FDNM (NU_FD)

To know the impact of FDNM (Nu_{FD}) with Da_W for distinct values of M_W at a given Br_W and Bi_W, plots are given in Fig. 7. As Da_W increases, Nu_{FD} decreases for every value of M_W, Br_W, and Bi_W. This fact is reported in LTE case (Bhargavi and Reddy [21]). Nu_{FD} increases with the increase of M_W, and for large Da_W this increment is more. It can also be seen that as Br_W increases from 0.2 to 10, Nu_{FD} is increasing. Additionally, from Fig. 7a, b, as Bi_W increasing Nu_{FD} increases. The impact of ratio κ on Nu_{FD} with Bi_W is given in Fig. 8. This shows that Nu_{FD} rises to a certain Bi_W and then it decreases as Bi_W increases for all the values of κ and for all the values of M_W, Da_W, and Br_W. So, a plot is given for the typical value of variables.
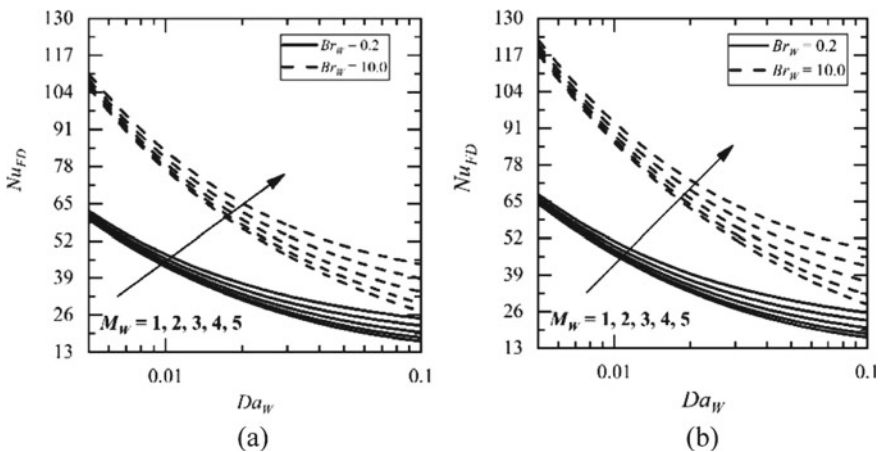
Fig. 7 Change in Nu_{FD} with Da_W for distinct values of M_W and for $Br_W = 0.1, 0.5$ at $\kappa = 1$ for **a** $Bi_W = 5$, and **b** $Bi_W = 50$

Fig. 8 Change in Nu_{FD} with Bi_W for distinct values of κ at $M_W = 2$, $Da_W = 0.05$, and $Br_W = 0.5$
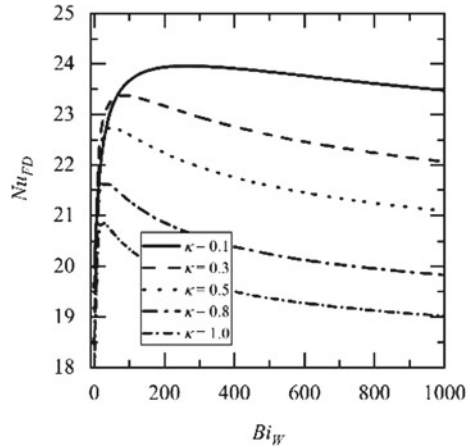
Table 1 At $M_W = 0$, a comparison of the value of parameter Nu_{FD} is conducted with the available literature (Kuznetsov [16] and Chel et al. [20])

Nu_{FD}			
Da_W	Present value	Chel et al. [20]	Kuznetsov [16]
0.001	63.262	63.274	63.412
0.010	20.043	20.028	20.971

Without considering the Hartmann number, ($M_W = 0$), a comparison of Nu_{FD} is made between the present study and relevant literature such as Kuznetsov [16] and Chel et al. [20], taking into account appropriate geometrical parameters. The consistency of published literature and the findings of the present study is noteworthy, particularly for high values of Da_W and Bi_W. A good level of agreement is observed (Table 1).

6   Conclusion

In this analysis, we discussed the mutation of Hartmann number, M_W on Couette flow under the consideration of LTNE model. Upper plate of channel is fixed and adiabatic, and lower plate moving and is at constant heat flux. Analytical expressions of temperatures and fully developed Nusselt numbers (Nu_{FD}) are discussed.

Magnitude of θ_f^* and θ_s^* increases with the increase of M_W, but decreases with the increase in Br_W. In the Couette flow model under LTNE, $\theta_s^* > \theta_f^*$ which validate the LTNE impact on the problem. As Br_W increases, Nu_{FD} increases. Also, Nu_{FD} increases with the increase of Bi_W. Nu_{FD} rises to certain Bi_W, then it decreases as Bi_W increases for all the values of κ and for all the values of M_W, Da_W, and Br_W.

Appendix

$A_1 = \varepsilon\left(1 + \mathrm{Da}M^2\right), A_2 = \sqrt{A_2}\big/2, A_3 = \mathrm{csch}\left[\sqrt{A_2}\right]A_4 = 4\mathrm{Da}_W\left(A_2 A_3\right)^2,$

$A_5 = \left(\varepsilon A_3^2 + A_4\right), A_6 = \left(\varepsilon A_3^2 - A_4\right)$

$B_1 = \sqrt{\kappa \mathrm{Bi}_W\big/2}, B_2 = \left(1 + e^{2\sqrt{2\kappa \mathrm{Bi}_W}}\right), B_3 = \left(\kappa \mathrm{Bi}_W - 2A_2^2\right),$

$B_4 = \left(\kappa \mathrm{Bi}_W - 4A_2^2\right), B_5 = \left(\kappa \mathrm{Bi}_W - 8A_2^2\right)$

$B_6 = \left(\kappa \mathrm{Bi}_W - 16A_2^2\right), B_7 = 2\varepsilon \mathrm{Bi}_W \sinh\left[2A_2^2\right]A_3 B_5, B_8 = \kappa \mathrm{Bi}_W cosh[4A_2]A_5$

$C_1 = B_7 + \mathrm{Br}_W A_2^2 B_3[B_8 - A_6 B_5], C_2 = -4A_2 A_6 B_5 + A_5 B_6 \sinh[4A_2]$

$C_3 = -12\varepsilon \sinh[4A_2]A_3 B_4 B_5 + \kappa \mathrm{Br}_W \sinh[3A_2]^2 A_5 B_3 B_6$

$C_4 = -4\varepsilon \mathrm{Bi}_W A_3 \sinh[2A_2] + \mathrm{Br}_W (1 + \kappa \mathrm{Bi}_W - cosh[2A_2])A_6 B_2 B_3 B_5$

$C_5 = 8\varepsilon \mathrm{Bi}_W A_2^2 A_3 - \kappa \mathrm{Br}_W (\mathrm{Br}_W B_3 \sinh[2A_2]A_6 + 4\kappa Bi_W A_3)B_5 + A_2 C_4$

$C_6 = \kappa \mathrm{Bi}_W \mathrm{Br}_W A_4 B_3 (B_6 - 8B_5) + \kappa \varepsilon \mathrm{Bi}_W \mathrm{Br}_W A_3^2 B_3 (B_6 + 8B_5)$
$\qquad - 16(1 + \kappa \mathrm{Bi}_W)B_7 + 2\mathrm{Br}_W B_3 B_5 B_8$

$C_7 = \sinh[2B_1]A_2 - \sinh[2A_2]B_1, C_8 = \sinh[2A_2]\sinh[2B_1]B_1 + A_2$

$C_9 = 32\kappa \varepsilon \mathrm{Bi}_W^2 cosh[A_2]A_3 B_5 + \sinh[A_2]C_6$

$C_{10} = A_2 B_2[\varepsilon 8A_3(\cosh[2A_2]B_4 - \kappa \mathrm{Bi})B_5 - \kappa \mathrm{Br}B_3 C_2] + \varepsilon 16 B_2 A_2^2 A_3$

References

1. Vafai K, Tien CL (1981) Boundary and inertia effects on flow and heat transfer in porous media. Int J Heat Mass Transf 24(2):195–2031
2. Quintard M, Whitaker S (1993) One and two-equation models for transient diffusion processes in two-phase systems. Adv Heat Transf 23:369–465
3. Gupta, N., Bhargavi. D.: The Influence of Magnetic Effect in a Channel Partially Filled with Porous Material: A Numerical Investigation. MMCITRE 2022, vol. 1440, pp. 415–426. Springer Nature, Singapore (2023).
4. Gupta, N., Bhargavi. D.: Effect of Magnetic Field on the Developing Thermal Field in a Duct Filled with Porous Media under Local Thermal Non-Equilibrium with a Nonlinear Flow Model. J Adv Res Fluid Mech Therm Sci 103(1), 87–104 (2023).
5. Vafai K, Sozen M (1990) Analysis of Energy and Momentum Transport for Fluid Flow Through a Porous Bed. ASME J Heat Transf 112(3):690–699
6. Amiri A, Vafai K (1994) Analysis of Dispersion Effects and Non-Thermal Equilibrium, Non-Darcian, Variable Porosity Incompressible Flow Through Porous Media. Int J Heat Mass Transf 37(6):939–954
7. Nield DA, Bejan A (2013) Convection in Porous Media, 4th edn. Springer, New York
8. Yi Y, Bai X, Kuwahara F, Nakayama A (2021) Analytical and numerical study on thermally developing forced convective flow in a channel filled with a highly porous medium under local thermal non-equilibrium. Transp Porous Media 136:541–567

9. Virto L, Carbonell M, Castilla R, Gamez-Montero PJ (2009) Heating of saturated porous media in practice: several causes of local thermal non-equilibrium. Int J Heat Mass Transf 52:5412–5422

10. Dehghan M, Valipour MS, Keshmiri A, Saedodin S, Shokri N (2016) On the thermally developing forced convection through a porous material under the local thermal non-equilibrium condition: an analytical study. Int J Heat Mass Transf 92:815–823

11. Ting TW, Hung YM, Guo N (2014) Viscous dissipative forced convection in thermal non-equilibrium nanofluid-saturated porous media embedded in microchannels. Int Commun Heat Mass Transf 57:309–318

12. Torabi M, Zhang K, Yang G, Wang J, Wu P (2015) Heat transfer and entropy generation analyses in a channel partially filled with porous media using local thermal non-equilibrium model. Energy 82:922–938

13. Buonomo B, Manca O, Lauriat G (2016) Forced convection in porous microchannels with viscous dissipation in local thermal non-equilibrium conditions. Int Commun Heat Mass Transf 76:46–54

14. Nakayama A (1992) Non-Darcy Couette flow in a porous medium filled with an inelastic non-Newtonian fluid. J. Fluid Eng 114(4):642–647

15. Pantokratoras A (2007) Fully Developed Couette Flow of Three Fluids with Variable Thermophysical Properties Flowing through a Porous Medium Channel Heated Asymmetrically with Large Temperature Differences. J Heat Transf 129(12):1742

16. Kuznetsov AV (1998) Analytical Investigation of Couette Flow in a Composite Channel Partially Filled with a Porous Medium and Partially with a Clear Fluid. Int J Heat Mass Transf 41(16):2556–2560

17. Kaurangini ML, Jha BK (2011) Unsteady Generalized Couette Flow in Composite Microchannel. Applied Math Mech. 32(1):23–32

18. Jha BK, Odengle JO (2015) Unsteady Couette Flow in a Composite Channel Partially Filled with Porous Material: A Semi-Analytical Approach. Transp Porous Media 107(1):219–234

19. Baig, F. M., Chen, G. M., Lim, B. K.: Thermal Viscous Dissipative Couette Flow in a Porous Medium Filled Microchannel. Proc of ASME 5th Int Conf Micro/Nanoscale Heat and Mass Transf Biopolis, Singapore 1–9 (2017).

20. Chen GM, Baig MF, Tso CP (2021) Local Thermal Nonequilibrium Viscous Dissipative Couette Flow in A Porous Medium. Spec Top Rev Porous Media 12(6):31–41

21. Gupta N, Bhargavi D (2022) Numerical investigation of heat transfer in a developing thermal field in the porous-filled duct under local thermal nonequilibrium: constant wall heat flux. Spec Top Rev Porous Media 13(5):49–81

22. Bhargavi D, Reddy JSK (2018) Analytical study of forced convection in a channel partially filled with porous material with the effect of magnetic field: constant wall heat flux. Spec Top Rev Porous Media 9(3):201–216

Design and Analysis of a Thermoacoustic Cooling System with Two-Stack Arrangement for Different Types of Stacks

M. Siva Sakthi, C. Swathiga Devi, and Surendra Bogadi

Abstract Thermoacoustic cooling is a method that converts acoustic power to temperature differential, which is then utilized to reduce the temperature of a hot body via heat exchangers. A typical thermoacoustic cooling system consists of a resonator, stack, driver and heat exchangers. Any thermoacoustic cooling system is categorized based on the frequency at which it operates which again controls the geometry of the resonator. A half-wavelength resonator will have two pressure antinodes, where stacks can be placed to obtain the temperature difference. The main objective of the present work is to design a half-wavelength resonator with two-stack arrangement and to analyse and compare the refrigerator's performance for various types of stacks. The resonator's length for the cooling system is chosen as 1 m, and it operates at a frequency of 500 Hz with helium as a working fluid at a temperature and pressure of 288.05 K and 10 bar, respectively. The drive ratio of the refrigerator is 0.03. The stacks are 4.295 cm in length with a thickness of 0.5 and 1 mm spacing between the adjacent stack plates. The placement of stack 1 is 35 mm from the driver end and of stack 2 is 35 mm from the closed end of the resonator. DeltaEC is an open-source tool used by many researchers for thermoacoustic problems. DeltaEC simulations for parallel, rectangular and circular type stacks show a temperature difference of 37.27 °C, 40.05 °C and 53.05 °C at stack 1, whereas a temperature difference of 8.07 °C, 12 °C and 20 °C at stack 2, respectively. Introducing ambient and cold heat exchangers adjacent to each of the stacks makes it possible for the refrigerator to take two heat loads at the same time. This increases the net cooling capacity of the refrigerator.

Keywords Thermoacoustics · Heat exchangers · DeltaEC

M. Siva Sakthi (✉) · C. Swathiga Devi · S. Bogadi
Rajalakshmi Engineering College, Rajalakshmi Nagar, Thandalam, Chennai 602105, India
e-mail: sivasakthi.m.2019.aero@rajalakshmi.edu.in

Nomenclature

A	Resonator area, m^2
CHX	Cold heat exchanger
C_p	Specific heat of gas at constant pressure, $Jkg^{-1} K^{-1}$
C_v	Specific heat of gas at constant volume, $Jkg^{-1} K^{-1}$
COP	Coefficient of performance
DR	Drive ratio
F	Driver frequency, Hz
HHX	Hot heat exchanger
k_v	Wave number of gas, cm^{-1}
K	Thermal conductivity of gas, $Wm^{-1} K^{-1}$
L	Length of the resonator, m
L_s	Length of the stack, m
L_{sn}	Normalized stack length, m
M	Mach number
P	Gas pressure, Pa
P_0	Dynamic pressure, Pa
P_m	Average pressure, Pa
t	Thickness of stack, m
T_{cx}	Temperature of cold heat exchanger, K
u	Velocity of sound in helium, ms^{-1}
W_{ns}	Normalized acoustic work input, W
x_n	Normalized stack position, mm
X_n	Stack centre position, mm
y_0	Half gas spacing in stack-heat exchangers sheet, mm
δ_k	Thermal penetration depth, mm
δ_v	Viscous penetration depth, mm
ε	Porosity/block ratio of stack-heat exchangers system
γ	Ratio of specific heats
ρ	Mass density of gas, kgm^{-3}
λ	Wavelength, m
ω	Angular frequency of acoustic wave, $rads^{-1}$
μ	Dynamic viscosity of working gas, $kgm^{-1} s^{-1}$

1 Introduction

The cooling methods have evolved over time and have seen many alterations based on the need and the aim towards sustainable development. Currently, conventional cooling systems follow a vapour compression cycle which consists of four main components: compressor, condenser, expansion valve and evaporator. The stated method involves chemical refrigerants such as CFCs which are very harmful to human

Fig. 1 Model of a thermoacoustic refrigerator [1]

beings as well as to the environment. This raises a major environmental concern to opt for alternative cooling technologies. Thermoacoustic cooling is one such alternative technology. Thermoacoustics is a study related to physical phenomena, where temperature gradient can generate sound waves, and vice versa. The advantages of this cooling system are no moving components, no use of refrigerants and lubrication, simpler design, low energy requirements and eco-friendly (Fig. 1).

1.1 Working Principle

Sound waves experience displacement and temperature oscillations in along with pressure variations. Due to thermoacoustic phenomenon, when these sound waves are subjected to oscillate through small ducts can produce temperature gradient within the duct. A simple thermoacoustic refrigerator includes an acoustic driver (or speaker) that generates oscillation of gas within the duct, a stack which can be thin layers of plates. Adjacent to the stacks there can be heat exchangers that can exchange the heat for doing useful such as cooling for many applications. Generally, the working gas filled in the duct can be air, helium or combination of other inert gases.

The Thermoacoustic cycle consists of four stages:

Stage 1: The gas particle between the stack plates gets compressed near the ends, and thus, pressure increases.
Stage 2: The compressed gas particle heats up and rejects heat to one side of the stack plate.
Stage 3: The wave moves back, causing the gas particle to expand.
Stage 4: The gas particle absorbs heat from the other side of the stack and reaches the initial state of the cyclic process.

The gas particles should oscillate as close to the stack surface to effectively transfer heat. The pressure distribution along the resonator tube at resonance is as shown below (Fig. 2).
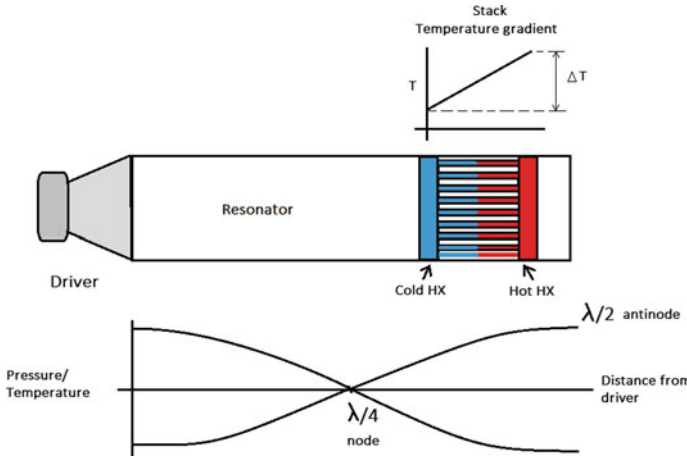
Fig. 2 Pressure distribution across the half-wave resonator

The pressure antinodes are formed at the rear ends of the closed tube. This makes it the suitable position for placing the two parallel plate stacks. As the pressure is higher at the respective end positions, it exerts more pressure on the gas particles and thus increases their temperature.

1.2 Applications

Thermoacoustic refrigeration has potential applications in various fields. The James Webb Telescope uses this refrigeration method for operating at cryogenic temperatures [2]. This existing application stands as the major motivation behind our study. Also, this alternative cooling procedure with further improvements in future has a huge scope in interplanetary space missions to hot planets [3]. In addition, this method can be used in applications demanding less noise and vibration, as it involves no moving parts. The stated refrigeration method is eco-friendly and is the best fit for sustainable applications.

2 Literature Survey

The frequency of the standing wave is directly related to resonator length, medium and boundary conditions. A high frequency is chosen, as the power density in the thermoacoustic device is a function of acoustic frequency. However, a very high frequency is not feasible as the thermal penetration depth is inversely proportional to the square of input frequency, which leads to stack plates with small spacing

Table 1 Properties of Delrin material

Property	Value
Thermal conductivity	0.23 Wm^{-1} K^{-1}
Density	1420 Kg m^{-3}
Specific heat	1.5 kJ kg^{-1} K^{-1}

[4]. Therefore, a value of frequency between 300–500 Hz is practical to conduct experiments. This project utilizes an acoustic frequency of 500 Hz. According to Prashantha et al., the resonator tube should be strong enough to sustain pressure greater than 10 bar and have a good surface finish to reduce heat dissipation losses. It must be made from low thermal conductivity material to minimize heat dissipation losses. Delrin, a crystalline-engineered thermoplastic, is suitable for resonator design due to its low thermal conductivity and high specific heat capacity [5]. It also has high tensile strength, high wear resistance and wide operating temperature which makes it a perfect choice (Table 1).

A simple cylindrical resonator geometry is an ideal choice for performing experimental calculations [6]. As per Amirin et al., the resonator performance depends on boundary conditions (open and closed). The resonator with both ends closed is chosen for this study, as the theoretical concept suggests an improvement in the resonator performance. The chosen resonator boundary condition is a viable choice for placing a stack closer to each end, as pressure antinodes are formed at the ends and therefore can be utilized by the stack to create temperature differences. The stack acts as the heart of the thermoacoustic refrigeration system. The resonator performance has a high dependency on the stack parameters such as its design, material, length, position, thickness and spacing. The stacks are supposed to have low thermal conductivity and a specific heat capacity higher than the medium used [7]. Mylar, a material made out of polyethylene terephthalate, is considered a suitable material for stack plates (Table 2).

As mentioned before, the stack spacing, the length between two stack plates depend on the thermal and viscous penetration depth. Based on the experiment conducted by Swift, the stack spacing equal to four times the thermal penetration depth is suitable for optimum stack performance [8]. Block ratio, also known as porosity, is a factor used to determine stack thickness. The block ratio explains the area occupied by the solid and gas. The other stack parameters, length and position are found using plots showing the coefficient of performance (COP) [6]. Heat exchangers are an important component of thermoacoustic refrigerators. This is a system that transfers heat between a source and a working fluid. It is placed at the

Table 2 Properties of Mylar material

Property	Value
Thermal conductivity	0.15 Wm^{-1} K^{-1}
Density	1358 Kg m^{-3}
Specific heat	0.89 kJ kg^{-1} K^{-1}

Fig. 3 Fin tube exchanger [9]
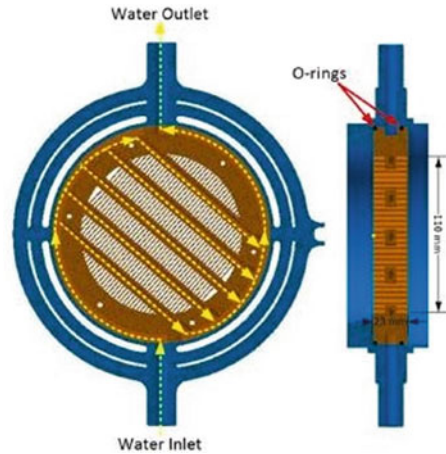
ends of the stack to exchange heat between the stack and the working medium. It is used in cases of both heating and cooling processes. The optimum dimensions of the heat exchangers are discussed by Swift [8], and the major factors to consider for design calculations are studied by Islam et al. in 2021 [9]. As per the literature, the fin tube heat exchanger is considered an optimum choice for both ambient and cold heat exchanger. The cross-sectional areas of heat exchangers and the stack should match for effective heat transfer. Generally, the fin and tubes are made out of copper, and water is majorly used as the cooling fluid [3, 9] (Fig. 3).

The resonator performance also depends on the gas used in the resonator. A working fluid with a low Prandtl number and a high ratio of specific heat is desirable [10–12]. The inert gases have been identified as the best working fluid for the thermoacoustic refrigerator by various researchers [4]. The cooling power is proportional to speed of sound waves in the fluid. The higher the speed of sound waves, the larger is the cooling power. In particular, the sound travels faster in inert gases such as helium [4], and it is chosen as a suitable option for this study (Table 3).

Table 3 Properties of helium

Property	Value
Sound velocity	999.54 m/s at 288.05 K, 10 bar
Density	1.6715 kg/m^3
Specific heat capacity	5193.4 J/kg K
Prandtl number	0.71 (100 °C)
Specific heat ratio	1.67

2.1 Methodology

Many methodologies have been carried out by researchers such as Tijani [6, 13] and Swift [8] for designing thermoacoustic refrigerators. The thermoacoustic refrigerator design strategy followed by Tijani is used as a reference for this study. This planning method is implemented to determine design calculations by obtaining the optimal dimensions and geometry of the refrigeration system, after which the data is analysed and the gained results are compared with DeltaEC software simulation. In this approach, several parameters must be assumed in order to proceed with further calculations. To initiate the study, the drive ratio (DR), block ratio, properties of the working medium, thermal penetration depth and expected temperature differential across the stack should be determined in advance. This strategy provides an idea to estimate the suitable cooling conditions inside the resonator, which is related to the size and geometry of the resonator.

Other parameters such as input frequency, resonator geometry, stack dimensions, and heat exchanger type. The hot heat exchanger length ($4x_n$), stack length L_s, cold heat exchanger length ($2x_n$) and stack centre position X_s are normalized by multiplying the wave number of gas used. The thermal and viscous penetration depths are normalized by dividing with stack plate spacing y_0. The DeltaEC software is used to simulate the refrigeration system, and the results are obtained in the form of pressure, temperature plots against the axial distance of the refrigerator (Fig. 4).
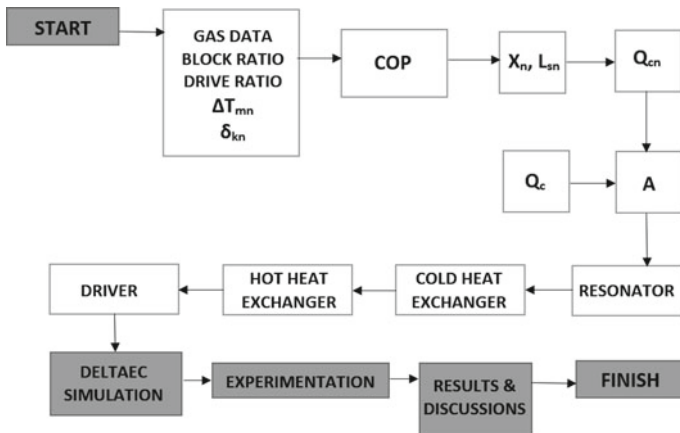
Fig. 4 Thermoacoustic refrigerator design approach

2.2 Design Calculations

The cylindrical half-wave resonator geometry with both ends closed is considered to accommodate two stacks at the possible extreme ends, with a frequency chosen to be 500 Hz (used for all present simulations). From referring to various papers on design parameters, the following calculations are performed.

2.3 Resonator

By considering the resonance conditions, the length of the resonator depends on the frequency and velocity of sound waves in that medium. The frequency is set at 500 Hz. For a half-wave resonator, the length is determined by using the stated formula [13]:

$$L = \frac{n\lambda}{2} = \frac{u}{f} = 0.999 \, \text{m} = 1 \, \text{m}$$

The diameter and thickness of the resonator are taken to be 10 cm and 12 mm, respectively [5].

2.4 Thermal and Viscous Penetration Depth

There are two values of thickness analogous to boundary layer thickness in fluid dynamics that decides movement of gas inside the stack. They are the thermal penetration depth (δ_k) and the viscosity penetration depth (δ_v) (Figs. 5, 6 and 7).

The thermal and viscous penetration depths are calculated to be 0.104 mm and 0.085 mm, respectively, using the stated formulae [13].

Fig. 5 Area of δ_k and δ_v on the stack [13]
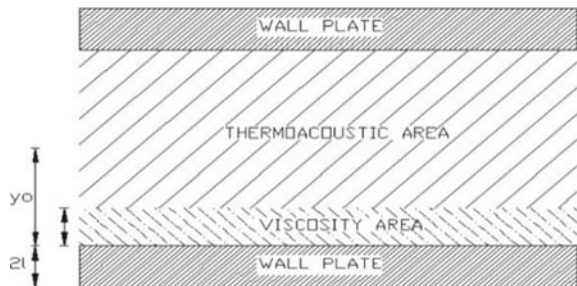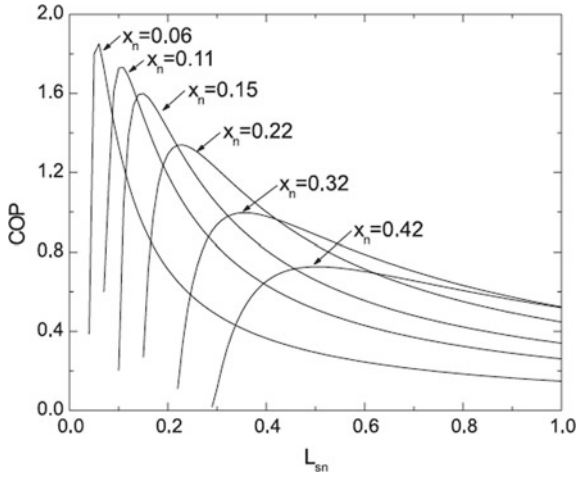
Fig. 6 COP as a function of the normalized stack length and centre position of stack [6]
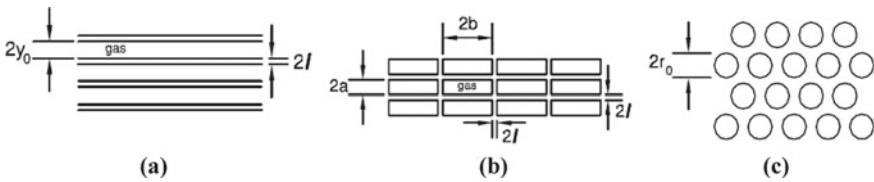
Fig. 7 **a** Parallel, **b** rectangular, **c** circular

$$\delta_k = \sqrt{\frac{2K}{\rho\omega c_p}}$$

$$\delta_v = \sqrt{\frac{2\mu}{\rho\omega}}$$

It can be observed that δ_k and δ_v are smaller than the stack spacing (y_0). Drive ratio (DR) is defined as the ratio of dynamic pressure ratio (p_0) to the average pressure (p_m) [13].

$$D = \frac{p_0}{p_m}$$

The pressure inside the resonator is directly proportional to the cooling system. Generally, a high value of average pressure is preferred. So, a pressure value of 10 bars is chosen. As per Tijani [6], the value of the Mach number is limited to 0.1 to avoid non-linear effects. Referring to pieces of literature [6, 14], the value of the drive ratio is considered as 0.03.

2.5 Stack

The stack design is very crucial as it directly affects the performance of thermoacoustic device. It pumps heat from the cold heat exchanger (CHX) to the hot heat exchanger (HHX). As per Tijani [6], the stack should be placed as close as possible to the driver, where the pressure is maximum (called as a pressure antinode). It is found that the maximum cooling is possible exactly between a pressure node and antinode [6].

From Fig. 7, $L_{sn} = 0.135$ and $X_n = 0.11$. Geometric parameters of the stack are shown in Fig. 8.

Length of the stack, $L_s = L_{sn}/k_v = 4.295$ mm.
Position of stack, $X_s = X_n/k_v = 35$ mm.
Wave number $(k_v) = 3.143$

$$k_v = \frac{w}{a}$$

As per Tijani [6], the suggested value of stack spacing, i.e. the distance between two stacks is 2–4 times of thermal penetration depth (δ_k). Also stack spacing of 4 times the thermal penetration depth is easy to experiment. The stack spacing is calculated to be 0.42 mm.

$$2y_0 = 4\delta_k$$

To determine the stack thickness, the block ratio/porosity (B) of the stack arrangement has to be fixed. In our study, the block ratio is chosen as 0.8, which is a very good assumption as per the literature survey [6].

$$B = \frac{y_0}{y_0 + t}$$

From the above relation, the thickness is found to be 0.105 mm.
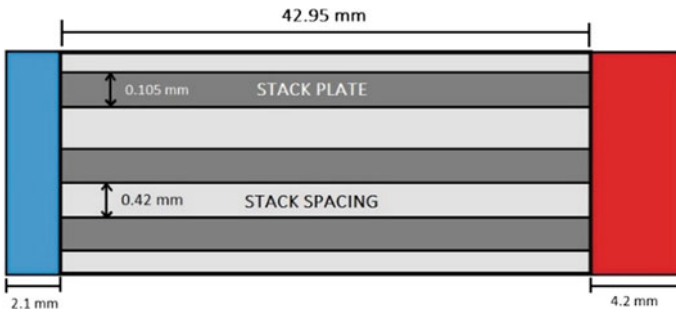
Fig. 8 Geometry of parallel plate stack with heat exchangers

The selection of stack material is also an important factor to take into consideration. Tijani [6] used stacks made of a type of plastic film called Mylar. Mylar has the property of low thermal conductivity and high specific heat capacity which are preferred for good results. Therefore, Mylar sheets are considered the material for the stack. The geometric view of the three types of stacks—parallel, rectangular and circular are represented in Fig. 8a–c, respectively. The respective geometry types with optimum dimensions are used in Sect. 3

2.6 Heat Exchangers

The design of heat exchangers should be done with utmost care to efficiently transfer heat. As one of the stack end's temperature drops, a cold heat exchanger is needed to introduce contact between the resonator and the stack. However, on the other end, the temperature rises which should be removed efficiently. This is done by a hot (or ambient) heat exchanger. The lengths of the heat exchangers depend on the gas displacement (amplitude) inside the resonator. The displacement amplitude is given as shown below [7]:

$$x = \frac{u}{\omega} = \frac{P_0}{\omega \rho_{\mathrm{m}} a} \sin \sin(kx)$$

$$x = 1.05 \, \mathrm{mm}$$

It is found that the optimum length of the cold heat exchanger is $2x$ [5]. As the HHX has to lose more heat to the environment, nearly double the heat supplied by the CHX, it is advisable to have for a HHX, double the length of the CHX. Therefore, the length of cold and hot heat exchangers is found to be 2.1 mm and 4.2 mm, respectively.

3 Simulation

Design **E**nvironment for **L**ow-amplitude **T**hermo **A**coustic **E**nergy **C**onversion is a simulation software that can simulate a thermoacoustic device and allow the user to design to achieve the expected performance. DeltaEC deals with one-dimensional sequences of acoustic and thermoacoustic elements, called segments [15]. The code numerically integrates a one-dimensional wave equation appropriate to a user-defined geometry in a user-selected gas or liquid [15]. For validation of the software, a typical thermoacoustic refrigerator presented in the paper [13] is used. The stated resonator is 61 cm long with a parallel stack sandwiched between two cylindrical ducts of diameter 3 and 1.5 in. The operating temperature and pressure are 300 K and 3 bar, respectively. The resonant frequency for the given model is set to 245 Hz. DeltaEC

Fig. 9 Schematic view of the resonator as per Amirin et al. [13]
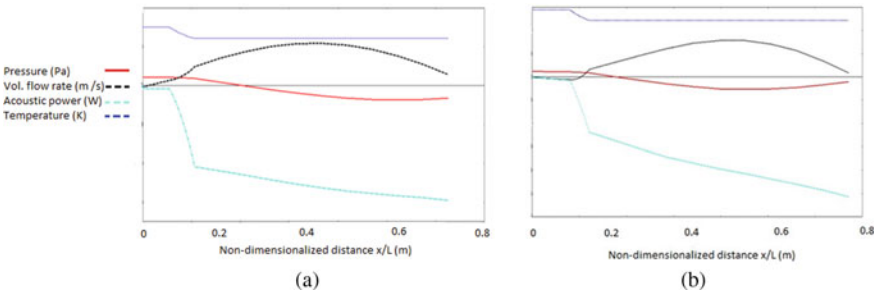
Fig. 10 **a** DeltaEC simulation result as per Amirin et al., **b** obtained DeltaEC simulation
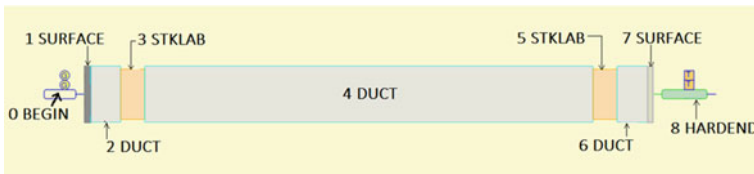
Fig. 11 Schematic view of the resonator

simulation is performed for the given model [13], and the obtained results are aided in the validation of our simulation results (Figs. 9, 10, 11 and 12).

The novelty of present work is in equipping two stacks in a single thermoacoustic refrigerator. The calculated design parameters as shown in Table 4 are used for simulation. Figure 13 is the schematic of the refrigerator equipped with parallel-type stacks as per DeltaEC software. Similarly, simulation is performed for refrigerators with circular- and rectangular-type stacks.

4 Results and Discussions

The temperature distribution obtained for parallel, rectangular and circular stack is plotted. For parallel plate stacks, as shown in Fig. 12, it is found that the hot and cold end of the stack at position 1 is at a temperature of 288.05 K (point a in Fig. 12) and
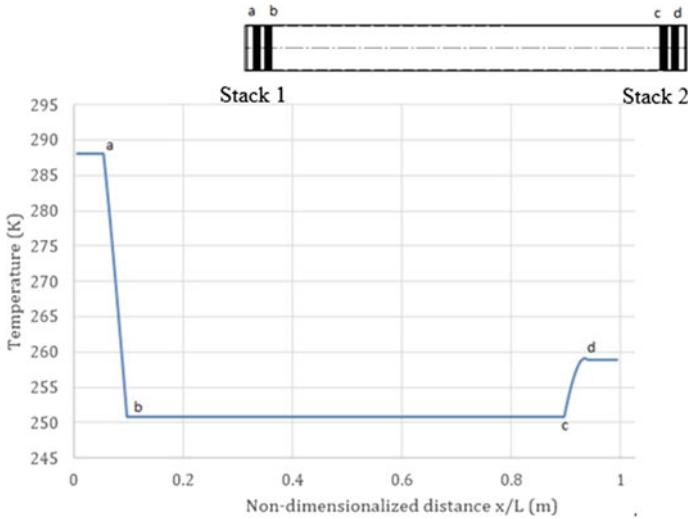
Fig. 12 Temperature distribution along the resonator for parallel-type stack

Table 4 Calculated parameters for simulation

Parameter	Value
Operating frequency (f)	500 Hz
Operating pressure (P_m)	10 Bar
Amplitude of pressure (P_0)	0.3 Bar
Operating temperature (K)	288.05 K
Drive ratio (DR)	0.03
Block ratio	0.8
Resonator length	1 m
Resonator diameter	100 mm
Stack length (L_s)	4.295 cm
Parallel stack spacing (y_0)	1.0 mm
Stack thickness (t)	0.5 mm
Rectangular stack thickness (a)	1.0 mm
Rectangular stack width (b)	10.0 mm
Circular stack radius (r_0)	1.0 mm

250.81 K (point b in Fig. 12), respectively, leading to a temperature difference of 37.27 °C. For stack at position 2, the hot and cold end of the stack is at a temperature of 258.88 K (point d in Fig. 12) and 250.81 K (point c in Fig. 12), respectively, leading to a temperature difference of 8.07 °C.

For rectangular type, as shown in Fig. 13 the hot (a) and cold end (b) of the stack at position 1 is at a temperature of 288.05 K and 248 K, respectively, leading to a
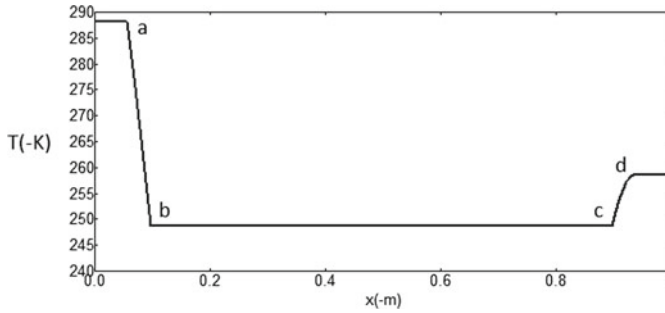
Fig. 13 Temperature distribution plot for rectangular stack from DeltaEC

temperature gradient of 40.05 °C. For stack at position 2, the hot (d) and cold end (c) of the stack is at a temperature of 260 K and 248 K, respectively, leading to a temperature gradient in the stack of 12 °C.

Similarly, for circular type, as shown in Fig. 14 the hot (a) and cold end (b) of the stack at position 1 is at a temperature of 288.05 K and 235 K, respectively, leading to a temperature difference of 53.05 °C. For stack at position 2, the hot (d) and cold end (c) is at a temperature of 255 K and 235 K, respectively, leading to a temperature difference of 20 °C.

Figure 15 illustrates that the temperature difference achieved in stack at position 1 is roughly 460% higher than that in stack at position 2 for parallel plate type stacks. Similarly, it is 240% and 400% higher in the stack at position 1 for circular and rectangular type stacks, respectively. The high magnitude of temperature difference achieved in stack at position 1 compared to stack at position 2 is due to its position in the resonator. As it is close to the acoustic driver, it receives more acoustic power than stack at position 2. Out of the three stack types, the temperature gradient achieved in circular type stacks is the highest and is nearly 140% higher when compared to rectangular and parallel plate type stacks. However, the circular type stacks are difficult to manufacture and cannot be used for practical purposes unlike parallel type stacks.
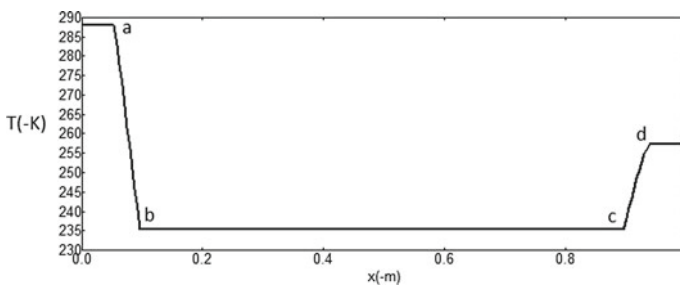
Fig. 14 Temperature distribution plot for circular stack from DeltaEC
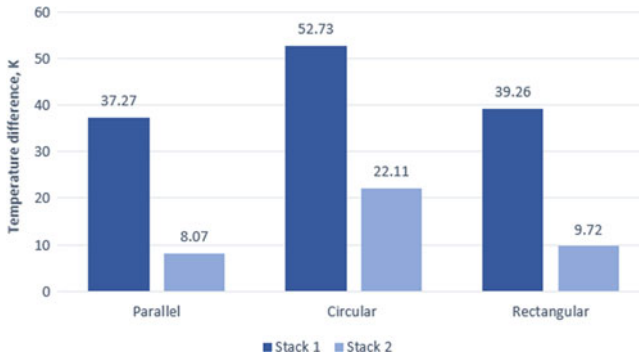
Fig. 15 Comparison of temperature difference for different types of stacks

5 Conclusion

In this study, a half-wave resonator with two stacks is designed and analysed. The half-wave resonator with the two-stack arrangement results in a temperature gradient at the two pressure antinodes as expected. From DeltaEC simulation, it is found that the highest temperature gradient of 52.73 K is achieved in circular type stacks. It is also observed that a significantly higher temperature gradient is achieved at stacks closer to the driver end than at the ones farther to driver. With a two-stack arrangement, a thermoacoustic refrigerator can take two heat loads at the two stacks by introducing cold and ambient heat exchangers. This can increase the net cooling capacity of the refrigerator.

References

1. Zander AC, Cazzolato BS, Howard CQ, Zoontjens L (2013) GradIEAust.: thermoacoustic refrigeration for the automotive industry. J Acoust Soc Am
2. NASA About page. https://webb.nasa.gov/content/about/innovations/cryocooler.html. Last accessed on 2023/01/28
3. Sastry S (2011) A thermoacoustic engine refrigerator system for space exploration mission. Case Western Reserve University
4. El-Fawal MH, Zolpakar NA, Mohd-Ghazali N (2016) Performance analysis of the standing wave thermoacoustic refrigerator—a review. Renew Sustain Energy Rev 54(C):626–634
5. Govinde Gowda MS, Narasimham GSVL, Prashantha BG, Seetharamu S (2017) Design construction and performance of 10 W thermoacoustic refrigerators. Int J Air-Conditioning Refrig 25(03)
6. Tijani MEH, Waele ATAM, Zeegers JCH (2001) Design of thermoacoustic refrigerators'. Cryogenics 42(1):49–57
7. Jaworski AJ, Yahya SGh, Mao X (2017) Experimental investigation of thermal performance of random stack materials for use in standing wave thermoacoustic refrigerators. Int J Refrig 75:52–63
8. Swift GW (1988) Thermoacoustic engines. J Acoust Soc Am 84(4)

9. Gardner D, Poignand G, Bailliet H, Ramadan IA (2021) Design, manufacturing and testing of a compact thermoacoustic refrigerator. Appl Therm Eng 189:116705
10. Bass HE, Belcher JR, Lightfoot J, Raspet R, Slaton WV (1999) Working gases in thermoacoustic engines. J Acoust Soc Am 105:2677
11. Bah A, Hafs H, Bouramdane Z (2018) Standing wave thermoacoustic refrigerator: the principle of thermally driven cooling. In: 6th International renewable and sustainable energy conference (IRSEC)
12. Aryaa B, Shivakumara NV (2020) Experimental performance evaluation of thermoacoustic refrigerator made up of poly- vinyl-chloride for different parallel plate stacks using air as a working medium. In: International conference on materials manufacturing and modelling, proceedings, 22
13. Amirin, Triyono, Yulianto M (2019) Experimental study of thermoacoustic cooling with parallel plate stack in different distances. In: International conference on design, energy, materials and manufacture, vol 539
14. Narasimham, Prashantha, Seetharamu (2022) Theoretical evaluation of stack-based thermoacoustic refrigerators. Int J Air-Conditioning Refrig
15. Ward B, Swift G, Clark J (2017) DeltaEC Version 6.4b2.7 Users Guide

Development and Study of a Low-Cost Mass Flow Characterization Technique for Port Fuel Injector

Manas Kumar Pal, D. Gnaneswar, L. Harish, M. Vishnu Chaitanya, and C. Aravind Reddy

Abstract Liquid fuel injection in the intake manifold is the source of fuel supply in the case of a gasoline engine equipped with a port fuel injection (PFI) system. The injected fuel breaks into small droplets which increases the vaporization rate and leads to proper mixing with the intake air. The amount of the injected fuel significantly influences the air–fuel ratio and as a result controls the combustion and emission formation. In the present work, a low-cost system is developed to measure the fuel flow rate of a PFI injector. The effect of fuel injection pressure, injection pulse width, off time between pulses, and fuel properties on the mass flow rate are studied. A solenoid-operated port fuel injector is taken for the study. A high-pressure chamber is designed and manufactured to control the injection pressure. An Arduino Uno board is used to control the pulse duration of the solenoid valve of the PFI Injector**.** Two fuels, diesel and petrol, and three different injection pressures (2, 4, and 6 bar) are considered for the study. The solenoid opening timings or the pulse width is varying from 2 to 10 ms. The off time between the two pulses is also varied. The experimental results show that increasing the injection pressure or opening time of the solenoid (pulse duration) increases the mass flow rate, but there is no effect of the off time between the two pulses on the mass flow rate. It is also noticed that different fuels show different mass flow rates at the same injection pressure and pulse duration.

Keywords Port fuel injector · Mass flow rate · Solenoid valve

M. K. Pal (✉)
School of Mechanical Engineering, VIT-AP University, Amaravati, Andhra Pradesh 522237, India
e-mail: manaspal2015iitm@gmail.com

D. Gnaneswar · L. Harish · M. Vishnu Chaitanya · C. Aravind Reddy
Department of Mechanical Engineering, Madanapalle Institute of Technology & Science, Angallu, Madanapalle 517325, India

1   Introduction

In the case of an internal combustion engine, the optimal air–fuel ratio has a major effect on the combustion process and hence influences the efficiency and performance of the engine [6, 8]. In most spark ignition (SI) engines, the air and fuel mixture enters the engine cylinder during the intake stroke. Depending on the load and speed conditions, an accurate amount of fuel is mixed with the air either outside or inside the engine combustion chamber. This fuel mixing rate controls the air–fuel ratio and as a result controls the combustion and emission formation [4]. Different fuelling mechanisms have been developed to ensure a very accurate mass flow rate of fuel. Mainly three types of fuel induction systems, namely carburetor, port fuel injection (PFI), and gasoline direct injection (GDI) are adopted in SI engines [12]. In carburetors, the fuel enters the throat of a venturi due to the pressure difference created by the high-velocity air stream. As the fuel amount is dependent on the pressure difference created by the flow of air, this technology cannot meet the accurate air–fuel ratio criteria needed for different conditions such as at low loads/speeds or at sudden load or speed fluctuations. These factors lower the performance and efficiency of engines fitted with carburetors. Due to this, even though traditional carburetors are cheap in cost, most automobiles in the present day either use a port fuel injection (PFI) system or a direct injection (GDI) system. Both systems use electronic fuel injectors to spray the fuel into the engine. The basic difference between PFI and GDI is in the position of the fuel injector. In PFI systems, fuel is sprayed into the intake manifold, whereas in GDI, fuel is directly injected inside the cylinder. Direct injection technology has multiple benefits such as better fuel economy and more power. However, GDI operates at a much higher injection pressure compared to the PFI system, and as a result, a dedicated high-pressure fuel injection system needs to be incorporated into the engine. This increases the cost of the engine. Thus, PFI systems are very popular nowadays. In this system, with a multi-hole injector, fuel is sprayed at the backside of the intake port where it is atomized and subsequently evaporates and mixes with the air and then is pulled into the combustion chamber Zhao et al. [15].

The port fuel injector consists of a solenoid to operate the needle lift of the injector and thus precisely control the mass flow rate of the fuel. When the Electronic Engine Control Unit (ECU) supplies an electric signal to the fuel injector, the solenoid in the fuel injector is energized. The energized solenoid pulls back the needle of the injector and as a result, fuel flows through the orifice of the injector into the intake manifold [5]. The amount of fuel injected depends on many parameters like orifice diameter, injection pressure, and injection pulse duration. The mass flow rate of fuel by the injector nozzle is given by the below equation [11].

$$m_\mathrm{f} = C_\mathrm{d} A_\mathrm{f} (2\rho_\mathrm{f} \Delta P)^{1/2} \Delta t,$$

where C_d is the orifice discharge coefficient, A_f is the flow area of the nozzle orifice, ΔP is the pressure drop across the nozzle, and Δt is the pulse width of the injector. Pulse duration is the time for which an electric pulse is given to the solenoid of the

injector, and as a result, the fuel injector remains open for that time. The engine control module (ECM) controls the injection pulse duration based on engine loads and speed conditions [14]. The airflow rate and the engine speed are the primary signals required to determine the pulse width. In general, the pulse width is directly proportional to air mass flow rate and engine speed. To control the air–fuel ratio accurately, precise measurement of airflow is important. In modern engines, the mass rate of airflow is directly measured by a hot-wire/hot-film anemometer. The microprocessor of ECM makes compensation for any airflow loss caused by valve adjustments, engine wear, and deposit buildup in the combustion chamber that may result from vehicle usage.

As discussed before, in PFI engines, fuel is injected in the inlet manifold at the back of the inlet valve. Typical injection pressure in a PFI injector is around 2–8 bar, whereas modern GDI injectors operate at 50–300 bar. Due to low injection pressure, atomization is poor in the PFI system, and as a result, big-size droplets are produced. Intake manifold and intake valve wetting commonly occur which leads to form a liquid film on the walls, and as a result, the fuel economy is reduced [13].

Lai et al. [7] investigated the effect of the geometry of exit holes of different types of PFI injectors and reported that the square hole was more effective in enhancing the spray breakup and led to a comparatively better atomization result than the round exit hole. They also reported that an increase in injection pressure enhanced atomization; however, due to mechanical difficulty, there was an optimized injection pressure for the port fuel injector. Aoki et al. [3] compared the spray pattern and droplet diameters between a straight-hole nozzle and a taper-hole nozzle. They found that straight-hole nozzles produced a liquid core and taper-hole nozzle produced liquid films. The droplet diameter of the taper hole was smaller than that of the straight hole. Anand et al. [2] studied the injection pressure effect on two different (two holes and four holes) PFI injectors. The spray angle and spray tip penetration were determined from the processed shadowgraph images. The backlit images also showed insights into the development of the spray. They reported that spray tip penetration and cone angle increased with higher injection pressure. Droplet sizes were determined at various times after the start of injection. It was observed that an increase in the injection pressure or a decrease in the diameters of holes in the injector decreased the Sauter mean diameter (SMD). Padala et al. [10] studied PFI injectors with two different nozzles (high flow rate and low flow rate) and two different fuels, gasoline and ethanol. For the same injection pressure, light components of gasoline droplets evaporated at a faster rate than ethanol droplets. Smaller-sized droplets of ethanol were imaged near the nozzle compared to gasoline. They explained that the breakup of ethanol sprays was much higher than gasoline sprays right after the introduction of fuel into the ambient gas. In another work by Anand et al. [1], spray characterization of gasoline–ethanol blends from a multi-hole port fuel injector had been examined. Similar volume flow rates and spray tip penetration were observed for different blends. The droplet sizes were also found to be similar for different fuels and their blends though a considerable difference in the viscosity among the fuels was present. Nakamur et al. [9] conducted an improvement of spray characteristics

in port injectors**.** They focused on the improvement of the atomization process with an optimized layout of nozzle holes.

The previous works on port fuel injectors show that there are multiple factors involved in controlling the fuel injector mass flow characteristic. It is also noticed that earlier works on port fuel injectors are mostly based on the spray structures and the atomization process. In particular, detailed data on mass flow characteristics with respect to changes in pulse duration, pulse dwell time, and injection pressure from the actual injectors used in modern engines are lacking. In addition to this, many automobile manufacturers are focusing on developing the port fuel injector with the same mass flow rate and better atomization. The mass flow rate needs to be studied for newly developed injectors. These factors motivated us to develop a cost-effective experimental technique for studying the mass flow characteristics of the port fuel injector with the effect of injection pressure, solenoid pulse duration, solenoid off time, and also the effect of different fuels. Above all, though this study will concentrate on the mass flow characterization of a PFI injector, the developed technique can be used to study any type of solenoid injector for example GDI or urea injector in the case of an SCR system.

2   Experiment Setup and Methodology

The experimental setup for testing the port fuel injector consists of mainly two major components, (a) a pressure chamber (operating pressure of 0–10 bar) to increase the pressure of the fuel to the required level and deliver it to the port fuel injector and (b) an Arduino circuit board to regulate the solenoid valve timings of the injector. Figure 1 shows a schematic of the experimental facility.

Fuel is poured into the pressure chamber and its pressure is raised by using compressed air via an air compressor. The pressure chamber is connected to the solenoid fuel injector through a high-pressure pipe. Once the chamber is raised to the required pressure, an electronic input signal in terms of pulse width and off time is given to control the opening timings of the fuel injector. The amount of fuel injected from the injector for a certain number of injections (1000 injection shots) is collected using a measuring beaker and its mass is measured using a digital mass balance. A photograph of the setup is given in Fig. 2.

2.1   Pressure Chamber

The pressure chamber is designed to withstand 20 bar pressure. Stainless steel of 304-grade material is chosen due to its high strength and corrosion-resistant capability. The inner diameter of the chamber is taken as 160 mm and the wall thickness is 6 mm. The thickness of the chamber is calculated using UG 27 Formula (ASME BPVC 2010-Section VIII, Division 1; Rules for construction of Pressure Vessels). It
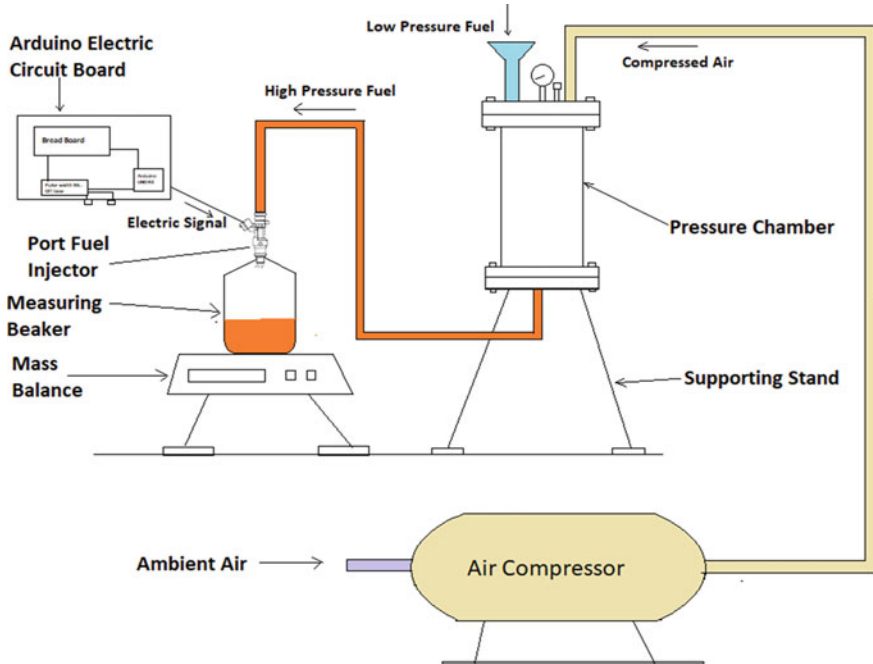
Fig. 1 Schematic of the experimental setup
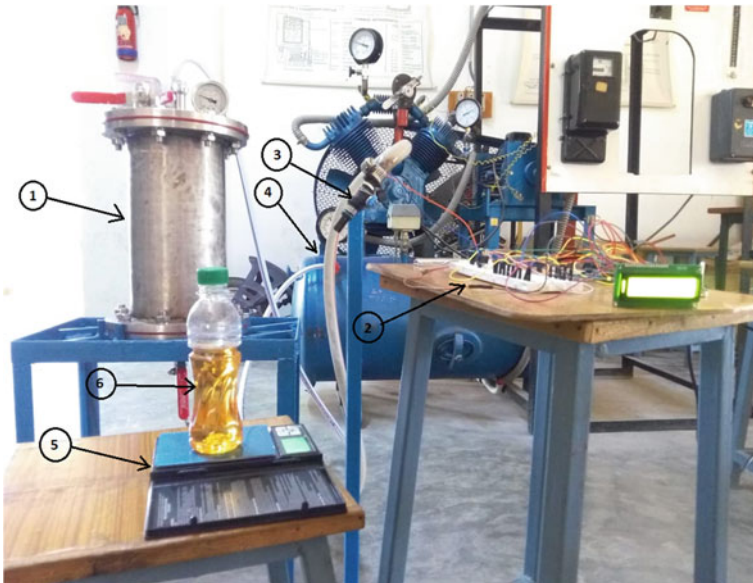
Fig. 2 Photograph of experimental setup (1. Pressure chamber, 2. Arduino circuit board, 3. port fuel injector, 4. high-pressure pipe, 5. mass balance, 6. collected fuel)

is manufactured by covering a cylindrical pipe with flanges on both sides. Two cover plates are used on each side of the cylinder. The cover plates are held together with the flanges using bolts. A silicone gasket sheet of thickness 4 mm is used in between the flanges and cover plates to avoid any leakages from the chamber. A pressure gauge and a safety valve are mounted on the top cover plates. A ball valve is used to fill the fuel and lock it during high pressure.

2.2 Arduino Uno Circuit to Control the Solenoid Valve of the PFI Injector

An Arduino Uno microcontroller is used to control the pulse width of the injector. It has 14 digital ip/op pins, six analog inputs, a USB connection, a power jack, and a reset button. It is connected to a computer with a USB cable to program the code of required functions. A solderless Bread Board is used for completing the circuit. A potentiometer and an LCD display are used for control and display.

2.3 Fuel Injector

A solenoid valve operated, low-pressure port fuel injector is used in this study. The injector has a multi-hole (12-hole) orifice and opens at 12-V electrical input. A photograph of the fuel injector used in this study along with its front cross-section is given in Fig. 3.

Fig. 3 Port fuel injector used for testing

Table 1 Properties of petrol and diesel

Fuel	Density (kg/m^3)	Viscosity (c-st)	Surface tension (mN-m)
Petrol	738.4	1.2	21
Diesel	814.4	3.2	28

2.4 Experimental Methodology

The experiments are conducted to measure the mass flow characteristics (mass injected per shot) of a port fuel injector. Three different injection pressures 2, 4, and 6 bar, five different injector pulse widths (2–10 ms), and four different injectors off times (20, 40, 60, and 80 ms) are adopted in this study. For each injection pressure, the mass of fuel injected is measured at different injection timings. The total time of injection for n number of injections is given by the following equation:

$$t = n \times \frac{(\text{pulse width in ms} + \text{solenoid off time in ms})}{1000},$$

where t is the total time of injection in seconds, and n is the no. of injection shots, pulse width, and solenoid off time in milliseconds. Initially, the experiments are conducted for a different number of injection shots, with all other parameters being constant. As there was no effect of the number of injection shots on the mass flow rate, all the experiments are conducted for 1000 shots of injection. Each set of experiments is conducted three times and the average value of the three samples is taken for analysis.

The properties of fuel such as density, viscosity, surface tension affect the flow of the fuel from the injector nozzle. Two common fuels, diesel and petrol, are used for the study. Though in general, diesel is not used in PFI injectors, it is chosen as a fuel with different properties compared to petrol. The properties of the fuels are given in Table 1.

3 Result and Discussion

3.1 Effect of Solenoid off Time on Mass Flow Rate

The solenoid off time is the time interval between the two solenoid opening pulses. During this time duration, the solenoid of the fuel injector remains in the deactivate position and thus is closing the injector holes. The solenoid off time mainly depends on the engine rpm. For high speeds, the solenoid off time is very low and vice versa for low speeds. The experiments are conducted at four different off times (20, 40, 60, and 80 ms). Figure 4 shows the mass of fuel injected per shot for different solenoid off timings. From the figure, it can be observed that the mass of fuel is constant for different solenoid off times at the same fuel, injection pulse width, and injection
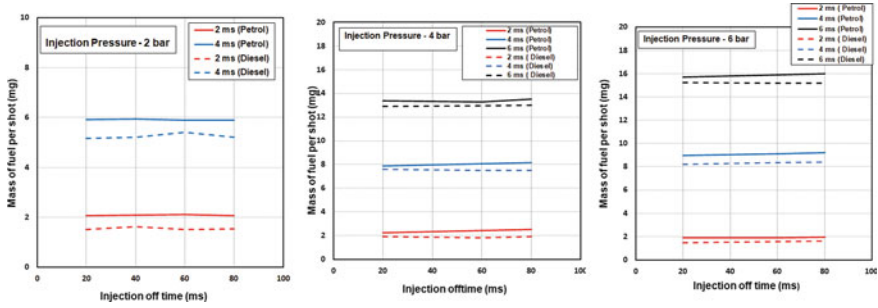
Fig. 4 Plot of solenoid off time versus mass of diesel and petrol at different injection pressures and different pulse times

pressure. Hence, it can be concluded that there is no effect of solenoid off time on the mass of fuel injected.

3.2 Effect of Pulse Width on Mass Flow Rate

Pulse width is the duration of the solenoid in the open position, or it is the amount of time for which electric current is supplied to magnetize the armature of the solenoid to pull back the needle valve of the injector. The pulse width depends upon the engine loading conditions and operating conditions. Generally, the pulse width is directly proportional to the engine load. Experiments are conducted at five different pulse widths (2, 4, 6, 8, and 10 ms) while keeping the fuel, solenoid off time, and injection pressure the same. Figure 5 shows the mass of fuel injected per shot at different pulse widths. From the figure, it is evident that the mass of fuel constantly increases with the increase in the injection pulse width at a constant injection pressure. The trend is the same for both fuels.

3.3 Effect of Injection Pressure on Mass Flow Rate

The pressure at which the fuel is injected into the intake manifold of the cylinder is called as the injection pressure of PFI. Generally, the injection pressure influences the spray characteristics and atomization of fuel. The injection pressure also affects the mass of the injected fuel. In the present study, experiments are conducted at three different injection pressures (2, 4, and 6 bar) for two different fuels and five different pulse widths. The solenoid off time is kept constant at 20 ms. Figure 6 shows the mass of fuel injected per shot at different fuel injection pressures. From the figure, it can be seen that the mass of injected fuel increases with an increase in the fuel injection pressure. The trend is the same for almost all pulse widths except one. It can

Fig. 5 Plot of injection
pulse width versus mass
injected per shot. Injection
off time is 20 ms and
injection pressures are 2, 4,
and 6 bar
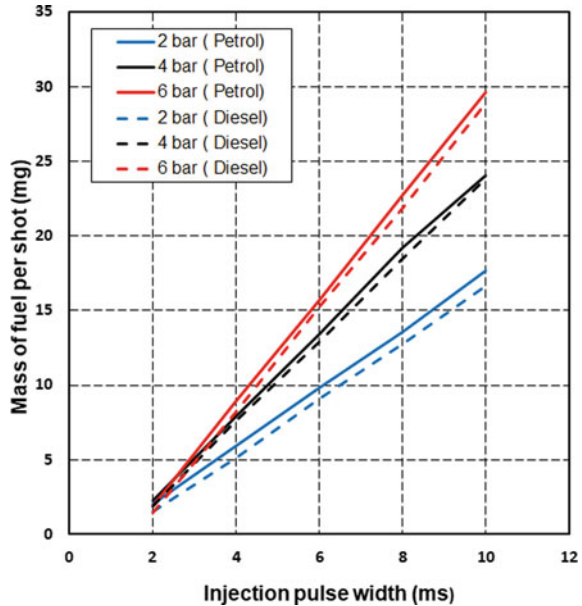
be noticed that for high injection pressure (6 bar) and small pulse width (2 ms), the
fuel injected is smaller than for low injection pressure (2 and 4 bar) and small pulse
width (2 ms). The possible reason for this phenomenon may be that at high pressure,
the electric current supplied during small pulse width is not enough to fully lift the
needle valve. Hence, the fuel mass flow rate decreases at high injection pressure with
low pulse duration.

3.4   Effect of Fuel on Mass Flow Rate

Figures 4, 5, and 6 compare the mass flow characteristics for diesel and petrol for
the same solenoid off time, injection pulse width, and injection pressure. The above
experimental results show that the mass of petrol injected is slightly higher than the
mass of diesel for the same injection pressures, pulse width, and solenoid off time.
Though the density of diesel is higher than that of petrol, still the mass flow rate is
low. This is due to the lower viscosity of petrol than diesel. Lower viscosity increases
the flow rate and hence increases the mass flow rate for petrol.

Fig. 6 Plot of injection
pressure versus mass of
diesel and petrol at different
solenoid timings. Injection
off time is 20 ms
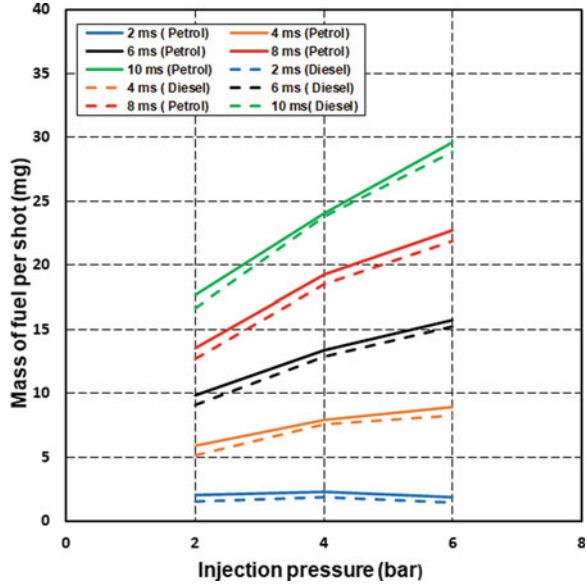
4 Conclusion

In the present work, a low-cost method is developed to measure the fuel flow rate of
a PFI injector. The effect of fuel injection pressure, injection pulse width, injector
off time, and fuel properties on the mass flow rate are studied experimentally. A
high-pressure fuel chamber is designed and manufactured to precisely control the
injection pressure. An Arduino Uno board is used to control the pulse duration of
the solenoid valve of the PFI injector. Three different injection pressures (2, 4, and
6 bar) are considered. The solenoid opening timings or the pulse width is varying
from 2 to 10 ms. The off time between the two pulses is also varied. Two fuels, diesel
and petrol, are used for the study. The experiments revealed the following.

(1) There is no effect of the off time of the solenoid between the two pulses on the
mass flow rate.
(2) Increasing the injection pressure increases the mass flow rate of the fuel for a
constant pulse duration.
(3) Higher pulse duration also increases the mass flow rate.
(4) At low pulse width like 2 ms, the mass flow is decreased for 6 bar injection
pressure compared to 2 bar injection pressure. At higher pressure, more current
is required to fully open the solenoid valve.
(5) At constant pulse width and injection pressure, petrol shows a small increase
in the mass flow rate compared to diesel. The lower viscosity of petrol is the
probable reason behind that.

References

1. Anand T, Mohan AM, Ravikrishna R (2012) Spray characterization of gasoline-ethanol blends from a multi-hole port fuel injector. Fuel 102:613–623
2. Anand TNC, Avulapati MM, Deshmukh D, Rayavarapu R (2010) Optical characterization of PFI gasoline sprays: effect of injection pressure, SAE Technical Paper Series vol 2010-32-0067
3. Aoki F, Enomoto S, Nakase Y (2005) Spray analysis of port fuel injector, SAE Technical Paper Series, vol 2005-01-1154
4. Åderemet B, Dinleri N (2022) Numerical investigation of the effects of intake valve geometry on air flow during intake stroke. Int J Energy Clean Environ 23:39–51
5. Gao J, Jiang D, Huang Z (2007) Spray properties of alternative fuels: a comparative analysis of ethanol-gasoline blends and gasoline. Fuel 86:1645–1650
6. Heywood JB (1998) Internal combustion engine fundamentals. McGraw Hill, Singapore
7. Lai MC, Zhao FQ, Amer AA, Chue TH (1994) An experimental and analytical investigation of the spray structure from automotive port injectors, SAE Technical Paper Series, vol 941873
8. Muthuveerappan A, Ajay C, Manimaran R (2021) Numerical investigation of hydrogen air mixture induction and diesel injection in a single cylinder 4-stroke compression ignition engine. Int J Energy Clean Environ 22:99–127
9. Nakamur J, Akabane A, Kitamura K, Sasaki Y (2012) Improvement of spray characteristics in port injectors, SAE Technical Paper Series, vol 2012-32-0071
10. Padala S, Le MK, Kook S, Hawkes ER (2013) Imaging diagnostics of ethanol port fuel injection sprays for automobile engine applications. Appl Therm Eng 52:24–37
11. Pundir BP (2010) IC engines combustion and emission. Narosa Publishing House, India
12. Raju TB, Hithaish D (2014) A review on gasoline direct injection system. Int J Res Aeronaut Mech Eng 2(3):224–231
13. Tang D, Luo F (2020) Effect of load on combustion cyclic variation in CNG/diesel dual-fuel engine. Int J Energy Clean Environ 21:25–39
14. Tang D, Luo F (2021) Investigation of the hydraulic flow characteristics of a common-rail injector during operation process in a diesel engine. Int J Energy Clean Environ 22:77–100
15. Zhao FQ, Lai MC, Harrington DL (1995) The spray characteristics of automotive port fuel injection-a critical review, SAE Technical Paper Series, vol 950506

Effect of Different Concentration of Carrageenan Additive on Pool Boiling Heat Transfer Augmentation

Shivprasad Tatyasaheb Waghmare, Nivedita Mangal Desale, Sagnik Pal, **Pankaj Tambe**, **Sameer Sheshrao Gajghate**, and **Himadri Majumder**

Abstract Adding a small concentration of surfactant additive in pure water considerably decreases the surface tension of the aqueous solution at the liquid–vapor interface and decides the asymptotic limit of reduction in surface tension with increasing additive concentration. The present investigation is to pool boiling heat transfer enhancement of aqueous carrageenan solution with and deionized water with and without carrageenan additive. Firstly different concentrations of carrageenan with deionized water has prepared, i.e., 100, 200 ppm. All experiments were carried out in saturated solutions at atmospheric pressure. Bubble behavior was studied using a Canon camera operating at 100 frames per second. The investigation was conducted at variable heat fluxes to check the effect of heat flux on bubble growth. The higher concentration of additive (carrageenan) 200ppm shows a 54% increment in HTC. The tiny bubble was observed at a higher heat flux of 854 kW/m^2, whereas additive bubbles could not be captured due to the milky color of the solution. The present study relieved the effect of additives on the heat transfer coefficient due to the change in thermal properties.

Keywords Surface tension · Carrageenan · Pool boiling · Bubble growth · Heat transfer coefficient

S. T. Waghmare · N. M. Desale · S. S. Gajghate (✉) · H. Majumder
Department of Mechanical Engineering, G H Raisoni College of Engineering and Management, Pune, Maharashtra 412207, India
e-mail: sameer.gajghate@raisoni.net; mtech_sameer@yahoo.in

S. Pal
Department of Mechanical Engineering, National Institute of Technology Agartala, Tripura 799046, India

P. Tambe
School of Mechanical Engineering, VIT-AP University, Amaravati, Andra Pradesh 522237, India

1   Introduction

Pool boiling is a significant heat transfer process in various industrial thermal applications such as electricity generation, refrigeration, and heat exchangers. Heat transfer in thermal applications depends on the surface and test fluid properties. In 2011, there was a failure in the nuclear power plant, which tends to a blast in Fukushima nuclear plant due to a tsunami in Japan. This incident study shows several flaws in the cooling of nuclear reactors and fusion reactions. So, tremendous work must be carried out to solve the issue of cooling a nuclear reactor, which can be solved by working on heater surface characteristics and fluid properties too. Many researchers worked on surface characteristics, liquid properties, and their impact on augmentation boiling heat transfer. In contrast, the enhancement in pool boiling concerning bubble dynamics study was based on additives in the working fluid, which has been increasingly important in recent years to improve the boiling heat transfer performance. The concerning studies were discussed in the following section.

Dehshali et al. [1] performed the experiments using a test platform with water as a working fluid and copper-stranded ribbon fins attached to the heating surface. The effect of heat flow and blade geometries modified parameters and the impact on heat transfer coefficient (HTC) and boiling heat transfer performance. The results indicate that using twisted-tape fins can significantly enhance the HTC and heat transfer performance, achieving optimal performance at specific fin geometries and heat flux values. The authors also provide correlations using experimental data to predict the heat transfer coefficient and boiling heat transfer efficiency. Overall, the research demonstrates the potential of twisted-band fins to improve pool boiling heat transfer effectively. Gajghate et al. [2] evaluate the effect of using ZrO_2 nanofluids on improving pool heat transfer when applied to copper surfaces with offset V-shaped rectangular grooves. The authors performed experiments and discovered that nanofluids improved the heat transfer coefficient on both grooved surfaces. The surface of the rectangular groove was also found to improve heat transfer from the V-shaped groove surface. The research results can be applied to the design of efficient heat transfer systems. Kiyomura et al. [3] research paper examine micro-fin surface's effect on boiling heat transfer using HFE-7100 as a working fluid. A team of Brazilian and Indian scientists conducted the study. The experimental setup involved a horizontal tube with a micro-fin surface and a plain surface, and the HFE-7100 was used as the working fluid. The results showed that the micro-fin surface improved the boiling heat transfer coefficient significantly compared to the plain surface. The study also found that the micro-fin surface reduced the heat transfer coefficient during the post-boiling phase. Overall, the research paper suggests that micro-fin surfaces can effectively enhance boiling heat transfer in specific applications. Vipassana et al. [4] introduce pool boiling, a standard heat transfer mechanism in various industrial applications. The authors note that pool boiling can be improved through the use of additives, which can improve the efficiency of heat transfer. Les. The authors conducted experiments using a cylinder copper tube with a heater at the bottom. Deionized water was used as a working fluid, and the additives used were

copper oxide, alumina, and zinc oxide nanoparticles. Experiments were conducted at different concentrations of nanoparticles and thermal flows. The results demonstrated that the addition of nanoparticles improves the boiling heat transfer coefficient of the pool versus deionized water alone. The most remarkable improvement was observed by adding copper oxide nanoparticles at 0.2%, which increased the heat transfer coefficient by 89.4% compared to deionized water. The authors conclude that adding nanoparticles can significantly improve the transfer of boiling pool heat to deionized water. The study provides valuable information to increase heat transfer efficiency in various industrial applications. Massoud et al. [5] investigated the influence of nucleation site size on bubble dynamics during nucleate pool boiling heat transfer. The experiments were conducted on a copper surface with DI water as the test fluid. The authors observed the dynamics of the bubbles using a high-speed camera. The experiments were repeated for various heat streams and surface orientations. The results have shown that the size of the nucleation site has a significant impact on bubble dynamics. The minor nucleation sites have produced smaller bubbles that have merged to form more giant bubbles. Bubbles were observed to drift away from the surface more rapidly, resulting in a higher heat transfer coefficient. The authors have observed that the increase in heat flow caused an increase in the starting diameter of the bubbles. In addition, the surface area guidance had a minor effect on bubble dynamics. Overall, the study provides information on the boiling mechanisms of nuclear pools and underlines the importance of the size of nuclear sites in determining heat transfer rates. The results may be obtained for possible applications in the design of heat transfer systems for different industries. Najim et al. [6] carried out experiments to measure the heat transfer coefficient and the size of bubbles when boiling in the presence of surfactants. They found that surfactants significantly affected the growth rate and release of bubbles in the heated area. A study also showed that the surfactant concentration critically affected bubble size and thermal transfer coefficient. Adding surfactant to the boiling liquid caused smaller bubbles and increased the heat transfer coefficient, leading to a more efficient heat transfer. On balance, the research paper provides valuable insight into the effect of surfactant additives on bubble growth during boiling heat transfer in the pool. The results can be applied to the design and optimization of heat transfer systems, especially in industries like electricity generation and electronic cooling.

After the extensive literature studies based on additives for pool boiling heat transfer, it was observed that no researchers have yet to consider carrageenan additives. Also, only some researchers were revealed the bubble dynamics studies while working on pool boiling. The present research shows the effect of carrageenan additive on pool boiling heat transfer performance and bubble dynamics study.

Fig. 1 a Sea-based carrageenan, and **b** Carrageenan in powered form

2 Experimental Methods

2.1 Eco-Friendly Additive

Carrageenan or carrageenin is a family of natural linear sulfated polysaccharides that are extracted from red edible seaweeds (see Fig. 1a). Carrageenan is widely used in the food industry for its gelling, thickening, and stabilizing properties. Their main application is in dairy and meat products due to their strong binding to food proteins. In recent years, carrageenan has emerged as a promising candidate in tissue engineering and regenerative medicine applications as they resemble native glycosaminoglycans (GAGs). Carrageenans are large, highly flexible molecules that form curling helical structures. It gives the ability to form various gels at room temperature. They are widely used in food and other industries as a thickening and stabilizing agent; a) Natural polysaccharide extracted from red algae was found to alter the hot heat transfer characteristics due to its unique rheological properties. The add-in from carrageenan (see Fig. 1b) to the working fluid can alter the surface tension and viscosity of the fluid, thus affecting the dynamics of bubbles when the pool boils. This study aims to study the effect of the carrageenan additive on bubble growth during pool boiling.

2.2 Experimental Setup

The experiments were conducted in a glass vessel pool using deionized water as a working fluid with and without additive. The heating surface was a $50 \times 50 \times 5$ mm copper plate placed at the bottom of the test heater. A test heater of stainless steel cylinder (5mm in length and 1mm in dia.) needle (hollow) was used. The two thermocouples (K—type) were used, one attached at the lower surface of the copper

sheet to measure the wall temperature and another suspended in the boiling vessel to measure the temperature of the test fluid. A dimmer stat used to measure the power supply to the heaters. The details of experimental setup are shown in Fig. 2, and instrument specification is shown in Table 1.

Initially, the 100 and 200 ppm concentration has been prepared using the relation.

$$1\,ppm = \frac{1mg}{Lit} \tag{1}$$

As per Eq. 1, the total volume considered for the experimentation is 900 ml. Accordingly, the digital weight balance weight has been calculated and added to the DI. The experiment was performed with DI water for the needle heater to study the single bubbles dynamics. First, the 900ml of DI water was added into the glass vessel, and the bulk heater was switched on to heat the test fluid until the saturation level; a parallel test heater was also kept on to get heated. As the temperature of DI water reaches saturation level, the bulk heater electric supply has

Fig. 2 Actual experimental setup with control panel and display

Table 1 Specification of instrument

Part name	Capacity/ accuracy	Made/type
Boiling vessel	$0.0054m^3$	Borosilicate
Ammeter, 0–10A	$\pm\,0.01$ A	Analog
Test heater (stainless steel)	$\emptyset = 1mm, L = 3mm$	Nickel chrome
Autotransformer, 10 A & 230 V	$\pm\,2$ V	Analog
Temp. indicator, 9999 °C	1 °C	Digital
Bulk heater, 1 kW	1 W	Nichrome
Thermocouple, 0–1200 °C	0.1 °C	K-type
Voltmeter, 0–270 V	$\pm\,1$ V	Analog

been cut. Then gradually, after every 15 min, the voltage of the test heater increases using the dimmer that knop, and parallelly reading is noted for current, and both the thermocouples through the digital display. Moreover, this process continues until the maximum voltage reaches 110 V, and the power supply is cut off. Same process has been followed for different concentration of carrageenan.

After the experimentation, the recorded values from measuring instruments were put into the equation to calculate the HTC as per the shown Eqs. (2) and& (3).

$$q = \frac{I \times V}{A} \tag{2}$$

$$h = \frac{q}{\Delta T} \tag{3}$$

where q is heat flux (W/m^2), and I, V, A, ΔT, h are current (amp), voltage (volt), the surface area of the needle (m^2), and wall superheat (Kelvin). The experiments were conducted at room temperature, and the heat input per unit area was gradually increased by 50 W/m^2.

2.3 Uncertainty Analysis

The error analysis was conducted for measuring instruments that Kline and McClintock [7] report. The exactness of the voltmeter and ammeter was ± 1 V, ± 0.01A, and the wall superheat of test fluid and heater were estimated by the calibrated K-type thermocouple 1°C. It shows a 67.5% of accuracy level. The error in calculated heat flux is $\pm 2.36\%$ at 100 and 200 ppm concentrations of aqueous carrageenan solution lie within limits.

3 Result and Discussion

The experiment was conducted under atmospheric temperature with and without additives in DI water for a variable range of heat flux. To check the consistency of the experimental outcomes, a repeatability test was conducted with DI water, as shown in Fig. 3, and observed the results were found to the consistency, with little deviation observed due to the vibration of the bubble phenomenon.

The experiment is carried out for DI water and different concentrations of aqueous Carrageenan, i.e., 100 and 200 ppm. The test was conducted for variable heat flux, and it has been observed that the wall superheats temperature decreases as the concentration increases. It might be due to the effect of the thermal properties of carrageenan additives added in DI water and the surface tension of liquids, which decreased the wall superheats shown in Fig. 4. Figure 5 shows that as the concentration increases,
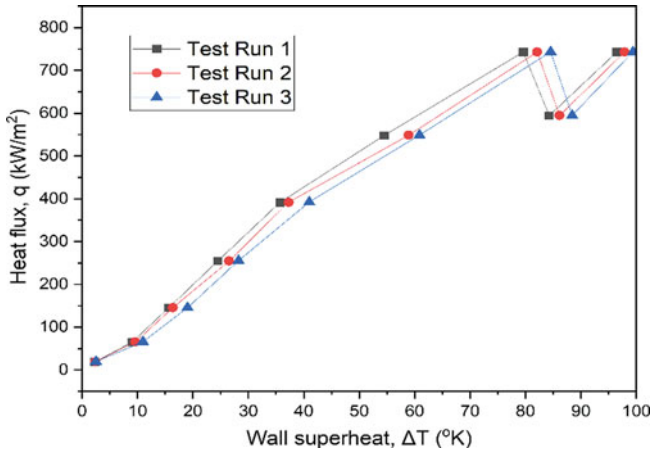
Fig. 3 Repeatability test of DI water

HTC increases, and the boiling curve is shifted to the left side with minimum super-heat. Hence, it was observed that 54% of HTC increases for 200 ppm of concentration compared to DI water and 38.49% for 100 ppm of solution (Fig. 5).

Further, a relative HTC test has been conducted with DI water and aqueous carrageenan additive solution to monitor the enhancement with the fluid considered. Moreover, it observed that the aqueous solution relative HTC increases compared to the DI water. The relation to calculating the relative HTC coefficient has been addressed by Wasekar and Manglik [8], as shown in Eq. 4.
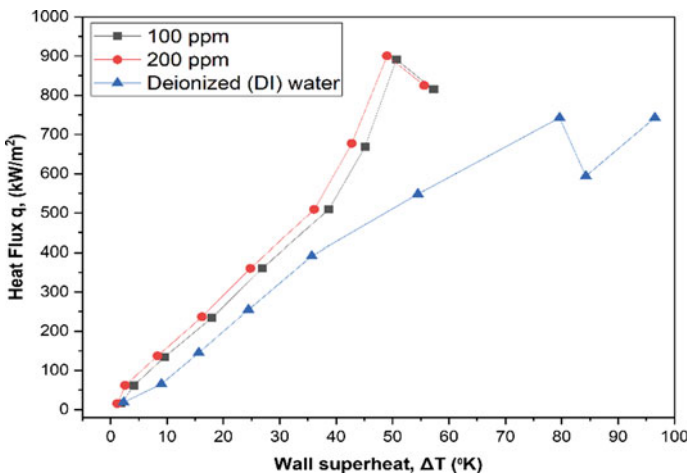
Fig. 4 Heat flux versus wall superheat for tested fluids
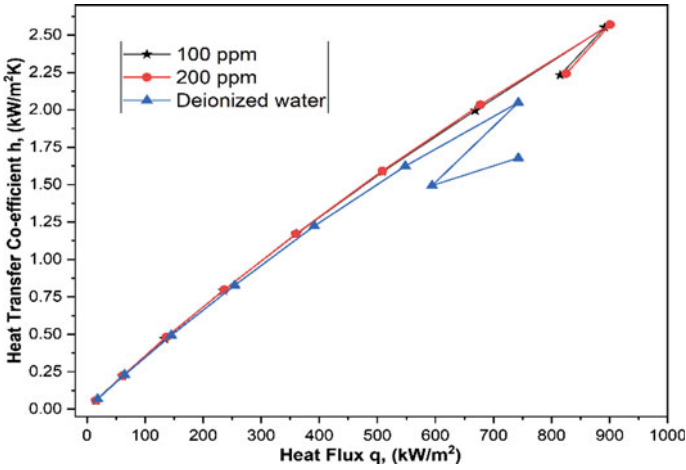
Fig. 5 Heat flux versus heat transfer coefficient for tested fluids
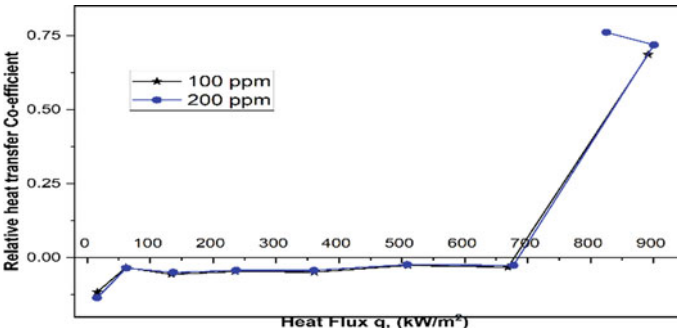
Fig. 6 Relative heat transfer coefficient for tested fluids

$$\frac{h - h_{\text{fluid}}}{h_{fluid}} = \left(\frac{q}{\Delta T} - \frac{q_{\text{fluid}}}{\Delta T}\right)\Big/\left(\frac{q_{\text{fluid}}}{\Delta T}\right) \tag{4}$$

In Fig. 6, the relative HTC has been calculated using Eq. 4, and observed that an increase in concentration relative HTC is increased. The maximum increased in relative HTC is observed for 200 ppm of carrageenan concentration till 900 kW/m² of heat flux beyond that limit the relative HTC is decreasing. Hence, relative HTC is increased by 73.87% compared to DI water. Furthermore, the adopted carrageenan concentration solutions need low energy to reach at HTC in compared to DI water, as shown in Fig. 7. The bubble behavior has been captured using an advance Canon camera with 100 frames per sec. In Fig. 7, the bubbles shown are of DI water, and as the color of the additives is white, no bubble behavior has been observed.

Fig. 7 Bubble behavior at maximum 852 KW/m^2 of heat flux
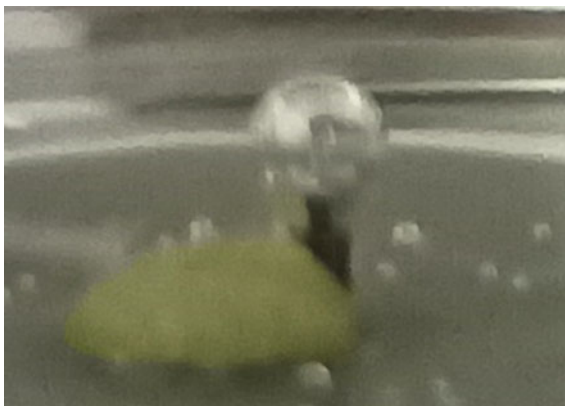
4 Conclusion

It was found that mixing carrageenan additive with deionized water improved boiling heat transfer performance due to changes in the thermal properties of the liquid, such as surface tension. The carrageenan additive promotes nucleation and increases the bubble starting point. The results showed that adding these additives significantly increases the heat transfer coefficient of the smooth needle surface. Additionally, using environmentally friendly additives can provide a sustainable solution for improving heat transfer without harming the environment. Overall 54% rise in heat transfer coefficient compared to DI water.

References

1. Dehshali EM, Seyyed ZNB, Fard A (2018) Pool Boiling heat transfer enhancement by twisted tape fins. Appl Therm Eng 135:170–177
2. Gajghate SS, Acharya AA, Pise AT, JAdhav GS (2014) Experimental study of heat transfer enhancement in pool boiling by using 2-Ethyl 1-Hexanol an additive. Appl Mech Mater 592:1601–1606
3. Kiyomura IS, Manetti LL, Da Cunha AP, Ribatski G, Cardoso EM (2017) Analysis of the effects of nanoparticles deposition on characteristics of the heating surface and on pool boiling of water. Int J Heat Mass Transf 106:666–674
4. Vipashana KM, Walke PR (2019) Anexperiment study of pool boiling heat transfer enhancement in deionised water using additive. Int Res J Eng Technol 6(7):1–9
5. Massoud ED, Seyyed ZNB, Ali HF (2018) Pool boiling heat transfer enhancement by twisted -tape fins. Appl Therm Eng 135:170–177
6. Najim A, Vasudha M, Thorat A, Patil S, Savale S (2017) Enhancement of pool boiling heat transfer using innovative non-ionic surfactant on a wire heater. Exp Thermal Fluid Sci 82:375–380
7. Gajghate SS, Barathula S, Das S, Saha BB, Bhaumik S (2020) Experimental investigation and optimization of pool boiling heat transfer enhancement over graphene-coated copper surface. J Therm Anal Calorimetry 140:1393–1411

8. Gajghate SS, Barathula S, Cardoso EM et al (2021) Effect of staggered V-shaped and rectangular grooves copper surfaces on pool boiling heat transfer enhancement using ZrO_2 nanofluids. J Brazilian Soc Mech Sci Eng 43:75

CMorse—Automated Laser-Based Morse Code Transmission Through Multi-layered Encryption

Peddiraju Sudheendra, Dharmapuri Sudheshna, Ambuj Sharma , **Anusha Sharma, Aparna Supriya, Rithy Raichel Soj, Abhinav Ramabhadran, Suyog Jhavar** , **and Pankaj Tambe**

Abstract Streamlining and boosting the effectiveness of Morse code communication are a major challenge that limits the application of Morse code in real-life and secure and flawless communication. The main objective of this research is to automate and increase the efficiency of short-range Morse code communication by using multiple laser diodes which allow each message character to be encrypted and transmitted simultaneously in place of the laborious and time-consuming traditional method of Morse communication. In the present approach, message characters are transmitted as a whole, one character at a time instead of a dot (.) or dash (–) at a time. The light rays are projected onto a screen at the transmitter side, and a camera on the descriptor end captures the projected rays and decrypts them using image processing. This reduces the time taken to transmit messages by a significant amount, enabling faster and more reliable Morse communication. Upon entering the desired message on the transmission side, it is encrypted using multiple layers of pangram cryptography. This message is transmitted letter by letter via the Arduino Mega ports onto the screen. The encryption uses a randomized set of pangram keys at each level, making it robust to interceptions and decryption by third parties.

Keywords Laser diode · Morse code · Image processing · Encryption · Decryption

1 Introduction

Morse code is a method used in telecommunication to encode text characters as standardized sequences of two different signal durations, called dots and dashes, or dits and dahs [1]. Due to the continued use of radio navigational aids like VORs and

P. Sudheendra · D. Sudheshna · A. Sharma (✉) · A. Sharma · A. Supriya · R. R. Soj · A. Ramabhadran · S. Jhavar · P. Tambe
VIT-AP University, Amaravati, A.P, India
e-mail: ambujsharma08@gmail.com

NDBs, Morse code is most common in the aviation and aeronautical professions. Although Morse code is less popular for day-to-day communication in this era, it is still useful for emergency purposes as it remains an efficient means of communication. It is the easiest method of lossless, encrypted communications for times when communications are restricted. As it takes relatively long to send a message in Morse code, transmitting stations, such as WWII clandestine agents, were prone to detection by means of Direction Finding (DF). During WWII, both the Germans and the Allies developed sophisticated methods for such Radio Direction Finding (RDF). During the Cold War, the risk of detection and Direction Finding was reduced by using a Burst Encoder, a device that could record a message in Morse code and play it back at very high speed. This also shortened the transmission time significantly. At the receiving end, the message was rewritten again by recording the transmission and playing it back at a much lower speed [2, 3]. The Burst Encoder still required the presence of personnel with sufficient knowledge of Morse code, with the decryption taking a little longer as the messages needed to be slowed down and played back. The characters of the messages were still transmitted dot by dot (or dash). The Morse code could be easily intercepted and was not very reliable as any person with knowledge of the code would be able to decrypt it.

Recently, Neu et al. utilized Morse code-based text input systems with minimal single-finger control, which was made possible using WIFI devices to track finger movements of the transmitting person, without contact and encode the movements into Morse code [4]. Morse code is used as a security enhancer [5] and implemented encoder and decoder circuitry using PIC18F452 microcontroller. Gold M created a transistorized special-purpose digital computer called Morse AUtomatic Decoder (MAUDE) to decode a hand-sent Morse message, which is printed on a teletypewriter [6]. It states 'Decoding a Morse message depends on the characteristics peculiar to the sender. In these cases, the sender paused for less time after a certain part of the message critical to its integrity'. In the paper, we have automated this process via software which reduces human error. Signal noise can be eliminated with noise filtering techniques for more accurate signal prediction [7, 8]. Sensor signals can also be modeled and simulated mathematically [9].

Using OpenCV and tree-based machine learning algorithms, a method is developed for translating Morse code from eye blinks using Python's OpenCV library [10]. The input video consisting of the message, via blinking of the eyes (15 s for a dash and 30 s for a dot), was captured and processed using various decision tree algorithms, with the highest recorded accuracy of 96% using the decision tree regressor. The input video is analyzed by OpenCV, which produces a vectorized data of dots and dashes, which are fed into the decision trees for prediction. As mentioned in the paper, the process of image input is quiet tiresome and time-taking as transmitting huge sentences would take a very long time.

The utilization of visual cryptography as a method to safeguard cloud data has been examined and deliberated over by numerous scholars [11–14]. On the idea how the data could be made more secured using visual cryptographic techniques, we have extrapolated this idea into the proposed system and used cryptography to encrypt and decrypt the message sent by the user, using the concepts of pangrams and

affine cipher. The encryption and decryption keys used for the pangram encryption will only be present on the two systems which are communicating, hence ensuring that the messages, even if intercepted, would not be understood by any interceptors. In this work, author tried to solve a few of the problems of Morse communication—human error, long transmission time, and the possibility of interception by automating the translation, transmission, and decoding of the message using laser-based communication. Cameras can record the transmitted rays of a laser, which can be sent at a considerably faster rate than acoustic communications. This removes the need to establish communication lines between both sides.

2 Methodology

International Morse code provides encryption for the 26 characters from A to Z, numerals from 0 to 9, procedural signs, a few sets of punctuations, and an accented letter (É) [15] (Fig. 1).

Although Morse code can be transmitted at any given speed, the relative timing between the various elements is fixed. Morse code consists of five elements: a dot, a dash, an inter-element gap, a gap between letters, and the gap between words. For proper Morse communication, it is required for both the sending and receiving sides to have personnel who can understand, encrypt, and decrypt the Morse code accurately and efficiently. Although the duration it takes for the whole communication would vary depending on the length of the words and sentences transmitted, the Federal

A	.-	S	...
B	-...	T	-
C	-.-.	U	..-
D	-..	V	...-
E	.	W	.--
F	..-.	X	-..-
G	--.	Y	-.--
H	....	Z	--..
I	..	1	.----
J	.---	2	..---
K	-.-	3	...--
L	.-..	4	....-
M	--	5	.....
N	-.	6	-....
O	---	7	--...
P	.--.	8	---..
Q	--.-	9	----.
R	.-.	0	-----

Fig. 1 Morse code representation

Communications' Commission has set a few standards for the speed of transmission [2].

3 Development of CMorse Communication System

The setup consists of an Arduino Mega 2560Rev3 board placed inside a 3D-printed casing. The casing consists of 15 holes where the laser diodes are slotted into. The working principle of CMorse communication system is shown in Fig. 2. The wiring between the diodes and the board is done through a breadboard. Tinkercad software was utilized to develop a three-dimensional model for an automated short-range Morse code communication system as shown in Fig. 3. Tinkercad provided efficient and accurate modeling, making sure that the model met project requirements. The model was designed with specific dimensions, including a length of 300 mm, a height of 79 mm, and a width of 60 mm. Dimensions of the proposed working prototype are mentioned in Table 1. It serves as the casing for the laser diodes and the Arduino board and has laser diode holes with a radius of 3.5 mm. The output of the design was saved in three different file formats, including STL, OBJ, and SVG, to ensure compatibility with multiple software programs. The STL file was used in combination with slicing software for 3D printing purposes. The casing provides a secure and organized structure for the components in the automated short-range Morse code communication system. Moreover, it added versatility to the project, allowing for easy assembly and maintenance of the components. One of the critical features of this model is that it provides a stable encasing for the laser diodes. This stability ensures that the laser projections on the screen are steady and easy for the camera to capture for further processing.
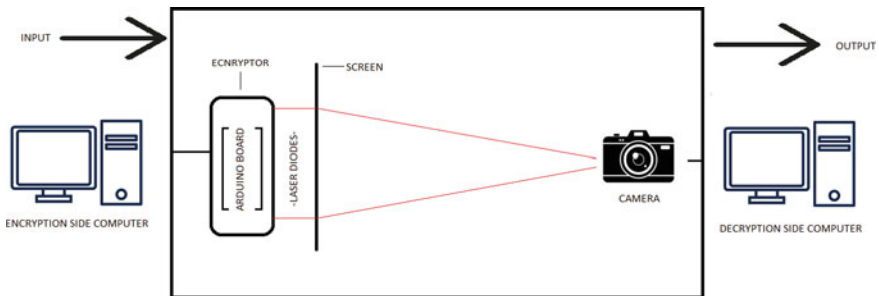
Fig. 2 Morse code communication setup
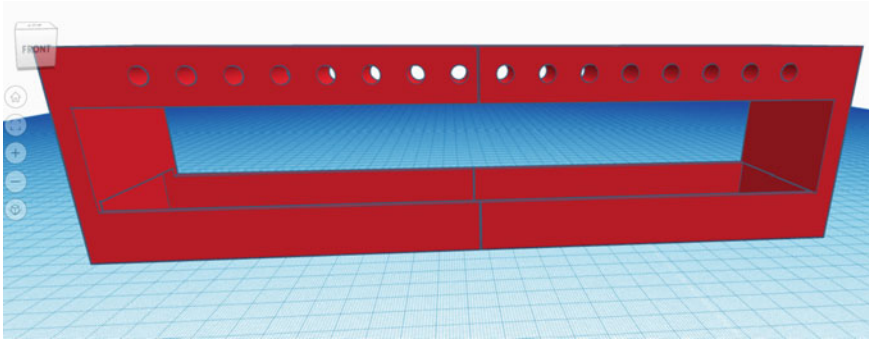
Fig. 3 Three-dimensional model for CMorse prototype

Table 1 Dimensions of the proposed prototype

Description	Length	Width	Height	Radius
Encasing	300 mm	60 mm	79 mm	–
Laser diode holes	–	–	–	3.5 mm

4 Working Concepts and System Integration

In the proposed CMorse communication technique, the entered message goes through the Arduino IDE software, which initializes the diodes to respond immediately. The front view of working prototype model with circuit connections for Morse code communications is shown in Fig. 4. Mechanical structure for the robust communication system can be built by nanocomposites or aluminum alloy [16–18]. The light from the diodes is caught and filtered with the presence of a translucent screen 2 to 3 inches from the assembled model. Presently, this distance between the model and screen has been found to be ideal, for the required filtering of light to capture images from the decryption side that are well within image processing capabilities. Projection of encryption of Morse code using laser diode is captured in the screen as shown in Fig. 5. Factors influencing image processing, which is the extraction part of the message, are how well light a room is, quality of camera capturing the image, speed of message, and time between each character. The capturing angle of the camera is flexible, as long as the image contains clear borders. The distance of capturing the image with proper quality for message extraction is steady till 5–6 feet from the screen to the decryption side. The image captured is processed using MATLAB and vectorized based on presence of objects (excluding the background). This vector is then converted into 1s and 0s representing ON and OFF. This is then inverted and sent to the decryption code and output is obtained.
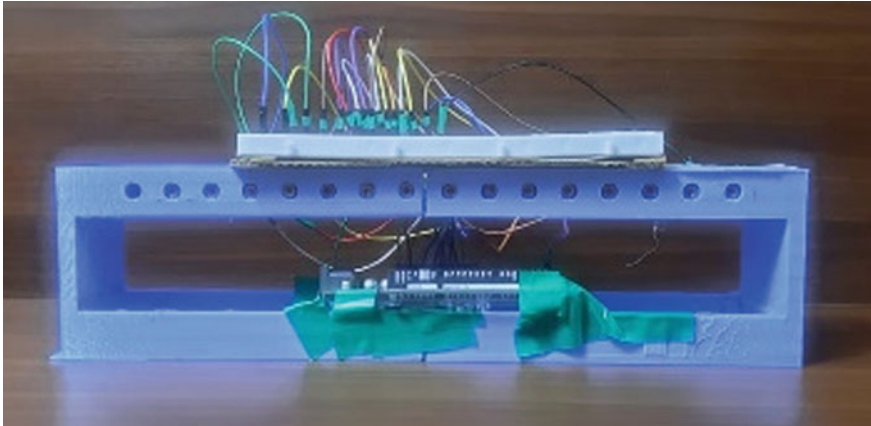
Fig. 4 Front view of working prototype model for Morse code communications
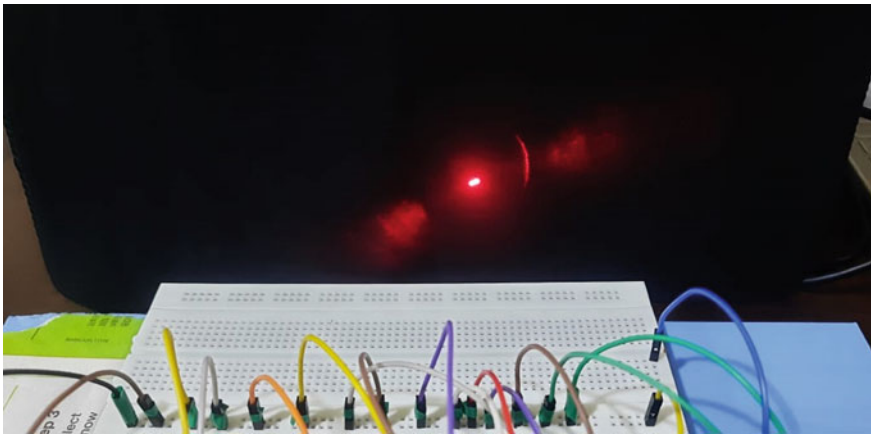
Fig. 5 Projection of encryption of Morse code using laser diode

5 Multi-layered Encryptions and Descriptions in CMorse

The concept of pangrams is used to encrypt the input messages. Pangrams are sentences which use all the letters of the English alphabet at least once. In this encryption system, we use such lesser-known pangrams as keys for cipher encryption of messages. The basic structure of the cryptosystem resembles that of a Data Encryption Standard or an Advanced Encryption Standard, but the inner workings, functions, calculations, and key selections are unique to this system alone. It relies more on simple and affine ciphers than memory allocations, storage of data, such as passwords, and conversions. Once the intended message is converted to code, the code is then translated into Morse code which is then relayed to the receiver using

laser diodes. Fifteen laser diodes display the coded characters one-by-one onto any surface the receiver can read the data from. Flowchart of working principle of Automated Laser-Based Morse Code Transmission through Multi-layered Encryption is depicted in Fig. 6.

The cryptosystem is coded using Embedded C, where the cryptosystem is programmed into the board using C programming, while the laser diodes and their respective output pins in the board are coded in the board using Serial Port programming. All laser diodes light up before and after a message transmission to denote the start and end of a transmission, respectively. This cryptosystem uses four different private keys, one affine cipher and a Morse code translator to encrypt and decrypt given messages. Out of the four private keys, three are pangrams (given below) and the last one is based on backward number allocation of English alphabets. The affine cipher used is of the form [19]:

$$E(x) = (5x + 8) \bmod 36. \tag{1}$$
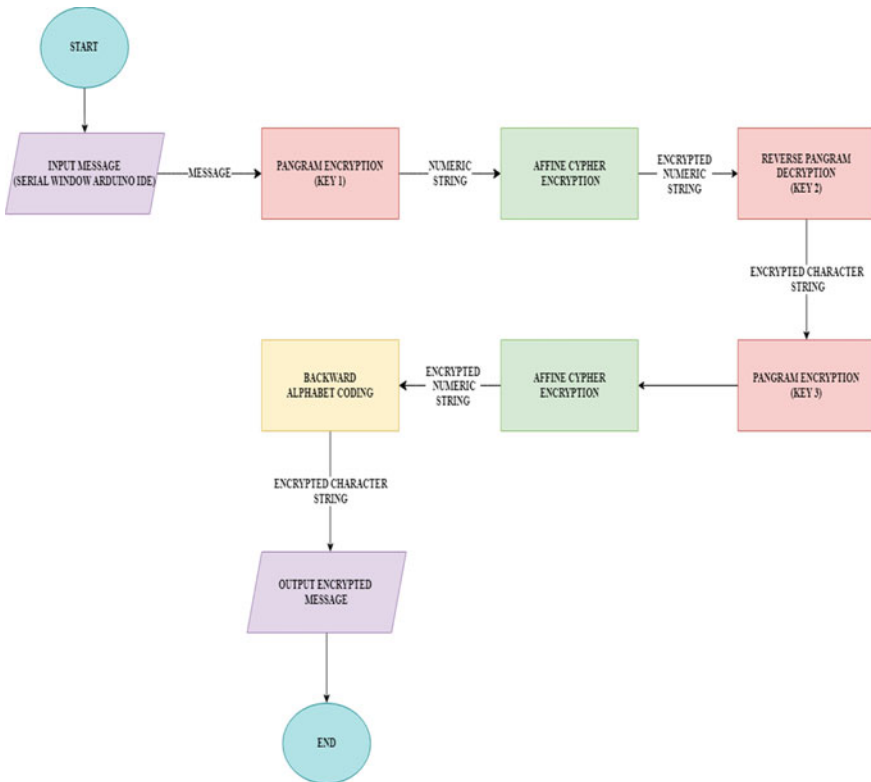
Fig. 6 Flowchart of working principle of automated laser-based morse code transmission through multi-layered encryption

The output of the cipher is used as another layer of encryption in between the program to convert numbers to characters using the keys.

The encryption follows seven steps: After receiving the input message from the Serial Monitor in the Arduino IDE, we encrypt it using Key 1. It is done by the following method. Each letter and number of the key are allocated a specific number or a memory allocation. For example, in this key, the letter 'A' has the allocation 13, the number '5' has the allocation 31, while the letter 'T' has the allocation 0. So, we take the input message and replace it with a number/position corresponding to the same letter in the key (Figs. 7, 8 and Table 2).

Since we got a numeric code as the output of the first layer of encryption by Key 1, we use Eq. (1) for affine cipher to encrypt the code into a new numeric code.

In the Arduino board, the program takes the input from the Serial Monitor, which is where the user types in the message to be encrypted. The program, as seen below, takes individual characters of the input message, compares them to the characters of the key, takes the equivalent character's position, like in Step 1, and applies the affine cipher to those positions to get the output of Step 2.

Fig. 7 Customized pangram 1 (Key 1): first layer of encryption
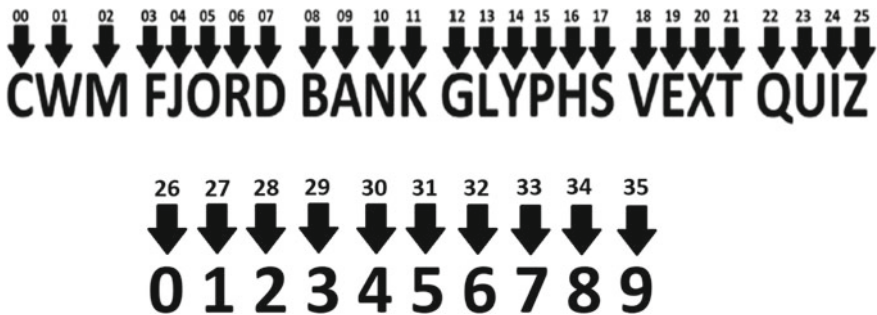
Fig. 8 Customized pangram 2 (Key 2): second layer of encryption

Table 2 Output of the affine cipher

Pangram (plain text) value	Affine cipher value	Pangram (plain text) value	Affine cipher value
0	8	18	26
1	13	19	31
2	18	20	0
3	23	21	5
4	28	22	10
5	33	23	15
6	2	24	20
7	7	25	25
8	12	26	30
9	17	27	35
10	22	28	4
11	27	29	9
12	32	30	14
13	1	31	19
14	6	32	24
15	11	33	29
16	16	34	34
17	21	35	3

Decrypt this set of codes using Key 2. Here, we do the reverse of what was done in Step 1. Here, we assign each number of the numeric code a specific alphabet or number from Key 2.

So, for example, the letter 'M' in the original message will become '19' in the first step, '31' in the second step and becomes the number '05' by the end of the third step. The output from Step 3 is then further encrypted with another pangram key, i.e., Key 3. The output is obtained just like in Step 1, but with the use of Key 3 instead of Key 1.

In the fifth, step, we repeat Step 2 as we use the same affine cipher to get outputs of the cipher. In the sixth step, we encrypt the outputs from Step 5 to get the final coded message, before Morse translation, using backward alphabet coding (Fig. 9 and Table 3).

Hence, taking the example given in Step 3, the letter 'M' in the message will be changed to the number '31' by the fourth step, the number '19' by the fifth step, and finally the letter 'H' by the sixth step. The seventh and final steps involve the Morse translation. Taking the previously used example of passing the letter 'M' through the cryptosystem, we get the letter 'H' as the final code of the sixth step. The letter 'H' becomes the dot–dash sequence '....' when converted to Morse code. This Morse translation is then outputted to the Serial Ports connected to the laser diodes, and
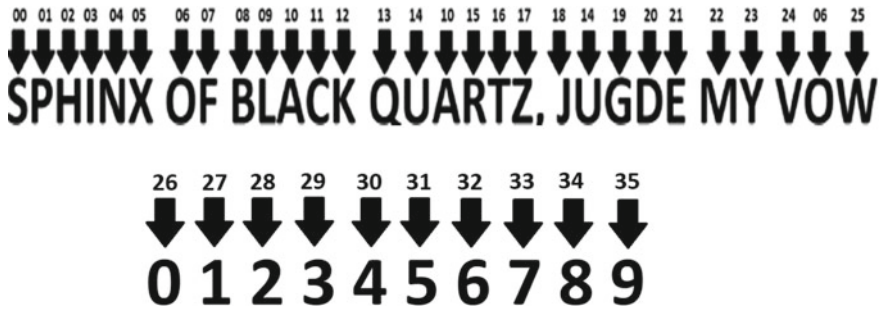
Fig. 9 Customized pangram 3 (Key 3): third layer of encryption

Table 3 Backward alphabet coding

Forward order position	Letters	Backward order position	Forward order position	Letters	Backward order position
1	A	26	14	N	13
2	B	25	15	O	12
3	C	24	16	P	11
4	D	23	17	Q	10
5	E	22	18	R	9
6	F	21	19	S	8
7	G	20	20	T	7
8	H	19	21	U	6
9	I	18	22	V	5
10	J	17	23	W	4
11	K	16	24	X	3
12	L	15	25	Y	2
13	M	14	26	Z	1

using the logics 'HIGH' and 'LOW', as seen below, the laser diodes light up in the order of the Morse code of the particular character, thus completing the encryption. Note that Blank spaces will remain the same and will not be encrypted or decrypted by the system. The symbol '%' follows every message transmission to denote the end of transmission. The '%' symbol will also remain untouched by the encryption program to ensure the accuracy of the decryption program. The transmission is through light. The message is represented by a series of laser diodes that are turned on and off in predetermined sequences within a fixed frame.

6 Conclusions and Future Work

The main objective of this project is to hasten the process of Morse communication. By using multiple laser diodes, the dot–dash translation of each of the characters is transmitted at once, instead of the traditional method of transmitting each dot and dash individually. This is achieved by using a set of 15 laser diodes controlled by the programmed Arduino Mega 2560Rev3 board. The input message is first encrypted using cryptography and then encoded into Morse. With the right model layout, the system can encrypt and decode a message and send it across a distance, even if there is temporary interference from an external obstacle. The research done for this project demonstrates that interference is an inevitable barrier to experimentation and communication of any kind. The proposed CMorse methodology makes an effort to establish Morse communication without a pre-existing link and without requiring the communicators to have a prior familiarity with Morse.

This system eliminates the requirement of personnel with knowledge of Morse code on both ends as encryption, transmission, reception, and decryption which is fully automated, minimizing possibilities of human error. However, the communication would still suffer from the drawbacks of light-based transmission such as material interference in the communication path. This could be solved by repeating the message transmission multiple times.

References

1. Beechey FS (1876) Electro-telegraphy. London, UK: E. & F.N. Spon. pp 71—via Archive.org
2. United States Code of Federal Regulations Title 47 §13.207(c), §13.209(d), §97.503 (1996)
3. https://www.cryptomuseum.com/radio/morse/
4. Niu K et al (2019) WiMorse: a contactless morse code text input system using ambient WiFi signals. IEEE Internet Things J 6(6):9993–10008. https://doi.org/10.1109/JIOT.2019.2934904
5. Morse Code—A Security Enhancer (2016) Int J Sci Res (IJSR) 5(8). Paper ID: ART20161152
6. Gold B (1959) Machine recognition of hand-sent Morse code. IRE Trans Inform Theory 5(1):17–24. https://doi.org/10.1109/TIT.1959.1057478
7. Sharma A, Kumar S, Tyagi A (2018) Noise filtering techniques for Lamb waves in structural health monitoring. Multidiscip Model Mater Struct 14(4):676–694
8. Sharma A, Kumar S, Tyagi A (2018) Selection of optimal noise filtering technique for guided waves in diagnosis of structural cracks. Int J Struct Integrity
9. Sharma A, Kumar S, Tyagi A, Ranjan KK (2019) Wavelet-based finite element simulation of guided waves containing harmonics. Int J Mater Struct Integrity 13(1–3):54–66
10. Deepak GSN et al (2021) An approach for morse code translation from eye blinks using tree based machine learning algorithms and OpenCV. J Phys: Conf Ser, vol 1921. pp 012070
11. Brindha K, Jeyanthi N (2015) Securing cloud data using visual cryptography. In: International conference on innovation information in computing technologies (ICIICT), Chennai, India
12. Straker EA, Stevens PN, Irving DC, Cain VR (1970) The MORSE code: a multigroup neutron and gamma-ray Monte Carlo transport code (Vol. 4585). Oak Ridge National Laboratory
13. Bhuvaneshwari M, Kanaga EGM, Anitha J, Raimond K, George ST (2021) A comprehensive review on deep learning techniques for a BCI-based communication system. In: Demystifying big data, machine learning, and deep learning for healthcare analytics, pp 131–157
14. Sayood K (2017) Introduction to data compression. Morgan Kaufmann

15. International Morse Code Recommendation. Radiocommunication Sector. itu.int (Report) (2009) ITU Recommendation. International telecommunication union. October 2009. ITU-R M.1677-1
16. Kundurti SC, Sharma A, Tambe P, Kumar A (2022) Fabrication of surface metal matrix composites for structural applications using friction stir processing–a review. Mater Today: Proc 56:1468–1477
17. Pasha SK, Sharma A, Tambe P (2022) Mechanical properties and tribological behavior of Al7075 metal matrix composites: a review. Mater Today: Proc
18. Harsha VSS, Sharma A, Tambe P (2022) Graphene oxide reinforced epoxy nanocomposites coatings for corrosion protection: a review. In: Journal of physics: conference series, vol. 2225(1), IOP Publishing, pp 012002
19. Laia O, Zamzami EM, Larosa FGN, Gea A (2019) Application of linear congruent generator in affine cipher algorithm to produce dynamic encryption. In: Journal of physics: conference series, vol 1361(1). IOP Publishing, 012001

Design and Evaluation of a Multi-Sensor Assistive Robot for the Visually Impaired

S. Bhaskar Nikhil, Ambuj Sharma ⊙**, Niranjan S. Nair, C. Sai Srikar, Yatish Wutla, Bhavanasi Rahul, Suyog Jhavar** ⊙**, and Pankaj Tambe** ⊙

Abstract Visual impairment affects approximately 285 million people worldwide, the profound challenge faced by those who are visually impaired or blind lies in the intricate task of maneuvering through different surroundings. The intricate nature of navigating both indoor and outdoor spaces poses significant difficulties for people with visual impairments. This paper presents an innovative undertaking that strives to address this very challenge by developing a cutting-edge robot dedicated to guiding the blind securely through various environments. Employing a sophisticated amalgamation of diverse sensors and a high-resolution camera, the robot adeptly identifies obstacles and furnishes the user with real-time information pertaining to their immediate surroundings. Remarkably, this state-of-the-art robot can be seamlessly operated through voice commands, facilitated by a bespoke mobile application, thereby enabling users to effortlessly guide it to their desired destinations. Equipped with comprehensive audio feedback capabilities, the robot effectively communicates crucial details to the user, encompassing obstacles, directions, and more. This robot can help blind people to navigate unfamiliar environments and travel independently.

Keywords Assistive robot · Multi-sensor · Visually impaired · Voice command · Obstacles avoidance

1 Introduction

According to the World Health Organization (WHO) in 2022, there are approximately 1 billion people that are blind or face moderate-to-high levels of vision impairment, a majority of which (826 million) is attributed to unaddressed presbyopia which causes near-vision impairment (NVI) and uncorrected refractive errors. Other causes include various conditions such as glaucoma, cataract, diabetic retinopathy [1]. Generally,

S. Bhaskar Nikhil · A. Sharma (✉) · N. S. Nair · C. Sai Srikar · Y. Wutla · B. Rahul · S. Jhavar · P. Tambe
VIT-AP University, Amaravati, A.P, India
e-mail: ambujsharma08@gmail.com

it is observed that in countries with low income, congenital cataract is a primary cause of vision loss in children, while in middle-income countries, the likelihood of retinopathy of prematurity being the cause of vision impairment is higher [2]. The advancements in the study of robotics and artificial intelligence have especially made great progress in recent times and are the reason for many breakthroughs in various fields including medical research.

Azeta et al. have developed an obstacle avoidance robot vehicle which uses ultrasonic sensors for the movement of the robot. The robot is built using an Arduino UNO. The study describes the design and implementation of an autonomous obstacle avoiding a robot which can direct itself whenever it detects an obstacle in its path [3]. Ultrasonic sensors are used for the detection of an obstacle. When the sensors detect an obstacle in their path, a command is sent to the microcontroller which then redirects the robot in a different path by actuating the motors depending on the signal received. The robot showed decent performance in different lighting conditions. Kulkarni et al. have proposed a system to assist visually impaired individuals in indoor navigation. The study highlights the importance of designing robots that are capable of engaging in interactions with human users. It also focuses on enhancing the user's experience while interacting with the robot [4]. An autonomous biped humanoid robot that detects obstacles to assist visually impaired individuals while traveling outdoors was developed by Ganguly & Paul [5]. Arduino Nano is used as the processor and ultrasonic sensor is used to detect obstacles. They build a cost-effective model that can be used to efficiently guide the visually impaired. Noise filtering techniques also can be used to remove the signal noise for efficient signal prediction [6, 7]. Mathematical modeling and simulation also can be performed for signals received from sensors [8]. It can also be a source of entertainment and can provide security. An investigation into the development and testing of an independently navigating robot for the blind has been proposed by some research groups [9–11].

Finding a feasible, accessible, and general solution becomes paramount because as stated, blindness and visual impairments are leading causes of many first-world problems. The current solutions available for those with visual impairment, such as the use of sighted guides or guide dogs, are subject to limitations imposed by biological variables. Additionally, alternative technologies that are currently available do not possess the necessary versatility to cater to a wide range of general applications. Furthermore, certain technical solutions that have been developed rely on sensors that are inefficient in their functionality. Although the number of people affected by visual impairments increases over time, technological advances are also accelerating quickly. In the proposed work, we tried to design and develop the assistive robot with the utilization of an advanced sensor array, including ultrasonic, LIDAR, and infrared sensors, alongside a sophisticated camera system, that enables the robot to effectively perceive and analyze its dynamic surroundings. The proposed robot enables blind individuals to confidently navigate unfamiliar terrains and embark on independent journeys.

Table 1 Components used to build the assistive robot

S. No	Component name	Quantity
1	Ultrasonic sensor	1
2	IR sensor	3
3	Arduino mega 2560	1
4	L293D motor driver shield	1
5	Servo motor	1
6	Battery holder	1
7	Bluetooth HC05	1
8	Lithium-Ion Batteries	3
9	TT gear motor and wheels	4
10	Jumper wires	30
11	GPS module	1

2 Design and Development of Methodology

The first step in the design and development of the robot involves creating a circuit diagram of the robot. The circuit is designed in the Proteus software. Once the circuit is designed, the next phase involves writing the embedded C code for the robot in the Arduino IDE. During the simulation of the circuit in the Proteus software, if errors are found, then the code is to be modified accordingly. The final code is uploaded to the Arduino microcontroller once there are no errors in the code. Next step involves building an application for transmitting voice commands and input signals to the microcontroller via Bluetooth module. The robot starts or stops functioning according to the input signal given by the user through the app which is then transmitted to the robot via the Bluetooth module. After building the app, DC motors attached to the wheels are to be integrated with the robot chassis and then connect the motor driver to the microcontroller. Once the connection between the motor driver and microcontroller is made, then the servo motors and DC motors are to be connected to the motor driver. Once all the connections are made, the next step is to arrange the IR sensors and Bluetooth module in their respective positions and place the ultrasound on top of the servo motor. Then, connect the power source and switch to the driver shield integrated with the Arduino. Table 1 shows the components used for constructing the robot.

3 Circuit Diagram

The components of the robot include an Arduino Mega Board, three IR sensors, an Ultrasonic sensor, an L293d motor driver shield, four DC motors, and an HC-05 Bluetooth module. All components are supported by an acrylic sheet chassis. The
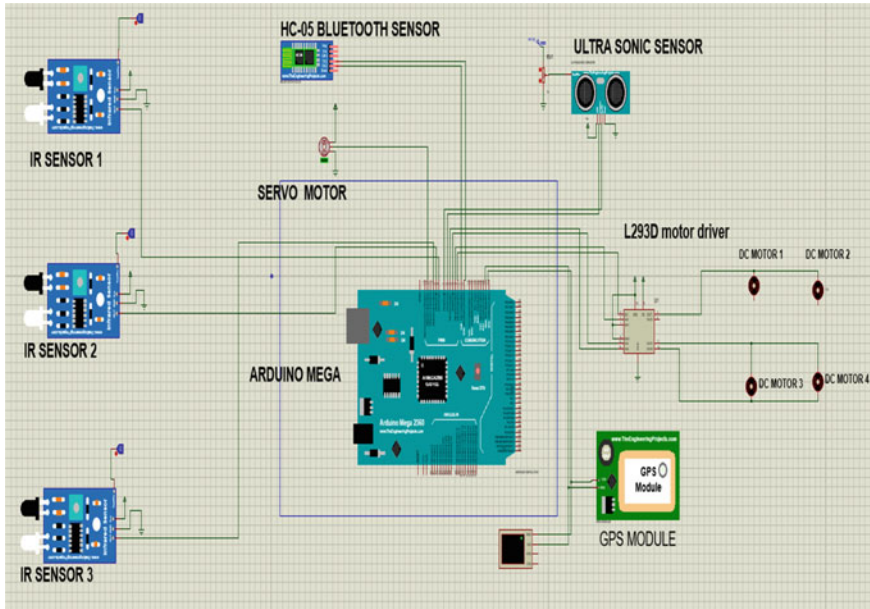
Fig. 1 Circuit diagram of the proposed assistive robot

Arduino provides control and helps in processing power for the robot. The two types of sensors which we used provide the input and feedback to the system. The four DC motors together provide the movement of the robot with the help of rubber wheels. We also used a GPS module for providing precise location and accuracy to the user. To facilitate the communication between the prototype and the app, a HC-05 Bluetooth module was integrated with the robot which transmitted voice commands from the user. The circuit diagram of the proposed assistive robot is given in Fig. 1.

4 Prototype Development

Firstly, a power supply or a battery is to be connected and then manually switch on the robot using the power switch. After turning on the switch, the user should open the custom-designed android application. Using the HC-05 Bluetooth module, connect the app to the robot. An input voice command is to be given through the Android application for the robot to start moving. By passing "START" as input voice command through the app, the Bluetooth module installed takes this input and then passes the signal to the microcontroller (Arduino UNO). When the microcontroller successfully detects the signal, the robot starts functioning (or start working or moving). The HC-SR04 ultrasonic sensors installed at the back of the robot start detecting or searching for human or the user throughout its motion, and it keeps on

checking the distance between the user and robot to ensure that the robot maintains a healthy distance throughout the journey. Once the robot detects the human, it starts moving by parallelly giving information about its surroundings to the user through the app, while in motion, the robot keeps searching for any obstacle. Once it detects an object through the IR sensors, the robot changes its direction. This information is then passed to the human user through the app and the robot continues searching for any obstacle in its path. It moves in a linear path until it finds an obstacle. Finally, once the user gives "STOP" command, the Bluetooth module sends a signal to the microcontroller to stop the motion of the robot. Aluminum alloy AA6061/AA7075 and nanocomposites can be utilized for the mechanical structure of the robot [12–14]. The flowchart for the construction of the robot is shown in Fig. 2. Figure 3 represents flowchart for working of the assistive robot. Figure 4 depicts the assistive robot's connections and internal status, whereas Fig. 5 provides a visual representation of the completed prototype.
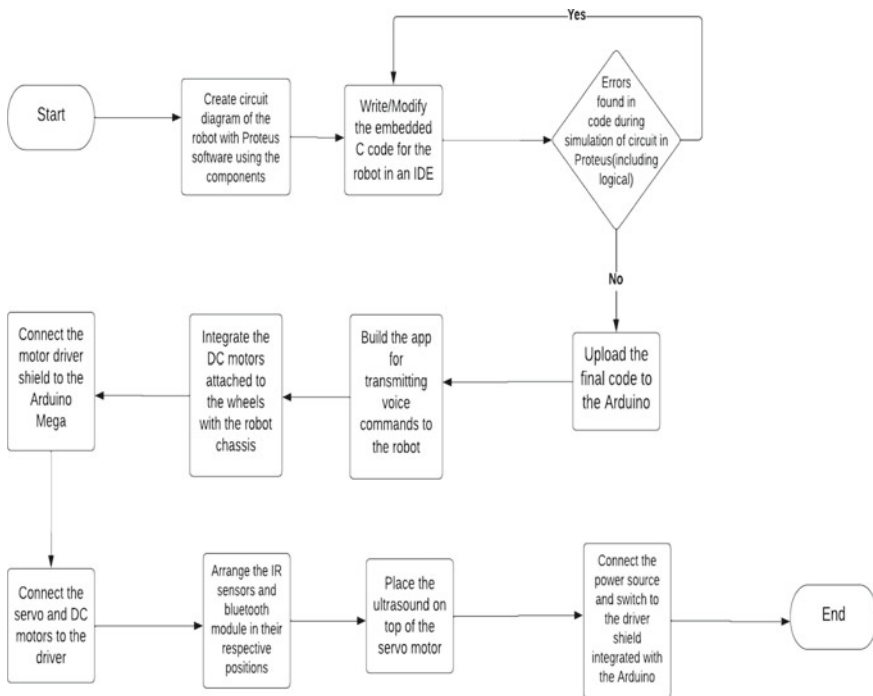

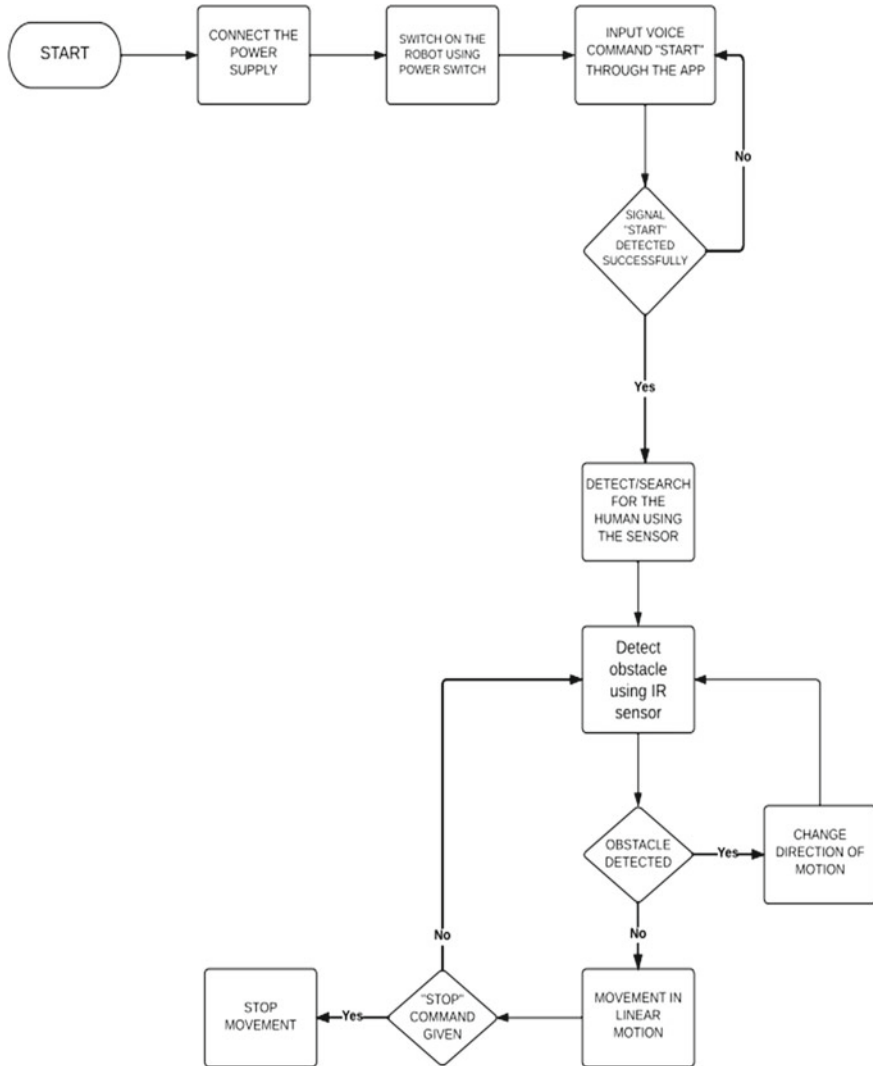**Fig. 2** Flowchart for construction of the robot

Fig. 3 Flowchart for working of the robot

5 Construction and Working of Custom Designed Android Application

The Android application used in this paper is designed using an App Inventor. The designing of the application using the App Inventor can be divided into two main phases: (a) designing and (b) programming.
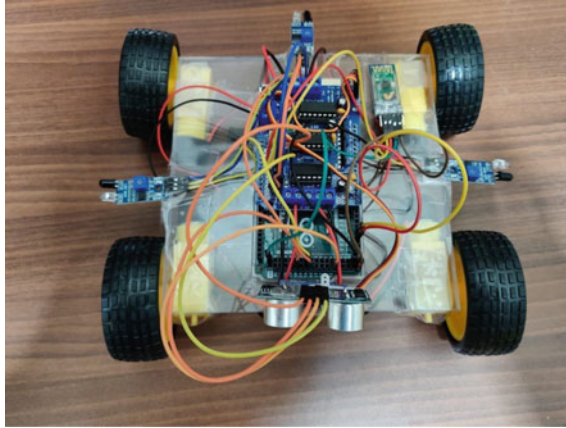
Fig. 4 Connections and internal state of the assistive robot

(a) Designing: The first phase, designing, takes place in the App Inventor Designer which involves selecting the components that will be used for designing the app. These components include the buttons, labels, textboxes, and images. In this phase, the basic layout and structure of the Android application are designed.

(b) Programming: The second phase of the process involves using the App Inventor Block Editor. Here, the user assembles blocks of code that specify how the components should behave visually. For example, the user might specify that when a button is pressed, a certain action should occur, such as displaying a message or changing the background color of the screen. This phase is where the user really brings the app to life, defining its functionality and behavior.

Once the designing and the programming phases of the app are complete, the application is now ready to run on an Android phone by connecting the phone to a computer, or it can be run on an Android Emulator if the user does not have a physical Android device. After testing the app, the user can download the app's.apk file and install it directly onto their Android device, allowing them to use the app like any other installed application. The app uses Google's speech recognition service to detect the user's speech and then convert it into text which is then sent to the microcontroller in the form of a signal. The speech-to-text module takes the user's commands and converts them into a digital signal that can be transmitted to the Arduino board. When the user speaks a specific set of commands, the speech-to-text module converts the speech into text using Google's online services. The converted text is then sent to an Arduino microcontroller through a Bluetooth connection. The microcontroller processes the input signal, which enables the robot to act accordingly based on the user's commands [15–17]. The user interface of the custom-made Android application is shown in Fig. 6.

The system is designed to be interactive, as it allows for real-time communication between the robot and the user. The app also uses a text-to-speech module that

(a) Top view

(b) Bottom view

(c)Side view
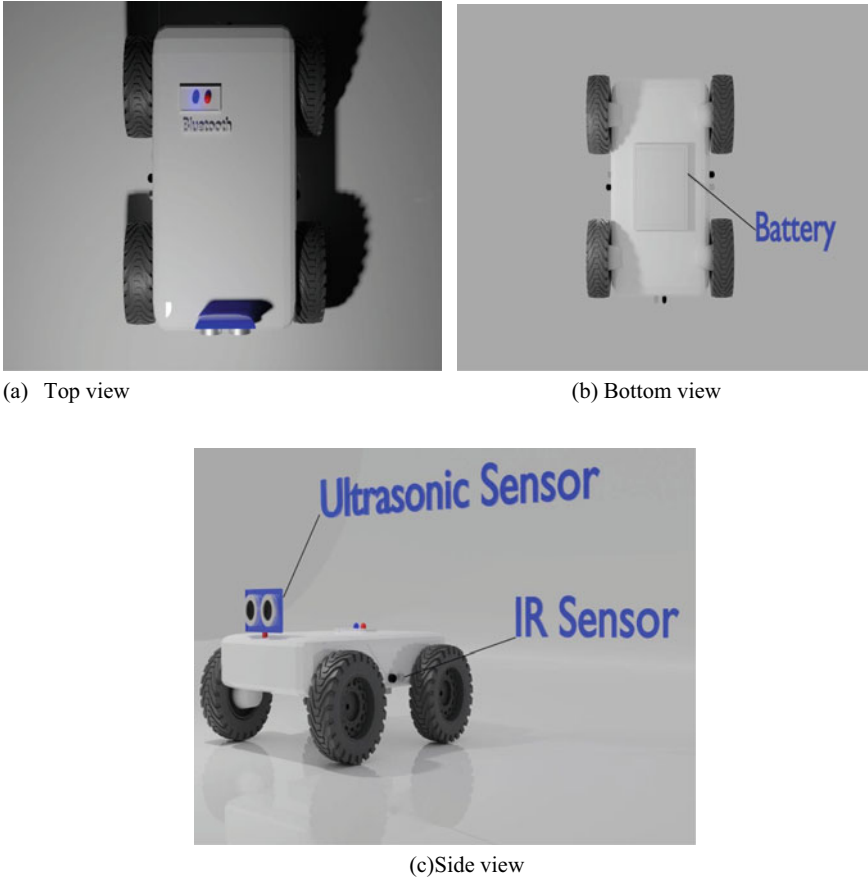
Fig. 5 Visualization of the final prototype

speaks out messages to the user. For example, when the robot detects an obstacle, the microcontroller sends a signal to the app via Bluetooth module. Using the text-to-speech module, the app speaks out the message to the user which allows the user to be informed of any obstacles in their path.

6   Results and Discussion

The results are quantified by taking the following factors into consideration: (a) no. of times tested vs. no. of times obstacle successfully detected; (b) time taken by Bluetooth app to recognize the users voice, i.e., to receive signal (time taken vs. test number, ten tests); (c) no. of times the blind person was not detected by the robot
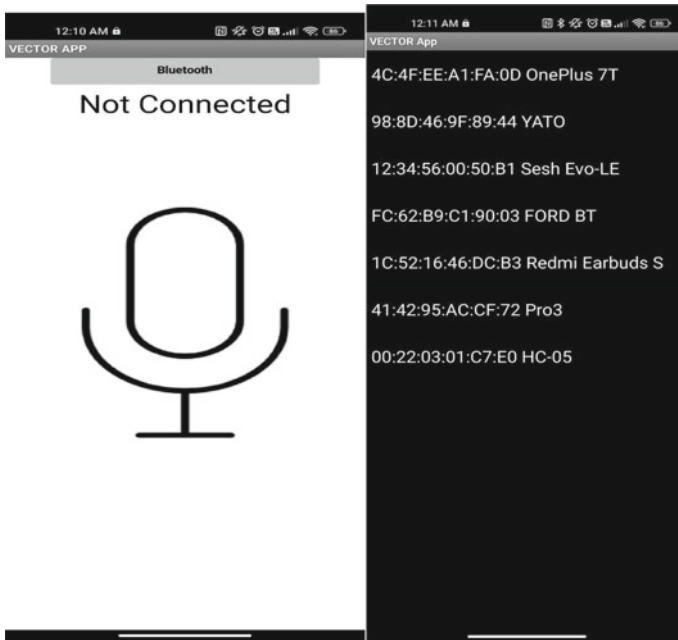
Fig. 6 Image of user interface of the custom-made Android application

(tested in different positions); (d) no. of times the obstacle was avoided completely; (e) time taken to cover certain distance milestones.

From Fig. 7, it can be inferred that the robot is mostly successful in detecting the obstacles and taking action through corresponding movements. Around 15 tests were done with obstacles in different positions (left, front, and right) with respect to the robot. The success rate of obstacle detection and corresponding movements appears to be highest when the obstacle is directly in front of the robot. This may indicate that the robot's sensors are more effective in this orientation. Some lighting conditions may also affect the performance of the IR sensors. Despite some variability in the success rate across different obstacle positions, the overall trend is that the robot is able to successfully detect and respond to obstacles in most cases. This is a positive result, as it suggests that the robot is well-suited to tasks that require obstacle avoidance. It is important to note that the graph only reflects the robot's performance in the specific testing scenarios that were carried out.

Figure 8 shows a clear trend in the time it takes for the Bluetooth module to register the user's voice commands on average 1–2 s. The time it takes for the Bluetooth module to register the user's voice commands may depend on a variety of factors. For example, it may depend on the distance between the user and the robot, the amount of background noise in the environment, or the specific words or phrases that the user is speaking. The voice commands were tested in a fairly noisy environment.
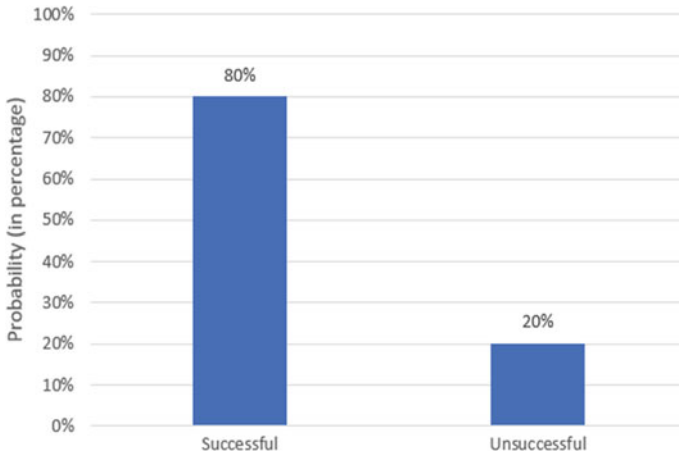
Fig. 7 Probability of successfully obstacle detected

Fig. 8 Time taken by Bluetooth app to recognize the users voice, i.e., to receive signal

From Fig. 9, it can be inferred that the person was detected around 70% of the times the tests were conducted and the failure rate is fairly less. The user was placed in different orientations with respect to the robot. There seems to be a higher detection rate when the person is facing the robot directly, as opposed to when they are turned to the side. We have conducted this test to track the user's walking speed and adjust robot's speed accordingly to match the user's speed.

Figure 10 shows that there were some tests where the robot struggled to maneuver the objects. Specifically, there were four tests where the robot was only partially successful in maneuvering the objects and one test where it failed completely. The ability of the robot to avoid the objects depends on the parameters of the objects,
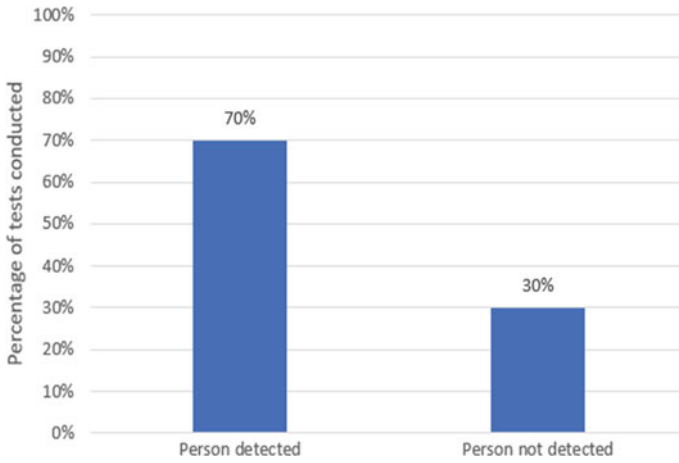
Fig. 9 No. of times the blind person was not detected by the robot (tested in different direction)

especially the size, shape, and width of it. The performance of IR sensors which are used to detect the objects can also be affected by factors such as the color and reflectivity of the objects being detected.

Figure 11 shows time taken to cover certain distance milestones. The graph helps us understand the speed of the robot. The speed of the robot is an important aspect to measure as it gives us an idea of how fast it should travel to guide the person and the time it takes to avoid the obstacles. In average the robot travels around 33.7 cm per second. The robot was allowed to run freely on a uniform terrain with no obstacles in its path. The robot may move more slowly on uneven or rough terrain or when it encounters obstacles that require it to slow down or change direction. There is some variation in speed in different distance milestones which is to be expected as uniform
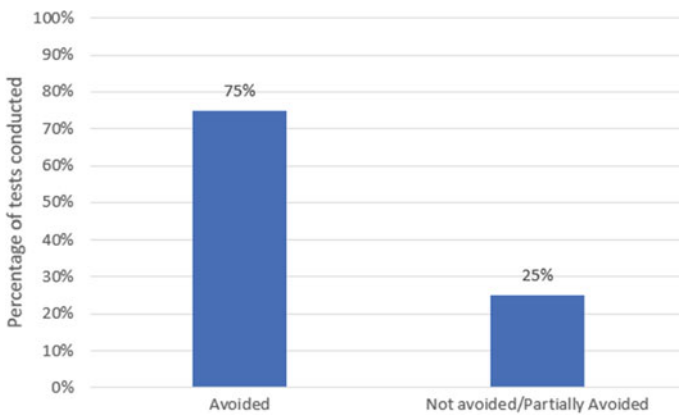
Fig. 10 No. of times the obstacle was avoided completely (same as first result bar graph)
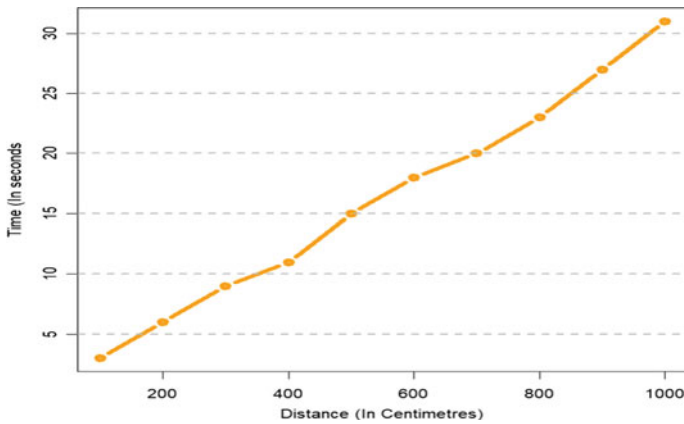
Fig. 11 Time taken to cover certain distance milestones

speed is hard to maintain due to factors like weight or battery power. The speed of the dc motors was set in the embedded C code.

The robot, vector, was tested in the lab and on an open ground, where we placed a few obstacles and the robot was allowed to move in a path. The robot changed its direction when it detected an obstacle. When an obstacle is detected, a message is sent to the Android app through which the user is notified about the obstacle.

7 Conclusion

The advancement of technology has led to creation of many innovative developments in the field of robotics which have transformed our lives in many ways. This assistive robot and mobile application utilizes cutting-edge speech recognition algorithms to accurately transcribe and interpret commands, allowing for intuitive control and seamless navigation toward desired destinations. The fusion of these technologies culminates in the generation of real-time auditory feedback, providing vital information about obstacles, navigation directions, environmental cues, and points of interest. Through the integration of state-of-the-art sensor technology, computer vision, and natural language processing, the robot empowers visually impaired individuals, offering them unparalleled independence and confidence to navigate unfamiliar environments and reach their desired destinations with ease.

References

1. https://www.who.int/news-room/fact-sheets/detail/blindness-and-visual-impairment
2. GBD 2019 Blindness and Vision Impairment Collaborators; Vision Loss Expert Group of the Global Burden of Disease Study (2021) Causes of blindness and vision impairment in 2020 and trends over 30 years, and prevalence of avoidable blindness in relation to VISION 2020: the right to sight: an analysis for the global burden of disease study. Lancet Glob Health. 9(2):e144-e160. https://doi.org/10.1016/S2214-109X(20)30489-7
3. Azeta J et al. (2019) Obstacle detection using ultrasonic sensor for a mobile robot. In: 2019 IOP Conference series: material science engineering, vol 707. pp 012012
4. Kulkarni A, Wang A, Urbina L, Steinfeld A, Dias B (2016) Robotic assistance in indoor navigation for people who are blind. In: 2016 11th ACM/IEEE international conference on human-robot interaction (HRI), Christchurch, New Zealand, 2016, pp 461–462. https://doi.org/10.1109/HRI.2016.7451806
5. Ganguly A, Paul B (2021) Tiny blind assistive humanoid robot. IntechOpen. https://doi.org/10.5772/intechopen.97333
6. Sharma A, Kumar S, Tyagi A (2018) Noise filtering techniques for lamb waves in structural health monitoring. Multidiscip Model Mater Struct 14(4):676–694
7. Sharma A, Kumar S, Tyagi A (2018) Selection of optimal noise filtering technique for guided waves in diagnosis of structural cracks. Int J Struct Integr
8. Sharma A, Kumar S, Tyagi A, Ranjan KK (2019) Wavelet-based finite element simulation of guided waves containing harmonics. Int J Mater Struct Integrity 13(1–3):54–66
9. Guerreiro JP, Sato D, Asakawa S, Dong H, Kitani KM, Asakawa C (2019) CaBot: designing and evaluating an autonomous navigation robot for blind people. In: Proceedings of the 21st international ACM SIGACCESS conference on computers and accessibility
10. Albogamy F, Alotaibi T, Alhawdan G, Faisal M (2021) SRAVIP: smart robot assistant for visually impaired persons. Int J Adv Comput Sci Appl 12. https://doi.org/10.14569/IJACSA.2021.0120739
11. Chen Y, Xu Z, Jian Z, Tang G, Yangli Y, Xiao A, Wang X, Liang B (2022) Quadruped guidance robot for the visually impaired: a comfort-based approach
12. Kundurti SC, Sharma A, Tambe P, Kumar A (2022) Fabrication of surface metal matrix composites for structural applications using friction stir processing–a review. Mater Today: Proc 56:1468–1477
13. Pasha SK, Sharma A, Tambe P (2022) Mechanical properties and tribological behavior of Al7075 metal matrix composites: a review. Mater Today: Proc
14. Harsha VSS, Sharma A, Tambe P (2022) Graphene oxide reinforced epoxy nanocomposites coatings for corrosion protection: a review. In: Journal of physics: conference series, March, vol 2225(1). IOP Publishing, pp 012002
15. Shah D, Osinski B, Ichter B, Levine S (2022) LM-Nav: robotic navigation with large pre-trained models of language, vision, and action
16. Ohki T, Nagatani K, Yoshida K (2012) Local path planner for mobile robot in dynamic environment based on distance time transform method. Adv Robot 26(14):1623–1647
17. Lee M-FR, Yusuf SH (2022) Mobile robot navigation using deep reinforcement learning. Processes 10(12): 2748

Crack Growth Prediction Models for a Pre-defined Semi-elliptical Crack Embedded in a Cantilever Bar Using Supervised Machine Learning Algorithms

Harsh Kumar Bhardwaj and **Mukul Shukla**

Abstract Any machine component or structure can fracture due to the presence of cracks. With the assistance of finite element tools, we can only dissect the stable crack growth that requires much computational time and is vulnerable. This work developed several ML models using supervised machine learning algorithms and compared their performance. These models have shown decent precision in detecting the crack growth behavior of a pre-defined semi-elliptical crack embedded in a cantilever bar. The correlation coefficient R squared (R^2), mean squared error (MSE), root mean squared error (RMSE), and mean absolute error (MAE) were used to evaluate and compare the performance of the developed ML models. The accuracy of the crack growth forecast is found to be ~ 86.47%, ~ 93.68%, ~ 91.50%, ~ 92.04%, and ~ 94.64% for linear regression (LR), quadratic polynomial regression (QPR), decision tree (DT), random forest (RF), and k-nearest neighbor (KNN), respectively; among them, KNN had the best prediction accuracy.

Keywords Fracture mechanics · Crack growth · Semi-elliptical crack · Machine learning · Regression model

H. K. Bhardwaj · M. Shukla
Department of Mechanical Engineering, Motilal Nehru National Institute of Technology Allahabad, Prayagraj, India

M. Shukla (✉)
Department of Mechanical and Industrial Engineering Technology, University of Johannesburg, Johannesburg, South Africa
e-mail: mukulshukla@mnnit.ac.in; mukuls@uj.ac.za

1 Introduction

Whenever a machine part is produced utilizing any casting, metal shaping, sheet metal, or welding process, a few residual stresses and cracks create in the part material itself. These cracks might be grown within the machine part or at the edge of the part. During the application of load and cyclic or fluctuating stress, these pre-defined cracks start to grow and cause the component to fracture at high-stress concentration points, usually at the ends of the crack.

Due to the application of brittle materials in numerous technological applications, predicting the crack initiation and growth in brittle materials has become more prominent among scientists and engineers. Brittle materials show shallow plastic deformation, resulting in a fast growth rate of randomly distributed and oriented cracks. To predict the length of the cracks, the distance between two cracks, their orientations, the path, and the time when the two cracks merge, Moore et al. [1] used artificial neural networks (ANNs), random forests (RFs), and support vector machines' (SVMs) algorithms to develop a prediction model. Carrara et al. [2] proposed a data-driven approach to replace the fracture-related material modeling assumptions with a discrete material dataset, that would lead to a model-free data-driven method. Hsu et al. [3] developed an ML model that predicts dynamic fracture propagation in brittle materials by using long short-term memory (LSTM) and convolutional neural network (CNN) algorithms.

Engineers prefer analytical and empirical methods for simplicity and reliability, but these methods are not feasible for complicated engineering problems. Liu et al. [4] adapted ML algorithms, regression trees, and neural networks (NNs) for material characterization of complex specimen geometries like a pentagonal cantilever bar to substitute these methods. Martinez et al. [5] used ML with the extended finite element method (XFEM) for stochastic crack propagation and reliability analysis. Alipour et al. [6] applied the conceptual ML model to predict the fracture length in shale samples subjected to nanoindentation by analyzing more than 1600 images. Bao et al. [7] developed an ML model based on SVM to predict the effect of defect location, size, and morphology on the fatigue life of SLM Ti-6Al-4 V alloy. Zhan et al. [8] demonstrated a continuum damage mechanics-based machine learning model using RF (CDM-RF) to predict the fatigue life of AM titanium alloys (TA2-TA15 and TC4-TC11).

Ductile fracture does not occur spontaneously. It involves a substantial expansion of plastic deformation at the fracture tip. To forecast ductile fracture, Chen et al. [9] used backpropagation NN with the genetic algorithm on simulated data to identify the parameters for ductile fracture of 2024 T3 Al alloy. Due to the high-temperature difference, the gas turbine blades and rotor experience high thermal stresses and are subjected to mechanical stress due to centrifugal loading. Both of these stresses cause fatigue failure of gas turbine parts. Hu et al. [10] used the Markov chain Monte Carlo algorithm and Gaussian process regression (GPR) to predict fatigue crack growth (FCG) in turbine disks. Badora et al. [11] used RF, multiple linear and polynomial

regression (PR), and kernel-based techniques. Nasiri et al. [12] reviewed the research from 1990 to 2016 and discussed them in four categories.

Yan et al. [13] consider the crack growth rate of fracture and stress intensity factor to devise three hybrid AI models to predict crack initiation pressure of supercritical carbon dioxide fracturing (SCDF), a waterless fracturing technology. Raja et al. [14] used backpropagation neural network (BPNN), extreme learning machine (ELM), and curve fitting method to predict the fatigue crack growth rate of cryo-rolled Al 2014 alloy. From a crystallographic perspective, small fatigue crack propagation direction and rate have contributed to significant fatigue failure. Rovinelli et al. [15] predicted this behavior of a small crack for titanium alloy (Ti-55531) using a data-driven machine learning algorithm, the Bayesian network. Lew et al. [16] utilized a convolutional LSTM-based machine learning model to predict the fracture behavior of Graphene in terms of crack instabilities and branching. Human error is the major cause of structural part damage at the design, construction, and operation levels. Nguyen et al. [17] applied the time-series algorithm LSTM and multi-layered neural network (MNN) to forecast the crack propagation in porous media for solid and hydraulic fracture.

This work uses the finite element approach and machine learning algorithms to examine the crack growth for a cantilever bar with a pre-defined semi-elliptical crack. In the finite element study, crack growth was investigated for different magnitudes of pressure and toughness. Also, the crack growth behavior was predicted by using machine learning algorithm regression analysis. A dataset of 128 data points has been prepared to train and test the developed model.

2   Materials and Methods

In our study, linear elastic fracture mechanics (LEFM) principles have been used to investigate the growth of a pre-defined semi-elliptical crack. When a semi-elliptical crack becomes critical, it may grow either along the major axis or minor axis or along both. Only mode-I (opening mode) has been considered for our analysis work. In mode-I, the crack will grow perpendicular to the applied load axis.

The critical stress intensity factor or fracture toughness in mode-I at a point of the crack tip is given by

$$K_I = \frac{1.12 P \sqrt{\pi b}}{I_2} \left[\sin^2 \theta + \left(\frac{b}{a} \right)^2 \cos^2 \theta \right]^{\frac{1}{4}}, \tag{1}$$

where I_2 is the elliptical integral of the second kind that depends upon the ratio of the major and minor axis and is given by
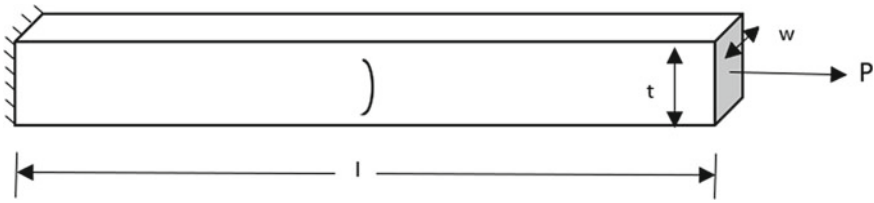
Fig. 1 Schematic representation of cantilever bar embedded with pre-defined semi-elliptical crack

$$I_2 = \int_0^{\frac{\pi}{2}} \left(1 - \frac{a^2 - b^2}{a^2} \sin^2 \theta d\theta\right)^{\frac{1}{2}}. \tag{2}$$

At the end of the minor axis ($\theta = 90°$), the stress intensity factor is given by

$$K_I^{90} = \frac{1.12 P \sqrt{\pi b}}{I_2}, \tag{3}$$

and at the end of the major axis ($\theta = 0°$), the stress intensity factor is given by

$$K_I^0 = \frac{1.12 P \sqrt{\pi b}}{I_2} \left(\frac{b}{a}\right)^{\frac{1}{2}}, \tag{4}$$

where P is the applied tensile pressure (MPa) at the right end of the cantilever bar (length, $l = 40$ mm, width, $w = 10$ mm, and thickness, t $= 0.5$ mm), a is the semi-major radius (0.4 mm), and b is the semi-minor radius (0.2 mm) of the crack, respectively, as shown in Fig. 1. The crack is located at the center of the cantilever bar. The cantilever bar is considered structural steel ($E = 200$ GPa and $v = 0.3$).

3 Finite Element Analysis

A cantilever bar with a pre-defined semi-elliptical crack at the center has been considered for our analysis. The bar is fixed on the left side, and pressure of tensile nature is applied at the right end of the bar. Modeling and behavior analysis of crack growth was done using a finite element tool. Around the corner of the semi-elliptical crack, mesh refinement was used to cut computation time (SMART Crack Growth). As the crack will grow during the fracture analysis, the smart crack growth method is used for meshing the crack that automatically readjusts the mesh of the crack during its growth. Figure 2 represents the mesh structure of the semi-elliptical crack.

The stress intensity factor in linear elastic fracture mechanics (LEFM) determines how much energy is stored in a material before it fractures. If the stress intensity factor of mode-I (K_I) is more than or equal to the material's fracture toughness (K_{IC}), the crack starts to grow. In mathematical terms,
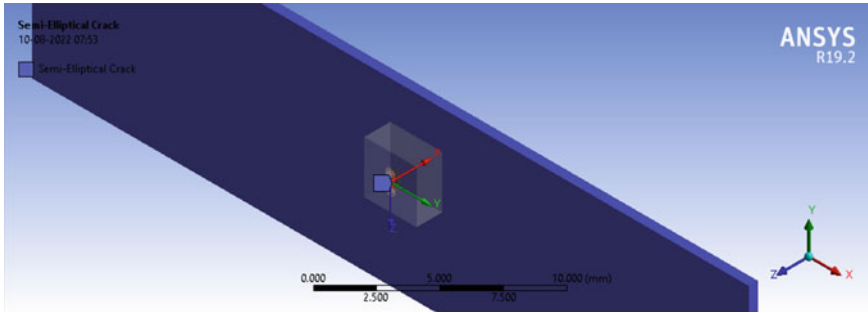
Fig. 2 FEA model of cantilever bar with crack

$$K_I \geq K_{IC}. \tag{5}$$

The stress intensity factor for mode-I is given by

$$K_I = Y\sigma\sqrt{\pi a}, \tag{6}$$

where Y = Geometry factor or stress intensity modification factor.
 σ = stress at the crack tip (MPa).
 a = crack length (mm).

The flowchart for finite element modeling and analysis of the cantilever bar with a pre-defined semi-elliptical crack is shown in Fig. 3. Crack propagation takes place in three stages; in the first stage, the crack will start to grow; in the second stage, the crack will grow stably; and in the third stage, the crack will grow unstable. We have considered only the second crack growth stage for our analysis work. Preprocessing is the first step in finite element modeling (define the geometry specification of the specimen). In the solver stage, we did the convergence analysis to reduce the variation in the desired output result. For this convergence, we use n-type refinement by varying the element edge length of the cantilever bar. Since the major and minor axis lengths of the pre-defined semi-elliptical crack are small compared to the cantilever's overall dimensional specification, we do not have much freedom to vary the mesh size of the crack, so we kept it constant. In the postprocessing step, we collect the data related to mode-I fracture (called K_I). We consider only crack opening for our analysis, as its value is much more significant the mode-II and mode-III. If the stress intensity factor of mode-I is more than or equal to fracture toughness, the crack begins to grow.

A dataset of 128 data points with applied pressure and fracture toughness as the input parameters and crack growth as the output parameter has been prepared.

Fig. 3 ANSYS flowchart
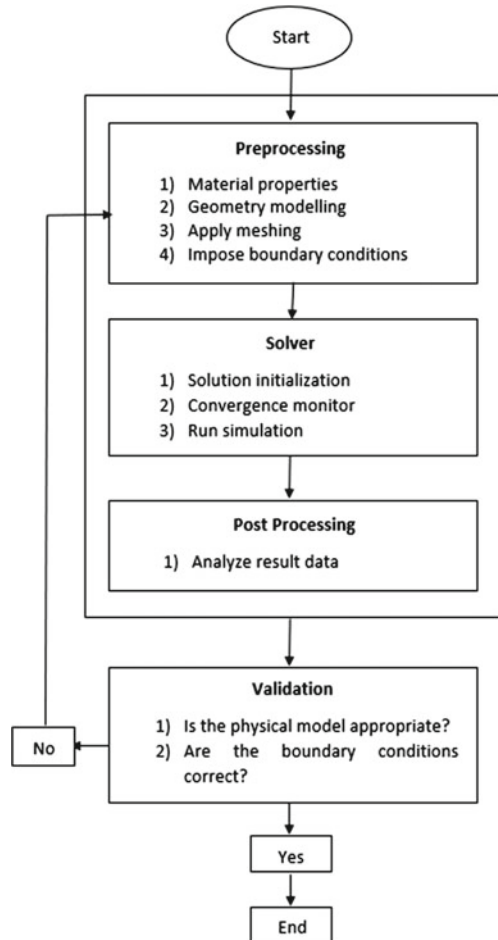
4 Machine Learning Algorithms

The branch of artificial intelligence, machine learning (ML), consists of several machine learning algorithms. A single algorithm cannot fit well for all real-world problems; their selection depends on many factors like dataset size, train–test split ratio, and tuning of other hyperparameters. Linear regression (LR), polynomial regression (PR), decision tree (DT), random forest (RF), and k-nearest neighbor (KNN) have been used in this study. Our primary aim is to compare machine learning models with finite element analysis (FEA) results and conclude with the best-fit model. Machine learning models are classified into classification, clustering, and regression. Classification algorithms are used for grouping labeled data; clustering algorithms are used for unlabeled grouping data; and regression algorithms are used
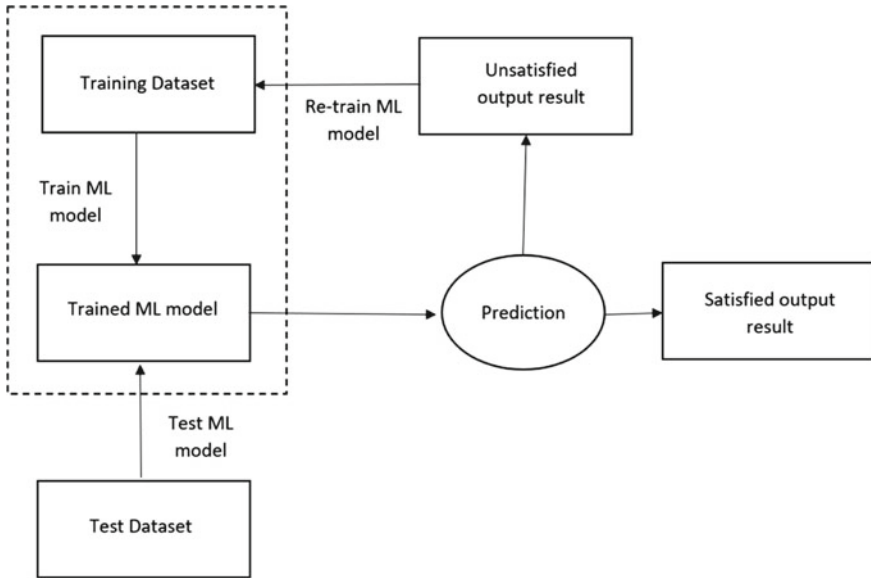
Fig. 4 Machine learning model flowchart

to calculate the numerical output value in response to the input value. The codes to develop the ML models were prepared using Python.

The ML model's flowchart is shown in Fig. 4. There is no need to develop the application from scratch because Python includes libraries.

4.1 Dataset

In this study, crack growth behavior has been predicted. For this purpose, a dataset has been prepared with the help of a finite element tool. This dataset consists of two input and five output variables. Among these five output variables, only one (crack growth) is our primary interest. The input and output attribute values are summarized in Table 1 with 128 data points.

4.2 Machine Learning Algorithms

Polynomial Regression Model

A dependent variable (y) and an independent variable (x) are related in an nth-degree polynomial relationship, according to the regression technique known as "Polynomial Regression." Here is the PR equation:

Table 1 Finite element analysis dataset

Index No	Applied pressure (MPa)	Fracture toughness (MPa $\sqrt{mm}$)	Crack growth (mm)	Total deformation (mm)	Von Mises stress (MPa)	Von Mises strain
0	10	1	0.100120	0.002005	36.036	0.000270
1	10	2	0.079153	0.002002	34.818	0.000289
2	10	3	0.058376	0.002000	32.434	0.000211
3	10	4	0.058396	0.002000	32.281	0.000214
4	10	5	0.038364	0.001998	30.339	0.000219
…	…	…	…	…	…	…
122	60	31	0.038364	0.011988	182.03	0.001312
123	60	32	0.038364	0.011988	182.03	0.001312
124	60	33	0.038364	0.011988	182.03	0.001312
125	60	34	0.018846	0.011978	165.44	0.001173
127	60	35	0.018846	0.011978	165.44	0.001173

$$y = a_0 + a_1 x + a_2 x^2 + \ldots + a_{n-1} x^{n-1} + a_n x^n, \tag{7}$$

where x is the input variable, y is the output variable, and the value of n depends on the polynomial type; is it linear, quadratic, or higher order?

Cross-validation and percentage split are the most used methods for evaluating regression models. The most straightforward technique is to divide the dataset into unequal data subsets of train and test data. This approach divides all the data into train and test subsets using a percentage definition. The model is trained using the training subset, and its effectiveness is assessed using the test subset. The FEA dataset is divided into unequally sized (80:20) subsets. The main criterion for selecting models and evaluating performance is metrics. The most often used metrics for assessing the effectiveness of regression models are mean squared error (MSE), root mean squared error (RMSE), mean absolute error (MAE), and coefficient of determination (R^2). The performance measures MSE, RMSE, MAE, and R^2 utilized in the regression method are listed in Table 2 [18–21].

Decision Tree

The DT is a well-liked method in statistics and data mining. In supervised learning, DT uses "if–then-else" decision rules for classification and regression [19, 22, 23]. Three fundamental steps make up the DT. The first node in the first phase is the most significant feature. The dataset is partitioned into subsets in accordance with this node in the subsequent phase. It is best to create subsets with identical data for each attribute in each subgroup. Repeat steps 1 and 2 in the third stage until the last nodes in each branch have been discovered. The DT divides a dataset into a smaller subset and parallelly builds classification or regression models in the background,

Table 2 Performance metrics for regression

Scoring parameter	Mathematical expression	Description
R squared (R^2)	$R^2 = 1 - \dfrac{\sum_{i=1}^{n}\left(y_i - \widehat{y_i}\right)^2}{\sum_{i=1}^{n}(y_i - \overline{y})^2}$	It measures how close each data point fits the regression line
Mean squared error (MSE)	$MSE = \dfrac{1}{n}\sum_{i=1}^{n}\left(y_i - \widehat{y_i}\right)^2$	MSE is also called the cost function and measures the average of the square of the absolute difference between predicted values $(\widehat{y_i})$ and observed values (y_i)
Root mean squared error (RMSE)	$RMSE = \sqrt{\dfrac{1}{n}\sum_{i=1}^{n}\left(y_i - \widehat{y_i}\right)^2}$	RMSE is also called the sample standard deviation and is equal to the square root of MSE
Mean absolute error	$MAE = \dfrac{1}{n}\sum_{i=1}^{n}\left|y_i - \widehat{y_i}\right|$	The average discrepancy between the predicted $(\widehat{y_i})$ and observed values (y_i) is calculated by MAE

like a tree structure. The algorithm's output resembles a DT root with leaves. DT can handle category and numerical data processing [24].

Random Forest

The design of the RF method mimics a DT forest. This algorithm uses many DTs to cluster the classification or regression data. The bootstrap approach is used to select a sample from the initial dataset, and a random number is chosen for each variable in each decision node to create each DT in the forest. The RF algorithm consists of four phases. From a total of m features, *n* features are initially randomly selected. In the second phase, you compute the node d from the n features using the optimal distribution point. You assess the target's progress in the third phase to see if it has attained the necessary number of final nodes; if not, you proceed to step 1; if not, move on to the following step. Build the forest in the last stage by performing steps 1 through 3 n times [19, 22, 25–27].

K-Nearest Neighbor

A machine learning method known as the KNN algorithm gauges how well it has learned a pattern by looking at the values of the K-closest neighbors. For classification and regression tasks, the KNN algorithm is a nonparametric approach [28]. It was initially used to solve the classification issue for news items [29]. The KNN method initially calculates the distance between each data point in the investigated dataset before beginning the learning process. The Manhattan, Euclidian, or Hamming distance functions calculate this length. The mean value of the following KNNs for each dataset is then calculated. The only hyperparameter of the KNN algorithm is the K value. A high K value creates an under-fit condition, while a small value of K generates overfitting results. The distance computation process, which

Table 3 Hyperparameter's tuning

Algorithm	Parameter	Search range	Value
PR	Degree of polynomial	2–6	2
DT	Maximum depth	2–87	101
RF	Maximum depth	2–100	100
KNN	Number of neighbors	2–5	2

increases the processing load as the data amount increases, is a downside of the KNN method [18, 19, 22].

4.3 Hyperparameter's Tuning

Hyperparameters should be adjusted appropriately because they are coefficients that significantly impact how effectively a machine learning algorithm performs. While creating a new ML model, we strictly do not know the optimal architecture for our model. In this case, we have to use the top-level parameters called hyperparameters to control the learning process of the algorithm. We must perform hyperparameter adjustment before training the ML model. Following the hyperparameter searches, Table 3 presents the optimum values employed in the algorithms.

In addition to the above-mentioned hyperparameters' tuning, the following parameters are also considered for better fitting of the ML models:

- Size of the dataset.
- Train–test split ratio.

5 Results and Discussion

In this study, pre-defined semi-elliptical crack growth behavior has been modeled and analyzed using finite element tools. ML models have been developed to predict crack growth. The result and discussion section is divided into two sub-sections; in the first sub-section, we study the effect of tensile pressure on stress intensity factor, deformation, stress, and strain. In the second sub-section, we develop and compare different ML models to predict crack growth behavior.

5.1 FEM Analysis

FEA analysis results for the parameters mentioned above are shown in Table 4.

The stress intensity factor for mode-I is dominant compared to mode-II and mode-III, so we consider the K_I value only for our analysis. The highest values for total

Table 4 Effect of tensile pressure on output parameters

Applied tensile pressure (MPa)	SIF (K_I) (Max) ($MPa\sqrt{mm}$)	Deformation (Max) (mm)	Von Mises stress (Max) (MPa)	Von Mises strain (Max)
10	6.9869	0.0019964	27.573	0.00019546
20	13.974	0.0039928	55.147	0.00039093
30	20.961	0.0059892	82.72	0.00058639
40	27.948	0.0079856	127.29	0.00078185
60	34.935	0.009982	137.87	0.00097732
60	41.922	0.011978	165.44	0.0011728

deformation, von Mises stress, and von Mises strain were discovered at 60 Mpa pressure when the FEA results were reviewed. As the applied pressure increases from 10 to 60 Mpa, the numeric values of all output attributes increase, as shown in Table 4.

The crack will grow in opening mode only if the stress intensity factor for mode-I (K_I) is more significant than the material's fracture toughness (K_{IC}), as explained in Eq. 5. This crack growth data have been generated for different fracture toughness values for different magnitudes of applied pressure ranging from 10 to 60 MPa. The fracture toughness value chosen for our analysis is below the K_I value for different pressure magnitudes. As much FEA data have been generated for our research, only the crack growth behavior for 60 Mpa pressure is shown in Fig. 5.

The crack growth decreases with an increase in the material's fracture toughness. This is because the increased fracture toughness resulted in reduced stress concentration at the crack tip position and thus slowed down the crack propagation.

Fig. 5 Crack growth behavior for different fracture toughness values at 60 Mpa pressure
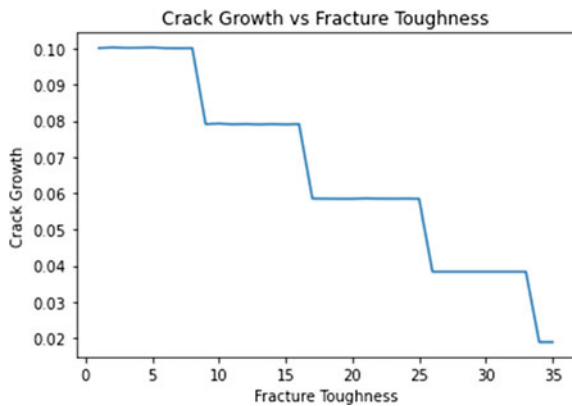
5.2   ML Models

The collinearity between the variables in our dataset was visualized using a heatmap. On both the x- and y-axes, each heatmap square depicts the relationship between the variables. Because the same two variables are grouped in those squares, the heatmap is symmetric about the diagonal.

The Pearson correlation coefficients between each input characteristic and the crack growth were calculated and displayed in the heatmap of Fig. 6 to determine the most correlated feature and its influence on the crack growth behavior. The range of Pearson correlation coefficients is -1 to 1. The parameter's value increases proportionately to how well it correlates with the crack growth, with 0 denoting no association. Cool colors (dark orange) denote lower absolute Pearson correlation values, while warm colors (light orange) denote more excellent definite Pearson correlations.

The equation for Person correlation takes the form.

$$r_{xy} = \frac{\sum_{i=1}^{n}(x_i - \overline{x})(y_i - \overline{y})}{\sqrt{(x_i - \overline{x})^2}\sqrt{(y_i - \overline{y})^2}}, \tag{9}$$

where (x_i, y_i) are the sample points, (n) is the sample size, and $(\overline{x}, \overline{y})$ are the sample means, respectively.

The algorithms are compared using the RMSE, MSE, and R^2 values in Fig. 7. Table 2 provides the justifications and formulae for these parameters. The most successful algorithms are those with reduced MSE, RMSE, and MAE values. The R^2 statistic ranges in value from 0 to 1. The accuracy of the algorithm's predictions
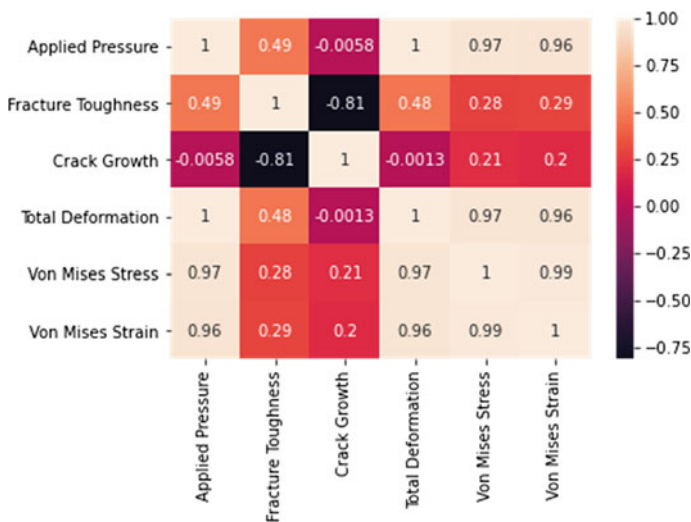
Fig. 6   Correlation between the variables
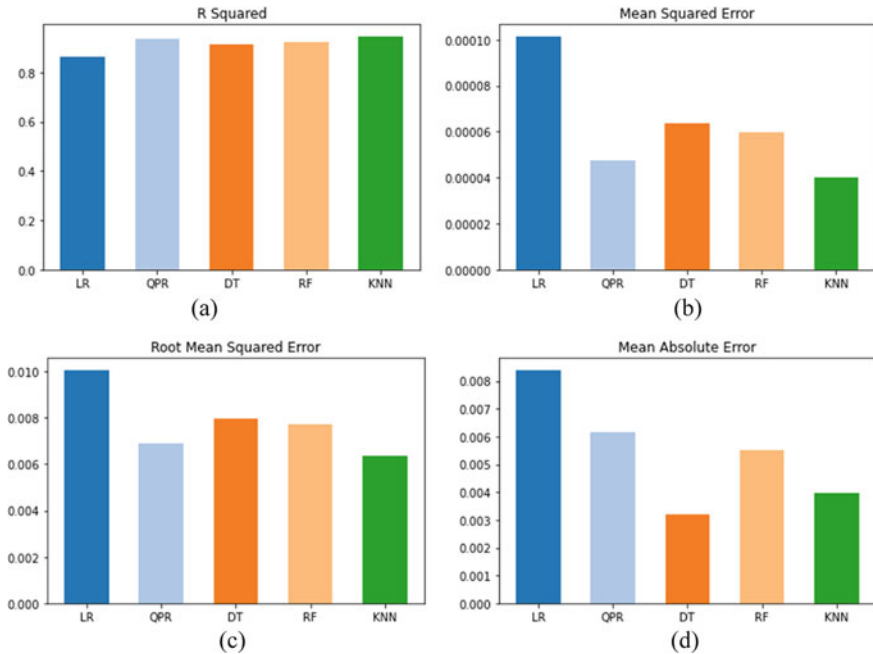
Fig. 7 Comparative study of R^2, MSE, RMSE, and MAE with the overall model performance

is improved when the R^2 is close to 1. The best algorithm can be chosen using just one of these metrics.

The three most effective algorithms when analyzing FEA outcomes in terms of MSE are KNN (0.000040), QPR (0.000047), and RF (0.000060). The three most effective methods when comparing the FEA results according to RMSE are KNN (0.0063), QPR (0.0069), and RF (0.0077). The top three algorithms for MAE are DT (0.0032), KNN (0.0040), and RF (0.0055), respectively. Examining the FEA findings for R^2, the three most effective algorithms are KNN (0.9464), QPR (0.9368), and RF (0.9204), respectively. After comparing the algorithms, it can be shown that KNN outperforms the others in regression performance, while LR performed the worst across the board.

Figure 8 shows the graphical representation of test values of crack growth with the predicted values for LR, QPR, DT, RF, and KNN regression models. It is evident from the graphical study that KNN shows the best fit (94.64% accuracy) among all proposed ML models.

Table 5 presents the comparative study of randomly selected (indicated by index number) test values with the predicted values for LR, QPR, DT, RF, and KNN. The current study's accuracy percentage of KNN is a maximum of (94.64%).

Fig. 8 Comparison of crack growth values obtained from FEA and ML algorithms, according to applied pressure and fracture toughness

Table 5 Comparison of predicted values with test values with proposed algorithms

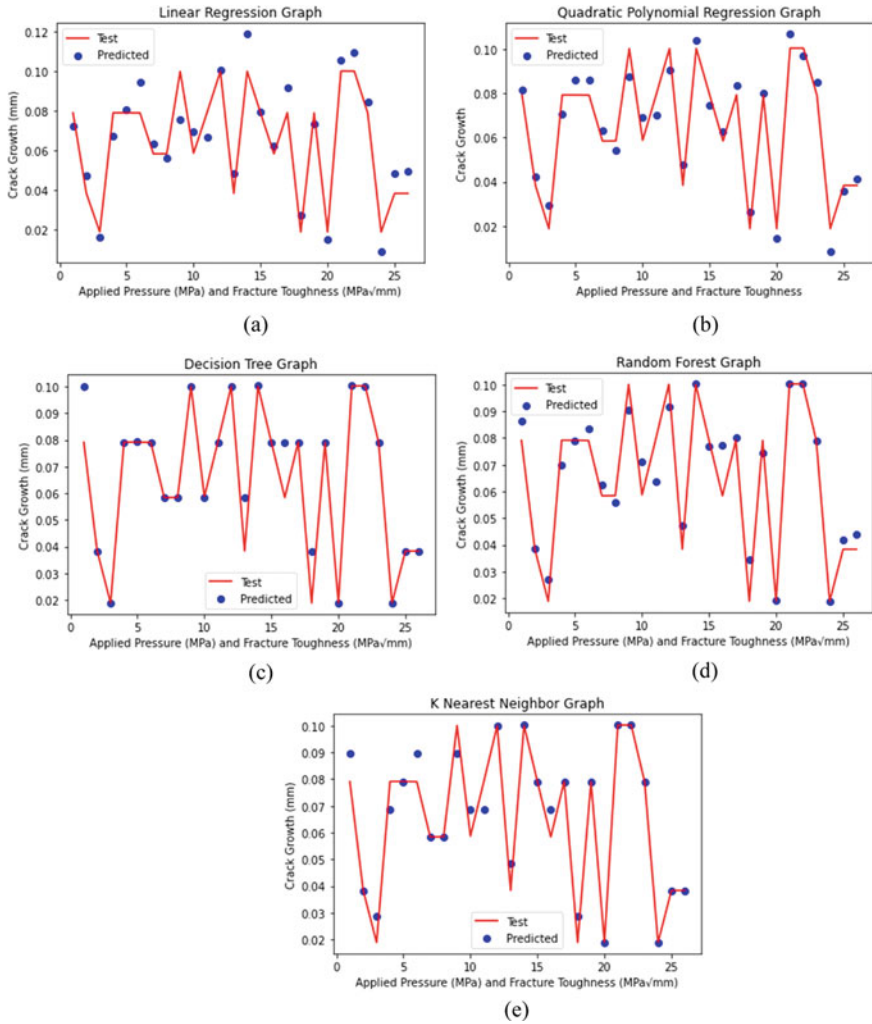| Index no	Test value	Predicted value				
		LR	QPR	DT	RF	KNN
8	0.0791	0.0727	0.0817	0.1001	0.0865	0.0896
51	0.0384	0.0474	0.0424	0.0384	0.0388	0.0384
127	0.0188	0.0161	0.0292	0.0188	0.0268	0.0286
24	0.0792	0.0161	0.0704	0.0791	0.0698	0.0688
40	0.0792	0.0807	0.0860	0.0793	0.0790	0.0791
100	0.0791	0.0948	0.0857	0.0790	0.0835	0.0896
73	0.0584	0.0635	0.0631	0.0585	0.0624	0.0585
48	0.0584	0.0565	0.0542	0.0583	0.0558	0.0584
7	0.1001	0.0757	0.0875	0.1001	0.0907	0.0896
71	0.0587	0.0696	0.0693	0.0585	0.0713	0.0688
10	0.0791	0.0666	0.0702	0.0792	0.0638	0.0688
98	0.1001	0.1009	0.0902	0.1002	0.0916	0.1002
78	0.0384	0.0484	0.0478	0.0585	0.0472	0.0484
92	0.1002	0.1190	0.1038	0.1004	0.1003	0.1003
105	0.0791	0.0797	0.0746	0.0790	0.0770	0.0790
2	0.0584	0.0626	0.0628	0.0792	0.0773	0.0688
101	0.0793	0.0918	0.0835	0.0790	0.0801	0.0791
85	0.0188	0.0272	0.0266	0.0384	0.0343	0.0286
22	0.0791	0.0736	0.0801	0.0791	0.0743	0.0791
89	0.0188	0.0151	0.0145	0.0188	0.0190	0.0188
59	0.1003	0.1059	0.1067	0.1003	0.1002	0.1002
95	0.1003	0.1099	0.0969	0.1002	0.1002	0.1003
66	0.0790	0.0847	0.0848	0.0790	0.0792	0.0791
91	0.0188	0.0090	0.0086	0.0188	0.0188	0.0188
16	0.0384	0.0484	0.0358	0.0384	0.0420	0.0384
30	0.0384	0.0494	0.0413	0.0384	0.0440	0.0384
Accuracy (%)		86.47	93.68	91.60	92.04	94.64

6 Conclusion

The crack growth behavior of a pre-defined semi-elliptical crack embedded inside a cantilever bar was examined using FEA and ML algorithms for various pressure magnitudes. The following general conclusions were drawn from this study:

- The proposed ML models are advantageous in applications where the experimental setup is expensive and computational cost is high for fracture analysis of complex models.

- From the accuracy (R^2) point of view, the KNN (94.64%) model prediction model shows the best result among other proposed ML models.
- The most effective prediction models in terms of MSE, RMSE, and MAE are KNN (0.000040), KNN (0.0063), and DT (0.0032) respectively.
- This study also observed that PR models with degrees more than five show negative R^2 values, which means that these models do not follow the data trend. So, such types of models cannot be considered for crack growth prediction.

Data Availability Statement
The researchers can access the training data and algorithms. This work uses upon reasonable request.

References

1. Moore B, Rougier E, O'Malley D, Srinivasan G, Hunter A, Viswanathan H (2018) Predictive modeling of dynamic fracture growth in brittle materials with machine learning. Comput Mater Sci 14:46–53
2. Carrara P, Lorenzis DS, Stainier L, Ortiz M (2020) Data-driven fracture mechanic. Comput Methods in Appl Mech Eng 372
3. Hsu YC, Yu CH, Buehler MJ (2020) Using deep learning to predict fracture patterns in crystalline solids. Materials 3(1):197–211
4. Liu X, Athanasiou CE, Padture NP, Sheldon BW, Gao H (2020) A machine learning approach to fracture mechanics problems. Acta Mater 190:105–112
5. Martinez ER, Chakraborty S, Tesfamariam S (2021) Machine learning assisted stochastic-XFEM for stochastic crack propagation and reliability analysis. Theoret Appl Fract Mech 112
6. Alipour M, Esatyana E, Sakhaee-Pour A, Sadooni FN, Al-Kuwari HA (2021) Characterizing fracture toughness using machine learning. J Petrol Sci Eng 200
7. Bao H, Wu S, Wu Z, Kang G, Peng X, Withers PJ (2021) A machine-learning fatigue life prediction approach of additively manufactured metals. Eng Fract Mech 242
8. Zhan Z, Hu W, Meng Q (2021) Data-driven fatigue life prediction in additive manufactured titanium alloy: a damage mechanics based machine learning framework. Eng Fract Mech 252
9. Chen D, Li Y, Yang X, Jiang W, Guan L (2021) Efficient parameters identification of a modified GTN model of ductile fracture using machine learning. Eng Fract Mech 245
10. Hu D, Su X, Liu X, Mao J, Shan X, Wang R (2020) Bayesian-based probabilistic fatigue crack growth evaluation combined with machine-learning-assisted GPR. Eng Fract Mech 229
11. Badora M, Sepe M, Bielecki M (2021) Predicting length of fatigue cracks by means of machine learning algorithms in the small-data regime. Maintenance and Reliab 23(3):575–585
12. Nasiri S, Khosravani MR, Weinberg K (2017) Fracture mechanics and mechanical fault detection by different methods of artificial intelligence: a review. Eng Fail Anal 81:270–293
13. Yan H, Zhang J, Zhou N, Li B, Wang Y (2021) Crack initiation pressure prediction for SC-CO2 fracturing by integrated meta-heuristics and machine learning algorithms. Eng Fract Mechan 249
14. Raja A, Chukka ST, Jayaganthan R (2014) Prediction of fatigue crack growth behaviour in ultrafine grained Al 2014 alloy using machine learning. Metals 10(10)

15. Rovinelli A, Sangid MD, Proudhon H, Ludwig W (2018) Using machine learning and a data-driven approach to identify the small fatigue crack driving force in polycrystalline materials. Comput Mater
16. Lew AJ, Yu CH, Hsu YC, Buehler MJ (2021) Deep learning model to predict fracture mechanisms of Graphene. 2D Mater Appl 48
17. Nguyen DLH, Do DTT, Lee J, Rabczuk T, Nguyen-Xuan H (2019) Forecasting damage mechanics by deep learning. Comput Mater Continua 61(3):951–977
18. Alpaydin E (2009) Introduction to machine learning. MIT Press, Cambridge
19. Seçkin AC, Coskun A (2019) Hierarchical fusion of machine learning algorithms in indoor positioning and localization. Appl Sci 9(18)
20. Willmott CJ (1982) Some comments on the evaluation of model performance. Bull Am Meteor Soc 63:1309–1313
21. Moriasi DN, Arnold JG, Van-Liew MW, Bingner RL, Harmel RD, Veith TL (2007) Model evaluation guidelines for systematic quantification of accuracy in watershed simulations. Trans ASABE 60:885–900
22. Seçkin M, Seçkin AC, Coskun A (2019) Production fault simulation and forecasting from time series data with machine learning in glove textile industry. J Eng Fibers Fabrics
23. Quinlan JR (1986) Induction of decision trees. Machine Learn 81–106
24. Quinlan JR (1987) Simplifying decision trees. Int J Hum Comput Stud 27:221–234
25. Liaw A, Wiener M (2002) Classification and regression by random Forest. R News 18–22
26. Akman M, Genç Y, Ankarali H (2011) Random forests yöntemi ve saˇglık alanında bir uygulama. Türkiye Klinikleri J Biostati 36–48
27. Breiman L (2001) Random forests. Machine Learn 5–32
28. Altman NS (1992) An introduction to kernel and nearest-neighbor nonparametric regression. Am Stat 46:175–185
29. Masand B, Linoff G, Waltz D (1992) Classifying news stories using memory-based reasoning. In: Proceedings of the 15th annual international ACM SIGIR conference on research and development in information retrieval, ACM, pp 59–65

Closed Blended Wing Body Concept Aircraft

Aman Jain, Agniv Biswas, Soumik Saha, and Pooja Chaubdar

Abstract Air travel has seen some rapid changes and development since the dawn of human flight in 1914. Scientists and researchers have since been in the lookout for new and better technology to help humans fly in a more efficient and comfortable way. Us, humans, have adopted the Traditional Aircraft Wing Body (TAW) as the basis of aircraft design. But it has its own cons, namely drag produced by the body, vortex generation at the wing tips and the fuselage generating little to no lift. Hence, we bring forth a concept design—Closed Blended Wing Body, with which we can minimize the vortex generation by incorporating fuselage made up of wing section, eliminating wing tips, giving the vertical connectors the ability to help with the directional stability, thus giving a higher L/D ratio and making a more efficient aircraft. This paper aims at testing the structural stability of the design concept.

Keywords Lift-to-drag ratio · Efficiency · BWB · Stability · Structural analysis

1 Introduction

Air transport was the future in 1914 when the first passenger plane flew, and the future is now, when we are witnessing the rapid changes and evolutionary changes in the aviation field and it will remain the future with the rapid growth of the aviation industry and its demand.

The evolution in the commercial aviation industry is greatly led by the efforts to minimize the drags in order to increase fuel efficiency. Drag is the unnecessary but unavoidable force in the direction parallel to freestream air. It is caused because of skin friction, pressure differences, shock formation, and downwash effect. Out of these, the shape of aircraft affects skin friction and pressure drag which is jointly called profile drag. Downwash effect is caused because of vortex formation at the wing tips, which gives rise to induced velocity resulting in induced drag and reduced

A. Jain · A. Biswas · S. Saha · P. Chaubdar (✉)
Kalinga Institute of Industrial Technology, Bhubaneswar, India
e-mail: pooja.chaubdarfme@kiit.ac.in

lift. Wave drag because of shock is for supersonic flows, which are not common in commercial aircrafts, in fact only two commercial aircrafts have break sound barrier, Tupolev Tu-144 and The Concorde.

Many efforts are done to reduce these drags. The conventional Tube and Wing (TAW) body aircraft uses its wings to generate lift and a large cylindrical tube called fuselage to accommodate cargo and crew. This design is great success and has been the base of all the research. Although the fuselage is designed aerodynamically, it contributes a little to no lift generation and large surface area gives rise to added skin friction drag. So, a lot of research has been continuing to incorporate fuselage on the wing section. This brings us to the Blended Wing Body (BWB) Aircraft.

BWB wing uses aerofoil section for fuselage, therefore contributing in generating more Lift and reducing form drag. Thus, BWB helps in better fuel efficiency and high Lift-to-Drag Ratio. Despite such benefits, BWB lags in stability as tail section has been removed and a lot of research needs to be done in this department. With advancement of computers and fly-by-wire control systems, BWB has a promising future. Also, the point left untouched in the various researches is induced drag which forms the problem statement for our research and brings us to Closed Blended Wing Body Aircraft Concept.

2 Closed Blended Wing Body Aircraft Concept

As BWB increases efficiency by using airfoil section for fuselage, but still the wing tip vortices contribute to drag to a great extent and also stability is a major issue.

Hence, we propose a closed Blended Wing Body Aircraft (see Fig. 1). A concept uses airfoil section for fuselage same as BWB and extends the structure to a closed loop wing to eliminate the wing tip vortices. Also, the vertical connectors that connects the lower wing or fuselage to upper wing can be used as vertical tails to achieve directional stability.

Figure 1 shows the different 2D views of the design. Although layout shows four engines, but the aircraft may contain different configurations of engine according to power requirements.

2.1 Validation of Model

To validate the model that we have designed, we performed an analysis similar to the one done by the authors of Reference [12]. The analysis settings of Reference [12] are shown in Fig. 2.

As shown in Fig. 2a, force is applied at C.G. point by using a plank design over it. Force to be applied is determined by dividing the force by the area of plank.

Figure 2b and c show the boundary conditions applied. Figure 2a shows the symmetry condition. The only displacement considered is the displacement in
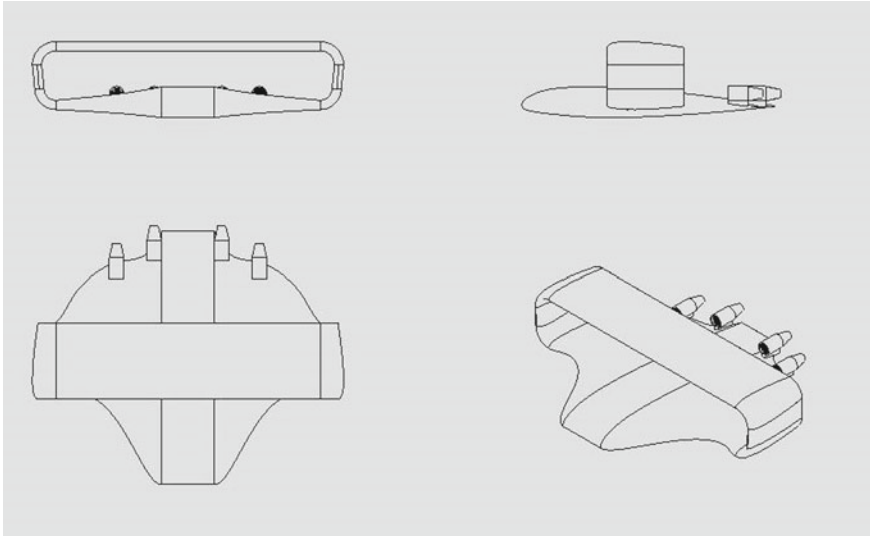
Fig. 1 Two-dimensional layouts of the concept

(a) Symmetry Condition   (b) Force applied   (c) Roller Support
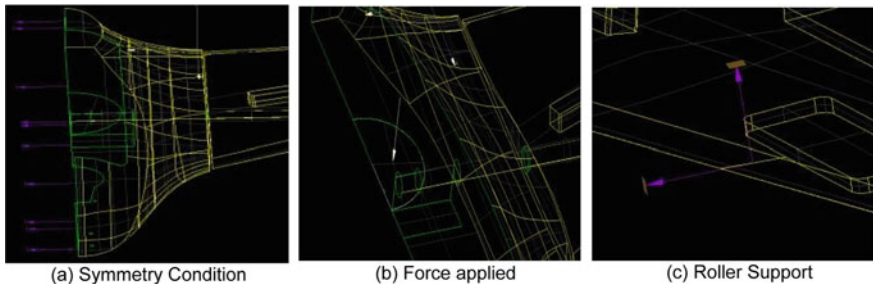
Fig. 2 Boundary conditions from [12]

vertical direction and the displacements in the other two directions as zero. Figure 2c shows the roller support applied at wing.

Similar conditions are applied to our model (see Fig. 3) with slight difference in force applied because of different mass conditions and the location of roller support is closer to the center of symmetry.

Then, the model is solved for two conditions, one is for force of 9573 N and other for double of the previous force as done by the author in reference paper [12] (see Fig. 4).

Then, the ratios of total displacements of the referred model and our model for both the cases were compared, and the results were approximately same.

Also, the pattern of deformation achieved is similar to a great extent with the consideration of different roller support locations.
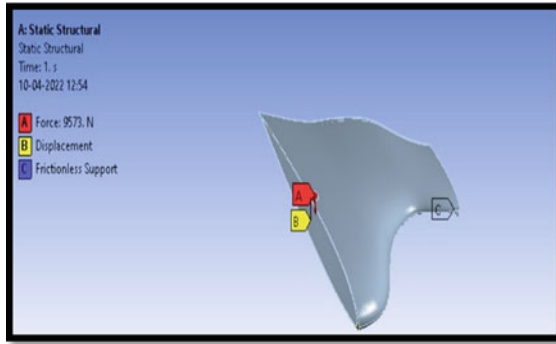
Fig. 3 Boundary conditions applied to our model
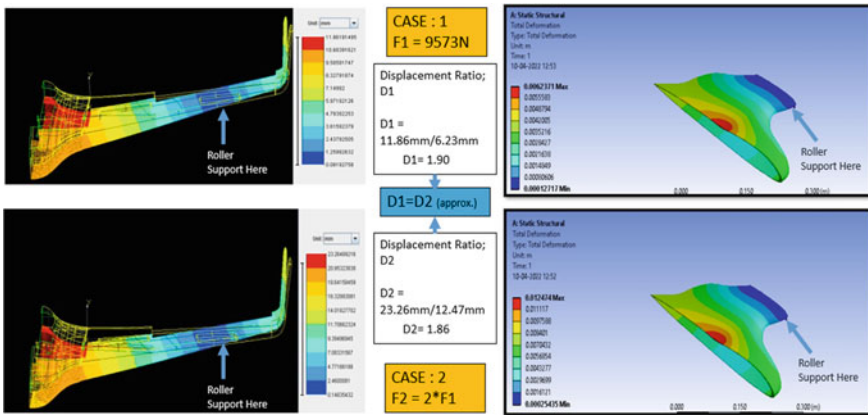
Fig. 4 Comparison between the results obtained in reference [12] and our model

3 Component-Wise Analysis

3.1 Meshing and Assumptions

Figure 5 shows the mesh generated for the different components of the aircraft.

All the mesh generations were done with default settings of Ansys. Also, for applying the force and pressure conditions, Sea-Level Conditions were considered that is:

$$\text{Pressure} = 101325 \, \text{Pa}, \ \text{Temperature} = 288.16 \, \text{K}, \ \text{Density} = 1.225 \, \text{Kg/m}^2.$$
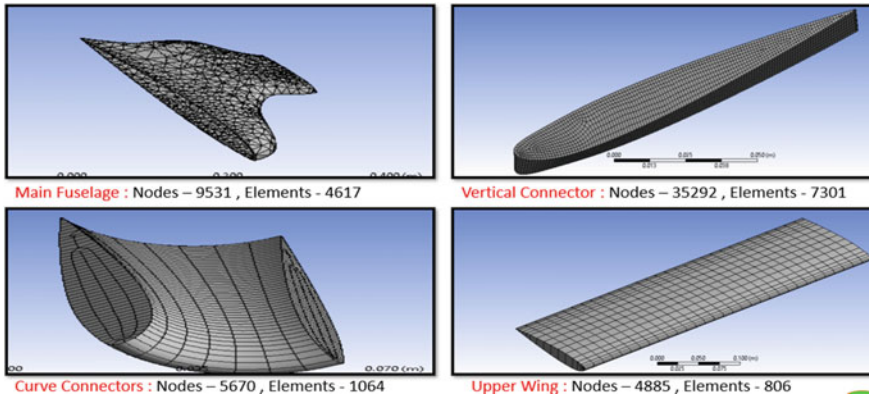
Fig. 5 Mesh generation

3.2 Main Fuselage

For the design of whole aircraft, NACA 23,012 Aerofoil is used (see Fig. 6). With the largest section at center of fuselage and smallest at the end of fuselage and further extending the same for wing in loop of aircraft.

From the total deformation plot, the results were satisfactory as the max. Deformation obtained is in micron range even though ribs and other structural supports are not considered in design or while.
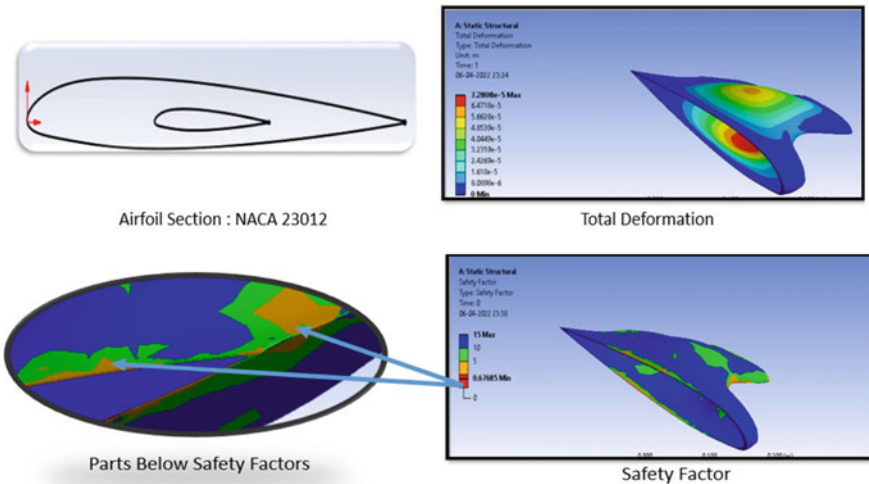
Fig. 6 Results of structural analysis on main fuselage

(a.) Shape Complexity of Connector

(b.) Safety Factor

(c.) Equivalent Stress Development

(d.) Total Deformation
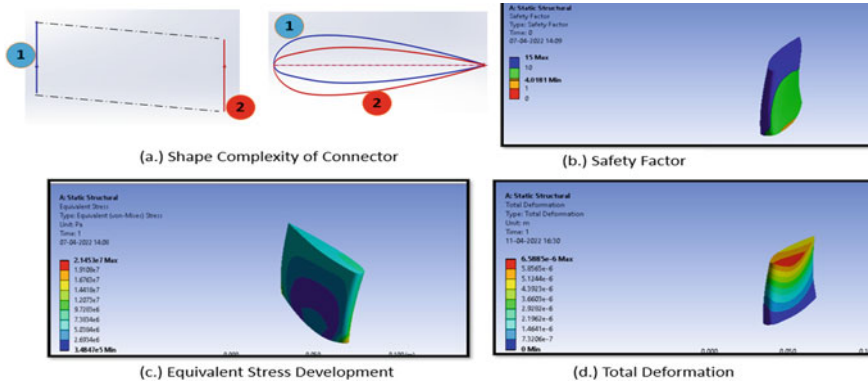
Fig. 7 Results of structural analysis on vertical connectors

The safety factor plot shows that several parts are getting below the limits, but this part is easily manageable by providing supports like ribs and cylindrical vessels for more uniformity.

3.3 Vertical Connector

Figure 7a shows the misalignment of sections that arises in vertical connector because of the rotation of the asymmetric aerofoil in two different directions for curve. This misalignment results in slight deflection of connector from the vertical line of aircraft.

Figure 7b, c, and d represent that the component is structurally stable as the respective values are well within the allowable limits.

3.4 Curve Connectors

In the design, four curve connectors are used (see Fig. 8a). Figure 8b shows the safety factor plot for the connector of fuselage to vertical connector. It shows that large part is getting out of the limiting value. This issue has to be resolved by replacing the material of curve connector from aluminum alloy to other material which may affect mass of aircraft but will improve structure.

(a.) Wing Geometry

(b.) Safety Factor

(c.) Equivalent Stress Development

(d.) Total Deformation
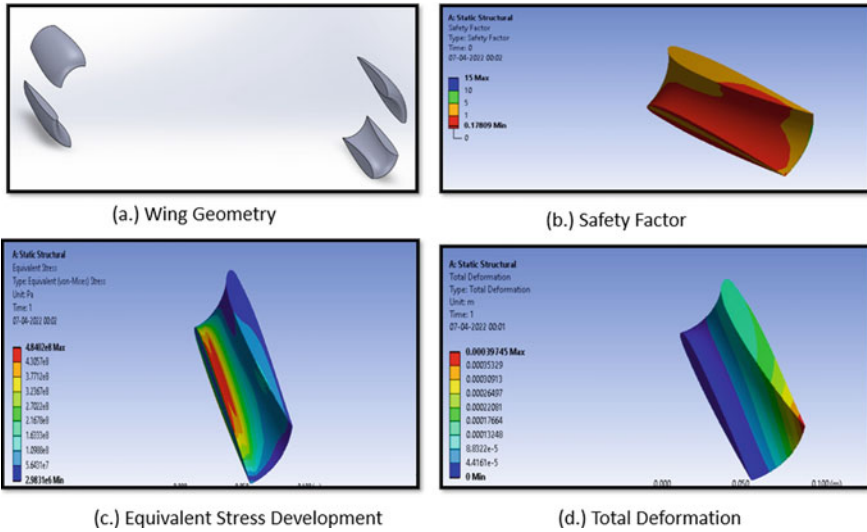
Fig. 8 Results of structural analysis on curve connectors

3.5 Upper Wing

Similarly, for the upper wing, all the values prove the static stability of the component (see Fig. 9).

Fig. 9 Result of structural analysis on upper wing

4　Conclusion

The purpose of the paper was to test the structural stability of the concept design and the results are greatly satisfactory. The minor lags can be fixed using ribs and other supporting elements in the structure.

Although the design increases the surface area exposed to air but provides much larger space to incorporate systems and payloads, and gives other efficiency improvements like increased L/D ratio, reduced drag.
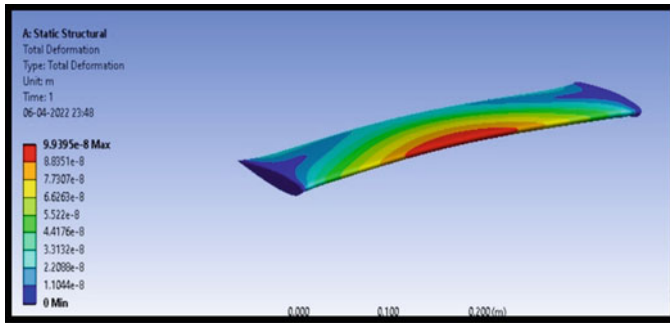
Also, the static and dynamic stability is to be seen if they are feasible as the structure promises.

Therefore, in detail CFD analysis to obtain Cl versus Cd plots, aerodynamic forces and efficiencies are the major work to be done.

References

1. Pandey S, Peifenga L, Binqiana Z (2011) Research gate. Chinese J Aeronaut
2. Tao Y, Li Y (2016) Transonic wing stall of a blended flying wing common research model based on DDES method. Chinese J Aeronaut
3. Zadeh PM, Sayadi M (2019) An efficient aerodynamic shape optimization of blended wing body UAV using multi-fidelity models. Chinese J Aeronaut
4. Zhenli C, Minghui Z (2019) Assessment on critical technologies for conceptual design of blended-wingbody civil aircraft. Chinese J Aeronaut
5. Zhenqing X, Zhenli C (2019) Nacelle-airframe integration design method for blended-wing-body transport with podded engines. Chinese J Aeronaut
6. Velázquez Salazar OE, Weiss J (2015) Development of blended wing body aircraft design. Research Gate
7. Dorsey A, Uranga A (2020) Design space exploration of blended wing bodies. Research Gate
8. Chaudhary S, Sharma D (2022) A comprehensive review on blended wing body aircraft. ResearchGate
9. Pandey S (2017) Blended wing body aircraft. Research Gate
10. Minghui Z, Zhenli C (2019) Effects of stability margin and thrust specific fuel consumption constrains on multi-disciplinary optimization for blended-wing-body design. Chinese J Aeronaut
11. Lixin W, Ning Z (2022) Stability characteristics and airworthiness requirements of blended wing body aircraft with podded engines. Chiense J Aeronaut
12. Noels L, Delvoie C (2016) Structural analysis of a blended wing body composite aircraft

Analysis of Acoustics Performance of Double-Layer Micro-perforated Panel Absorbers: A Finite Element Analysis

D. K. Agarwalla and A. R. Mohanty

Abstract Micro-perforated panel (MPP) combined with desired cavity depth is considered as a next-generation sound absorber and a better alternative due to the improved acoustic performance in low-to-medium frequency range and sustainable features in hostile environments compared to the traditional porous materials. A single-layer MPP absorber facilitates absorption in one to two octaves, which can be improved using multiple MPPs in the absorber structure. The acoustic impedance of the single-layer MPP absorber is estimated using Maa model and equivalent electro-acoustical circuit (EAC) analysis. The predicted absorption coefficients of the single-layer MPP absorber were validated through measurement in two microphone impedance tubes or numerical analysis in which the actual experimental conditions were simulated. In this study, the absorption characteristics of double-layer MPP absorbers are better predicted through the transfer matrix method (TMM), in which individual transfer matrices of constituting elements of the absorbers are considered. The predicted results are validated through a finite element analysis (FEA) which incorporates the determination of acoustic impedance through a pore and the effect of pore–pore interaction for MPP. The sound absorption characteristics of double-layer MPP absorbers obtained from FEA show good agreement with the predicted results, thus making the proposed FEA reliable. Moreover, the variation in the sound pressure level of the double-layer MPP absorber along the propagation direction is illustrated, justifying the sound absorption phenomena.

Keywords Double-layer micro-perforated panel absorber · Finite element analysis · Sound absorption · Transfer matrix method · Maa model

D. K. Agarwalla (✉) · A. R. Mohanty
Department of Mechanical Engineering, IIT Kharagpur, Kharagpur, West Bengal, India
e-mail: dips50k@iitkgp.ac.in

1   Introduction

Micro-perforated panel (MPP) combined with desired cavity depth is considered as a next-generation sound absorber and a better alternative due to the improved acoustic performance in low-to-medium frequency range and sustainable features in hostile environments compared to the traditional porous materials [1–3]. Maa determined the theoretical foundations and design assumptions of the potential MPP absorber [1, 4, 5]. The MPP absorber is a thin membrane or panel with a less perforation ratio (0.5–5%), an air-back cavity, and a hard rigid wall [6, 7]. The sound attenuation through the MPP absorber is attributed to two kinds of losses: the formation of Helmholtz resonator (HR) between the trapped air in the pore and back cavity and the frictional losses against the wall of the pores [8, 9]. MPP absorbers are improved over the years for structural modifications [9, 10], cavity optimizations [8, 11], and the addition of extra elements like mechanical impedance plate [12], mass block [13], HR [14], etc. and composite absorbers [15, 16] using the traditional electro-acoustical circuit (EAC) analysis [1, 7, 9]. The multilayered absorbers' acoustic impedance and absorption coefficient were accurately predicted using the transfer matrix method (TMM) [15–17]. The TMM is a preferable investigative tool for multilayered absorbers than the EAC [18]. Most of the theoretical models proposed for MPP absorbers and their modifications [7–10] are validated through impedance tube facility following ASTM E1050 standard. The use of the finite element method (FEM) for the analysis of the absorption properties of MPP absorbers was very limited [19, 20]. The FEM is suitable to validate the MPP models for multilayered absorbers combined with porous absorbers and in the case where the precise mounting of the absorber is very complicated.

The current study focuses on TMM through which the double-layer MPP (DMPP) absorbers' absorption characteristics are forecasted, in which individual transfer matrices of constituting elements of the absorbers are considered. The predicted results are validated through a finite element analysis (FEA) which incorporates the determination of acoustic impedance through a pore and the effect of pore–pore interaction for MPP. The sound absorption characteristics (SAC) of DMPP absorbers obtained from FEA are compared with the predicted results to check the reliability of FEA. Moreover, the variation in the sound pressure level of the DMPP absorbers along the propagation direction is illustrated, justifying the sound absorption phenomena.

2   Theory of Double-Layer MPP (DMPP) Absorber

The schematic diagram of sound traveling through a DMPP absorber is presented in Fig. 1. It consists of two layers of MPP (MPP_{1st} and MPP_{2nd}) with air cavities (D_1 and D_2) separating them and the rigid wall. The panel thickness of both MPP layers is considered as 1 mm. The total cavity depth ($D_1 + D_2$) in the current analysis

is considered as 30 mm. The sound propagates through MPP_{1st}, D_1, MPP_{2nd}, D_2, and rigid wall. Due to the presence of multiple propagation media, the TMM [17, 18, 21] is employed to estimate the sound absorption of the DMPP absorber. The TMM is a better-investigating tool than EAC for multilayered absorbers [18]. In this case, four individual transfer matrices are required for two separate MPPs and two air-back cavities of depths D_1 and D_2 to evaluate the surface impedance of the DMPP absorber. The transfer matrices of MPP_{1st}, MPP_{2nd}, D_1, and D_2 are presented in matrix form (2 × 2) as,

$$T_{MPP_{1st}} = \begin{bmatrix} 1 & Z_{MPP_{1st}} \\ 0 & 1 \end{bmatrix} \tag{1}$$

$$T_{MPP_{2nd}} = \begin{bmatrix} 1 & Z_{MPP_{2nd}} \\ 0 & 1 \end{bmatrix} \tag{2}$$

$$T_{D_1} = \begin{bmatrix} \cos(k_0 D_1) & j Z_{Air} \sin(k_0 D_1) \\ \frac{j}{Z_{Air}} \sin(k_0 D_1) & \cos(k_0 D_1) \end{bmatrix} \tag{3}$$

$$T_{D_2} = \begin{bmatrix} \cos(k_0 D_2) & j Z_{Air} \sin(k_0 D_2) \\ \frac{j}{Z_{Air}} \sin(k_0 D_2) & \cos(k_0 D_2) \end{bmatrix} \tag{4}$$

Z_{MPP1st} and Z_{MPP2nd} are the acoustic impedance of MPP_{1st} and MPP_{2nd}, which are the combination of acoustic resistance (r_{1st}) and mass reactance (ωm_{1st}) of MPPs and their respective cavities. The acoustic impedance (Z_{MPP1st}) can be written as proposed by Maa [1],
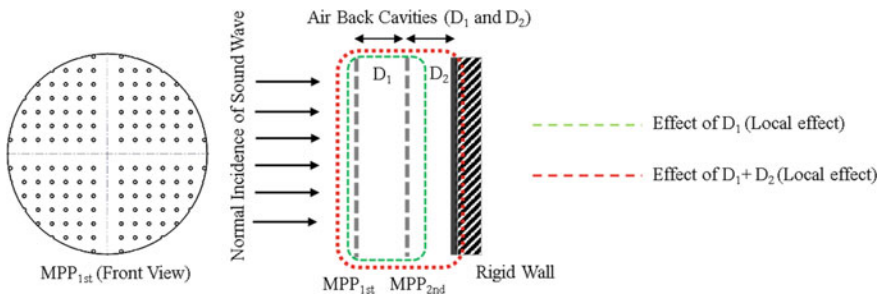

Fig. 1 Schematic of sound propagation through double-layer MPP absorber illustrating the local and global effect

$$\left.\begin{aligned}
z_{\mathrm{MPP_{1st}}} &= r_{1st} + j\omega m_{1st} \\
r_{1st} &= \frac{32\eta t_{1st}}{\phi_{1st}\rho_0 c d_{1st}^2}\left(\sqrt{1 + \frac{k_{1st}^2}{32}} + \frac{\sqrt{2}k_{1st}d_{1st}}{8t_{1st}}\right) \\
m_{1st} &= \frac{t}{\phi_{1st}c}\left(1 + \frac{1}{\sqrt{9 + k_{1st}^2/2}} + \frac{0.85d_{1st}}{t_{1st}}\right) \\
k_{1st} &= \frac{d_{1st}}{2}\sqrt{\frac{\omega\rho_0}{\eta}}
\end{aligned}\right\} \tag{5}$$

The meaning of all symbols mentioned in the above equations is defined in Table 1.
The acoustic impedance of second layer MPP (Z_{MPP2nd}) may be similarly determined using Eq. (5).

The effective transfer matrix of the DMPP absorber can be presented as the multiplication of individual transfer matrices of the intermediate mediums, such as MPP layers and air-back cavities,

$$T_{\mathrm{DMPP}} = \prod_{i=1}^{n} T_i = T_{\mathrm{MPP_{1st}}} \cdot T_{D_1} \cdot T_{\mathrm{MPP_{2nd}}} \cdot T_{D_2} = \begin{bmatrix} T_{11} & T_{12} \\ T_{21} & T_{22} \end{bmatrix} \tag{6}$$

Let p_i and u_i be incident sound pressure and particle velocity on the $\mathrm{MPP_{1st}}$ layer's surface. Therefore, p_o and u_o represent the output sound pressure and particle velocity at the rigid wall's surface. Therefore, the value of u_o is zero. The input and output sound pressures and particle velocities can be written in the form of the following matrix relationship,

$$\begin{bmatrix} p_i \\ u_i \end{bmatrix} = \begin{bmatrix} T_{11} & T_{12} \\ T_{21} & T_{22} \end{bmatrix} \begin{bmatrix} p_0 \\ 0 \end{bmatrix} \tag{7}$$

The surface impedance, sound absorption coefficient, and sound absorption average (SAA) of the DMPP absorber can be determined as,

$$Z_{DMPP} = \frac{T_{11}}{T_{21}} \tag{8}$$

Table 1 Nomenclature

Symbols	Meaning
ρ_0	Density of air
c	Velocity of sound in air
η	Coefficient of viscosity of air
Φ_{1st}, Φ_{2nd}	Perforation ratios of $\mathrm{MPP_{1st}}$ and $\mathrm{MPP_{2nd}}$, respectively
ω	Angular frequency of sound wave
d_{1st}, d_{2nd}	Pore diameters of $\mathrm{MPP_{1st}}$ and $\mathrm{MPP_{2nd}}$, respectively
k_{1st}, k_{2nd}	Perforate constants of $\mathrm{MPP_{1st}}$ and $\mathrm{MPP_{2nd}}$, respectively

$$\alpha_{\mathrm{DMPP}} = \frac{4\mathrm{Re}(Z_{\mathrm{DMPP}}/\rho_0 c)}{[1 + \mathrm{Re}(Z_{\mathrm{DMPP}}/\rho_0 c)]^2 + [\mathrm{Im}(Z_{\mathrm{DMPP}}/\rho_0 c)]^2} \tag{9}$$

$$\mathrm{SAA} = \left(\frac{1}{12} \sum_{f_o} \alpha_{f_o} \right) \times 100 \tag{10}$$

where f_o indicates frequencies of 1/3rd octave spectrum (12 numbers) within 200–2500 Hz, and the sound absorption average (SAA) can be effectively used to elaborate the SAC of the absorber in the low-to-medium frequency range [9, 22]. The SAA expressed in percentage is presented in Eq. 10. The absorption coefficients in the desired frequency range (50–4000 Hz) of DMPP absorbers are illustrated in Section 4 subjected to the change in geometrical properties of MPP$_{1st}$ and MPP$_{2nd}$ layers.

The sound absorption coefficient and SAAs of DMPP absorbers are predicted using Eqs. (1–10) and compared in Fig. 2a and b , respectively. The combination of each layer of MPP and its adjacent cavity forms a mass-spring-damper system which is nothing but a Helmholtz resonator (HR). Each HR produces a distinct resonant frequency leading to peak absorption. The resonant frequencies are coupled to facilitate broadband sound absorption, as shown in Fig. 2a. The DMPP absorber has an advantage over the single-layer MPP absorber with respect to two aspects. The first aspect is the coupled resonant frequencies of the individual layer with their respective cavity depths. The second aspect is attributed to the combination of local and global effects, as shown in Fig. 1. The local effect occurs due to the individual cavity depths adjacent to two layers of MPPs. The global effect is realized for the MPP$_{1st}$, which is backed by two walls (MPP$_{2nd}$ and rigid wall). The SAAs of the three absorbers' configurations also indicate that the DMPP absorber has an acoustic advantage over the individual MPP absorbers. Among the individual absorbers, the MPP$_{1st}$ provides an absorption peak corresponding to a lower frequency, backed by higher cavity depth.

3 FEA of DMPP Absorber

As the DMPP absorbers consist of two single-layer MPPs backed by their adjacent cavities, it is crucial to estimate the acoustic impedance of a single layer of MPP. The single-layer MPP absorber consists of an MPP layer with an air-back cavity behind the rigid wall. The plane sound wave is allowed to propagate through the absorber to dissipate the sound energy; hence, sound attenuation is achieved. The related physics of the DMPP absorber is captured using the FEA tool, which estimates the changes in acoustic properties along the sound propagation direction. The most crucial element of the absorber is MPP, as the sound wave strikes this layer first and dissipates a significant amount of acoustic energy. Therefore, the governing equation used for the FEA of MPP is presented below.
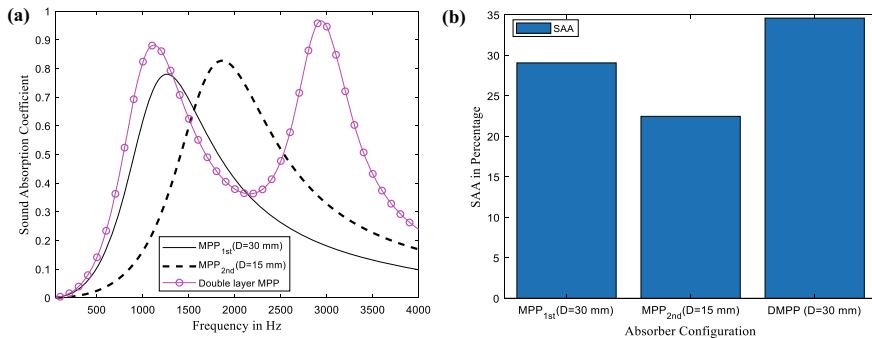
Fig. 2 Comparison of sound absorption characteristics of different absorber configurations and their SAAs **a** DMPP absorber ($d_{1st} = d_{2nd} = 0.5$ mm, $\Phi_{1st} = \Phi_{2nd} = 3\%$, $D_1 = 15$ mm, $D_2 = 15$ mm) and MPP absorbers ($d = 0.5$ mm, $\Phi = 3\%$, $D = 30$ mm), ($d = 0.5$ mm, $\Phi = 3\%$, D = 15 mm) **b** Comparison of SAAs of DMPP and individual MPP absorber

The FE model of MPP considers a single pore along the x-axis direction, which is the direction of sound wave propagation, as shown in Fig. 3a. Sound propagation is assumed to be parallel to the x-axis through the entire pore area. The pore is of diameter d and length t (MPP thickness). The variation of sound pressure (p) and velocity (v) is expressed as,

$$p(x) = pe^{-jkx} \tag{11}$$

$$v(x) = ve^{-jkx} \tag{12}$$

The transfer impedance associated with a panel is realized as the ratio of pressure change across the panel to velocity on its surface, and

Fig. 3 Schematic diagram of sound propagation through a single pore and its end correction effect **a** sound propagation through a single pore **b** representation of end correction effect

$$Z_i = \frac{\Delta p}{v} = \frac{p_+ - p_-}{v} \tag{13}$$

p_+ and p_- are sound pressure along the $+$ ve and $-$ve x-axis.

Using the above Eqs. (10–12), the simplified expression obtained as,

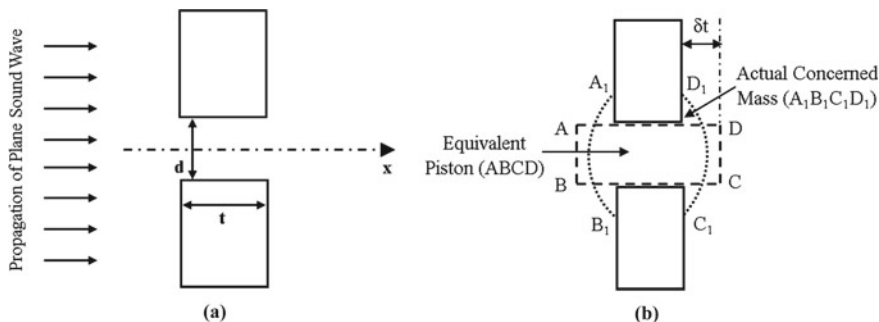$$Z_i = -2jz_c \sin(kt/2) \tag{14}$$

where z_c and k are characteristic impedance and complex wavenumber [23–26], respectively, resonating the low-reduced frequency models for narrow region acoustics for circular ducts given as,

$$z_c = \rho c \big[\{\gamma - (\gamma - 1)\psi_h\}\psi_v \big]^{-1/2} \tag{15}$$

$$k = \frac{\omega}{c} \left[\{\gamma - (\gamma - 1)\psi_h\} \frac{1}{\psi_v} \right]^{-1/2} \tag{16}$$

Ψ_h and Ψ_v are F_{ok} functions due to the thermal and viscous effect inside the pore. The pore thickness is minimal (1 mm only), so the thermal effects are neglected. Moreover, ψ_v is a function of ζ [25], which is the ratio of pore diameter (d) and pore spacing (b),

$$\psi_v(\xi) = 1 + x_1\xi + x_2\xi^2 + x_3\xi^3 + \ldots + x_8\xi^8 \tag{17}$$

where $x_1, x_2, x_3, x_4, x_5, x_6, x_7$, and x_8 are arbitrary constants.

The normalized transfer impedance through a pore is given by,

$$z_i = \frac{Z_i}{\rho c} = -\frac{2j \sin\left(\frac{kt}{2}\right)}{\sqrt{\big[\{\gamma - (\gamma - 1)\psi_h\}\psi_v\big]}} \tag{18}$$

$$z_i = -\frac{jkt}{\psi_v} = -\frac{j\omega t}{c\psi_v} \quad \left[As\ kt \ll 1,\ \sin\left(\frac{kt}{2}\right) = \frac{kt}{2} \right] \tag{19}$$

When the panel thickness is more, both viscous and thermal effects are included, as shown in Eq. 17. Equation 18 is simplified and valid for thin panels, which consider only viscous effects and discard the thermal effects. If the sound propagation is through the lattice of uniform pores throughout the panel (MPP), we need to consider the panel's perforation ratio (Φ). For uniform distribution of pores with pore spacing b, the perforation ratio is given by,

$$\phi = \frac{\pi d^2}{4b^2} \tag{20}$$

Therefore, the transfer impedance expression of a pore in MPP is obtained as,

$$z_{\text{MPP}} = \frac{z_i}{\phi} \tag{21}$$

The pore is equivalent to a piston (ABCD) of length t, as shown in Fig. 3b. But the actual mass ($A_1B_1C_1D_1$) of the concerned fluid subjected to the normal incidence of a sound wave is more than the mass trapped inside the pore. The actual mass of the fluid can be computed by incorporating end corrections δt on each side of the piston to obtain an equivalent piston. In the case of higher values of Φ, the adjacent pores are positioned close to each other. Therefore, the actual mass of the fluid associated with each pore overlaps. Therefore, total effective mass reduces compared to the sum of the individual masses, and the end correction is reduced by a pore–pore interaction effect (f_{ppi}), which is a function of the perforation ratio and Fok function [25]. The transfer impedance associated with end correction can be obtained by including Φ and f_{ppi} and replacing t with $2\delta t$ (presence of the same medium on both sides of the pore) in Eq. 18. The relevance of Eq. 18 in computing the end correction is more due to the absence of thermal conduction outside the pore (ψ_h is ignored). The transfer impedance can be rewritten, including the end corrections, as,

$$z_{ec} = -\left(\frac{j\omega}{c\phi}\right)\left(\frac{2\delta t}{\psi_v}\right) f_{\text{ppi}} \tag{22}$$

The end correction δt can be expressed as a combination of the resistive and reactive parts as,

$$\delta t = \delta t_r + \delta t_m \tag{23}$$

The transfer impedance associated with the end correction can be written as a combination of the real and imaginary parts as,

$$z_{ec} = -\text{Re}\left(\left\{\frac{j\omega}{c\phi}\right\}\left\{\frac{2\delta t_r}{\psi_v}\right\} f_{\text{ppi}}\right) - j\text{Im}\left(\left\{\frac{j\omega}{c\phi}\right\}\left\{\frac{2\delta t_m}{\psi_v}\right\} f_{\text{ppi}}\right) \tag{24}$$

Therefore, the final expression of the transfer impedance associated with a pore of a thin panel is obtained by combining Eqs. 18 and 23,

$$z_i = -\text{Re}\left(\left\{\frac{j\omega}{c\phi}\right\}\left\{\frac{t + 2\delta t_r}{\psi_v}\right\} f_{\text{ppi}}\right) - j\,\text{Im}\left(\left\{\frac{j\omega}{c\phi}\right\}\left\{\frac{t + 2\delta t_m}{\psi_v}\right\} f_{\text{ppi}}\right) \tag{25}$$

Equation 24 presents the expression of z_i through the MPP pore with the end corrections and the presence of the same medium outside the pore, which forms the basis of FEA of transfer impedance through the MPP layer used in the commercial FE tool (Acoustics module, COMSOL Multi-physics).

The representative diagram of the FE model of the DMPP absorber is depicted in Fig. 4a. It comprises two layers of homogeneous MPPs, such as $\text{MPP}_{1\text{st}}$ and $\text{MPP}_{2\text{nd}}$, with a total lateral dimension limited to 30 mm, as mentioned in Sect. 2. The FE
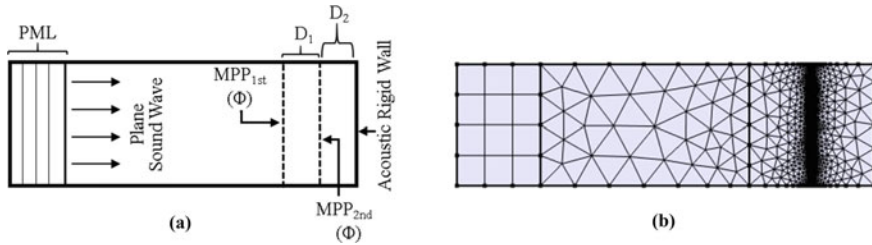
Fig. 4 Representative diagram of sound propagation through DMPP absorber and its meshed diagram **a** schematic of FE model of DMPP absorber and **b** its discretization diagram

Table 2 Description of discretization properties of DMPP absorbers

DMPP absorbers	No. of triangular elements	No. of quadrilateral elements	No. of edge elements	No. of vertex elements	Minimum size of elements (mm)
$D_1 = 15$ mm, $D_2 = 15$ mm	5308	12	510	12	0.027
$D_1 = 20$ mm, $D_2 = 10$ mm	5267	12	508	12	0.027

modeling of the DMPP absorber ($d_{1st} = 0.2$ mm, $d_{2nd} = 0.3$ mm, $\Phi_{1st} = \Phi_{2nd} = 3\%$) is accomplished using Eq. 24 (for MPP layers), and characteristics impedance of the air cavities D_1 and D_2. Equal ($D_1 = D_2 = 15$ mm) and ($D_1 = 20$ mm, $D_2 = 10$ mm) unequal air-back cavities are considered for the current analysis. The discretization diagram of the DMPP absorber of equal cavity depths is depicted in Fig. 4b, and its geometrical details are presented in Table 2.

The sound absorption coefficients obtained through FEA of DMPP absorbers with different configurations using COMSOL Multi-physics are presented and compared with their theoretical results (Maa model and transfer matrix method) in Sect. 4.

4 Results and Discussions

This section presents the sound absorption characteristics of DMPP absorbers with varying geometrical properties of first and second MPP layers (pore diameters and perforation ratios) and air-back cavities. Moreover, sound absorption coefficients of DMPP absorbers with selected configurations obtained from theoretical (Maa model and TMM) and FEM are compared. Pore diameters (d_{1st}, d_{2nd}) and perforation ratios (Φ_{1st}, Φ_{2nd}) of two layers of MPPs are increased and decreased to optimize the sound absorption characteristics. The air-back cavities (D_1, D_2) are also considered in increasing and decreasing manners to maximize the acoustic performance of the
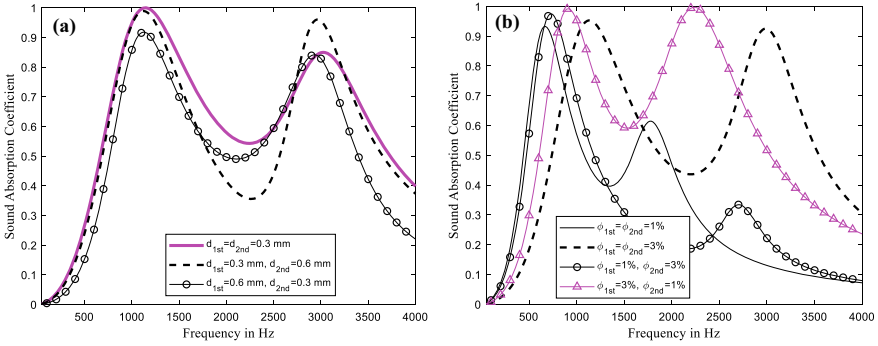
Fig. 5 Influence of d_{1st} and d_{2nd} on sound absorption of DMPP absorbers with equal D ($D_1 = D_2$ = 15 mm) **a** DMPP absorber ($\Phi_{1st} = \Phi_{2nd} = 3\%$) **b** DMPP absorber ($d_{1st} = d_{2nd} = 0.4$ mm)

DMPP absorbers. Their SAAs are compared for better estimation and comparison of absorption properties.

4.1 Effect of Unequal d_{1st}, d_{2nd} and Φ_{1st}, Φ_{2nd}

The effect of unequal pore diameters (d_{1st}, d_{2nd}) and perforation ratios (Φ_{1st}, Φ_{2nd}) on sound absorption of DMPP absorbers is depicted in Fig. 5a and b, respectively. It has been observed from Fig. 5a that equal pore diameters (SAA = 47%, $d_{1st} = d_{2nd}$) and pore diameters in increasing order (SAA = 42%, $d_{1st} < d_{2nd}$) of two layers provide better absorption properties compared to the pore diameters in decreasing order (SAA = 39%, $d_{1st} > d_{2nd}$). The perforation ratios of two layers (Φ_{1st}, Φ_{2nd}) are maintained constant at 1% (SAA = 45%) and 3% (SAA = 40%). However, the Φ_{1st} and Φ_{2nd} of two MPP layers are considered in increasing (SAA = 41%) and decreasing order (SAA = 51%) to identify the better configuration of the DMPP absorber, as shown in Fig. 5b.

4.2 Effect of Unequal Air-Back Cavities (D_{1st}, D_{2nd})

The influence of air-back cavities (D_1 and D_2) on sound absorption properties of DMPP absorbers is illustrated in Fig. 6. In this analysis, the values of D_1 and D_2 are considered in three ways such as (a) equal ($D_1 = 15$ mm and $D_2 = 15$), **b** increasing order ($D_1 = 10$ mm, $D_2 = 20$ mm, and $D_1 = 5$ mm, $D_2 = 25$ mm), and **c** decreasing order ($D_1 = 20$ mm, $D_2 = 10$ mm and $D_1 = 25$ mm, $D_2 = 5$ mm). Their effect on sound absorption is compared in Fig. 6a and b. The related SAAs for increasing values of cavities are (53, 51 and 49%) and 53, 53 and 52% for decreasing values of
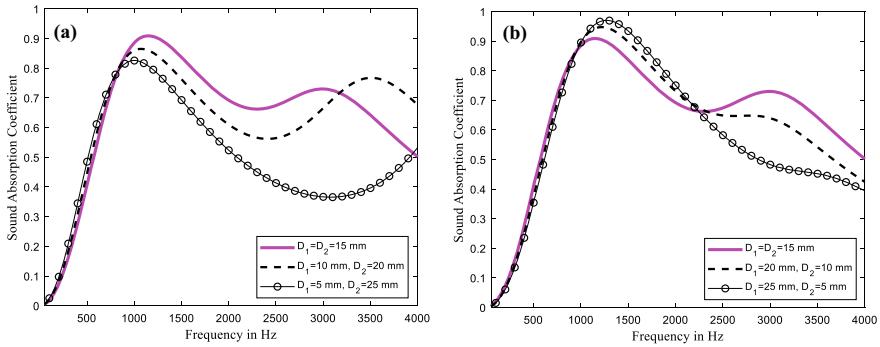
Fig. 6 Influence of air-back cavities (D_1 and D_2) on sound absorption of DMPP absorbers with equal d ($d_{1st} = d_{2nd} = 0.2$ mm) and Φ ($\Phi_{1st} = \Phi_{2nd} = 3\%$) **a** D_1 increasing and D_2 decreasing **b** D_1 decreasing and D_2 increasing

cavities. Therefore, it can be seen that equal and decreasing cavity depths result in higher SAAs.

4.3 Comparison of Theoretical and FE Results

The SAC of DMPP absorbers with equal and reducing cavity depths obtained through theoretical (Maa model and TMM) and FE methods is compared in Figs. 7 and 8, respectively. DMPP absorbers shown in Figs. 7a, b and 8a, and b with different geometrical properties show excellent agreement between the theoretical and FE results in the frequency range of 50 Hz–2500 Hz. However, FEM results deviate marginally from theoretical results beyond 2500 Hz.

The SPL through the DMPP absorbers with different configurations is presented in Fig. 9. The SPL through the DMPP absorbers with equal cavities and unequal cavities is presented in Fig. 9a and b , respectively. Both absorbers show a decrease in SPL while propagating along it, but the equal cavities' configuration has an advantage over the unequal cavities.

5 Conclusions

The sound absorption characteristics of double-layer MPP absorbers are predicted through the Maa impedance model of the MPP layer and transfer matrix method. The predicted results are validated using the FEA of the DMPP absorbers, in which the transfer impedance through the MPP layer is determined considering the end correction of pores and the pore–pore interaction effect. The effect of DMPP is realized through the local and global effects provided by the cavities. The DMPP absorbers
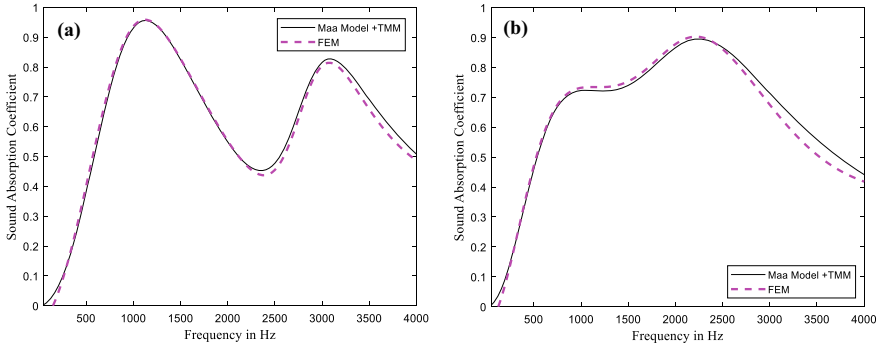
Fig. 7 Comparison of sound absorption of double-layer MPP absorbers with equal D ($D_1 = D_2 = 15$ mm) obtained through theoretical (Maa model and TMM) and FE method **a** DMPP absorber ($d_{1st} = 0.2$ mm, $d_{2nd} = 0.4$ mm, $\Phi_{1st} = \Phi_{2nd} = 3\%$ **b** DMPP absorber ($d_{1st} = d_{2nd} = 0.2$ mm, $\Phi_{1st} = 3\%$, $\Phi_{2nd} = 1\%$)
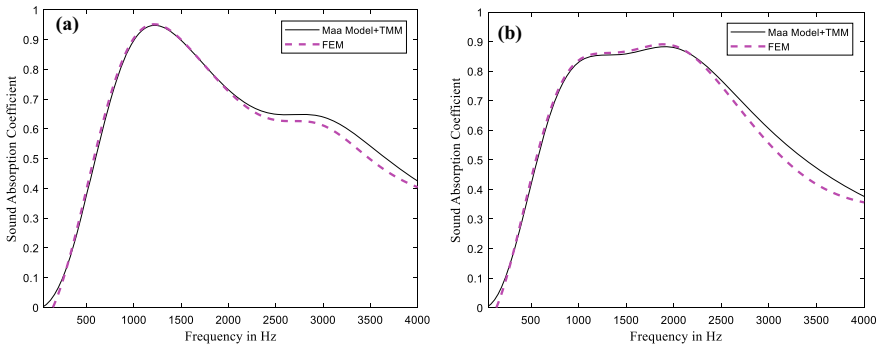
Fig. 8 Comparison of sound absorption of DMPP absorbers with unequal D ($D_1 = 20$mm, $D_2 = 10$ mm) obtained through theoretical (Maa model and TMM) and FE method **a** DMPP absorber ($d_{1st} = d_{2nd} = 0.2$ mm, $\Phi_{1st} = \Phi_{2nd} = 3\%$) **b** DMPP absorber ($d_{1st} = d_{2nd} = 0.2$ mm, $\Phi_{1st} = 3\%$, $\Phi_{2nd} = 1\%$)

Fig. 9 Variation of SPL along the DMPP absorber with equal and unequal D ($D_1 = 20$ mm, $D_2 = 10$ mm) **a** DMPP absorber ($d_{1st} = d_{2nd} = 0.2$ mm, $\Phi_{1st} = 3\%$, $\Phi_{2nd} = 1\%$, $D_1 = D_2 = 15$ mm) **b** DMPP absorber ($d_{1st} = d_{2nd} = 0.2$ mm, $\Phi_{1st} = \Phi_{2nd} = 3\%$, $D_1 = 20$ mm, $D_2 = 10$ mm)

have better acoustic performance compared to the individual MPP absorbers. The sound absorption results of the DMPP absorber with different configurations obtained thr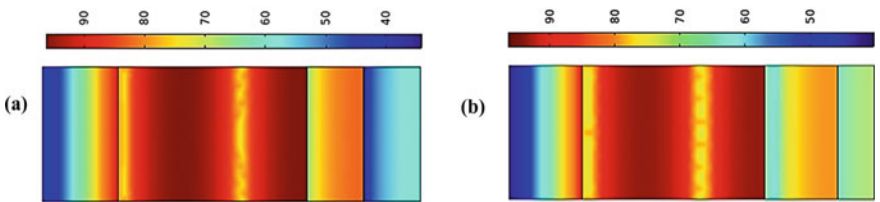ough FEA and theoretical methods show excellent agreement. Therefore, FEA can be used as an effective tool to analyze and validate the theoretical models of multi-layer and composite MPP absorbers.

References

1. Maa D-Y (1998) Potential of microperforated panel absorber. J Acoust Soc Am 104:2861–2866. https://doi.org/10.1121/1.423870
2. Sakagami K, Morimoto M, Koike W (2006) A numerical study of double-leaf microperforated panel absorbers. Appl Acoust 67:609–619. https://doi.org/10.1016/j.apacoust.2005.11.001
3. Sakagami K, Morimoto M, Yairi M (2009) A note on the relationship between the sound absorption by microperforated panels and panel/membrane-type absorbers. Appl Acoust 70:1131–1136. https://doi.org/10.1016/j.apacoust.2009.03.003
4. Maa D-Y (1975) Theory and design of micro perforated-panel sound-absorbing construction. Sci Sin 18:55–71. https://doi.org/10.1360/YA1975-18-1-55
5. Maa DY (1987) Microperforated panel wideband absorbers. Noise Control Eng. J. 29:77–84. https://doi.org/10.3397/1.2827694
6. Sakagami K, Nakamori T, Morimoto M, Yairi M (2009) Double-leaf microperforated panel space absorbers: a revised theory and detailed analysis. Appl Acoust 70:703–709. https://doi.org/10.1016/j.apacoust.2008.09.004
7. Bucciarelli F, Malfense Fierro GP, Meo M (2019) A multilayer microperforated panel prototype for broadband sound absorption at low frequencies. Appl Acoust 146:134–144. https://doi.org/10.1016/j.apacoust.2018.11.014
8. Gai XL, Xing T, Li XH, Zhang B, Wang F, Cai ZN, Han Y (2017) Sound absorption of microperforated panel with L shape division cavity structure. Appl Acoust 122:41–50. https://doi.org/10.1016/j.apacoust.2017.02.004
9. Kumar D, Amiya A, Mohanty R (2023) Broadband sound absorption technique using micro——perforated panel absorber with perforated extended panel. J Vib Eng Technol. https://doi.org/10.1007/s42417-023-00855-2
10. Mosa AI, Putra A, Ramlan R, Prasetiyo I, Esraa AA (2019) Theoretical model of absorption coefficient of an inhomogeneous MPP absorber with multi-cavity depths. Appl Acoust 146:409–419. https://doi.org/10.1016/j.apacoust.2018.11.002
11. Liu J, Herrin DW (2010) Enhancing micro-perforated panel attenuation by partitioning the adjoining cavity. Appl Acoust 71:120–127. https://doi.org/10.1016/j.apacoust.2009.07.016
12. Zhao XD, Yu YJ, Wu YJ (2016) Improving low-frequency sound absorption of micro-perforated panel absorbers by using mechanical impedance plate combined with Helmholtz resonators. Appl Acoust 114:92–98. https://doi.org/10.1016/j.apacoust.2016.07.013
13. Gai XL, Xing T, Li XH, Zhang B, Cai ZN, Wang F (2018) Sound absorption properties of microperforated panel with membrane cell and mass blocks composite structure. Appl Acoust 137:98–107. https://doi.org/10.1016/j.apacoust.2018.03.013
14. Gai XL, Xing T, Li XH, Zhang B, Wang WJ (2016) Sound absorption of microperforated panel mounted with helmholtz resonators. Appl Acoust 114:260–265. https://doi.org/10.1016/j.apacoust.2016.08.001
15. Liu Z, Zhan J, Fard M, Davy JL (2017) Acoustic properties of multilayer sound absorbers with a 3D printed micro-perforated panel. Appl Acoust 121:25–32. https://doi.org/10.1016/j.apacoust.2017.01.032
16. Liu Z, Zhan J, Fard M, Davy JL (2017) Acoustic measurement of a 3D printed micro-perforated panel combined with a porous material. Meas J Int Meas Confed 104:233–236. https://doi.org/10.1016/j.measurement.2017.03.032

17. Song BH, Bolton JS (2000) A transfer-matrix approach for estimating the characteristic impedance and wave numbers of limp and rigid porous materials. J Acoust Soc Am 107:1131–1152. https://doi.org/10.1121/1.428404
18. Zou J, Shen Y, Yang J, Qiu X (2006) A note on the prediction method of reverberation absorption coefficient of double layer micro-perforated membrane. Appl Acoust 67:106–111. https://doi.org/10.1016/j.apacoust.2005.05.004
19. Carbajo J, Ramis J, Godinho L, Amado-Mendes P (2019) Perforated panel absorbers with micro-perforated partitions. Appl Acoust 149:108–113. https://doi.org/10.1016/j.apacoust.2019.01.023
20. Meng H, Galland MA, Ichchou M, Bareille O, Xin FX, Lu TJ (2017) Small perforations in corrugated sandwich panel significantly enhance low frequency sound absorption and transmission loss. Compos Struct 182:1–11. https://doi.org/10.1016/j.compstruct.2017.08.103
21. Verdière K, Panneton R, Elkoun S, Dupont T, Leclaire P (2013) Transfer matrix method applied to the parallel assembly of sound absorbing materials. J Acoust Soc Am 134:4648–4658. https://doi.org/10.1121/1.4824839
22. Taban E, Soltani P, Berardi U, Putra A, Mousavi SM, Faridan M, Samaei SE, Khavanin A (2020) Measurement, modeling, and optimization of sound absorption performance of Kenaf fibers for building applications. Build Environ 180:107087. https://doi.org/10.1016/j.buildenv.2020.107087
23. Stinson MR, Shaw EAG (1985) Acoustic impedance of small, circular orifices in thin plates. J Acoust Soc Am 77:2039–2042. https://doi.org/10.1121/1.391776
24. Melling TH (1973) The acoustic impendance of perforates at medium and high sound pressure levels. J Sound Vib 29:1–65. https://doi.org/10.1016/S0022-460X(73)80125-7
25. Tayong R, Dupont T, Leclaire P (2011) Experimental investigation of holes interaction effect on the sound absorption coefficient of micro-perforated panels under high and medium sound levels. Appl Acoust 72:777–784. https://doi.org/10.1016/j.apacoust.2011.04.011
26. Fok VA (1941) Theoretical research of the conductivity of a round aperture in a partition across a pipe. Doklady akademii nauk, SSSR

Electric Vehicle Battery Pack Prediction of Capacity Degradation Based on Deep Learning Architecture and Internet of Things

Maharshi Singh and K. Janardhan Reddy

Abstract As electric cars (EVs) become more widespread, research into battery life is becoming highly significant. Electric car batteries are now constantly connected and transmit information on a massive scale. The huge amounts of data produced, quite apart from the widespread use of the internet by these battery packs, provide new challenges for researchers and regulators. A unique deep learning model with use of internet of things (IoT) is suggested in this paper to produce a universal and accurate Li-ion battery aging prediction. On the other hand, deep learning (DL) is an efficient strategy for handling IoT problems including data analysis, prediction, and categorization. However, it is challenging to get the best data for deep learning in IoT for real-time prediction. The accuracy and robustness of prediction will be determined by data collecting components such as sensors and cameras. In this article, deep learning model Long Short-Term Memory (LSTM) method is used to training and testing of the deep learning architecture. Root Mean Square Error (RMSE) value for the deep learning model is 0.69, which will accurately predict vehicle battery pack data. Numerous articles have been published on improving deep learning models for RUL estimate of battery packs; however, there is no research of capacity degradation of battery pack estimation using IoT and deep learning approaches in the literature. In this research, a strategy for estimating the RUL of an electric car battery pack is described using deep learning and IoT.

Keywords Electric vehicle battery pack · Internet of things · Discharge pattern · Real-time alert · End of life · Deep learning

M. Singh · K. J. Reddy (✉)
School of Mechanical Engineering, Vellore Institute of Technology, Chennai Campus 600127, India
e-mail: kjanardhanreddy@vit.ac.in

1 Introduction

Throughout the modern era, there have been many shifts in the automobile industry, with every manufacturer making strides in vehicle production and moving increasing inclination for automated vehicle ecosystems [1]. With the scarcity of fossil fuels and the pressing need to address environmental and energy concerns, electric vehicles (EVs) represent a better means of mobility. Electric vehicles are competitive with gasoline and diesel in terms of economy, speed, and driving range. In addition, these EVs benefit greatly from having an additional energy supply option, especially when covering long distances [2]. Electric vehicles (EVs) are becoming more popular for several reasons. They include declining costs and increased attention to climate change and environmental concerns. As the battery is a crucial component of electric vehicles, the life left in the battery pack needs to be determined. Many resources have been spent to encourage and develop the move from conventional gasoline or diesel (ICE)-based cars to EVs due to the potential for substantial energy savings and seamless integration with renewable smart power grids [3]. The use of lithium-ion batteries and the accompanying battery management technology has become more widespread in the context of electric vehicles due to their numerous advantages over other types of batteries [4, 5]. Due to its special characteristics, a battery management system (BMS) is required to keep track the battery's vital parameters and keep it in check when it is being charged and discharged [6]. The BMS's primary function is to control and supervise battery operations including charge and discharge cycles, guarantee battery health, and lessen the likelihood of battery damage so that vehicles may run on their stored energy [2]. The BMS circuit was employed to keep an eye on the battery's vitals throughout operation, such current, voltage, temperature, charging, and discharging. Measuring health of battery pack, it evaluates energy levels, state of charge and state of health [7].

A cell's state of charge represents the current capacity as a percentage of the maximum possible capacity (SOC). Values of SOC might be anything from 0 to 100%. Hundred percent SOC signifies a fully charged battery, whereas 0% means the battery is dead. As it is not allowed for the SOC to go beyond 50% in real-world scenarios, the cell is charged whenever the SOC drops below 50%. The maximum SOC of a cell also declines with aging. Based on these results, it is feasible to infer that a healthy cell's 75%–80% SOC is similar to an elderly cell's 100% SOC. An accurate estimation of the battery's state of charge (SOC) is essential for effective battery management. It works well for characterizing the real energy level of the battery. The state of charge (SOC) must be evaluated not only to estimate the energy available from the battery but also to calculate the expected lifespan of the battery. Battery SOC may be determined in a number of ways, the vast majority of which depend on the battery's electrochemical properties and the actual loading conditions. Integration of real-time loading conditions with battery electrochemical properties may provide an estimate of battery SOC. The SOC estimation approach should not be reliant on the battery's starting condition to avoid battery relaxing time in real-time loading circumstances. Accurate SOC estimate has long been a significant topic

in BMS. Accurate assessments may be used to determine a battery's reliability and provide useful information, such how much life is left in the pack [8]. SOC is a measure of the battery's remaining capacity and may be used to estimate an EV's potential range. This feature also safeguards the Li-ion battery from being overcharged or drained [9]. The performance of a Li-ion battery may change depending on factors including how old it is, how hot or cold it is, and how often it is charged and discharged. This is because the battery's electrochemical scheme is time-varying, very complex, and nonlinear. Because of this inability of physical sensors to provide instantaneous feedback, estimating the SOC of Li-ion batteries is a difficult task [10]. Li-ion battery SOC estimation has been an active area of study in recent years. Several engineering fields make use of optimization algorithms to better a system's or process's performance [10].

Compared to SOC estimate, battery SOH estimation and RUL prediction have less published works. Battery RUL forecasting is complicated by the ongoing disagreement about the idea of SOH. Power, on the other hand, is a sign of how quickly electricity can be provided, while capacity indicates how much energy can be stored. Each one represents a different aspect of the battery's overall condition. Both capacity and power fading were used by Pattipati et al. [11]. Despite the recent presentation of a novel health indicator by Liu et al. [12] based on visible characteristics rather than battery properties, further evidence of its usefulness is required. A battery is considered to be at its end of life (EOL) when its full-charge capacity (FCC) falls below a particular percentage of its rated capacity (typically 20–30%) [13, 14]. Determining the SOH's k-step-ahead forecast and then translating capacity estimates into time-to-end-of-life (EOL) [13] are required steps toward predicting the RUL using the SOH.

Electric vehicle (EV) battery management systems (BMSs) are challenging to design (SOH) due to the frequency with which they communicate the battery's state of charge (SOC) and health. Establishing its k-step-ahead projection and converting capacity estimates to time-to-EOL are required to predict the RUL from the SOH [14, 15]. Electric vehicles need a reliable method of estimating the battery's charge and condition in real time due to the fact that overcharging and draining predictably degrade batteries. Specifically, our proposed model provides an optimizer for IoT-based EVs' battery management system that makes use of deep learning.

2 Deep Learning

The initial deep learning concept was proposed by Hinton et al. in 2006 [16], when they developed a deep neural network (DNN). Many fields have seen success using DL, including natural language processing [17], image retrieval [18], picture identification [19], search engines [20], and information retrieval [21]. The purpose of creating DL methods is to break free from the limitations of conventional methodologies. Nonetheless, DL systems benefit greatly from their deep architecture and supervised or unsupervised learning methodologies [22, 23]. The capability of DL

methods to uncover previously unseen patterns in data is one of its most potent strengths. The model may take into account features from all levels because of DL's interconnection between the current and prior layers.

For the input layer to function properly, some neurons must be kept around to represent inputs as vectors, create weight vectors, and send those weight vectors on as output. Neurons in the hidden layer take the output of the preceding layer as input, processing it through filtering and a feature map, for example. Transfer of the generated data to the last layer is crucial. The output layer gathers the information from the final hidden layer and uses it to make predictions, perform classifications, and calculate a loss function based on successful and unsuccessful predictions using optimization techniques.

2.1 Convolutional Neural Network

Recognition, classification, detection, and prediction are all areas where convolutional neural networks (CNNs) find use. When trained in parallel for a predictive modeling purpose, convolutional neural networks have the potential to automatically learn a huge number of abstract features [24].

2.2 Recurrent Neural Network (RNN)

The phrase "deep learning" is sometimes used interchangeably with "machine learning;" however, a recurrent neural network (RNN) is a part of a neural network that is trained on data collected over time. Because of its architecture, RNNs are utilized for tasks such as natural language processing (NLP), speech recognition, and picture captioning, all of which need real-time processing. Consequently, the output of the final (output) layer is reliant on the input of the first (input) layer [24].

2.3 Long Short-Term Memory (LSTM)

Long Short-Term Memory (LSTM) is a deep learning paradigm for recurrent neural networks. Each neuron in an LSTM is equipped with a memory cell that can be used to link up with other neurons for the purposes of storing information and providing feedback during training.

2.4 Autoencoders (AEs)

With an autoencoder neural network, the target values match the inputs and the network learns features unsupervised via backpropagation. AEs create a reconstructing side from a reduced encoding of a representation as near to the original input.

2.5 Generative Adversarial Networks (GANs)

The generative adversarial network (GAN) is a paradigm for deep learning presented by Goodfellow et al. [26]. New images are generated using GANs using the concept of minimax games and generative and discriminative networks. Discriminative networks' principal function is to separate input data from generative network output. In several domains, including as NLP and image processing, GANs have shown to be quite effective.

2.6 Restricted Boltzmann Machine

A Restricted Boltzmann machines (RBMs) are a kind of deep learning model with two layers of generative stochastic computation. Like other Boltzmann machines, RBM relies on chance and full interconnection between neurons of different layers to achieve its results. Whereas other deep learning models used techniques like feedforward and backpropagation, RBMs depended on autoencoder characteristics.

2.7 Deep Belief Network

As a probabilistic and generative model with several layers of stochastic latent variables, deep belief networks (DBNs) are utilized in deep learning. Classification, recognition, and other difficult issues are only some of the many applications for deep belief networks [27].

As was previously established, the utility of any given deep learning model is context-dependent. For instance, because of its architecture, CNN is optimized for image problems but struggles when applied to NLP issues. The RNN and LSTM are the preferred models for time-series problems like NLP due of their Backpropagation Through Time (BPTT) and usage of memory cells. Yet AEs have specialized in signal–noise challenges thanks to their development of coding and decoding. In addition, GAN is widely used as a generative model in the entertainment industry. On top of that, RBM and DBN excel at recognition jobs and hard problems. A
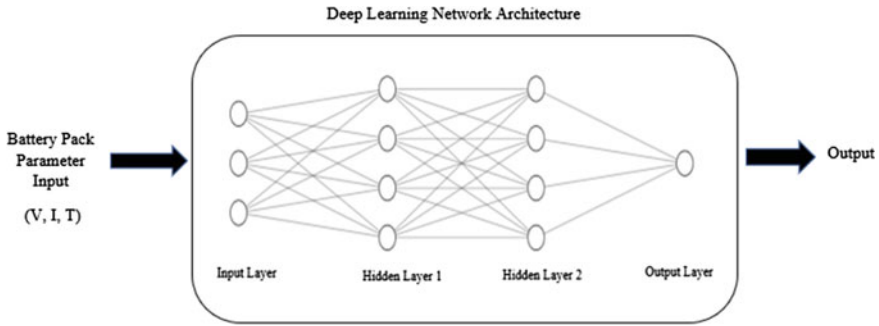
Deep Learning Network Architecture

Fig. 1 Deep learning network architecture for battery pack

generalized deep learning architecture is shown in Fig. 1. Inputs include voltage, current, and temperature, while the network itself consists of two discrete layers. These hidden layers are linked to the deep learning network's subsequent output.

3 IoT and Its Applications

Adding sensors and other technologies to ordinary things enables them to become "smart," allowing them to share information with one another and produce new kinds of data in the so-called "Internet of Things" [28]. The IoT paradigm, in its simplest form, refers to the use of a broad variety of communication architectures to interconnect a large number of previously unconnected items and systems [28]. Every high-tech device needs sensors to gather information and a communication protocol to send it.

3.1 Sensors and Gateways

The sensing layer is made up of several sensors (physical objects) that gather and interpret data in real time from a wide range of sources, including images, voltage, temperature, and current. Because of their low computational capacity, IoT sensors might be a hindrance despite their main goal of producing and disseminating data [16]. The exponential growth of IoT devices and the massive amounts of data they produce presents new obstacles, such as the question of how to practically analyze this data in real time.

Due to the sensor's limited storage capacity, this data must be transmitted after the data produced by the preceding layer. Nevertheless, these gadgets cannot reach their targets without being linked to them. As a network router, the IoT gateway facilitates communication between IoT gadgets and the cloud.

3.2 IoT-Enabled Cloud Platforms

Now that there are so many cheap and readily available sensors, the battery pack and other vehicle components may generate enormous volumes of data [18]. Vehicle actions need to be connected to the digital world before these data sources may be used. Meaning that acquiring, networking, and digitally storing RUL data is essential for analysis. Commercially accessible IoT solutions like GE's Predix, ABB's Ability, Siemens's MindSphere, Schneider Electric's EcoStruxure Platform, and Honeywell's Forge may help data centers make better use of big data.

Amazon Web Services (AWSs), Microsoft Azure, Google Cloud, Oracle, and IBM's IoT platforms are just a few cloud service providers that provide functionalities that may be put to use in a wide range of contexts. Distributed computing, big data analytics solutions, data and device management tools, and a plethora of other services are often bundled into a cloud system's offering in addition to M2M communication capabilities.

3.3 Internet of Things-Based End-To-End Big Data Analytics Platform for Battery Pack

The proposed solution takes a data-centric approach to creating a reference architecture that is safe, open, robust, and extensible. It aims to be a practical place where businesses of all sizes, from multinationals to start-ups, may experiment with and improve their processes, products, and services at little cost. There are five main layers to the structure:

(1) Control and sensing layer.
(2) Data collection layer.
(3) Data integration layer.
(4) Data layer for analytics and storage.
(5) Data presentation layer.

3.3.1 Control and Sensing Layer

Sensors, actuators, tags, machines, controllers, and gadgets are all included under the umbrella word "things" in the internet of things. All of them have one thing in common: They provide rich information for tracking performance and assessing reliability. All current, voltage, and temperature readings, as well as all data from sensors and controllers, are part of this layer's raw data. It is the starting point of the economic process.

3.3.2 Data Collection Layer

The machinery and controls that make up a modern manufacturing line are complex. For a versatile and adaptable setup, it may be necessary to use components from many brands, such as programmable logic controllers (PLCs) and energy monitoring sensors. Because of proprietary protocols, networking needs in these configurations are more difficult. The significance of implementing this layer resides in its capacity to optimize the quantity of data to be absorbed while also offering data encryption and safe endpoints for inter-layer communication.

3.3.3 Data Integration Layer

The internet of things expands current battery pack operating technology networks. The procedures used in a conventional operational technology environment are likely to vary from those employed in current working contexts. The communication protocol and message format of battery packs must be standardized in accordance with the application programming interfaces and databases for the operational technology to converge.

3.3.4 Data Layer for Analytics and Storage

The data sent by battery packs is often urgent, semi-structured, and transferred in bulk while having very modest payloads. For this reason, the platform uses Influx DB, a free and open-source database designed specifically for time-series data. This allows for the efficient storage of all battery-related metrics and events. It allows for clustering, has adaptable data modeling, is horizontally scalable, and has a high availability.

3.3.5 Data Presentation Layer

This layer consists of a multi-platform, open-source data visualization web application. The platform has dynamic and adaptable online user interfaces, a variety of visualization options, and a streamlined system for user identification and access control.

4 Proposed Architecture of Deep Learning Prediction and IoT Applications

Now, every vehicle has a lot of sensors on it to keep track of its condition at all times. The most expensive part of an electric car is the battery. So, the status of the battery pack needs to be checked all the time. With the help of deep learning, Amazon Web Services' (AWSs) cloud platform, and the EcoStruxure platform, this research article creates an architecture for continuous monitoring of electric vehicle battery packs.

The vehicle battery pack is outfitted with various sensors that will collect data in real time. This information is collected by the battery management system (BMS). BMS will use the data gathered to restore the battery pack to normal operation. The cloud server has access to the battery pack dataset provided by the battery pack manufacturer. This dataset will be used to send instructions to the BMS via the internet. The data collected by the BMS from various sensors attached to the vehicle is very large in this proposed architecture. So, the EcoStruxure platform is used to separate all information collected by BMS and take data related to voltage, current, and temperature. This data is sent to an AWS cloud server, where it is compared to data provided by the battery pack manufacturer. On that basis, it will forecast the battery pack's real-time status. This real-time status is communicated to BMS, and BMS will alert the vehicle driver on the vehicle dashboard, as shown in Fig. 2.

This prediction of battery pack capacity degradation is based on the dataset provided by the manufacturer. Only voltage, current, and temperature data are used for prediction in this proposed architecture because these are the only parameters that directly affect battery pack capacity. In this configuration, if the battery pack capacity falls below 95%, an instruction is sent by cloud server to the BMS to visit a service center for corrective maintenance. This data will be communicated to the vehicle's driver. Similarly, if capacity is less than 95% but greater than 80%, the cloud server
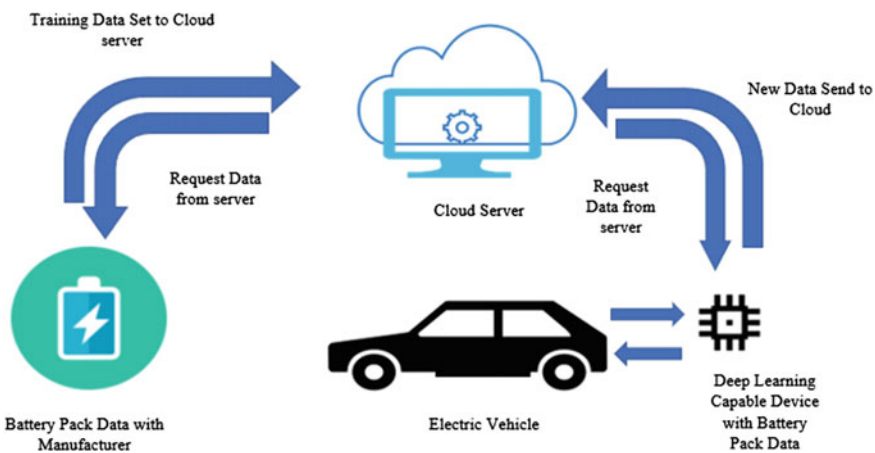

Fig. 2 Electric vehicle battery pack internet of things and deep learning architecture

will send information to the driver to visit a nearby service station for preventive maintenance and will also recommend a nearby service station, as shown in Fig. 3. If the battery pack capacity falls below 80%, the cloud server will notify the driver and recommend a nearby battery pack recycling center. This continuous monitoring of battery pack data will help to avoid the condition of battery pack failure and will improve battery pack life span by suggesting timely preventive maintenance.

Deep learning is used to validate the proposed setup. This deep learning method will work best with IOT to predict battery pack capacity depletion. This result of the generalized deep learning method will save space on cloud servers. This will aid in the prediction of capacity fade patterns in any vehicle battery pack.
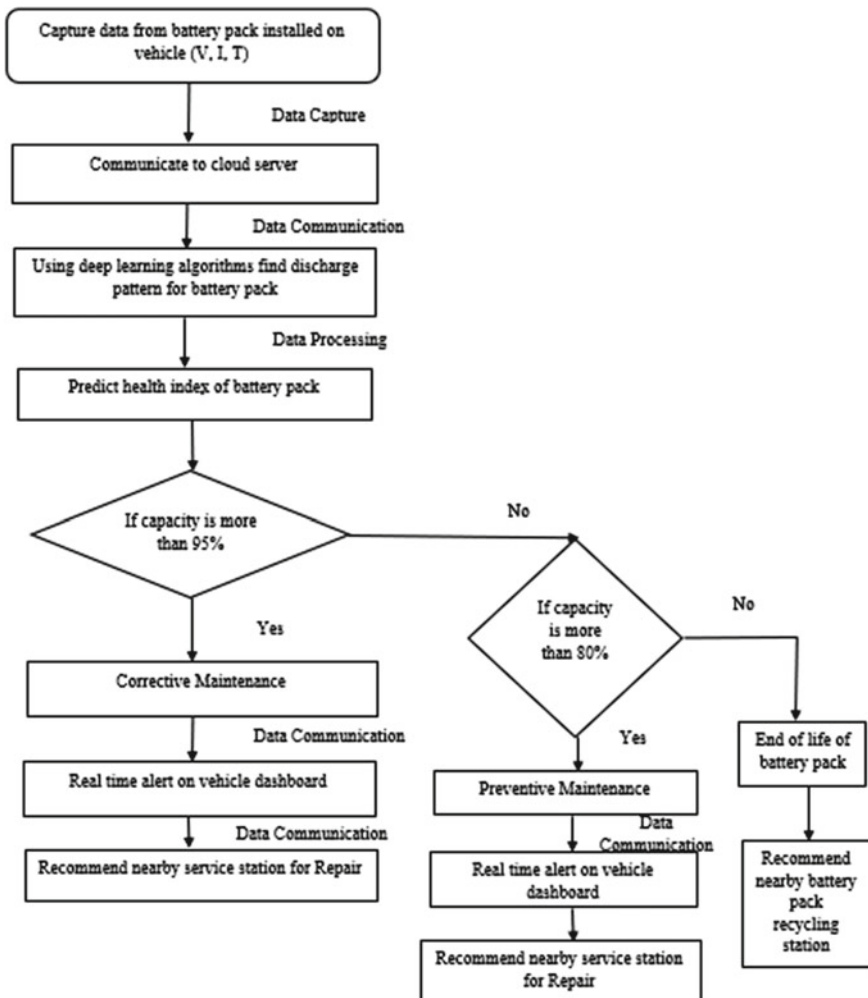

Fig. 3 Proposed flowchart by internet of things real-time monitoring of electric vehicle battery
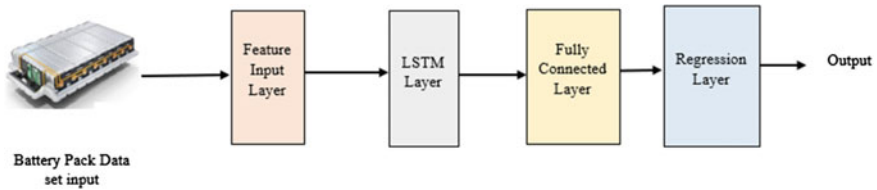
Fig. 4 LSTM deep learning model for battery pack capacity data prediction

The Long Short-Term Memory (LSTM) approach is used in the deep learning (DL) method. For deep learning approach ARB new energy battery pack data is used for training and testing of deep learning models. In the experiment, a battery pack with the specifications 28V, 30Ah is used. Temperature in the lab is kept constant at 40 degrees Celsius. At 1C, the battery pack is operated thoroughly. This dataset is used in the development of a DL model. DL models are created using the MATLAB software. The deep network designer app in MATLAB is used to create an LSTM model. Four layers are used in the LSTM approach to predict battery pack capacity fade. Figure 4 depicts the feature input layer, LSTM layer, fully connected layer, and regression layer. Seventy percent of the dataset is used for training in deep learning, while the remaining thirty percent is used for model validation. Take the feature input size to be 1, the number of hidden layers to be 50, the validation frequency to be 50, and the number of epochs to be 250 in the deep learning model. After validating the model, the RMSE value is 0.69972, and the loss is less than 1%, as shown in Fig. 5a, b. This demonstrates that the LSTM deep learning model accurately predicts battery pack behavior and, as a result, provides alerts to the driver.

This deep learning LSTM method could be used for any vehicle battery pack. That result will be saved on cloud server, so when input from any vehicle could receive to the cloud server, it can send retime alert to driver.
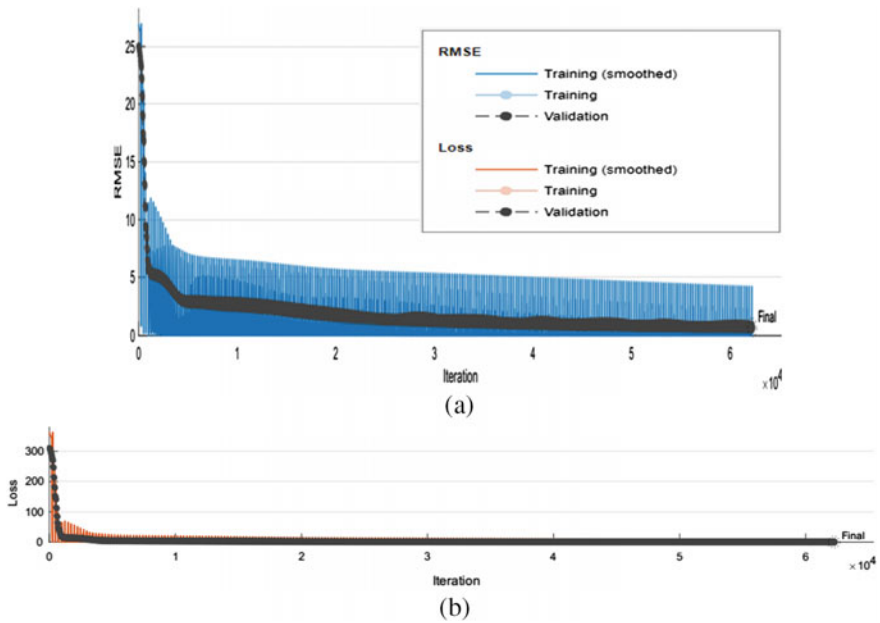
Fig. 5 LSTM deep learning model results **a** plot between number of iterations and root mean square error of model, **b** plot between loss and number of iterations during validation of model

5   Conclusion

The issue would be that developing an IoT and deep learning-based architecture for predicting the capacity degradation pattern of the batteries in electric vehicles requires a large upfront expenditure. This will take the shape of modifications to the vehicle and the creation of data centers for monitoring and forecasting the state of the battery pack in real time. A more accurate forecast of the battery pack's state will be advantageous to both the user and the manufacturer. The prediction of battery pack degradation is done by LSTM method which have RMSE value 0.69972 for 250 epochs and learning rate is 0.001. This model can predict any vehicle running time battery pack data and provide real-time alerts to vehicle driver by use of Amazon Web Service. This will be useful for recycling the battery pack and doing preventative maintenance. As batteries are an expensive component of electric vehicles, some of the old battery material may be recycled and utilized for making new batteries. Also, it helps in lowering the price of a new battery pack.

6 Future Work

The author of this paper attempts to estimate the electric vehicle battery pack's capacity degradation pattern. It will be beneficial in finding cost-effective methods to utilize (for other application) and recycle the battery pack. There is a lot of potential for future research because of the lack of data availability from battery pack manufacturers and the growing speed of internet.

References

1. Guo L, Yang B, Ye J (2021) Detection and diagnosis of long-term cyber-attacks for predictive energy management system in hevs. In: 2021 IEEE applied power electronics conference and exposition (APEC), June, IEEE, pp 842–848
2. Tudoroiu N, Zaheeruddin M, Tudoroiu RE (2020) Real time design and implementation of state of charge estimators for a rechargeable lithium-ion cobalt battery with applicability in HEVs/EVs—a comparative study. Energies 13(11):2749
3. Verma S, Mishra S, Gaur A, Chowdhury S, Mohapatra S, Dwivedi G, Verma P (2021) A comprehensive review on energy storage in hybrid electric vehicle. J Traffic and Transport Eng (English Edition) 8(5):621–637
4. Ding N (2020) Energy management system design for plug-in hybrid electric vehicle based on the battery management system applications (Doctoral dissertation, Auckland University of Technology)
5. Murugandhan D, Valli R, Senthilkumar N, Arunmozhi S (2021) Enhancement of energy storage capacity in lithium polymer batteries incorporated with zirconium oxide nano powders. Mater Today: Proc 37:1313–1319
6. Jiang J, Jiang Q, Chen J, Zhou X, Zhu S, Chen T (2021) Advanced power management and control for hybrid electric vehicles: a survey. Wirel Commun Mob Comput 2021:1–12
7. Lim H, Su W (2018) Hierarchical energy management for power-split plug-in HEVs using distance-based optimized speed and SOC profiles. IEEE Trans Veh Technol 67(10):9312–9323
8. Jiaqiang E, Zhang B, Zeng Y, Wen M, Wei K, Huang Z, Deng Y (2022) Effects analysis on active equalization control of lithium-ion batteries based on intelligent estimation of the state-of-charge. Energy 238:121822
9. Zheng C, Tian X, Nie G, Yu Y, Li Y, Dong S, Xiong B (2020) State of power and state of charge estimation of vanadium redox flow battery based on an online equivalent circuit model. In: 2020 IEEE 18th international conference on industrial informatics (INDIN), July, vol 1. IEEE, pp 633–638
10. Vasanthkumar P, Revathi AR, Devi GR, Kavitha RJ, Muniappan A, Karthikeyan C (2022) Improved wild horse optimizer with deep learning enabled battery management system for internet of things-based hybrid electric vehicles. Sustain Energy Technol Assess 52:102281
11. Pattipati B, Sankavaram C, Pattipati K (2011) System identification and estimation framework for pivotal automotive battery management system characteristics. IEEE Trans Syst Man Cybernet Part C (Appl Rev) 41(6):869–884
12. Liu D, Wang H, Peng Y, Xie W, Liao H (2013) Satellite lithium-ion battery remaining cycle life prediction with novel indirect health indicator extraction. Energies 6(8):3654–3668
13. He W, Williard N, Osterman M, Pecht M (2011) Prognostics of lithium-ion batteries based on Dempster-Shafer theory and the Bayesian Monte Carlo method. J Power Sour 196(23):10314–10321
14. Saha B, Goebel K, Poll S, Christophersen J (2008) Prognostics methods for battery health monitoring using a Bayesian framework. IEEE Trans Instrum Meas 58(2):291–296

15. Ng SS, Xing Y, Tsui KL (2014) A naive Bayes model for robust remaining useful life prediction of lithium-ion battery. Appl Energy 118:114–123

16. Sethi P, Sarangi SR (2017) Internet of things: architectures, protocols, and applications. J Electri Comput Eng

17. Otter DW, Medina JR, Kalita JK (2020) A survey of the usages of deep learning for natural language processing. IEEE Trans Neural Netw Learn Syst 32(2):604–624

18. Saritha RR, Paul V, Kumar PG (2019) Content based image retrieval using deep learning process. Clust Comput 22:4187–4200

19. Pak M, Kim S (2017) A review of deep learning in image recognition. In: 2017 4th international conference on computer applications and information processing technology (CAIPT), August, IEEE, pp 1–3

20. Gupta M, Kumar N, Singh BK, Gupta N (2021) NSGA-III-Based deep-learning model for biomedical search engines. Math Probl Eng 2021:1–8

21. Schmidhuber J (2015) Deep learning in neural networks: an overview. Neural Netw 61:85–117

22. Hinton GE, Srivastava N, Krizhevsky A, Sutskever I, Salakhutdinov RR (2012) Improving neural networks by preventing co-adaptation of feature detectors. arXiv preprint arXiv:1207.0580

23. Khelili MA (2022) Deep Learning and parallelization of meta-heuristic methods for IoT cloud (Doctoral dissertation, Université de mohamed kheider biskra)

24. Agarap AF (2018) Deep learning using rectified linear units (relu). arXiv preprint arXiv:1803.08375

25. Pascanu R, Gulcehre C, Cho K, Bengio Y (2013) How to construct deep recurrent neural networks. arXiv preprint arXiv:1312.6026

26. Dai B, Fidler S, Urtasun R, Lin D (2017) Towards diverse and natural image descriptions via a conditional gan. In: Proceedings of the IEEE international conference on computer vision. pp 2970–2979

27. Navamani TM (2019) Efficient deep learning approaches for health informatics. Academic Press, In Deep learning and parallel computing environment for bioengineering systems, pp 123–137

28. Al-Fuqaha A, Guizani M, Mohammadi M, Aledhari M, Ayyash M (2015) Internet of things: a survey on enabling technologies, protocols, and applications. IEEE Commun Surv Tutorials 17(4):2347–2376

A 3D Location Estimating Model for Harvesting the Fresh Chili Fruit Using Yolov5

Quoc-Khanh Huynh, Van-Cuong Nguyen, Chi-Ngon Nguyen, Quang-Hieu Ngo, Huu-Cuong Nguyen, Phuong Lan Tran-Nguyen, Thanh-Thuong Huynh, and Hong-Phuc Vo-Nguyen

Abstract Chilies and their products have become popular in everyday life. However, in Vietnam today, their care and harvesting of them are done mainly by manual methods. As a part of the project to develop an automatic harvesting robot, this research focuses on detecting and locating chili fruits in three-dimensional space. First, the Yolov5 model is fine-tuned and trained to detect the fresh chili fruit object. Then, a stereo camera is used to capture an image and determine the disparity of the fruits in the left/right images using matching methods. The distance and 3D location are estimated by the triangle method via the disparity. In addition, an image calibration method is also implemented to obtain the camera's focal length parameters as well as to reduce the camera's fisheye effect, increasing estimation accuracy. The model can detect a chili at a size of 9.4×55 mm up to a distance of 600 mm and an

Q.-K. Huynh (✉) · V.-C. Nguyen · C.-N. Nguyen · Q.-H. Ngo · H.-C. Nguyen ·
P. L. Tran-Nguyen · T.-T. Huynh
College of Engineering, Can Tho University, Can Tho City, Viet Nam
e-mail: hqkhanh@ctu.edu.vn

V.-C. Nguyen
e-mail: nvcuong@ctu.edu.vn

C.-N. Nguyen
e-mail: ncngon@ctu.edu.vn

Q.-H. Ngo
e-mail: nqhieu@ctu.edu.vn

H.-C. Nguyen
e-mail: nhcuong@ctu.edu.vn

P. L. Tran-Nguyen
e-mail: tnplan@ctu.edu.vn

T.-T. Huynh
e-mail: thanhthuong@ctu.edu.vn

H.-P. Vo-Nguyen
School of Medicine, Can Tho University of Medicine and Pharmacy, Can Tho City, Viet Nam
e-mail: vnhphuc@ctump.edu.vn

image resolution of 480×480 pixels. In further studies, this position data will be transferred to the robotic arm to perform necessary operations such as harvesting and avoiding obstacles. The positioning accuracy as well as the ability to detect small fruits would be improved to enhance the working ability of the whole system.

Keywords 3D location model · Chili fruit · Yolov5

1 Introduction

Chili is very popular in Vietnam, especially in the Mekong Delta with certain large social-economic values [1, 2]. However, both the care and the harvesting process were done mainly by manual method. Following the trend of developing high-tech agriculture, it is necessary to automate the care and harvesting stages. And this research focuses on building a model for detecting and locating chili fruits in space for further automatic harvesting operations.

Yolov5 is a predefined object detection model which has been trained for 80 popular objects [3, 4]. In this study, it is retrained to detect the fresh chili fruit in Chi-Thien varieties, common varieties in the Mekong Delta (Fig. 1a). When the object is detected by the Yolov5 model, then matching method is used to determine the disparity of chili in left and right images [5]. And, the depth and location of the fruit could be estimated [6]. To increase accuracy during matching, the input images are calibrated to reduce curvature due to the fisheye effect of the camera [7–9]. Experimental results have evaluated the ability to identify chili peppers as well as location accuracy. This will be an important basis for further development of the robotic arm to support farming in future studies.
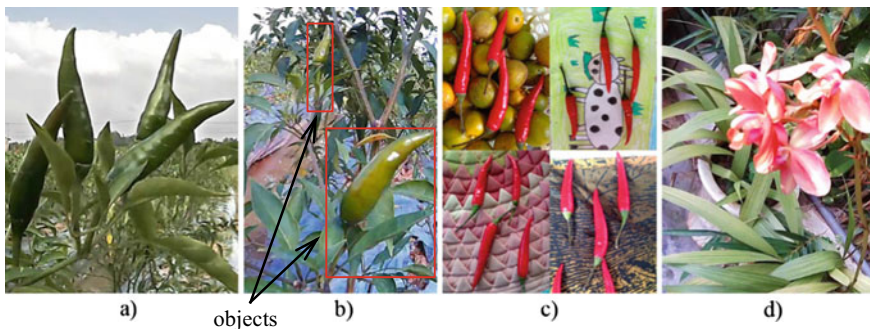

Fig. 1 Chili fruit **a** and training dataset **b–d**

2 Methods

2.1 The 3D Location Estimation Method

The location estimating model of chili is proposed as shown in Fig. 2. The 3D camera takes left and right images for calibrating. Then, the calibrated left image is checked to find the chili fruit by the Yolov5 model. If the fruit is detected, then its positions in the left image (X_L) are extracted; otherwise, the system will turn back to capture a new image. In case there is more than one fruit, the highest confidence objects will be processed.

As in Fig. 2, the chili object in the left image is matched to determine its position in the right image (X_R) [5]. The disparity d (pixel) in the X-direction is:

$$d = |X_R - X_L|. \tag{1}$$

The distance Z (mm) from the chili to the left camera in Z-direction is [9]:

$$Z = Z_{\text{coef}} \times \left(\frac{B \times f}{d} \right), \tag{2}$$

where $B = 62$ mm is the distance between two cameras of the 3D camera.

$f = 573$ mm is the focal length of the camera.

Z_{coef} is the conversion coefficient (pixel/mm).

The X and Y locations are estimated by:

$$X = \frac{X_{coef} \times X_L}{Z},$$
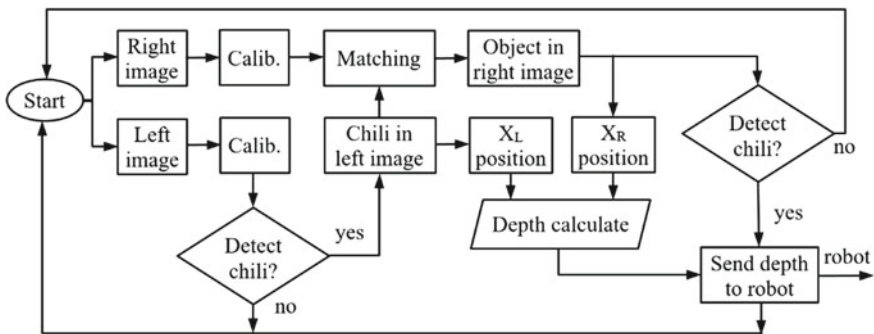$$Y = \frac{Y_{coef} \times Y_L}{Z}, \tag{3}$$

Fig. 2 Location estimation model of chili using Yolov5

where X and Y are the distances from the left camera to chili in millimeters.

X_L and Y_L are the distances from the left camera to chili in pixels.

X_{coef} and Y_{coef} are the conversion coefficients (mm^2/pixel).

After matching, the matched area of chili in the right image is extracted and checked by Yolov5. If this area is identified as chili with a certain confidence rate, the location data will be sent to the robot arm and the next cycle will be continued. Otherwise, the next loop will continue without sending the data to the actuator.

2.2 Custom Training of Yolov5 to Detect Chili Fruit

Training data acquisition

The training image is collected by using a camcorder to record at $1,280 \times 720$-pixel resolution, and then images are extracted and selected to scan objects by makesense.ai (Fig. 1b). In addition, to diversify the training object, a single chili fruit is placed on different backgrounds to collect training images (Fig. 1c).

Training process

The total number of training images is 4,800 with approximately 17,000 chili objects. The training and evaluation images are respectively 3,787 and 1,013. To eliminate false negatives, there are 600 images which are background (Fig. 1d), of which 470 images are for training and 130 images for evaluation. The initial number of training epochs is 300. The training process was performed on a Google Colab computer with a learning rate of 0.01. And the training is early stopping at 295 epochs after 6h45'.

Training results are shown in Fig. 3. Precision P, mAP50, and mAP50-95 are respectively achieved at 0.904, 0.772, and 0.452. From epoch 200, the precision and other training parameters have no significant improvement, and early stopping occurs at epoch 295.

2.3 Detection Test

To independently evaluate the ability to detect a chili object, a single fruit in size of $\Phi 9.4 \times 55$ mm was placed in front of the orange at a predetermined distance every 100 mm in the range of 100–1,000 mm (Fig. 4a). The detection is run with the camera resolution of 480×480 pixel. And the confidence rate is recorded to evaluate the detection ability of our current model. At each distance, the recognition process is performed 100 times, and thus there is a total of 1,000 testing times.
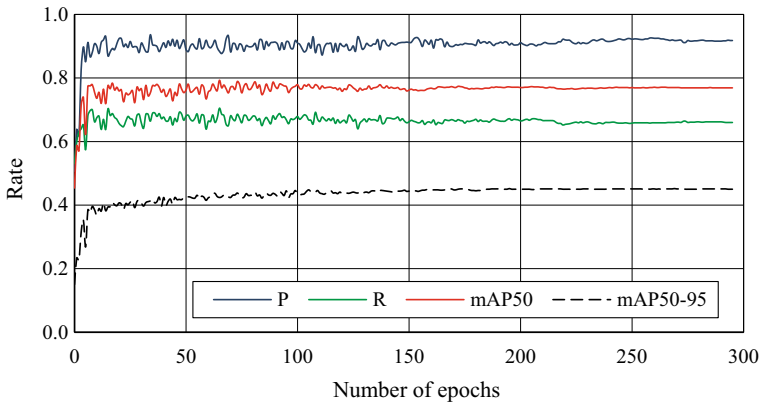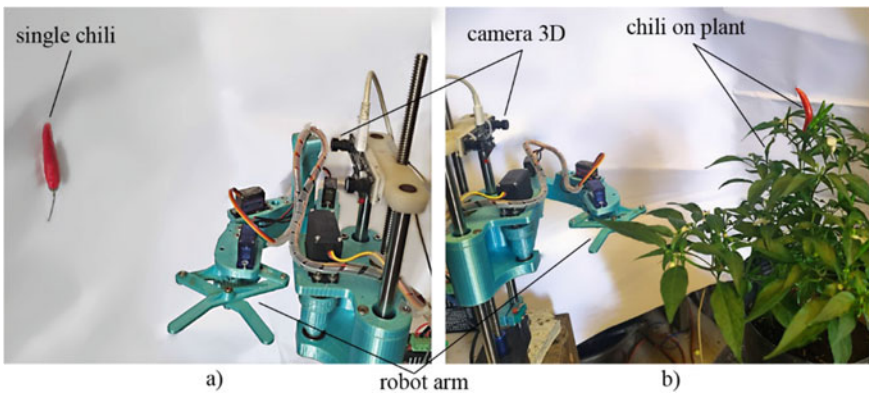
Fig. 3 Training results

Fig. 4 Detection test **a** and depth estimating test **b**

2.4 Location Calibration for 3D Camera

The disparity values on the image are in pixels, while the actual location is usually specified in millimeters or centimeters, so the conversion coefficients X_{coef}, Y_{coef}, and Z_{coef} need to be determined to calibrate the location values. The chili on a plant is placed in front of the camera at the exact location, and then the identification process is run with the initial value of $X_{\text{coef}} = Y_{\text{coef}} = Z_{\text{coef}} = 1$. The returned X, Y, and Z coordinates are recorded to calculate the coefficients X_{coef}, Y_{coef}, and Z_{coef} from Eqs. 2 and 3.

To determine Z_{coef}, detection experiments with single fruit (Fig. 4a) were performed at certain predefined distances: 100, 200, 300, 400, 500, 600, 700, and 800 mm. At each distance, the return value was recorded 40 times. From Eq. 2, the averaged value is: $Z_{\text{coef}} = (Z \times d)/(B \times f) = 0.9045 \, \text{pixel/mm}$.
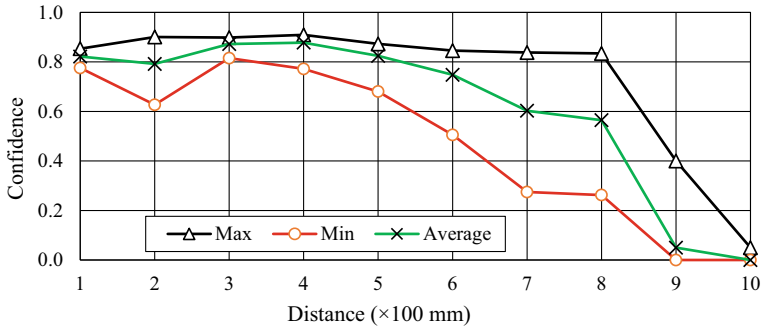
Fig. 5 Confidence coefficient in detection test of a single chili

For X_{coef} and Y_{coef}, based on the detection ability in Fig. 5, the calibration was executed only in the range of distance from 100 to 500 mm to obtain a confidence rate higher than 0.5. At each distance, the model is tested 40 times. From Eq. 3, the average result is calculated: $X_{coef} = Y_{coef} = 205$ mm^2/pixel.

The values of X_{coef}, Y_{coef}, and Z_{coef} will be used as constant factors during the location test in Section 3.2.

3 Results and Discussions

3.1 Detection Results of a Single Fruit

The results of the detection test are presented in Fig. 5. At a distance in the range of 100–500 mm, the stable confidence rate is stable, fluctuating around 0.8. It then drops to 0.748 at a distance of 600 mm, and around 0.6 at 700–800 mm. In the range of 100–700 mm, there is almost no false positive recognition, while at a distance of 800 mm, the false positive is approximately 18%.

As shown in Fig. 5, chili fruit is completely unrecognizable at the distance farther than 900 mm. And the confidence rate falls to lower than 0.1. This is supposed to be caused by the low resolution of the input image of 480×480 pixels which leads to a very small object (chili fruit) area to detect.

Another reason for being unrecognizable at a distance farer than 900 mm may be that the image is blurred due to the low light intensity. When the flashlight is used to lighten the object, the chili could be detected at a distance of 900–1000 mm. However, the confidence rate is relatively low, not exceeding 0.4, and the possibility of a false positive is high.

Figure 6 depicts an identification experiment performed in an environment with a complex background. The fruits on the plants are detected quite a lot, but in some cases when they are obscured or not fully viewed, the confidence rate is quite low.
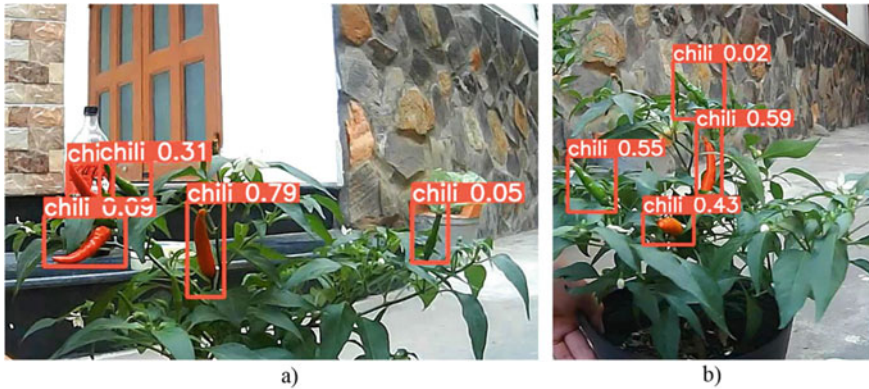
Fig. 6 Detection test on chili plant (extracted from video)

3.2 3D Location Test Results

As described in Fig. 7, the pre-calibrated image (Fig. 7a) is calibrated to reduce image curvature and detect the chili with the highest confidence rate in the left image (Fig. 7b). The object in the left image (Fig. 7b) is matched for finding similar one in the right image (Fig. 7c). Then, the disparity d is calculated for estimating the (X, Y, Z) positions. The object in the right image (Fig. 7c) must be detected again. If the confidence rate is high enough (≥ 0.5), an appropriate signal would be sent to the actuator.

In the previous detection experiment, chili was detected accurately at a confidence rate ≥ 0.5, so this value is chosen as the threshold to detect. As shown in Fig. 5, the testing distance should be ≤ 600 mm to accurately evaluate the location estimating ability. There are some cases where many fruits are detected with different coefficients, and only the one with the highest coefficient and ≥ 0.5 will be extracted to estimate the location.

The results of the depth (Z) estimating are presented in Fig. 8a. The average Z distance error is less than 8 mm (at 400 and 600 mm). In percentage, it is always
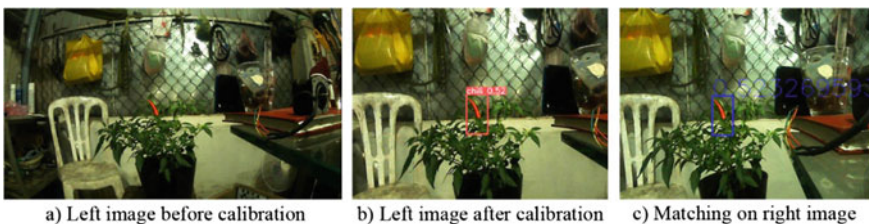

a) Left image before calibration   b) Left image after calibration   c) Matching on right image

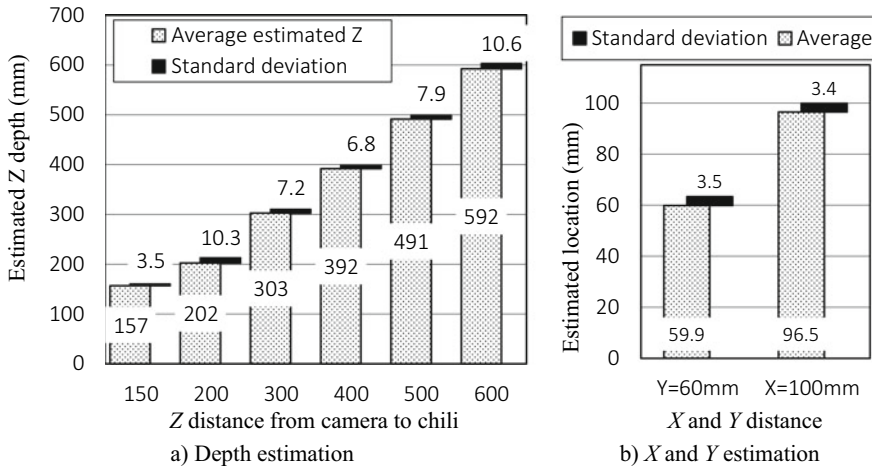**Fig. 7** Image calibration and matching in 3D location estimation

Fig. 8 Average depth estimated and standard deviation

less than 4.5%, while the mean standard deviation is within $\pm$ 7.7 mm and does not exceed the maximum $\pm$ 10.6 mm at the distance of 600 mm.

The results in X and Y directions are presented in Fig. 8b. Accordingly, when the chili is placed at the position $(X, Y) = (100, 60)$ mm, the predicted result is $X = 96.5 \pm 3.4$ mm and $Y = 59.9 \pm 3.5$ mm.

This study only evaluates the ability to locate chili fruits with a 3D camera. In further studies, this location data will be sent to the manipulator to perform the necessary operations to complete a proper job.

Positioning is the first primary function, and other works such as selecting ripened fruits for harvesting or cutting diseased ones could be performed to complement the application of this study.

4 Conclusions

This study has built a model to estimate the position of the fresh chili fruit in space using Yolov5 and a 3D camera. The average accuracy is achieved at $\pm$ 7.7 mm in the range from 0 to 600 mm. This result will be the basis for continuing to build an automatic system to harvest or perform other care operations. In addition, this model also opens up the possibility of using simple, low-cost 3D cameras for future applications.

References

1. Elizanilda RdR, Mailson MdR, Fernando LF (2016) Production and breeding of chilli peppers (Capsicum spp.). Springer International Publishing, Switzerland
2. FAO (2022) Chillies and peppers production of Vietnam. https://www.fao.org/faostat/en/#data/QCL. Last Access 20 Dec 2022
3. Ultralytics Yolov5 (2022). https://doi.org/10.5281/zenodo.4418161. Last Access 20 Dec 2022
4. Wang F et al. (2022) Xiaomila green pepper target detection method under complex environment based on improved YOLOv5s. Agronomy 12(6)
5. Swaroop P, Sharma N (2016) An overview of various template matching methodologies in image processing. Int J Comput Appl 153:8–14
6. Kamencay P et al. (2012) Improved depth map estimation from stereo images based on hybrid method
7. Chen X et al (2021) Calibration of stereo cameras with a marked-crossed fringe pattern. Opt Lasers Eng 147:106733
8. Camera Calibration (2022) https://docs.opencv.org/4.x/dc/dbb/tutorial_py_calibration.html. Last Access 20 Dec 2022
9. Malm H, Heyden A (2003) Simplified intrinsic camera calibration and hand-eye calibration for robot vision. In: Proceedings 2003 IEEE/RSJ international conference on intelligent robots and systems (IROS 2003) (Cat. No.03CH37453), vol 1. pp 1037–1043

Performance Analysis of Orthopedic Screw Used for Fixation of Fracture of Bone

Sushama Agarwalla and Deepak Kumar Agarwalla

Abstract In orthopedic surgery, various implants, such as screws, plates, and nails, are used to fix fractured bones. Often the fracture pattern influences the use of such implants, which facilitates the union. The conventional screw used mainly depends on the significant structure of the thread design. However, screws are used independently or with plates for the fixation of fractures of bones. Axial compressive load, bending load, and rotational load (Torsion) are experienced by the bone of the human body. Therefore, the orientation of screws in the bone is exposed to such limitations. Hence, it has been pertinent to analyze the efficacy of the direction of the screw being fixed in bone concerning immobilization of the fracture site for the union. In this study, the effect of axial compressive and rotational loading has been given prime importance since the bone has been minimally exposed to bending load. Further comparative analysis of maximum deformations and stresses for two different orientations of screws subjected to other limitations and torques simultaneously have been performed. A cortical section of the femur bone of a middle-aged man has been modeled, and subsequent finite element method (FEM) analysis was conducted subjected to comprehensive axial and rotational loads. It has been observed that the maximum deformation (8.1252 mm) and maximum stress (3179.9 Mpa) have been more in the case of the screws placed at 45° to the long bone axis than the screws normal to the long bone axis.

Keywords Orthopedic surgery · Femur bone · Finite element analysis

S. Agarwalla (✉)
Indian Institute of Technology Hyderabad, Hyderabad 502285, India
e-mail: ch20resch11007@iith.ac.in

D. K. Agarwalla
Indian Institute of Technology Kharagpur, Kharagpur 721302, India

1 Introduction

Internal fixation of bone fractures is gaining momentum as people's lifestyles evolve in the modern era. Surgical treatment technically ensures anatomical reduction with precise fixation and restores the bone to a pre-fracture state. Different methods, such as screws, screws with plates, and extramedullary and intramedullary nails, are employed for the internal fixation of fractured bones. Few of these implants contribute to load transmission, and few still bear load transmission during activities. Subsequently, the mechanical behavior of implants under load should also affect fracture fixation and union. Independently used for fracture fixation, the screw plays a vital role in bringing fragments together with correct anatomical reduction, and it also contributes to load bearing along with the right bone. Therefore, the performance of the screw about its position in the bone seems to be of utmost priority and requires biomechanical investigation. The bones in the body are primarily subjected to axial compression and torsional strain during everyday routines. During axial compression, bones with an arch configuration are observed to encounter a small amount of bending load. Thus, it suggests that once the screw is fixed to the bone, axial compression and torsional strain play a significant biomechanical role in the load that the screw can bear. As a result, the mechanical analysis of the screw's structure for fixation in the bone has a significant impact on how effectively implants function in terms of fixing fractures and supporting the union. Nine different pedicle screws with various bone densities have been developed by Kim et al. [1], who also analyzed the various geometric parameters affecting the fixing strength and pullout strength of the screws. They have combined several thread profile varieties and afterward incorporated them into various grades of polyurethane foam. The material testing system has then been used to determine the spinal screws' pullout strength. They decided that the pullout strength was a consequence of the screw's geometry rather than bone density. By using the finite element approach, Hsu et al. [2] developed and assessed three-dimensional models of spinal pedicle screws and tibia locking screws. They used a Taguchi orthogonal array and random choice to select the learning and verification data. After establishing substitute objective functions using multiple linear regression or an artificial neural network, an evaluation was performed to ensure the model's robustness. They have observed that, in contrast to the multiple linear regression method, the artificial neural network is more efficient for forecasting the objective functions of the spinal pedicle screws and the tibial locking screws. Furthermore, they have concluded that adopting surrogate objective functions significantly reduces the effort and time required for the design optimization process of orthopedic screws. By comparing the stress and strain energy densities, Haase and Rouhi [3] conducted a parametric investigation using finite element analysis on the bone–screw models to assess the stress shielding of the stimuli (SED). They discovered that the stimulus transfer parameters caused stress and SED to be transferred between the bone and the screw. However, they found that the screw with an angle thread and a small diameter increased the transfer of both stimuli, and the reduction of the screw's elastic modulus increased the transfer of stress. SED has decreased in both

cases, indicating that the bone–screw model analysis needs a proper SED assessment. Efstathopoulos et al. studied the performance of two trochanteric nails (the Gamma trochanteric nail and the ACE trochanteric nail). The two implants were randomly examined in over 100 patients whose average age was 78 [4]. Following the procedure, the patients were given twenty hours to move around and bear weight in a tolerable manner, and the authors reported that, regardless of whether they used an ACE or Gamma trochanteric nail, the fracture at the trochanteric location had been successfully repaired. To properly position a lag screw inside the femoral head after a proximal femoral fracture, Parmar et al. [5] examined the two techniques of tip apex distance and Parker's ratio method. They have concluded that the lag screw used to treat proximal femoral fractures should be positioned centrally about the femoral head to reduce bone cutout and prevent the effects of eccentricity on the bone and fracture interface imposed by mobility.

Parker has conducted studies to determine the efficacy of several implant types used to treat femoral neck fractures [6, 7]. In addition to the types of implants used, he has suggested that the location of the implant and the surgical methods may play an important role in fracture healing [6]. Different implants for femur head fixation have been tested in Torsion and flexion under conditions of dynamic strain by Swiontkowski et al. [8] According to their study, the optimized number of screws to fix a broken femoral neck is three, and bone density is a significant factor in how well a bone will be set. The various fixation methods have been thoroughly studied by Taljanovic et al. [9]. They have suggested that the primary purpose of internal and external fixators is to aid in healing bone fractures. For the stability of broken bones, doctors even use bone grafts. Numerous implants, including screws, pins, and side plates, have been examined by Parker and Stockton [6] for the internal fixation of intracapsular hip fractures. For this, they gathered and analyzed the data from more than 5,000 patients. He concluded by saying that it is impossible to draw definitive conclusions on the best implants for fixing internal fractures. Four different implant types, including cannulated screws, dynamic hip screws, dynamic condylar screws, and locking proximal femoral plates for vertical femoral neck fractures, have been examined by Aminian et al. [10]. They stated that the locking plate was revealed to be the strongest for various loading patterns, while the cannulated screw was proven to be the weakest. Five different internal bone fracture repair implants have been subjected to testing by Jarvis to determine how well they perform when put under cyclic strain. The relative movement of the femoral neck has been used to compare the effectiveness of each fixator. He has concluded that plates with sliding screws can withstand the shear cycle strain more than pins, nails, and screws. Puers et al. [11] have presented a small system to detect hip prosthesis loosening using vibration approaches. The capacitive accelerometer was installed inside the prosthesis, and the vibration data was collected using a telemetric link. In order to forecast the status of the prosthesis, they have finally examined the data. Cicero et al.'s analysis of the causes of a hip implant failing nine months after surgery. They used scanning electron microscopy to pinpoint the failure mechanism at the point where the base material and fixing coating meet [12]. They concluded that fatigue was to blame for the failure and to support their claim, they used the fracture mechanics approach. To measure

the mechanical characteristics of cadaveric bone, Taylor et al. performed a modal analysis on the bone and verified their findings using both experimental and finite element analyses [13]. In a study on a cancellous bone, Swider et al. used empirical modal analysis to assess the mechanical properties, namely Young's modulus [14]. Before being applied in actual practice, they stated that the results from their study needed to be verified by additional means.

The literature mentioned above makes it clear that researchers have made an effort to investigate the impact of various factors, including implant type, surgical technique, implant placement, bone characteristic, loading pattern, and vibration, on the success rate of implants used for stabilizing fractured bone. There have been limited attempts to evaluate the effectiveness of different implant orientations and numbers in aiding fracture repair in the human bone under various loading scenarios. The purpose of this study is to examine the efficiency of cortical screws implanted in two different contexts and at two different angles (perpendicular and inclined to the long axis of the femur bone) (with two and three cortical screws).

2 Methodology

2.1 Finite Element Analysis of Bone and Screw Assembly

In recent years, numerous biomechanical issues and circumstances have been examined by developing computational models to understand better the fundamental phenomena, which subsequently helps biomedical engineers and healthcare experts conduct their studies and practice effectively. In these kinds of situations, finite element analysis, also known as FEA, has played a significant role in analyzing the computational model to obtain the various parameters to gain a better understanding of the model under a variety of loading and boundary conditions. These parameters include deformation, stress, frequencies of vibration, and so on. The current study used computational modeling software to create a model of the cortical portion of the femur bone of a man who is in the middle years of his life. The model assumed that the bone was cylindrical. The earlier research has provided us with the dimensions for the cortical section, which we have inherited. To replicate the fracture condition of the femur bone when it is in the cortical zone, the same model has been given an oblique crack that has been formed. Additionally, the orthopedic screws that will be used to fix the fractured bone model have been designed using the same modeling program with the standard dimensions that were accessible.

Four distinct configurations of the bone and screws have been assembled, such as the bone with two and three screws positioned normally to the long bone axis and independently inclined at a 45° angle to the long bone axis. The combined models were then discretized and fed into the computer analysis program. As depicted in Table 1, the mechanical characteristics of bone and screw have been introduced in the

Table 1 Mechanical properties of bone and screw

Material	E (Gpa)	P (kg/m^3)	Υ
Bone	20	1750	0.37
Screw	200	7850	0.30

computational analysis software, and boundary conditions have been implemented for the combined bone and screw model.

After that, the models have been individually loaded with torques of 10 Nm, 15 Nm, and 20 Nm, respectively, and axial compressive loads of 500, 600, and 700 N. Additionally, they are subjected to combined loading patterns such as 500 N (axial compressive loads) and 10 N m (torque), 600 N (axial compressive loads) and 15 N m (torque), and 700 N (axial compressive loads) and 20 N m (torque). Maximum deformations and maximum equivalent stress have been evaluated for each scenario using the static analysis module of the computational analysis software.

3 Results and Discussion

The findings of the analysis performed on the fractured bone model have been discussed. The broken femur bone was examined in the cortical zone, and the angle of inclination of the fracture was determined to be 45° concerning the axis of the long bone. This evidence was used in the analysis, as shown in Fig. 1b. A total of three screws were used in the first case to repair the fracture, and two screws were used in the second case. For both numbers of screws, the orientation of the fixing element was considered in two distinct situations, one of which was normal to the axis of the long bone, as shown in Fig. 1a, c, and the other with 45° concerning the long bone's axis as depicted in Fig. 1b, d.

The deformations and stresses of the bone with three models (normal to the long bone axis, 45° to the long bone axis) subjected to an axial compressive force of 700 N, a torque of 20 N m, and a combined load of 700 N axial load applied and 20 N m of torque have been depicted in Figs. 2a and 3f. The fracture bone model along with the screws with different orientations was loaded with three other cases: 500, 600, and 700 N compressive forces along the long bone axis, 10, 15, and 20 N m torques around the long bone axis, and combined loads of 500 N (compressive force) and 10 N m (torque), 600 N (compressive force) and 15 N m (torque), and 700 N (compressive force).

The corresponding deformations and stresses were calculated from the bone model's computational analysis when it was subjected to compressive loads of magnitudes 500, 600, and 700 N acting along the long bone axis. These results have been presented in Tables 2 and 5. The deformations and stresses that were caused by the torques of 10, 15, and 20 N m about the long bone axis have been presented in Tables 3 and 6. The deformations and stresses that were caused by the combined loads of 500 N (compressive force) and 10 N m (torque), 600 N (compressive force)
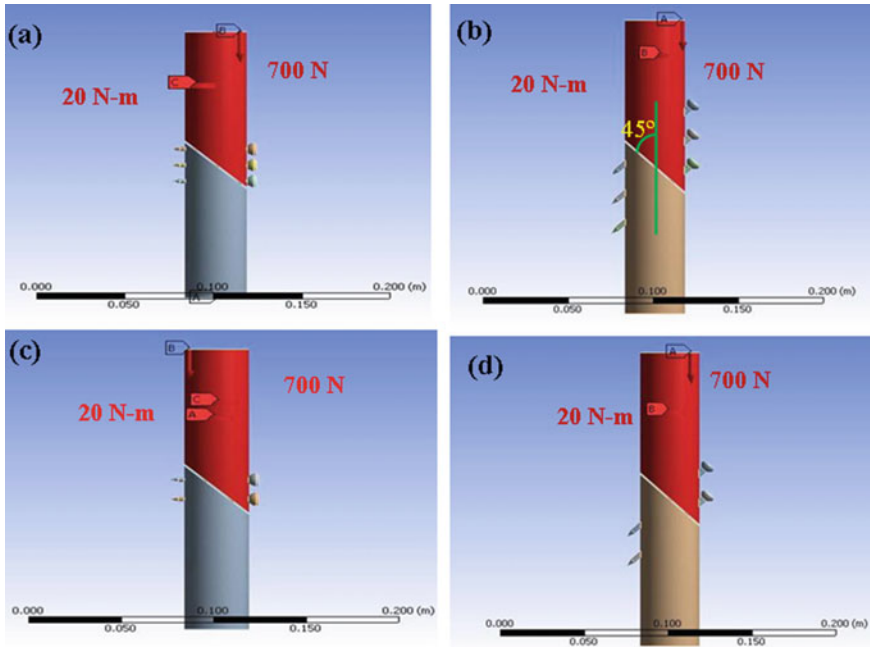
Fig. 1 **a–d** Four different scenarios of assembled models of bone and screws

and 15 N m (torque), and 700 N (compressive strength) and 20 N m (torque) simultaneously have been presented in Tables 4 and 7. The analysis of the findings presented in Table 2 reveals that, for the three screw scenarios, the maximum deformation and stress rise as the compressive load magnitude increases. This was observed.

In the case of the screws placed at 45° to the long bone axis, the maximum deformation on the bone model was found to be 0.55040 mm, and the maximum stress on the bone model was found to be 640.87 megapascals (MPa). This was in comparison with the screws that were placed parallel to the long bone axis. The comparison of maximum deformation and maximum stress found in the bone model is shown in Table 3, along with three screws, for applied torques ranging from 10 to 20 Nm. The screws have been aligned at an angle of 45° in addition to normal to the long bone axis.

It was discovered that the magnitude of the applied torques, in this case, 10, 15, and 20 Nm, led to an increase in the maximum deformation and stress. In the case of screws placed normally to the long bone axis, a greater amount of maximum deformation (4.3435 mm) and maximum stress (1172.90 MPa) was observed on the bone model than in the case of screws placed at a 45-degree angle to the long bone axis. Table 4 compares the maximum deformation and maximum stress for the bone model with three screws when they were subjected to combine loading of various magnitudes simultaneously. These loadings included 500 N (compressive
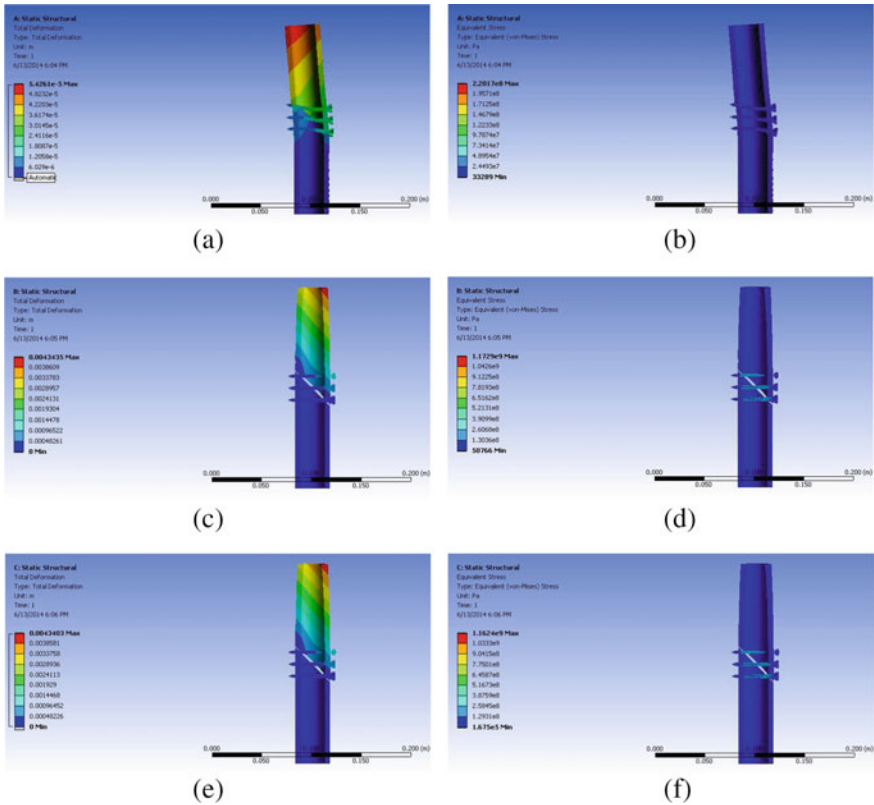
Fig. 2 **a** Deformation due to 700 N (Compressive). **b** Stress due to 700 N (Compressive). **c** Deformation due to 20 N m (Torque). **d** Stress due to 20 N m (Torque). **d** Stress due to 20 N m (Torque). **e** Deformation due to 700 N (Compressive) and 20 N m (Torque). **f** Stress due to 700 N Compressive) and 20 N m (Torque)

force) and 10 N m (torque), 600 N (compressive force) and 15 N m (torque), and 700 N (compressive force) and 20 N m (torque), respectively.

In the case where the screws were placed at an angle of 45° to the long bone axis, the maximum deformation was found to be 5.6363 mm, and the maximum stress was found to be 2173.50 megapascals (MPa). This was in contrast to the case where the screws were placed perpendicular to the long bone axis.

In two different scenarios, with screws positioned at 45° to the long bone axis and with screws placed normally to the long bone axis, Table 5 shows the maximum deformation and maximum stress for a two-screw assembly with a bone model used for fracture fixation and subjected to compressive loads of magnitudes 500, 600, and 700 N. In the case of screws mounted at a 45-degree angle to the long bone axis, the maximum deformation and maximum stress have been observed to increase with an increase in the magnitude of the applied compressive force, whereas they have been observed to remain constant in the case of screws mounted normal to the long bone
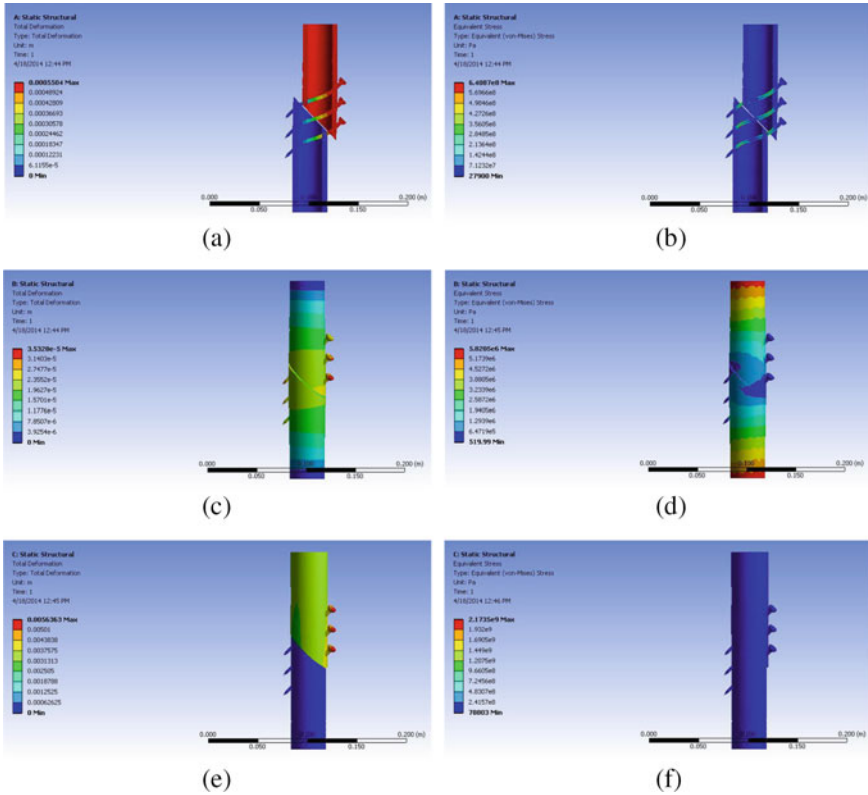
Fig. 3 **a** Deformation due to 700 N (Compressive). **b** Stress due to 700 N (Compressive). **c** Deformation due to 20 N m (Torque). **d** Stress due to 20 N m (Torque). **e** Deformation due to 700 N (Compressive) and 20 N m (Torque). **f** Stress due to 700 N (Compressive) and 20 N m (Torque)

Table 2 Comparison of maximum deformations and stresses for two different orientations of screws (three screws) subjected to different loads

Load (N)	Normal to long bone axis		Inclined at 45° to long bone axis	
	Maximum deformation (mm)	Maximum stress (Mpa)	Maximum deformation (mm)	Maximum stress (Mpa)
500	0.03876	157.27	0.39314	457.76
600	0.04651	188.72	0.47177	549.32
700	0.05426	220.17	0.55040	640.87

axis. Maximum deformation (0.79310 mm) and maximum stress (963.73 MPa) were found to be higher for screws installed at a 45-degree angle to the long bone axis than for screws fixed at a normal angle.

In Table 6, the maximum deformation and maximum stress for applied torques ranging from 10 to 20 Nm for the bone model and two screws are compared. The

Table 3 Comparison of maximum deformations and stresses for two different orientations of screws (three screws) subjected to different torques

Torque (N m)	Normal to long bone axis		Inclined at 45° to long bone axis	
	Maximum deformation (mm)	Maximum stress (Mpa)	Maximum deformation (mm)	Maximum stress (Mpa)
10	2.1717	586.44	0.01766	2.9103
15	3.2576	879.66	0.02650	4.3654
20	4.3435	1172.90	0.03533	5.8205

Table 4 Comparison of maximum deformations and stresses for two different orientations of screws (three screws) subjected to different loads and torques simultaneously

Load (N)/torque (N m)	Normal to long bone axis		Inclined at 45° to long bone axis	
	Maximum deformation (mm)	Maximum stress (Mpa)	Maximum deformation (mm)	Maximum stress (Mpa)
500/10	2.1696	578.98	2.8323	1144.7
600/15	3.2550	870.71	4.2333	1648.0
700/20	4.3403	1162.4	5.6363	2173.5

Table 5 Comparison of maximum deformations and stresses for two different orientations of screws (two screws) subjected to different loads

Load (N)	Normal to long bone axis		Inclined at 45° to long bone axis	
	Maximum deformation (mm)	Maximum stress (Mpa)	Maximum deformation (mm)	Maximum stress (Mpa)
500	0.4257	731.84	0.56649	688.38
600	0.51084	878.21	0.67979	826.05
700	0.59598	1024.6	0.79309	963.73

Table 6 Comparison of maximum deformations and stresses for two different orientations of screws (two screws) subjected to different torques

Torque (N m)	Normal to long bone axis		Inclined at 45° to long bone axis	
	Maximum deformation (mm)	Maximum stress (Mpa)	Maximum deformation (mm)	Maximum stress (Mpa)
10	2.5902	1518.2	0.017774	2.9130
15	3.8853	2277.3	0.026661	4.3695
20	5.1804	3036.4	0.035548	5.8260

screws were positioned with the long bone axis at a 45-degree angle and normal to it, respectively. When applying torques of N, 15, and 20 N to screws positioned at 45° to the long bone axis and to screws oriented normally to the long bone axis, it was found

Table 7 Comparison of maximum deformations and stresses for two different orientations of screws (two screws) subjected to different loads and torques simultaneously

Load(N)/torque (N m)	Normal to long bone axis		Inclined at 45° to long bone axis	
	Maximum deformation (mm)	Maximum stress (Mpa)	Maximum deformation (mm)	Maximum stress (Mpa)
500/10	2.6258	1648.6	4.0864	1680.3
600/15	3.9201	2433.4	6.1040	2420.1
700/20	5.2165	3218.3	8.1252	3179.9

that the maximum deformation and maximum stress both increased with increasing torque magnitude. Compared to screws positioned at a 45° angle to the long bone axis, the maximum deformation (5.1804 mm) and maximum stress (3036.4 MPa) were higher in the case of screws placed normally to the long bone axis.

For the bone model with two screws subjected to combining loading patterns such as 500 N (compressive force) and 10 N m (torque), 600 N (compressive force) and 15 N m (torque), and 700 N (compressive force (Figs. 2a and 3a) and 20 N m (torque) (Fig. 2c–f) simultaneously, Table 7 compares the maximum deformation and maximum stress. It has been discovered that as the amount of applied compressive force and torques increases, so does the maximum deformation, as shown in Figs. 2c, e and 3c, e and maximum stress (Figs. 2b and 3b). The screws positioned at a 45-degree angle to the long bone axis experienced more significant maximum deformation (8.1252 mm) and maximum stress (3179.9) than the screws positioned at a normal angle to the long bone axis.

4   Conclusion

The response of screws that have been independently fixed in two different configurations (normal to the long bone axis and 45° to the long bone axis of bone) to axial compressive loading and rotational loading has been found to be distinct from the response of screws that have been used in conjunction with a plate. The screws that are normal to the long bone axis of bone are able to withstand the largest amount of axial loading, but they are not as strong when subjected to rotational force. Screws oriented normally to the fracture line are capable of withstanding the maximum axial compressive force, but they are susceptible to failure under rotational loads. The screws that are put at an angle of 45° to both the long axis of the bone and the fracture line are able to withstand the maximum amount of load for both types. In order to give the fracture some kind of rigidity, a minimum of six points need to be fastened in any plane. If there are three screws aligned normally with the fracture line, the structure will have a greater maximum resistance to torsional deformation.

References

1. Kim YY, Choi WS, Rhyu KW (2012) Assessment of pedicle screw pullout strength based on various screw designs and bone densities-an ex vivo biomechanical study. Spine J 12(2):164–168
2. Hsu CC, Lin J, Chao CK (2011) Comparison of multiple linear regression and artificial neural network in developing the objective functions of the orthopaedic screws. Comput Methods Programs Biomed 104(3):341–348
3. Haase K, Rouhi G (2013) Prediction of stress shielding around an orthopedic screw: using stress and strain energy density as mechanical stimuli. Comput Biol Med 43(11):1748–1757
4. Efstathopoulos NE, Nikolaou VS, Lazarettos JT (2007) Intramedullary fixation of intertrochanteric hip fractures: a comparison of two implant designs. Int Orthop 31(1):71–76
5. Parmar V et al (2005) Review of methods to quantify lag screw placement in hip fracture fixation. Acta Orthop Belg 71(3):260–263
6. Parker MJ, Stockton G (2001) Internal fixation implants for intracapsular proximal femoral fractures in adults. Cochrane Database Syst Rev 2001(4):Cd001467
7. Parker MJ (2002) Evidence-based results depending on the implant used for stabilizing femoral neck fractures. Injury 33(Suppl 3):C15-8
8. Swiontkowski MF et al (1987) Torsion and bending analysis of internal fixation techniques for femoral neck fractures: the role of implant design and bone density. J Orthop Res 5(3):433–444
9. Taljanovic MS et al (2003) Joint arthroplasties and prostheses. Radiographics 23(5):1295–1314
10. Aminian A et al (2007) Vertically oriented femoral neck fractures: mechanical analysis of four fixation techniques. J Orthop Trauma 21(8):544–548
11. Puers R et al (2000) A telemetry system for the detection of hip prosthesis loosening by vibration analysis. Sens Actuat A 85(1–3):42–47
12. Cicero S et al (2007) Failure analysis of a hip implant by using the FITNET fitness for service procedure. Eng Fract Mech 74(5):688–702
13. Taylor W et al (2002) Determination of orthotropic bone elastic constants using FEA and modal analysis. J Biomech 35(6):767–773
14. Swider P et al (2009) Characterization of bone-implant fixation using modal analysis: Application to a press-fit implant model. J Biomech 42(11):1643–1649

Development of a Payload-Dropping Quadcopter Using Landing Gears with Electronic Servo

E. M. Maheshwar, R. Ibrahim, and K. K. Nithiyanantham

Abstract Over the last few years, unmanned aerial vehicles (UAVs) have been widely used for various purposes such as payload dropping, thermal imaging scanning, and spraying of agricultural pesticides. This report focuses on the design of a multirotor UAV with the primary objective of picking up and releasing a payload. The vehicle is a quadcopter and uses electronic servo motors for the payload release mechanism, which is accomplished by the quadcopter's landing gears using a four-bar mechanism. This paper highlights the various possible technologies used to minimize human efforts in payload-dropping operations using quadcopters. The payload release mechanism demonstrates innovation in design. The discussed system involves designing and building a simple and cost-effective prototype. The promising results of this method pave the way for future research on using quadcopters for product delivery.

Keywords UAV · Payload dropping · Quadcopter/Drone · Servo motors · Landing gear

E. M. Maheshwar (✉) · R. Ibrahim · K. K. Nithiyanantham
Department of Aeronautical Engineering, Rajalakshmi Engineering College, Chennai, India
e-mail: maheshwar.em.2019.aero@rajalakshmi.edu.in

R. Ibrahim
e-mail: ibrahim.r.2019.aero@rajalakshmi.edu.in

K. K. Nithiyanantham
e-mail: nithiyanantham.kk@rajalakshmi.edu.in

Nomenclature

UAV	Unmanned Ariel Vehicle
FCS	Flight Control System
BLDC	Brushless Direct Current
RC	Radio Control
PWM	Pulse-Width Modulation
APM	ArduPilot Mega
KV	Kilo-Volts
ESC	Electronic Speed Controller
g	Acceleration due to gravity (m/s^2)
RPM	Revolutions per Minute (kv)

1 Introduction

The utilization of unmanned aerial vehicles, commonly known as UAVs, has gained widespread recognition in various sectors and has grown significantly in recent years, with a wide range of applications being explored. These vehicles, commonly known as drones, have the ability to operate autonomously and remotely, enabling them to fly in the air and perform various tasks as required. The benefits of UAVs are numerous, from cost savings to improved safety, and they are used across many fields such as agriculture, search and rescue, package delivery, racing competitions, military surveillance, photography, videography, and monitoring of wildlife among others.

Payload picking and dropping drones have been gaining attention in recent years as a solution for various problems. These drones can be equipped with mechanical arms or grippers that allow them to grasp and release objects in mid-flight, making them useful for tasks such as delivery purposes, and even search and rescue. The use of payload picking and dropping drones has the potential to revolutionize the way goods are transported and tasks are performed, making them faster, more efficient, and more cost-effective (Fig. 1).

Fig. 1 Model of a payload picking and dropping quadcopter

1.1 Objectives

The primary aim of this project is to create and construct a multirotor unmanned aerial vehicle (UAV) that possesses the capability to safely lift and release diverse payloads. This will be accomplished by implementing a novel payload drop mechanism integrated with a reliable landing gear system. The system includes fixed and movable hinges, four-bar mechanisms, and servo motors to release various shapes of payloads. The design aims to create an innovative, self-sufficient, and cost-effective payload dropping quad drone that can use its landing gear for both take-off and landing, as well as picking up and dropping payloads. This project builds upon prior research [1–4] to achieve a robust and reliable system for aerial operations.

2 Project Ideation

The aim of this project is to create a cost-effective drone capable of picking up and dropping payloads. It can be utilized for delivering food or releasing fire-extinguishing balls in difficult-to-access areas. With recent advancements in technology [5–8], such as aircraft technology, software, sensors, and communication, drones have become useful for a variety of applications, including search and rescue, environmental monitoring, surveillance, and delivery. This research aims to tackle the technical difficulties faced in developing drones for payload dropping purposes.

3 Literature Survey

Autonomous payload drop system using mini-unmanned aerial vehicles [9] is the payload-dropping drone where the payload is manually made to be placed in the handles made of wooden cuffs. It carries bottle- or tube-shaped payloads in the wooden cuffs connected with high torque servo motors with a thick iron strip. The payload is made to be dropped autonomously by calculating the release coordinates by programming the algorithm into the flight control system (FCS). The problem of these drones is that they cannot carry higher payload weights (Fig. 2).

Fig. 2 Model of the payload drop system [9]
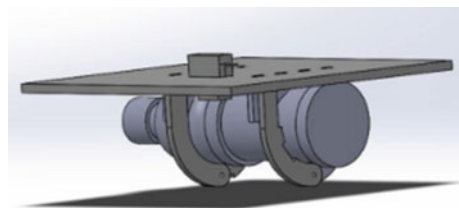
Fig. 3 Model of the payload
drop mechanism using
fire-extinguishing balls [10]

The use of a payload drop mechanism for fire-fighting services [10], as described in the literature, showcases the application of remote-controlled UAVs in carrying and releasing fire-extinguishing balls. This innovative system enables effective fire combat in areas that are difficult for human access. With the mechanism's ability to transport and drop up to four balls using servo motor operation, it proves to be a valuable tool. However, it is important to address the limitation of the mechanism in terms of its compatibility with various ball diameters and non-round-shaped objects (Fig. 3).

Multiple-object-dropping mechanism using RC plane [11] uses UAVs to drop circular-shaped objects using a servo mechanism where the payload is manually loaded into the drone. The drone's servo-based mechanism enables the release of objects, such as those mounted under the wing or within the fuselage, by rotating the system. However, a limitation of the drop-type wing-mount mechanism is that it does not allow for a second object to be reloaded and dropped while the drone is still in flight. Furthermore, in cases where multiple objects are loaded onto a door-type mechanism for dropping, there is a lack of individual object control, resulting in simultaneous release of all objects when the drop is initiated (Fig. 4).

Hexacopter payload dropping UAV [12] combines a hexacopter and dropping mechanism. It is a typical type of dropping mechanism that consists of horizontal handles-like structures located at the landing gear area which is used to hold the payload of certain shapes and sizes. There is no servo mechanism used here. The drone is just used to carry the payloads (Fig. 5).

The development of an automated object retrieval system for UAVs [13] incorporates a four-bar mechanism that enables the gripper to navigate to the designated location for object retrieval. It is crucial to consider the weight of any additional components, as it affects both the payload capacity and flight duration of the UAV. Consequently, the arm mechanism needs to be lightweight while maintaining structural integrity, without compromising the UAV's stabilization limits due to shifts in its centre of gravity. Moreover, the drone is equipped with balancing systems to counteract external factors such as wind, ensuring stable flight conditions. The choice of

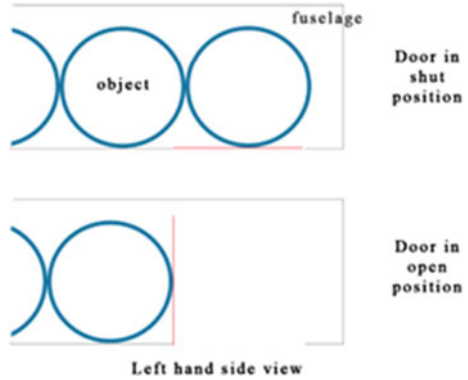Fig. 4 Shut and open-door positions as desired [11]

Fig. 5 Hexacopter payload dropping UAV [12]

servo motors was a crucial factor in meeting the peak torque demands of the drone's mechanism. In addition, the design team had to perform a reachability analysis to ensure that the drone's components could move as intended. Finally, cost was also a key consideration in the development of these drones. The main disadvantage of this type is that the payload should be placed in a certain position before picking up by the arms (Fig. 6).
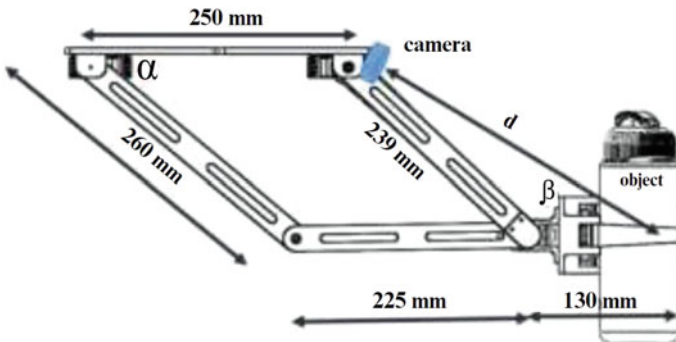

Fig. 6 Model of the payload dropping UAV using four-bar mechanism grippers [13]

We overcome the disadvantage of payload constraint, which was in the first literature [9] (two wooden cuffs with 2 degrees of motion), by using the retractable landing gear of the quadcopter to pick up and drop payload of multiple shapes and sizes. Furthermore, unlike the second literature [10] (which works only with a specific diameter of balls) and the third literature [11] (round-shaped objects), the retractable landing gear idea is not constrained by the diameter of the ball, it can pick up and drop payloads of different shapes and sizes. We don't need to face the difficulty of picking up only certain shaped objects that fit in the landing gear in our idea, like in the fourth literature [12]. The object/payload that needs to be picked up can be in any position while being picked up. Our ideas do not face the same difficulties as those in the fifth literature [13].

4 Design Calculation

4.1 Estimation of Preliminary Weight of the Drone

Design calculations for a quadcopter involve determining the various components and parameters needed for the drone to fly successfully. Firstly, the appropriate components to build the UAV are chosen and the weight estimation of each component is done in such a way that they don't weigh more (Fig. 7).
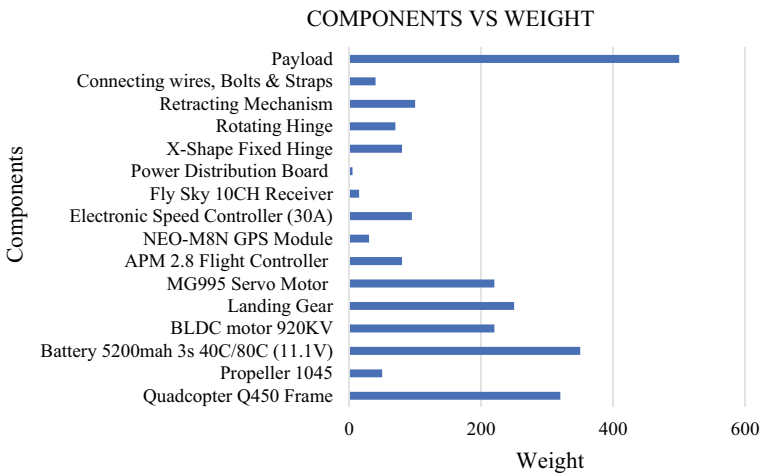
Fig. 7 Weight estimation chart of the quadcopter

4.2 Parameter Calculations

Parameter calculations help in ensuring that the drone is stable and has enough lift capacity to fly. The main calculations involved in designing a quadcopter are as follows:

Total Weight Calculation The weight of the drone is determined by summing the weights of various components, such as the frame, motors, batteries, electronics, and payload. It plays a significant role in determining the drone's lifting capability. According to the data provided in Table 1, the total weight of the drone, including the payload, is recorded as 2400 g.

Thrust Calculation Thrust is the force produced by the motors to lift the drone off the ground. The thrust produced by a motor is determined by the power of the motor, the efficiency of the propeller, and the air density. The total thrust produced by all motors must be equal to or greater than the total weight of the drone for it to fly. The calculation of the required thrust for a single motor in a drone involves determining the total weight of the drone, the number of motors, and the specifications of the motors and propellers.

Table 1 Estimated weight of the drone components

Components	Quantity	Weight (g)
Quadcopter Q450 frame	1	320
Propeller 1045	4	50
Battery 3300mah 4s 3s 40C/80C (11.1 V)	1	350
BLDC motor 920 kV	4	220
Landing gear	4	250
MG995 servo motor	4	220
APM 2.8 flight controller	1	80
NEO-M8N GPS module	1	30
Electronic speed controller (30 A)	4	95
Fly sky 10CH receiver	1	15
Power distribution board PDB (BEC 5 and 12 V)	1	5
X-shape fixed hinge	1	80
Rotating hinge	4	70
Retracting mechanism	8	100
Connecting wires, bolts and straps	Required	40
Payload	1	500
Total weight without payload		1900 = 1.9 kg
Total weight with payload		2400 = 2.4 kg

$$\text{Lift} = \frac{1}{2} \times \text{Propeller Disc Area} \times (\text{Propeller Velocity})^2 \times \text{Propeller Efficiency}$$

$$(1)$$

To determine the thrust required for a single motor, the calculation of the total thrust is required to lift the drone, which is equal to the total weight of the drone multiplied by the acceleration due to gravity (g).

$$\text{Thrust} = \frac{\text{Lift}}{g} \tag{2}$$

Then, by calculating the static thrust of the propeller using the propeller velocity and disc area, and the dynamic pressure of the air. Finally, by calculating the actual thrust produced by each motor by dividing the total thrust produced by all motors by the number of motors. So, from the above calculations the minimum thrust required by a single BLDC motor is 665050 gm. Totally for four motors, it is 2600 gm.

Motor Selection The type and size of the motor used in the drone are crucial in determining the lift capacity of the drone. The motor specifications such as kV rating, maximum power, and maximum current are used to determine the thrust produced by the motor. The number of motors used in the drone and the total thrust produced by all motors must be sufficient to lift the drone off the ground. Here the total weight of the drone is 2.2 kg and four brushless DC motors with a kV rating of 920, a maximum current of 30 A, and a maximum power of 330 W are used (Fig. 8).

A BLDC 2212 920 kV motor can produce a maximum thrust of 650 gm, and four motors are used in the quadcopter. To determine whether this is sufficient for your

Fig. 8 Ready-To-Sky 2212 920 kV brushless DC motors

drone to fly, the calculation of the total thrust produced by all four motors is carried out. If the total thrust is equal to or greater than the total weight of the drone, then the quadcopter should be able to fly.

In this case, the total thrust produced by all four motors would be 650 gm × 4 = 2600 gm = 2.6 kg. Since the total weight of the drone is 2.4 kg, the calculated total thrust is sufficient for the drone to fly.

Propeller Selection The size and pitch of the propeller used in the drone also play a role in determining the lift capacity of the drone. The propeller specifications such as diameter, pitch, and the number of blades are used to calculate the thrust produced by the motor. The propeller which is suitable for the selected BLDC motor has a pitch of 4.5 in., a diameter of 9.5 mm, and two blades.

$$\text{Propeller Velocity} = \frac{\text{RPM} \times \text{Pitch}}{60 \, \text{s/min}} \tag{3}$$

The propeller efficiency will depend on several factors, including the type of propeller, the size and shape of the blades, the speed and power of the motor, and the altitude and air temperature. In general, a propeller efficiency of 60–80% is considered good for a quadcopter. However, a high efficiency may result in a lower thrust output, while a low efficiency may result in a higher thrust output. The best propeller efficiency for a quadcopter will depend on the specific requirements and operating conditions of the quadcopter.

$$\text{Rotational Velocity} = \frac{\text{RPM} \times 2\pi}{60} \tag{4}$$

The thrust output and the power input are calculated using rotational velocity (4), which is used to calculate the propeller efficiency.

$$\text{Thrust output} = \frac{\rho \times (\text{Propeller Diameter})^2 \times (\text{Rotational Velocity})^2}{2\pi} \tag{5}$$

$$\text{Power Input} = \text{Thrust} \times \text{Propeller Velocity} \tag{6}$$

$$\text{Propeller Efficiency} = \frac{\text{Thrust Output}}{\text{Power Input}} \times 100 \tag{7}$$

Flight Controller Selection The APM 2.8 Flight Controller is a highly versatile and reliable device that offers a host of features to improve the stability and control of drones. Its advanced gyro sensors and algorithms provide precise and accurate flight control, even in challenging conditions. Moreover, its compatibility with a wide range of motors and ESCs enables it to work with various types of drones, making it a popular choice among drone enthusiasts and professionals alike. The flight controller also features improved power management and monitoring capabilities, ensuring that

Fig. 9 APM 2.8 flight
controller
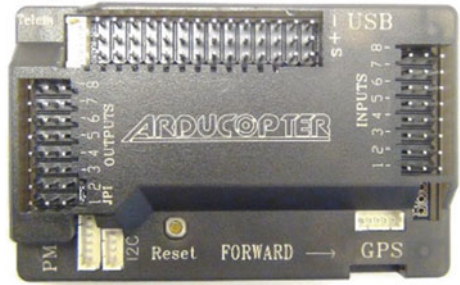
your drone is always powered and functioning optimally. With an intuitive and user-
friendly interface that can be customized through open-source software and firmware,
the APM 2.8 Flight Controller is an excellent option for anyone looking to enhance
their drone's performance and capabilities (Fig. 9).

Power Distribution Boards PDB Selection The Matek Mini Power Hub PDB is a
power distribution board designed for use in multirotor aircraft. It features a built-
in BEC with 5 and 12 V outputs, which can power the flight controller, receiver,
camera, and other auxiliary equipment. The PDB also includes solder pads for the
ESCs, making it easy to connect the power and signal wires. The board is small and
lightweight, making it an ideal choice for mini- and micro-quadcopters (Fig. 10).

Additionally, the Matek Mini Power Hub PDB has built-in protection features
such as over-current protection and short-circuit protection to ensure the safety of
the components connected to it (Table 2).

Fig. 10 Matek mini power
hub PDB (BEC 5 and 12 V)

Table 2 Parameters calculated using the formulae

Parameter	Value
Propeller length	10 in.
Propeller pitch	4.5 in.
Propeller shaft diameter	9.5 mm
Propeller disc area	0.44 in.^{2}
Propeller velocity	4.66 m/s
Rotational velocity	15.7 rad/s
Thrust output	0.124 N
Power input	0.578 W
Propeller efficiency	21.51%
BLDC motor mechanical power	35 W
BLDC motor electrical power	330 W
BLDC motor efficiency	10.6%
BLDC motor RPM	920 kV
BLDC motor maximum thrust	650 gm
Maximum current (ESC)	30 amps

5 CAD Model and Drawing

Figure 11 shows the three-dimensional CAD model of the payload-dropping quadcopter designed using CATIA V5R20 software.

Figures 12 and 13 show the CAD drawing of the innovative designed X-Type fixed hinge and rotating hinge and their respective dimensions.

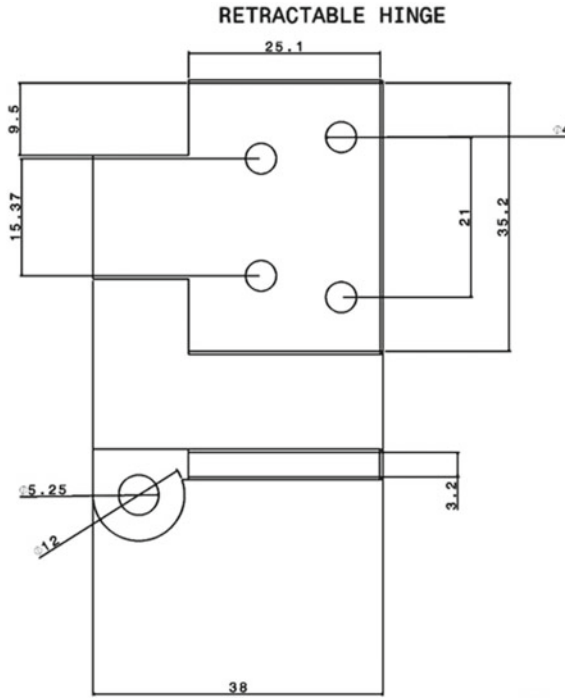**Fig. 11** Retracted landing gear CAD model

Fig. 12 CAD drawing of rotating hinge

6 Methodology

For picking up and dropping off the payload, small modifications are made around the landing gear area of the existing quadcopter. The four-bar mechanism concept is being introduced and applied in the landing gear using servo motors and hinges so that the landing gear will retract inward and holds the object that is to be picked up. The main component that is used to pick up and drop the payload is the landing gears (Fig. 14).

6.1 X-Type and Rotating Hinges

X-Type and rotating hinges are 3D printed as shown in Fig. 15 and are used for the retraction purpose of the landing gears which holds and drops the payload as in Fig. 16.

X-TYPE FIXED HINGE

ALL DIMENSIONS ARE IN mm
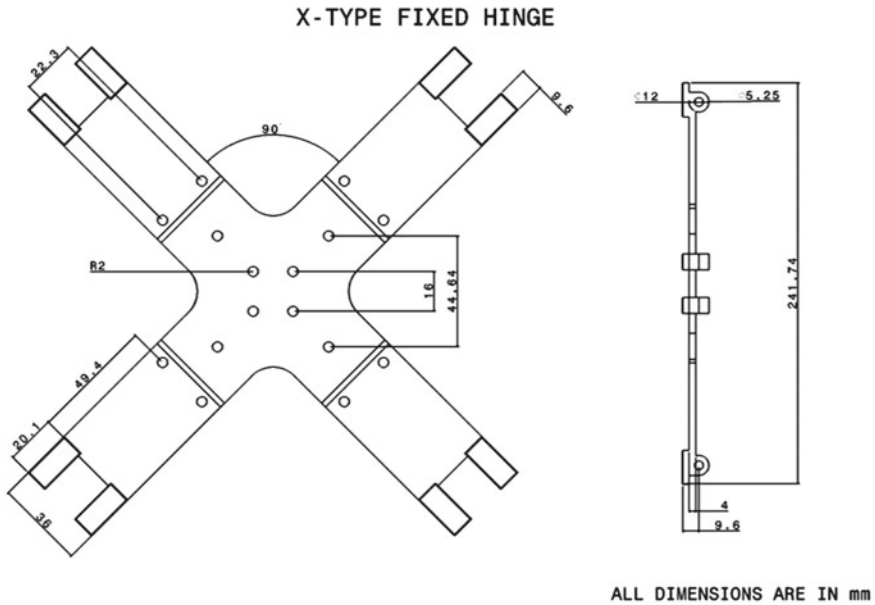
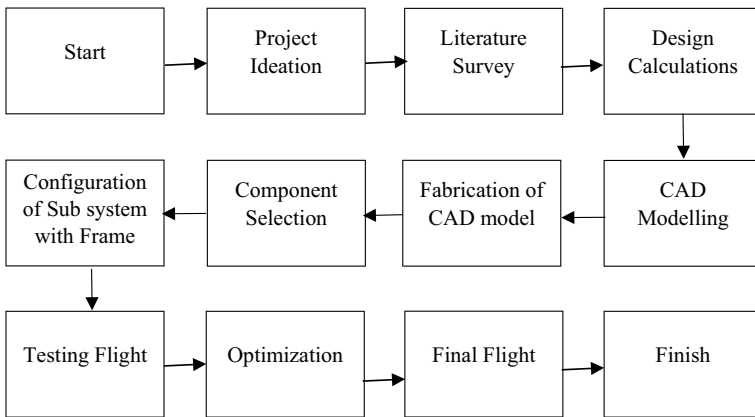**Fig. 13** CAD drawing of X-Type fixed hinge

Fig. 14 Project approach

6.2 Four-Bar Mechanism Linkages

The landing gears are retracted using servo motors connected by four-bar mechanism linkages to the landing gears. To restrict the four-bar mechanism for unwanted rotations which could lead to the failure of the objective, portions of first bar (link)
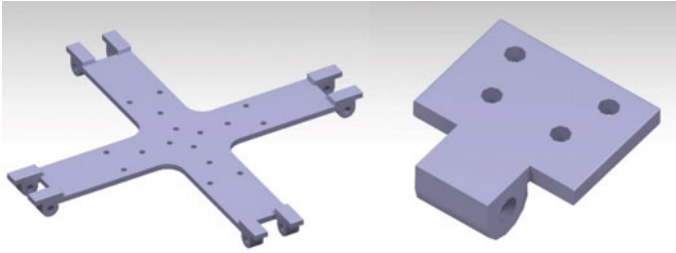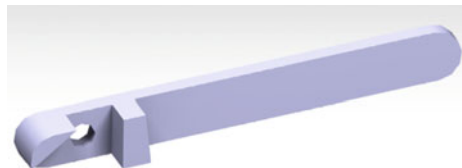
Fig. 15 Isometric view of X-Type hinge and rotating hinge

Fig. 16 Isometric view of landing gear connected with hinges

Fig. 17 Portions of the first bar raised

are raised as shown in Fig. 17. This restricts the full free movement of the second and allows it to rotate in the angle between 0° and 131° as shown in Fig. 18.

6.3 Advantages of Fully Retracted Landing Gears of Quadcopter After Take-Off

Using fully retractable landing gears after take-off can provide several advantages for quadcopters. Firstly, retracting the landing gears can improve aerodynamics by reducing drag and air resistance, which leads to increased speed and efficiency. Secondly, retractable landing gears provide greater maneuverability and freedom for complex movements. Thirdly, retractable landing gears reduce the risk of damage
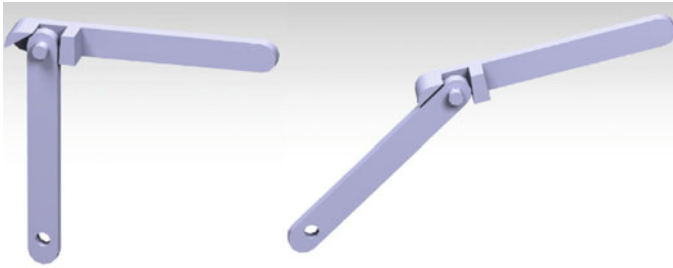
Fig. 18 Rotation restrictions of the mechanisms

during flight or landing in tight spaces. Additionally, retractable landing gears are typically lighter than fixed ones, which can result in longer flight times for the quadcopter. Finally, retractable landing gears offer safer landings as there is no risk of them getting entangled with any obstacles during landing, reducing the chances of damage to the quadcopter and its surroundings. These benefits make fully retractable landing gears a valuable addition to quadcopter designs for improved performance and safety.

7 Construction

7.1 Connection Between Hinges and Quad Base Plate and Mechanisms

The X-Type fixed hinge is a crucial component in the design of the drone. It is a 3D-printed part that connects the drone's frame, specifically the quad base plate, to the retractable hinges. These hinges are also 3D printed and are connected to the landing gears using connecting pins. To retract the landing gears inward, the design implements a four-bar linkage mechanism, which is operated by four Tower Pro MG 995 Servo Motors. These motors are attached to the corners of the fixed hinge and connected to the battery, flight controller board, and electronic speed controller. When the servos are rotated using the remote control, the four-bar linkage mechanism moves in a clockwise direction, causing the landing gear to retract inward and pick up a payload. This allows the drone to take off and drop the payload as desired (Fig. 20).

7.2 Connections Between Servo Motors, PDB, and Receiver

To connect the components, attach the battery's positive and negative wires to the power distribution board's battery input. Connect the PDB's output to the flight controller's input. Connect the signal wires of the four Tower Pro MG 995 Servo Motors to the corresponding PWM output channels of the PDB. Connect the receiver to the flight controller and configure the PWM output channels for the servo motors in the flight controller software. Power on the system and test the servo motors' operation using the remote control. Verify the functionality of each motor individually. These steps will ensure proper setup and testing of the system.

8 Result

The proposed system of payload picking and dropping quadcopter is shown in Fig. 19. The drone is assembled in the correct manner, the fixed hinge is connected with the quadcopter base plate, and the hinges are fitted correctly. The servo motors are placed in the predicted location on the X-Type hinge, and the four-bar linkage mechanisms are connected with each servo motor and landing gears, respectively, as shown in Fig. 19. The servo and receiver connections are linked to the power distribution board successfully, and by operating using the channel key in the transmitter, the landing gears are made to retract inwards perfectly and are also successful in picking up and holding the payload as well as dropping off the payload (Figs. 21 and 22).

Fig. 19 Quadcopter with fully retracted landing gears in air without payload

Fig. 20 Quadcopter having retractable landing gears for payload picking and dropping
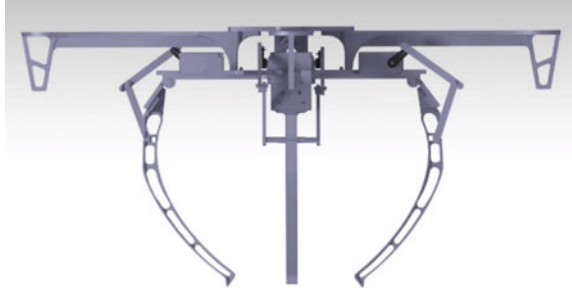

Fig. 21 A distinct perspective of the quadcopter transporting a payload while utilizing its landing gears which are retracted inwards
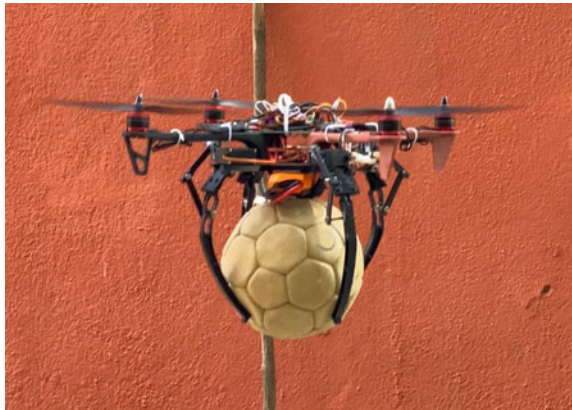

Fig. 22 A distinct perspective of the quadcopter as it drops the payload by retracting its landing gears outwards

9 Conclusion

In the current study, as mentioned previously, we introduced a quadcopter equipped with an innovative payload drop mechanism integrated with landing gear. This newly devised system enables the release of various payload shapes through servo motors connected to bar mechanisms and landing gear. It encompasses two primary components, namely the fixed and movable hinges, which facilitate the efficient operation of the mechanism. The mechanism is tested and optimized. The developed retractable landing gear system offers a significant advantage for aerial operations, providing the ability to pick up and transport payloads while minimizing the risk of damage to the drone during take-off and landing. Several tests were conducted to ensure that the prototype designed could fly successfully. Overall, a single unmanned air vehicle was completed as part of this project.

References

1. Tale I (2012) Quadcopter design and implementation. In: IEEE Intrnational conference, Gaponov
2. Scott J, Scott C (2017) Drone delivery models for healthcare. In: Paper presented at the Proceedings of the 50th Hawaii international conference on system sciences
3. Perez S (2017) UPS tests show delivery drones still need work. https://techcrunch.com/2017/02/21/ups-tests-show-deliverydrones-still-need-work/. Accessed 3 May 2017
4. Köse O, Oktay T (2019) Non simultaneous morphing system desing for quadrotors. Eur J Sci Technol 16:577–588
5. Naidoo Y, Stopforth R, Bright G (2011) Development of an UAV for search & rescue applications. In: IEEE Africon 2011—The falls resort and conference centre, Livingstone, Zambia, 13–15 Sept 2011
6. Deakin MAB Troup GJ (1998) Approximate trajectories for projectile motion with air resistance. Am Assoc Phys Teachers 66(1)
7. Salih L, Moghavvemil M, Mohamed HAF, Gaeid KS (2010) Flight Pid controller design for a Uav quadcopter. Sci Res Essays 5(23):3660–3667
8. Singh RP, Garg A Autonomous Payload drop system using mini—Unmanned aerial vehicles. Int J Innov Eng Technol (IJIET)
9. Singh RP, Garg A (2016) Int J Innov Eng Technol (IJIET) 7(3). ISSN 2319-1058 (Department of Electrical and Electronics Engineering Delhi Technological University, Delhi, India)
10. Soliman S (2019) Payload drop mechanism for firefighting services using fire extinguishing balls. Mechanical Engineering Department, Engineering Faculty, Mersin University, Mersin. Published SN Applied Sciences
11. Gupta G (2014) Multiple objects dropping mechanism using RC plane. IOSR J Mech Civil Eng (IOSR-JMCE) 11(5) version I (Mechanical Engineering, Visvesvaraya National Institute of Technology, Nagpur)
12. Jadhav S (2022) Hexcopter payload dropping UAV. Int Res J Mod Eng Technol Sci 04(08) (K.K. Wagh Institute of Engineering Education and Research, Nashik, Maharashtra)
13. Mohammad M (2020) Design of an automatic item pick-up system for unmanned aerial vehicles. Celal Bayar Univ J Sci 16(1)

Performance Enhancement of a Vertical Axis Wind Turbine (NACA 25112) Using Deflector Plates as an Augmenter

Karthik Selva Kumar ⓘ**, Mohammed Jaseel, R Brintha, Aruna Devi, Krishna Kumar Jaiswal** ⓘ**, B M Sangmesh** ⓘ**, A Suresh** ⓘ**, and P S Balaji** ⓘ

Abstract In order to overcome the self-starting issues in vertical axis wind turbines (VAWT), it is proposed to introduce the deflector plates as a power augmenter. In this study, a computational analysis on a wind turbine rotor with three-bladed NACA 25112 has been performed to understand the significance of power augmenters and their impact on the overall performance of the wind energy conversion system. The rotor motion of the proposed model has been simulated by introducing a sliding mesh technique with reference to the SST-turbulence model. The simulation has been performed at different flow velocities ranging from 4 to 7 m/s to understand the effects of power augmenters with respect to the enhancement in the initial torque. The observed results showed a significant improvement in the enhancement of initial torque, the aerodynamic behavior of the airfoils, and the power coefficient of the wind turbine.

K. S. Kumar (✉) · M. Jaseel · K. K. Jaiswal · B. M. Sangmesh
Department of Green Energy Technology, Pondicherry University, Puducherry, India
e-mail: kksk88@pondiuni.ac.in

R. Brintha
Department of Computer Applications, Saradha Gangadharan College, Puducherry, India

A. Devi
Department of Computer Science and MIS, OCMT, Barka, Oman

A. Suresh
Department of Mechanical Engineering, NIT Warangal, Hanamkonda, India

P. S. Balaji
Department of Mechanical Engineering, NIT Rourkela, Rourkela, India

1 Introduction

Attainment of sustainable solution for energy and its storage has become a critical phenomenon from time to time. In recent years, the focus is more toward the sustainable energy in the form of clean and green which mutually helps society and the environment [1]. To fulfill such criteria, it is anticipated that the sources of green and clean energy with a lesser carbon footprint compared with the other renewable energy sources. The carbon footprint represents the emission of harmful carbon to the environment for attaining energy or activities from a reliable or renewable source. Such harmful carbon emission leads to various environmental impacts, which directly and indirectly affect each individual's socioeconomic and health pattern and the neighboring population embracing such resources. To avoid aggregating such emission of carbon and to lead a healthy generation of young minds in the future, in recent years the focus is toward the sustainable clean and green energy. Among such resources for clean and green energy for a sustainable environment, the carbon footprint of the energy from the naturally available wind is approximate of 11 g of carbon dioxide/kilowatt hour, whereas the natural gas and coal emit 460 and 980 g, respectively, for producing the similar amount of energy with additional cost of health and environment [2].

A tremendous amount of research work on wind energy is carried out from time to time, from designing of turbine components, structure and an effective way to enhance the end life of the turbines and also focused on how the fiber composites of blades can be replaced/recycled in an effective way without affecting the environment [3, 4]. In this research work, it is proposed to design a vertical axis wind turbine for a rural environment and how effectively the performance enhancement and other issues can be rectified with the help of augmentation techniques has been examined.

2 Materials and Methodology

In this research work, a vertical axis wind turbine with NACA 25112 airfoil is proposed for a sustainable energy conversion system for a rural environment. The study focused on the enhancement of turbine performance and resolving issues by introducing deflector plates as augmentation techniques have been examined. The computational study has been performed with discretization on the spatial domain by considering two sub-domains for the energy conversion system [Stator and Rotor]. As illustrated in Fig. 1, the wind energy conversion system with a three-bladed rotor is considered for one of the sub-domains.

The power augmenter (deflector plates) has been included in the other sub-domain, i.e., stator. Further, the study has been supported with 0.6% of blockage ratio, 4.18 as a tip speed ratio, and 0.5% as the turbulent intensity. A well-posed boundary condition has been defined to obtain the solution in an efficient manner as follows, the inlet wind
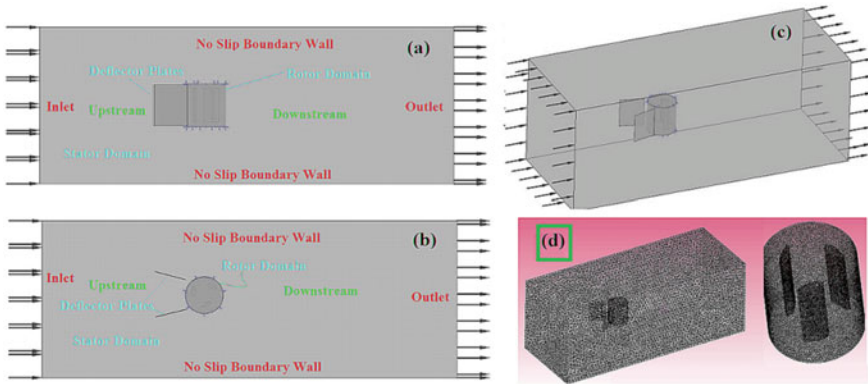
Fig. 1 Computational domain of the wind energy conversion system (VAWT) with power augmenter (deflector plates) [5]

velocity is analyzed at $u = 7$ m/s with an outlet gauge pressure at 0 atmosphere, the other surfaces of the stator domain have been uniformly fixed with a no-slip boundary conditions. An effective transfer of fluxes from subsequent zones and interfaces can be attained by adopting a sliding mesh technique. The study has been undergone with the pressure-based time-dependent solver by embracing the URANS. The first-order upwind and first-order implicit schemes have been employed to understand the nature of kinetic energy with respect to the momentum and transient formulation, respectively. After the successful revolution of the rotor domain in the wind energy conversion system, the second-order upwind scheme has been empowered with a wall criterion $Y+$ as 1. To ensure the independent nature of the mesh generated for computational study, the torque coefficient has been considered and monitored concerning the rotor domain. The convergence of the torque coefficient has been attained at 0.0652 with an error ratio of lesser than 1. The obtained précised result for the complicated aerodynamics flow phenomenon problems with negative gradients by employing a double equation viscosity model, i.e., shear stress transport (SST-$K\omega$) turbulence model, was chosen. The torque coefficient response with respect to different azimuthal angle has been shown in the (Fig. 2). AS well as the quality of the mesh has been evaluated through the mesh independency study test, shown in the Table 1.

Fig. 2 Torque coefficient
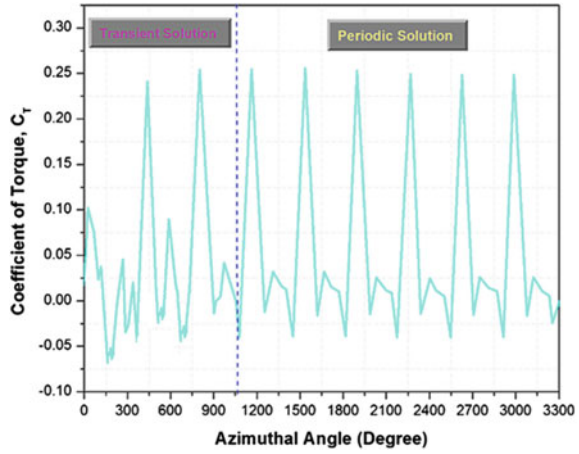with respect to the periodic
and transient solutions

Table 1 Mesh independency study

Mesh	No of cells	C_T	Simulation time (h)
M1	1,786,374	0.06932	16
M2	1,412,283	0.06774	14
M3	1,102,841	0.06526	13

3 Result and Discussion

The computational study has been incorporated to understand the significance of employing deflector plates in the flow path of the upstream velocity as a power augmenter for a vertical axis wind energy conversion system. In which the proposed model is designed with a NACA 25112 for a three-bladed rotor domain, the study emphasizes understanding the flow phenomenon along with the changes in the intrinsic property for well-defined boundary value problems. The simulation was performed by introducing two deflector plates by placing them in the upstream velocity; the study focused on how the deflector plates and their orientation can enhance the overall power output, improving the initial torque and other significant properties of the system.

Figure 3a represents the mass and momentum with respect to various time steps during the computational analysis; it reveals that the initial stage of the revolution of rotor domain with respect to the varying flow phenomenon; the pattern of the mass and momentum displacement at the initial time steps was observed to be higher; it signifies the initial enhancement in the torque generation of the energy conversion system. So it satisfies the requirement of the higher torque at staring of the rotor domain. Further, the displacement of mass and momentum was identically
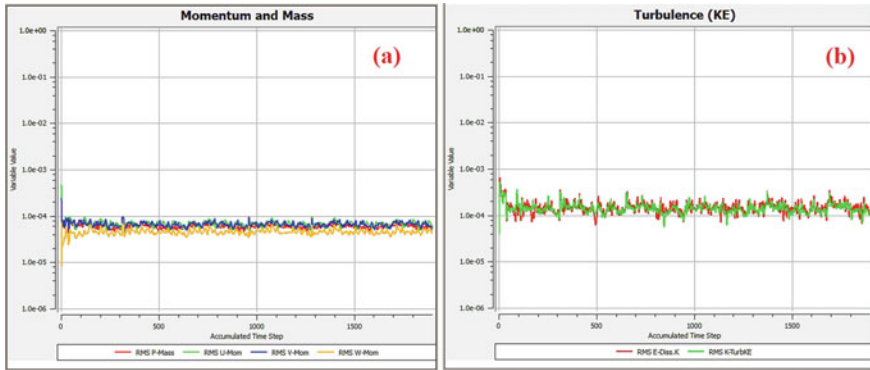
Fig. 3 **a** Mass and momentum displacement with respect to the computational time steps. **b** Energy dissipation and turbulence behavior over the computational time steps

distributed over the subsequent time steps without any significant peak formation, which may represent the disturbance in the flow phenomenon and the rotor motion. Subsequently, the energy dissipated to obtain the anticipated power output by monitoring the turbulence nature of the overall flow pattern in and over the rotor domain has been illustrated in Fig. 3b.

Throughout the computational study on understanding the power augmentation in the wind energy conversion system, the momentous intrinsic properties such as torque and pressure coefficients, which will decide or impact the overall power output, were briefly analyzed. The coefficients of the pressure gradient with respect to the varying chord length for different operating conditions and orientations were illustrated in Fig. 4. Subsequent to the brief analysis with respect to obtained pressure gradient, the main objective of the study is focused on the obtained coefficients of torque with respect to various operating environment. Figure 5a illustrates the significant impact of deflector plates, and its orientation has been represented in a graphical form. In which the curve of the initial stage with its respective orientation shows an enhanced peak formation of the required torque. The effectiveness of the deflector plates and its function as a power augmenter has been indicated with respect to its orientation. Further, the individual blade performance with respect to the torque enhancement at different orientations has been illustrated in Fig. 5b, respectively.
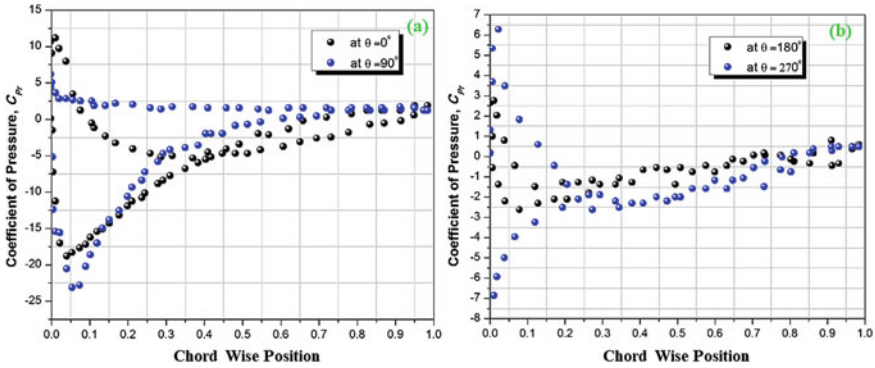
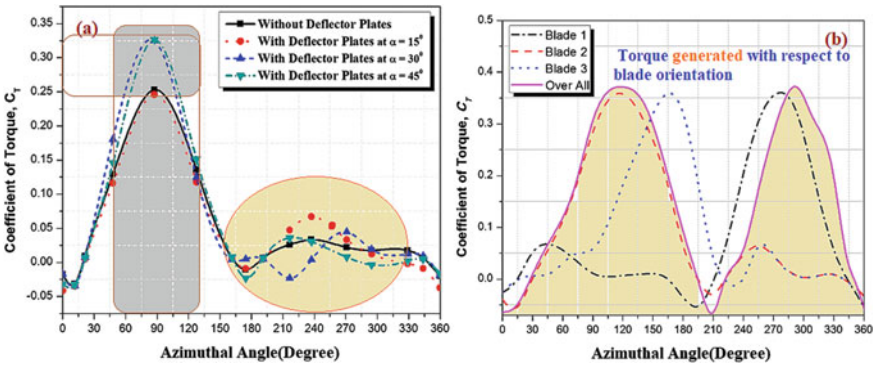**Fig. 4** Coefficient of pressure gradient with respect to chord position

Fig. 5 Coefficient of torque with respect to blade orientation associated with the revolution of rotor domain

4 Conclusion

From the observation of the computational study, the implication was as follows:

- The NACA 25112 is observed to significantly impact the aerodynamics behavior with respect to varying operating conditions.
- The accumulation and distribution of pressure gradient on the turbine blade were more concentrated near the hub than the blade tip position on the outer surface facing the stator domain.
- The orientation of the deflector plates at $\alpha = 30°$ and $45°$ shows a significant improvement in enhancing the torque generation and the overall power output.

References

1. Karthik Selva Kumar K, Kumaraswamidhas LA (2020) Investigation on stability of an elastically mounted circular tube under cross-flow in inline square arrangement. Iran J Sci Technol Trans Mech Eng 44:313–325
2. Carroll J, McDonald A, McMillan D (2016) Failure rate, repair time and unscheduled O&M cost analysis of offshore wind turbines. Wind Energy 19(6):1107–1119
3. Karthik Selva Kumar K, Kumaraswamidhas LA (2015) Experimental investigation on flow-induced vibration excitation in an elastically mounted circular cylinder in cylinder arrays. Fluid Dyn Res 47(1):015508
4. Aftab SMA, Ahmad KA (2017) CFD study on NACA 4415 airfoil implementing spherical and sinusoidal Tubercle Leading Edge. PLoS ONE 12(8):0183456
5. Karthik Selva Kumar K, Kulkarni V, Sahoo N (2019) Investigation on flow characteristics and performance of a vertical axis wind turbine with deflector plates. In: ASME gas turbine India conference

Design and Development of Automatic Tennis Ball Collector

S. Shankar, R. Nithyaprakash, C. Maheswari, M. Harish, M. Kishore, and V. Moneesh

Abstract Tennis players frequently practice from one side of the court without an opponent on the other side to return by hitting many balls. During practice sessions, personally collecting the balls took more time. The aim of this project is to design and construct a tennis ball-collection robot that can automatically gather the balls from one half of the court, releasing the player to rest rather than physically collecting the balls. This work includes a detailed design, a background data, prototypes, and concept models. We developed a novel autonomous or semiautonomous mobile robot for the purpose of gathering tennis balls for our capstone project. Two independently operating wheels help the robot move, while a castor serves to stabilize it. Tennis balls are pushed into a basket on top of the robot by a rotating brush, which serves as the novel collection mechanism. The drum spins with the help of a motor at a speed that has been confirmed through trial. To ensure that the adopted concepts and conceptual designs are practical and solid, three subsequent functional prototypes have been conceived, constructed, and tested. Tennis players can also use Arduino programming to direct the robot to move and collect the balls if it is unable to locate, identify, and gather tennis balls on its own. All tennis balls on the court will be recognized and localized in future using global cameras and a centralized image-processing system. Furthermore, it is believed that this system will handle navigation for mobile robots as well as path planning for the best possible outcome.

Keywords Tennis court · Autonomous mobile robot · Path planning · Ball-picking mechanism

S. Shankar (✉) · R. Nithyaprakash · C. Maheswari · M. Harish · M. Kishore · V. Moneesh
Department of Mechatronics Engineering, Kongu Engineering College, Erode,
Tamilnadu 638060, India
e-mail: shankar@kongu.ac.in

1   Introduction

Tennis is a sport that is often played between two teams of two players each. The tennis ball is hit over the net by each player using a racquet, causing it to land on the court of the opposition. European monks invented the game in the beginning so that it could be played during religious events for amusement purposes. The ball was hit with a hand during the first phase. Before the racquet with adaptable handling and efficient hitting and serving was invented, the leather glove quickly became a thing [1]. Similarly, the tennis ball has undergone numerous changes, transitioning from a wooden ball to the synthetic fibre ball we use today. The tennis ball used today has an optic yellow colour and a diameter of about 6.7 cm. The width and colour of tennis courts haven't changed much over the years. The most typical tennis court configuration used in major competitions nowadays measures 78 feet in length and 36 feet in width. The purpose of this project is to generate information that will be helpful in determining the presence and location of tennis balls. The necessary data will then be exported and used as input by the tennis ball robot navigation system. All robots are made to replace humans in tasks, which is fundamental to both their design and function. There are a lot of repetitive jobs in life, and if robots are capable of doing them, that load may be lessened. Having said that, there are many situations in which robots are a perfect substitute for people. Tennis players train with multiple balls one after the other in order to hone their skills through repetition. The player and the instructor must pick up the balls again to resume the lesson when they are finished, costing them money and important time. These days, balls are picked up and delivered to the ball dispenser by humans utilizing machines with trolleys, but they are always operated by people. The requirement for dedicated and specialized vehicles is becoming a necessity in order to improve this work.

The two main issues that come up when discussing mobile robots are motion control and path planning. Robot route planning, according to Strandberg [2], involves the detection of collision-free path from one place to another. There are a few things to take into account while designing a path for a mobile robot, including the environment in which the robot workspace is located, the path planning algorithm, and the different path planning methodologies.

1.1   Robot Locomotion

Mobile and stationary robots are the two categories into which robots may be separated. Robots that can't move or, to put it another way, have a fixed posture are called stationary robots. Mobile robots were characterized by Lima and Ribeiro [3] as a device that was very adaptable to its environment. Additionally, mobile robots require a system with the following functional properties: mobility, which denotes complete freedom of movement in relation to its environment; minimal human supervision; and perceptual capacity, which denotes the ability to sense and respond in any

circumstance. To sum up, the mobile robot's main strengths are its ability to move around its environment and to navigate on its own. These two traits are the exact antithesis of industrial robots, which depend on hard-coded codes to carry out their repetitive jobs and are fixed to their station. As the need for mobile robots grows in this day and age, many different varieties are designed and developed for usage in a variety of fields. Legged and wheeled robots, on the other hand, are the most prevalent and frequently created by scientists.

Wheeled mobile robots (WMR) are mobile robots that move around their surroundings by employing powered wheels, typically equipped with motors. WMR are extensively and frequently used by researchers and engineers because they are simple to develop, simple to implement, and effective for robots that need speed. As their centre of gravity does not alter when they are moving or at rest, they also exhibit greater superior stability under static as well as dynamic motion in comparison with legged robots [4]. Although WMR may have a different number of wheels, three wheels are thought to be sufficient for static and dynamic balance.

In order to select the greatest and most functional wheel for the robot, attention should be paid to its design and requirements. When all you need to do is steer and connect wheels to a motor, fixed wheels work fine. Robot balance is best achieved with spherical and orientable wheels. Although expensive and less effective, omni wheels are a great option for both steering and driving. When utilized for positioning control, wheels can slip, rendering the system unstable robot on wheels. This sort of WMR predominates. The easiest setup to design and construct is this one. The added cost of the fourth wheel and occasionally an additional motor to propel them is a disadvantage of this arrangement compared to the three-wheeled configuration, but their benefits outweigh these disadvantages. Three different configurations of this kind of robot exist: (1) two powered, two free spinning wheels, (2) two-by-two powered wheels for tank-like movement, and (3) two-by-two powered wheels with car-like steering. Figure 1 depicts the movement of two motorized wheels and two free-turning wheels.

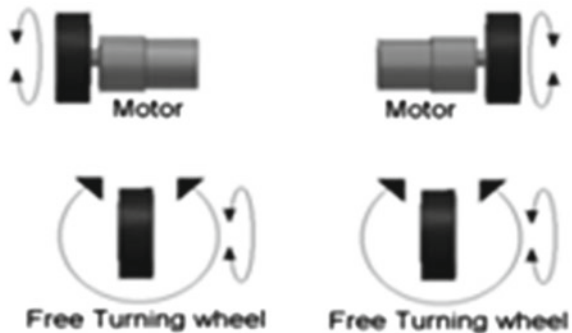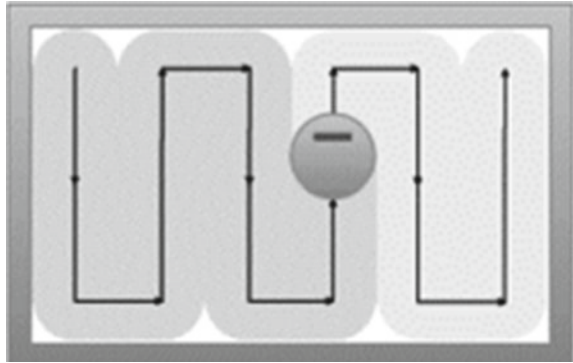**Fig. 1** Two powered, two free-turning configurations

1.2 Path Planning Techniques

Finding a collision-free path from one point to another is what robot path planning is all about, claims Strandberg [2]. When a robot runs into barriers, deviates from the course, or travels too slowly to the desired location, the path planning is deemed insufficient. The environment of the robot workspace, the route planning algorithm, and different path planning methodologies are a few things that should be taken into account while designing a path for a mobile robot. The static and dynamic environments can be described as the surroundings or environment of the workspace. Dynamic obstacles can move, such as a human moving around or another mobile robot using the same workspace, whereas static obstacles are any objects or obstructions in the workspace that are not moving. The robot proceeds in that direction if a yellow colour ball is there, otherwise it avoids that object, according to the path planning algorithm utilized in this system, which detects the presence of an object using an ultrasonic sensor and then sends a signal to the camera lens module. The robot will attempt to complete its objective while avoiding obstacles using sensors [5]. Cai [6] claims that the design of an intelligent robot's path can be divided into two parts: complete coverage optimization path planning and point-to-point optimization path planning. Coverage path planning (CPP) based on Enric and Marc [7] is the process of figuring out a route that avoids barriers and covers every point in a region or other designated place. Robots that collect objects, clean with vacuums, mow lawns, and other similar devices all heavily rely on CPP (Fig. 2). The path planning methods for various robotic applications were clearly detailed in previous literatures [8–11].

2 Existing System

There are few other existing systems are existing with various ball-picking mechanisms and autonomous tennis ball-collecting robot. The section deals with the other similar existing systems related to automatic tennis ball collector.

Fig. 3 Robot with multiple channel tennis ball

2.1 Smart Phone Interfaced Intelligent Tennis Ball-Collecting Vehicle

An autonomous vehicle that is fitted with a unique tennis ball collector that is sophisticated enough to collect tennis balls. The robot's innovative tennis ball collector has various channels and is made up of two parallel acrylic discs connected by four springs. Each disc has a hole drilled through the centre so that it may be attached to an axle. The two discs in Fig. 3 are composed of a material that is robust and have four springs attached in order to accommodate the tennis balls between them (Fig. 3). The ball is then forced between the two discs as the discs roll through the tennis balls, as seen in Fig. 3.

2.2 Collecting Using Vacuum and Suction

The collecting device, which operates in a similar manner to a sweeper, uses air to gather up the balls from the ground Fig. 4. This concept is a form of garbage collection technique. All balls currently on the ground will be collected using this method. However, for this method to be effective, very precise location, a strong power source, and the possibility of other things on the ground besides balls must be taken into consideration.
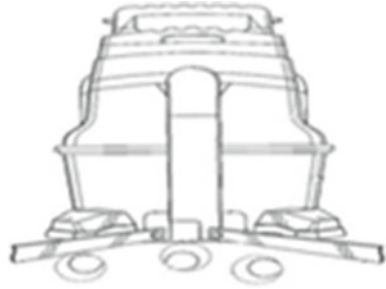
Fig. 4 Vacuum collecting robot

**Fig. 5** Collecting using two cylinders with vertical actuator

2.3 Two Cylinders with Vertical Actuators for Collecting Tennis Ball

The basic working principle of this concept is illustrated in Fig. 5, where two revolving cylinders connected to two vertical motors are used to gather the balls and deposit them in a storage space. This technique has a low collecting speed, which does not meet our needs, but it has a high speed of collection and may be utilized with scattered balls.

2.4 Collecting Using a Rough Conveyor

The idea behind it is to employ a robot-attached oblique conveyor to move a rough conveyor that picks up balls and deposits them in a storage area Fig. 6. It appears to be a technique for gathering crops. Despite the high effectiveness of this method in collecting balls, it does not satisfy our needs due to its slow collecting pace.
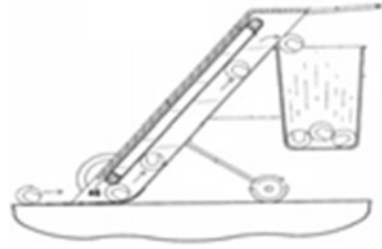
3   Proposed System

Robotic service workers are a growing trend and a great asset to society. They participate in a few sporting events as well. Tennis players will have less work to accomplish because they won't have to stop and pick up tennis balls. For a robot that collects tennis balls, there are two main jobs. Tennis ball identification is one of them; establishing a path is necessary when collecting balls. Machine learning algorithms are capable of carrying out these two tasks. The majority of traditional machine learning techniques, sensing the present of object using ultrasonic sensor then signal sent to camera lens module, if yellow colour ball is present, the robot moves on that direction or else it avoids that object. However, it requires human defined parameters and are therefore useless for these robotic jobs. Approaches based on deep learning that use nonlinear models have a lot of potential for solving these issues. The problem of the travelling salesman serves as the basis for our route planning (TSP), i.e. a man whose duty it is to travel around and promote goods or services, frequently within a designated area or territory. To find tennis balls, we also use the You Only Look Once (YOLO) method; i.e. it was a breakthrough in the object detection field as a first approach that treated object detection as a regression problem. These two models are implemented on the Arduino Uno board. When the proper training data set and training progression are utilized, these two models perform good on the tennis ball-collection robot. The majority of tennis players would prefer to take a rest after lengthy practice sessions than collect tennis balls. Instead of using energy to manually pick up the tennis balls, they would prefer an autonomous gadget to rapidly collect them so they may drink water, rest and chat with their training partner.

3.1   Need of Automation

Unfortunately, we cannot spend all of our time playing by collecting scattering of tennis balls after the practice. The tennis ball retriever is now a necessary piece of tennis equipment. They are not working for every person who play tennis. And sometimes, the player wants to practice whole the night, in that time the ball persons are not available. So, the main focus is to automate this process. Because of collecting

the tennis ball, the advanced version of bots is used in many foreign nations. The goal of our proposed method is to collect the balls over the field automatically when the player gets relax as much as we desire (remotely).

3.2   Advantages of Automatic Tennis Ball Collector

The controlling operations of the automatic tennis ball collector bot is to be easy and simple. The bot has an automation system with its solution. So, we need only one bot for the ground to get entire balls in it. At the same time, this bot control and efficient usage of resources and it can be used in longer time and in efficient way.

4   Methodology

Designing and creating path planning strategies for a robot that retrieves tennis balls is the main goal of this project. During solitary practice, the robot will clean up every ball that has been left lying around the court. The robot will try to stay in one place and sweep all of the balls while avoiding any impediments. The design and implementation of the automatic tennis ball collector are the main topics of this section. To test the robot more directly in its physical capacity, the experiment was carried out on a real tennis court. A number of variables, including robot locomotion, geometry, wheel design, and others, affect how a robot moves. These elements are taken into account in the light of the literature review. The robot has a few sensors, including proximity and sonar sensors, which are used to detect impediments. Data was gathered from the studies while a few path planning techniques were incorporated into the robot.

4.1   Tennis Ball Retriever Robot

Figure 7 depicts the built robot in isometric view of the actual tennis ball retriever robot. The robot can endure being struck by a tennis ball since its body is composed of stainless steel. After the robot was constructed, its characteristics, including its turning radius, velocity, and overall weight, were established through calculations and trials. In this subtopic, the tennis ball retriever robot's specifications will be displayed.

Fig. 7 Actual tennis ball retriever robot in isometric view

4.2 Mechanism of the System

The workflow of the automatic tennis ball collector. Workflow contains six stages of process, the first stage is detection of balls using ultrasonic sensor and mapped signal is passed to the microcontroller, microcontroller commends the motor drive to rotate the motor front, the ball-collecting mechanism rotates continuously to collect the tennis balls and the mechanism repeats itself based on the Arduino code to the area to detect another ball. The entire process is done by microcontroller embedded program shown in Fig. 8. In this, we connect the DC motor into drive which gives equal coordinates with similar controllers and the drive is connected by Arduino Uno. In which the coordinates and camera are connected to that system. In which the other DC motor is connected from front side to the battery. The bot is moved, rotate and stop based on the comments. Then it will claim the tennis ball by ball-picking mechanism system connected with DC motor. The DC motor is worked on a principle based on relative speed mechanism. It generates velocity and torque depending on the voltage and current input. The front DC motor operates as a closed loop system, delivering torque and velocity in response to commands from a speed based on the DC drive operating the two DC motors. The loop is closed by a feedback device. RC controller, both with and without a microprocessor, and use it for a range of tasks. The Motor A and Motor B screw terminals should be connected with our robot's motors. The L298N Motor Driver is a controller that conveniently regulates the direction and speed of up to two DC motors using an H-Bridge. The mechanism of the sytem for ball colleting was based on previous literatures [12–15].

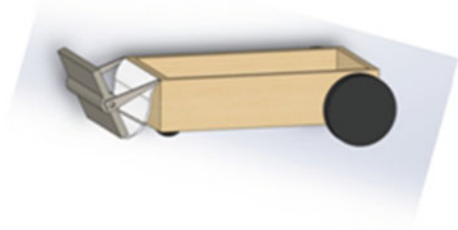**Fig. 8** Flowchart for working of automatic tennis ball collector

4.3 CAD Modelling

The design phase is the most crucial for any product. SolidWorks software was used to design this machine. The part drawings are initially created to the desired dimensions, and the parts are subsequently assembled. 3D model of tennis ball collector are shown in Fig. 9. SolidWorks' simplicity of use as a work environment is the primary factor in choosing it over AutoCAD. The motors' step-by-step actuation is shown in vivid detail. Every product has a design phase, which is its most important stage. Utilizing the software SolidWorks, this machine was created. SolidWorks were chosen over AutoCAD because of the issues with the latter's working environment. AutoCAD is the simpler tool to use if a total beginner was to compare the two, and after gaining a basic understanding of 2D drafting, the user might advance to 3D modelling and more complicated designs that would contain several parts, assemblies, and animations.

4.4 Electrical Section

The microcontroller, relay, and rectifier circuits are the three main components of the electrical sector. All of the circuits—aside from the microcontroller circuit, which is constructed using a microcontroller development board—are built on dot boards. Relays on a relay board translate microcontroller signals into commands for actuators. Figure 10 displays the actual electrical circuit in use. The Johnson motor, a torque-controlled motor, a motor driver, and a microcontroller make up the electrical part. Jumper wires are used to construct every circuit. The signals from the microcontroller are converted by the motor driver to actuate the components. Microcontrollers make up the electrical circuit. Planning, creating, testing, or supervising the development and installation of electrical equipment, such as lighting equipment, power systems, power distribution, receiver and transmitter-controlled systems, data communications infrastructure and electronic components falls under the category of electrical design. All the actuators are connected to the microcontroller's digital and analogue ports. The electrical section is shown in Fig. 10.

5 Design Specification

An automatic tennis ball collector is setup with 12 V output lithium phosphate (4X3 cells in parallel connection) rechargeable battery for power supply to robot, reason for using lithium phosphate cells instead of battery is to reduce cost with same efficiency. The battery backup is upon minimum of two hours. The flat blade with plastic brushes attached top and bottom is used as a ball-picking mechanism in this project, the mechanism is rotating clockwise direction to pick tennis ball using a DC gear motor attached to the mechanism. Johnson gear motor with specification of 100 rpm, 12-V input is used in this project for motion. Path planning for robot to collect a tennis ball in a tennis court is done by programming a whole dimension of the tennis court in regarding to collect a tennis ball is programmed in UNO Adriano. By the above inputs, the automatic tennis ball collector is planned to make with more efficiency though many works are done under the same problem using high
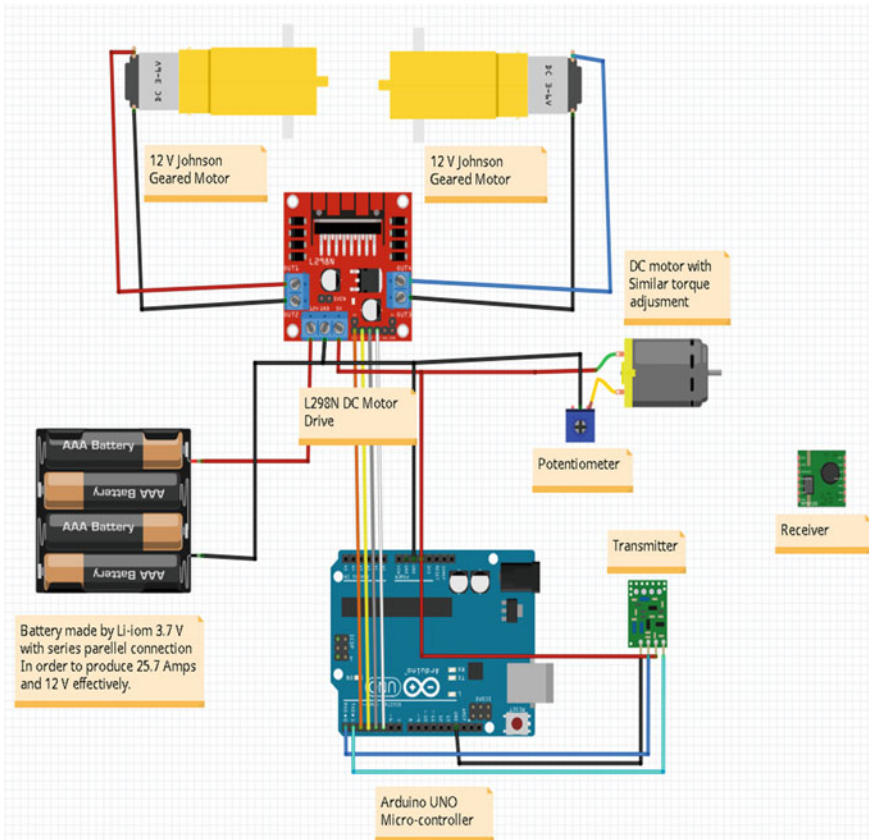
Fig. 10 Electrical section

specification cameras with object deduction (tennis ball), Raspberry Pi, costly ball-picking mechanism, etc. This work is also useful for physically challenged people involving in practice sessions to collect balls.

6 Conclusion

The concept has been designed with the help of existing automatic tennis ball retriever in order to prevent ball boy and to effectively promote night practice. This will stop the player from practising as much. It will take 3 to 4 h for it to start working. Some learning techniques are used to analyse the sensor data as when the drive with motor will be automated. The devices here interact with one another through built-in remarks, automate with intelligence, and are easy for humans to operate. The main objective of this project is to improve the efficiency of the automated ball-gathering

system. The above existing system has a low rate of collecting ball and lagging of ball in ball-picking mechanism while collecting a tennis ball to avoid it, this system consists of brushes to collect balls using Arduino Uno, which are affordable control devices; this system was built. The prototype for the intended robotic tennis ball collector was successfully made. A remote-control platform and two extra circuits are combined in the design. The first circuit takes in the analogue signal from the remote-control unit and uses a microcontroller and transistor to convert it to binary. The second circuit receives the binary signal that controls whether the ball cavity enclosure's claws are open or closed. The prototype demonstrates how to move about with ease and avoid any hazards.

References

1. Mnubi SA (2016) Motion planning and trajectory for wheeled mobile robot. Int J Sci Res (IJSR) 5(1):1064–1066
2. Strandberg M (2004) Robot path planning: an object-oriented approach, Stockholm. Royal Institute of Technology (KTH), Sweden
3. Lima P, Ribeiro MI (2002) Introduction to mobile robotics. In: Mobile robotics. Instituto Superior Técnico/Instituto de Sistemas e Robótica, pp 22–24
4. Zhao Y, BeMent SL (1992) Kinematics, dynamics and control of wheeled mobile robots. In: International conference on robotics and automation, Nice
5. Leena N, Saju KK (2014) A survey on path planning techniques for autonomous mobile robots. IOSR J Mech Civil Eng 76–79
6. Cai Z (2014) Research on complete coverage path planning algorithms based on A* algorithm. Open Cybern Syst J 8:418–426
7. Enric G, Marc C (2013) A survey on coverage path planning for robotics. University of Girona Press, Catalonia
8. Cao ZL, Huang Y, Hall EL (1988) Region filling operations with random obstacle avoidance for mobile robotics. J Robot Syst 5(2):87–102
9. Choset H (2001) Coverage for robotics: a survey of recent results. In: Annals of mathematics and artificial intelligence. Kluwer Academic Publishers Hingham, Pennsylvania, pp 113–126
10. Geraerts R, Overmars MH (2002) A comparative study of probabilistic roadmap planners. In: Workshop on the algorithmic foundations of robotics, pp 43–57
11. Kavralu LE, Svestka P, Latombe J-C (1996) Probabilistic roadmaps for path planning in high-dimensional configuration spaces. IEEE Trans Robot Autom 12(4):568–571
12. Szondy D (2014) Murata's dancing robotic cheerleaders showcase advanced group control. New Atlas, Tokyo
13. Elamvazuthi I, Singh V (2015) Development of an autonomous tennis ball collector
14. Farrell M, Hack J, Irwin R (2009) Bear claw: tennis ball collector. University of California, Berkeley
15. Ford D (1999) The BallBot project. In: Encoder: the newsletter of Seattle robotics society, pp 1–12

Multiphysics Modelling and Simulation of Hydrogel Membrane for Water Desalination

Pavan Kumar Gurrala and **Ingit Trivedi**

Abstract A new method to desalinate water by making use of swollen hydrogels under externally applied pressure-difference-driven diffusion is being proposed. The swelling process of hydrogel involves diffusion, polymer–solvent interaction, and mechanical deformation. The present research aims to investigate the use of FEA model to simulate hydrogel as a semi-permeable membrane. Diffusion of water molecules in hydrogel is modelled using Fick's law, polymer–solvent interaction described by the Flory–Huggins mixing theory and mechanical deformation reported with the theory of rubber elasticity. The FEA model yielded a set of partial differential equations with ordinary differential equations for which COMSOL Multiphysics 5.5 is selected as the simulation software. A parametric analysis is conducted to evaluate the overall significance of the model parameters on hydrogel's behaviour. Reproduction of the hydrogel's poroviscoelastic behaviour to the exterior incentives and the transport phenomena of species through hydrogel has been successfully demonstrated and validated for a new methodology of water desalination considering NaCl (salt) as a permeate. The salt rejection ratio has been estimated, and it is found to be 40% with an average salt volume fraction reducing from 0.5 M to 0.3 M. The suggested model may also be explored to design and optimize hydrogels for biological separations.

Keywords Hydrogel · Poroviscoelastic model · Swelling · Solution–diffusion model · Reverse osmosis · Desalination

1 Introduction

In contemporary years, stimuli-sensitive hydrogels have pulled greater consideration for their potential in an extensive array of different purposes, specifically in the biomedical and biotechnical areas. Hydrogels are a 3D network of long polymer

P. K. Gurrala (✉) · I. Trivedi
Department of Mechanical Engineering, Pandit Deendayal Energy University, Gandhinagar, India
e-mail: go4pavankumar@gmail.com

molecules and cross-linked hydrophilic polymeric networks able to absorb cum desorb an enormous measure of water based on external inducements [1]. This is accomplished using polyelectrolyte gels, and the phrase "superabsorber" is acknowledged [2]. Hydrogel has high hydrophilic, biocompatibility, and low fouling potential. Due to these characteristics, it can be utilized as a membrane in the laboratory, biological separations, drug delivery systems and applications, namely artificial skin and corneal prostheses [3]. This hydrogel is used for various applications in greater volume. This material is utilized in agricultural soil to increase water-holding capacity [4] and in underwater cable insulations [2] to name a few. However, the wide-reaching market is individual cleanness commodities [5, 6]. The increasing utility of this material makes researchers cognize that mechanics is fundamental across all fields. As a result, many attempts are done to acquire a numerical model to characterize the swelling and shrinking behaviour of stimuli-sensitive hydrogels.

Out of many variants of the proposed swelling theories, the most fundamental is the phenomenological theory regarding the modelling of the enlargement behaviour of gels, proposed by Flory and Huggins in 1943. Flory–Rehner model is additional work of Flory–Huggins. In this theory, elastic deformation due to absorption and desorption has been performed using water in gels [6]. The chemo-electro-mechanical behaviour model for the pH-responsive hydrogel consists of two nonlinear equations: Nernst–Planck, Poisson's equation for electric potential followed mechanical field equation [7]. Kang Lu et al. proposed a complete mathematical model of protein gel swelling, and it was modelled using the Generalized Maxwell–Stefan (GMS) equation [8]. Johannes Höpfner et al. introduced an approach to desalinating water by charged hydrogels while applying external forces, Donnan Theory [9]. D. Caccavo et al. proposed the monophasic model to describe the poroviscoelastic performance of the hydrogel within the area of continuum mechanics [10]. From the studies, different mathematical models have been proposed to characterize the swelling and shrinking behaviour of stimuli-sensitive hydrogels. These are broad of two approaches: multiphasic and monophasic. In terms of the multiphasic model, the hydrogel exists in two phases, a polymeric network, the interstitial water, and the conceivable existence of other classes. The multiphasic model is defined in the framework of continuum mechanics. The multiphasic model is difficult to achieve as many PDEs are to be solved. Alternatively, in the later method, the gel is considered a mono phase where many species co-occur. In comparison, monophasic method is based on a thermodynamical principle [10]. Due to this reason, the monophasic method is adopted. The solution–diffusion method is widely recognized method for moving across these hydrogel films. The estimates of this classic are in better arrangement than of the experimental data.

2 Methodology

After a broad literature survey, the methodology as described in Fig. 1 is arrived to achieve the objective of this research. As the objective of this research is to project hydrogel as a membrane for desalination and to characterize the nonlinear performance of hydrogel, in a branch of nonlinear solid mechanics. Additional step is to transport the diluted species of known concentration through the swelled hydrogel. To achieve these goals, a constitutive equation is taken count which support the mass and linear moment balance equation. The polymer network is taken as viscoelastic and described using SLS model and time-dependent elastic stretch is calculated by affine network theory. The Flory–Huggins solution theory is appropriate for interpreting the interaction between polymer and solvent. The water flux and salt rejection are to be predicted by solution–diffusion model. The developed PDEs are reduced to a 2D-axisymmetric problem to get a shape of a RO membrane and then transformed into weak form and solved by using FEM software.

2.1 The Poroviscoelastic (PVE) Model

Poroviscoelasticity is a specific property of a hydrogel. Hydrogel processes the viscoelastic properties poroelastically through absorbing/desorbing water. For which kind of properties should a body have to be considered as a continuum? The body is considered as a continuum by taking the whole-body uniform without leaving any cavities. Mathematically, the deformation of a continuous body can be described in Lagrangian approach and Eulerian approach. These kinematic fields however alone cannot predict the final configuration of the body under the action of the external loading. To predict the final configuration, it is required to generalize the law of mechanics (Balance Laws) parallelly for particles to the continuum bodies. So here mass balance and moment balance equations are taken into count in along with volumetric constrain equation. Here the dry gel is referred to be at an initial state.

And the constitutive equations are to be formulated in such a way that there is a balance between mass and momentum equations. In this work, the dissipation inequality approach [11] also known as "free energy imbalance" has been considered while deriving the constitutive equations in the reference coordinates is expressed in Eq. 1.

$$\frac{\partial A_D}{\partial t} - \overline{\overline{P}} : \dot{\overline{\overline{F}}} - \mu_1 \dot{c}_1 + \overline{h}_1 \cdot \overline{\nabla} \mu_1 \leq 0 \tag{1}$$

Equation 1 states that, total change in the free energy (A_D is Helmholtz free energy density) of system are affected by established influence exerted on ($\overline{\overline{P}} : \dot{\overline{\overline{F}}}$) and by thrust transmitted into the system through the solvent transport ($-\mu_1 \dot{c}_1 + \overline{h}_1 \cdot \overline{\nabla} \mu_1$).
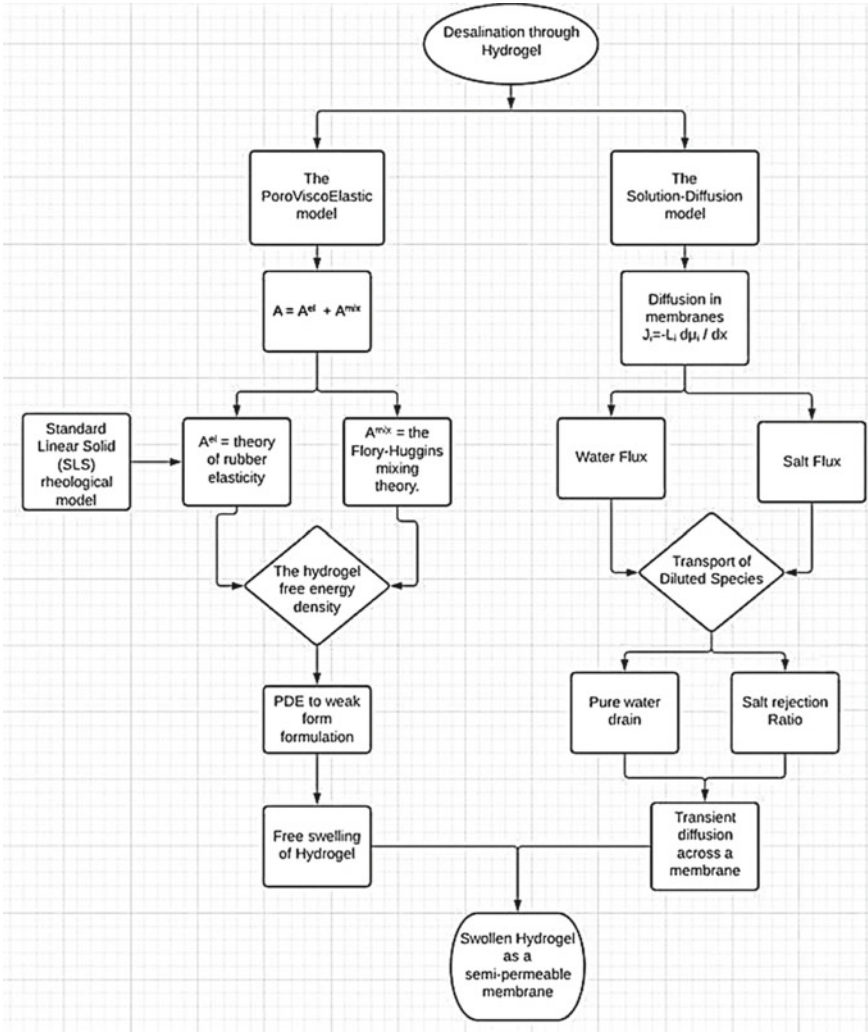
Fig. 1 Method employed to investigate the hydrogel as a semi-permeable membrane application

As per free energy model [12, 13] the Helmholtz free energy density (A_D) is defined as the linear addition of the free energy of elastic stretch of the polymer network and the free energy of mixing of dry configuration of the body, as expressed in Eq. 2.

$$A_D = A^{el} + A^{mix} \tag{2}$$

The elastic components are as adopted from the Flory–Huggins theory of mixing. Elastic component is acquired from rubber elasticity theory, while mixing component

is obtained Flory–Huggins theory of mixing. In the present work, viscoelasticity of a polymer network is described using a rheological standard linear solid (SLS) model. Therefore, we can rewrite (Eq. 2) for the total free energy density as:

$$
A_D\left(\overline{\overline{F}}_D, c_{1D}, \overline{\overline{F}}^{\text{visc}}\right) = \frac{G_1}{2}\left[\overline{\overline{F}}_D : \overline{\overline{F}}_D - 3 - 2\log(J_D)\right]
$$
$$
+ \frac{G_1}{2}\left[\overline{\overline{F}}_D\overline{\overline{F}}^{\text{visc}^{-1}} : \overline{\overline{F}}_D\overline{\overline{F}}^{\text{visc}^{-1}} - 3 - 2\log\left(\det\left(\overline{\overline{F}}_D\overline{\overline{F}}^{\text{visc}^{-1}}\right)\right)\right]
$$
$$
+ RT\left[c_{1D}\ln\left(\frac{\Omega_1 c_{1D}}{1 + \Omega_1 c_{1D}}\right) + \frac{c_{1D}\chi_{12}}{1 + \Omega_1 c_{1D}}\right] \tag{3}
$$

Due to the absence of solvent molecules in dry state of polymer network, there is no polymer–solvent interaction happened. This leads Eq. 3 to mathematical singularity, $(\Omega_1 c_{1D} = 0)$. To encounter such problem a need to add one reference state in between dry and deformed state. After taking reference state as an initial state, we can rewrite the (Eq. 3) as,

$$
A_D\left(\overline{\overline{F}}, c_1, \overline{\overline{F}}^{\text{visc}}\right) = \frac{1}{J_0}\left\{ \frac{G_1}{2}\left[\overline{\overline{F}}_0\overline{\overline{F}} : \overline{\overline{F}}_0\overline{\overline{F}} - 3 - 2\ln\left(\det\left(\overline{\overline{F}}_0\overline{\overline{F}}\right)\right)\right] \right.
$$
$$
+ \frac{G_1}{2}\left[\overline{\overline{F}}_D\overline{\overline{F}}^{\text{visc}^{-1}} : \overline{\overline{F}}_D\overline{\overline{F}}^{\text{visc}^{-1}}\right.
$$
$$
\left. -3 - 2\log\left(\det\left(\overline{\overline{F}}_D\overline{\overline{F}}^{\text{visc}^{-1}}\right)\right)\right]
$$
$$
\left. + RT\left[J_0 c_1\ln\left(\frac{J_0\Omega_1 c_1}{1 + J_0\Omega_1 c_{1D}}\right) + \frac{c_1 J_0\chi_{12}}{1 + J_0\Omega_1 c_1}\right]\right\} \tag{4}
$$

where J_0 is the volumetric deformation $\left(J_0 = \det\overline{\overline{F}}_0\right)$ of polymer network. Equation 4 describes the consistent deformation to the reference configuration from the dry state. To obtain constitutive equations, preliminary investigations have been performed in prior to using (Eq. 4) in the dissipation inequality (Eq. 1). As the volumetric constraint is imposed on deformation, it shows numerical uncertainty and causes locking phenomena. To overcome these uncertainties and find out the local maxima and minima of the function, Lagrange-multiplier method (two-field) is adopted. While solving in the FEA software the equations of the derived constitutive equation for stress $(\overline{\overline{P}})$, water chemical potential (μ_1), kinetic laws for the dashpot deformation $(\overline{\overline{F}}^{\text{visc}})$, and water flux $(\overline{h}_1)$ are defined as a variable.

In most of the cases, hydrogels are used as carriers to deliver or absorb or transfer through certain species as these respond to an external stimulus. Coupling of PVE model with a diffusion of species through the hydrogel is hence an important step towards the depiction of actual systems using hydrogels as a separation agent. In the following section, the upgradation of the proposed PVE model is coupled with a suitable transport model to recast hydrogel as a membrane.

2.2   The Classical Solution–Diffusion (SD) Model

In any filtration processes, it is desired to remove a solute molecule selectively, relative to a solvent molecule. This can be achieved using the difference between the pressure that is used to initiate the diffusion through a polymer membrane [14–19]. According to the SD model permeants diluted in the membrane and afterwards dispersed across the membrane then drop the concentration. Permeants are detached due to differences in the respective solubilities in the membrane material and changes in the rates through that they detach across the membrane as shown in Fig. 2 [20]. It seems to be quite reasonable to say that salt can permeate only through polymer membrane in which polymer membrane is a solvent of the salt as well. Diffusive permeability of 5% NaCl aqueous solution through some hydrated polymer membranes was investigated [21] using a theory based on the free volume theory of diffusion. According to this theory, a molecule of solute distributes through the hydrogel by "jumping" into the voids existing in the network. Free volume is thus formed on statistical bases due to random thermal motions [22].

The SD model is very much applicable to reverse osmosis in polymer membrane through the principle of membrane diffusion through a dense layer. A classical SD model is shown in Eq. 5:

$$J_w = \frac{D_{wm} C'_{1m} \overline{V}_m}{RT\delta}(\Delta P - \Delta \pi)$$
$$= A_w(\Delta P - \Delta \pi) \tag{5}$$

The diffusivity of water inside the membrane, D_{wm} (m^2/s), and feed flow water concentration, C'_{1m} (mol/m^3), and so water permeability inside membrane (A_w) are supposed to be constant at a particular temperature. $\Delta P = P_1 - P_2$ is hydrostatic

Fig. 2 Molecular transport through membranes in SD model
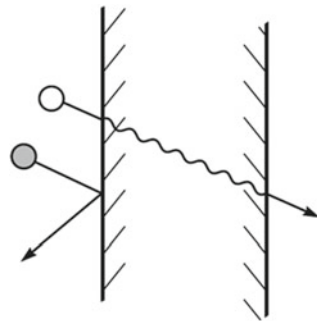
Dense solution-diffusion membranes separate because of differences in the solubility and mobility of permeants dissolved in the membrane material
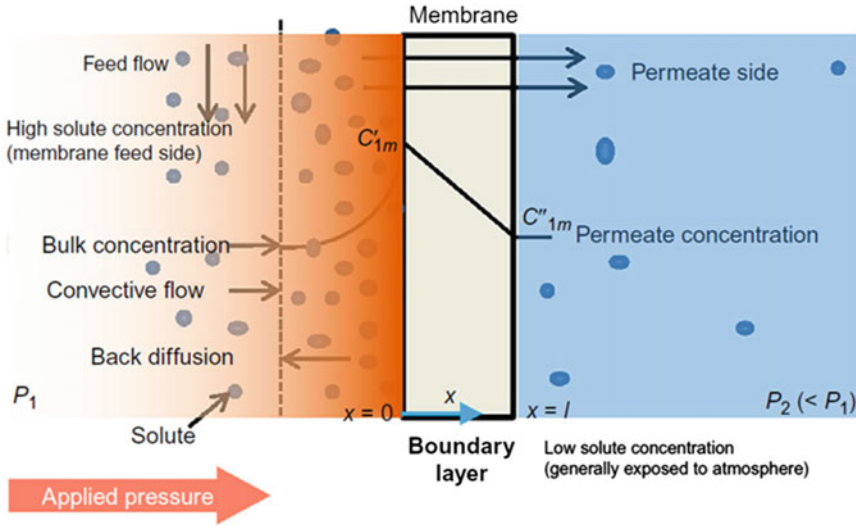
Fig. 3 Thermodynamic principle of reverse osmosis [22]

pressure difference. P_1 is the applied pressure on the feed side and P_2 on permeate side (atm) and $\Delta\pi = \pi_1 - \pi_2$ is the difference of osmotic pressure of feed solution to that permeate solution. $\overline{V}_m$ (m³/mol) represents the molar volume of solvent. Figure 3 shows a representation of solvent and solute transport in the reverse osmosis process. C'_{1m} and C''_{1m} are the feed and permeate side solute intensities.

For the diffusion of solute through the film/membrane the flux equation is mentioned in Eq. 6:

$$
\begin{aligned}
J_s &= \frac{D_{sm} K_s}{\delta \Gamma} \left(C'_{1m} - C''_{1m} \right) \\
&= A_s \left(C'_{1m} - C''_{1m} \right) \quad \text{where } A_s = \frac{D_{sm} K_s}{\delta}
\end{aligned}
\tag{6}
$$

$J_s =$ solute flux $\left(\text{kg solute/s m}^2 \right)$

$D_{sm} =$ Diffusivity of solute in membrane (m^2/s)

$K_s =$ distribution coefficient

$A_s =$ solute permeabitity constant, (m/s).

Equation 7 demonstrates the solute rejection ($\mathbb{R}$) ratio.

$$
\mathbb{R} = \left(1 - \frac{C''_{1m}}{C'_{1m}} \right) \times 100\%
\tag{7}
$$

The SD model is composed of the various physical properties D_{wm}, D_{sm}, and K_s of the membrane, and it should be determined experimentally for every membrane.

3 Finite Element Formulation of the Problem

Both the mathematical model which represents the hydrogel's poroviscoelastic behaviour (Study: 1) and the transport of diluted species through hydrogel (Study: 2) have been coupled together and implemented in 2D-axisymmetric geometry, COMSOL Multiphysics® 5.5 [23] then solved in Lagrangian frame. Coupling of both the models is carried out in software in such a way that one model's solution is working as an initial condition for the second model. It has to be taken care of when formulating the problem in a 2D-axisymmetric requires cylindrical (R, θ, Z) coordinates, that eases to (R, Z) in axisymmetric assumption. Care needs to be taken while 2D-axisymmetric problems (to reduce computational work with a provision of having finer mesh sizes) where in the coordinate system has to be changed from Cartesian to Cylindrical coordinates. The axisymmetric nature thereby reduces the coordinates to (R, Z).

3.1 Weak Formulation of the Study: 1

For many of the different types of physics simulated with COMSOL Multiphysics by applying a weak formulation. It is used behind the scenes to build up the mathematical model as shown in Fig. 4.

3.2 Transport of Diluted Species for Study: 2

In the software, "The Transport of Diluted Species" interface facilitates a defined background to investigate the evolution of chemical species transported by diffusion and convection with assumption that all species present are diluted; their concentration is small as compared to a solvent fluid or solid. From Fig. 4, J_i (SI unit: $mol/(m^2 s)$) is the mass flux (relative to mass averaged velocity). It is used as boundary condition and also while computing the flux. Transport of diluted species is because of the diffusion of the molecular species. The mass flux J_i is also coined as diffusive flux, as mentioned in Eq. 8:
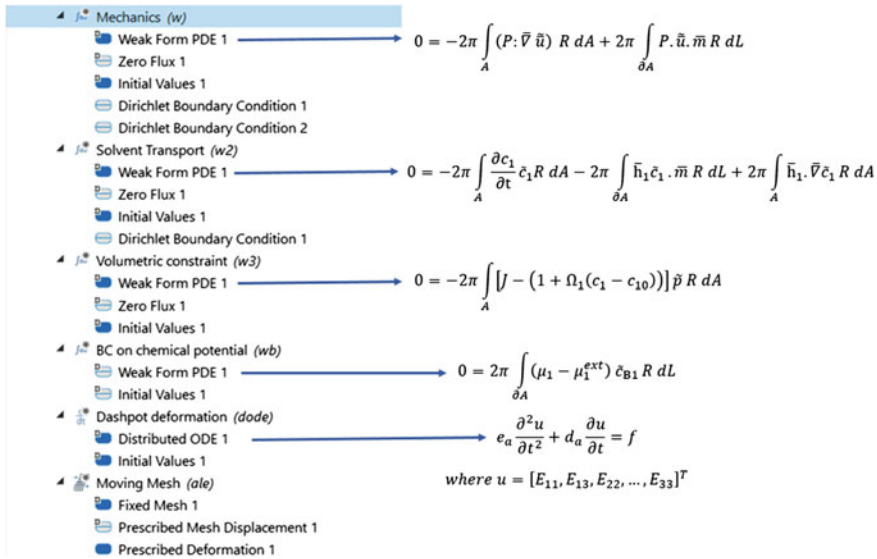
$$J_i = -D.\nabla C_i \tag{8}$$

▲ ⌐ Mechanics *(w)*
　　📖 Weak Form PDE 1 ——————————→ $0 = -2\pi \int_A (P : \bar{\nabla}\,\tilde{u})\, R\, dA + 2\pi \int_{\partial A} P.\tilde{u}.\bar{m}\, R\, dL$
　　🗒 Zero Flux 1
　　📖 Initial Values 1
　　⊝ Dirichlet Boundary Condition 1
　　⊝ Dirichlet Boundary Condition 2
▲ ⌐ Solvent Transport *(w2)*
　　📖 Weak Form PDE 1 ——————————→ $0 = -2\pi \int_A \dfrac{\partial c_1}{\partial t}\,\tilde{c}_1 R\, dA - 2\pi \int_{\partial A} \bar{h}_1 \tilde{c}_1.\bar{m}\, R\, dL + 2\pi \int_A \bar{h}_1.\bar{\nabla}\tilde{c}_1\, R\, dA$
　　🗒 Zero Flux 1
　　📖 Initial Values 1
　　⊝ Dirichlet Boundary Condition 1
▲ ⌐ Volumetric constraint *(w3)*
　　📖 Weak Form PDE 1 ——————————→ $0 = -2\pi \int_A \left[J - \left(1 + \Omega_1(c_1 - c_{10})\right)\right] \tilde{p}\, R\, dA$
　　🗒 Zero Flux 1
　　📖 Initial Values 1
▲ ⌐ BC on chemical potential *(wb)*
　　🗒 Weak Form PDE 1 ——————————→ $0 = 2\pi \int_{\partial A} \left(\mu_1 - \mu_1^{ext}\right) \tilde{c}_{B1}\, R\, dL$
　　🗒 Initial Values 1
▲ ⌐ Dashpot deformation *(dode)*
　　📖 Distributed ODE 1 ——————————→ $e_a \dfrac{\partial^2 u}{\partial t^2} + d_a \dfrac{\partial u}{\partial t} = f$
　　📖 Initial Values 1
▲ ⌐ Moving Mesh *(ale)* 　　　　　　　where $u = [E_{11}, E_{13}, E_{22}, \dots, E_{33}]^T$
　　📖 Fixed Mesh 1
　　🗒 Prescribed Mesh Displacement 1
　　⬤ Prescribed Deformation 1

Fig. 4 Weak form implementation in COMSOL

The solution–diffusion (SD) model is implemented in the framework of transport of diluted species and solved with time-dependent case, because SD model describes the transport mechanism in reverse osmosis closely.

As per the SD model water flux (J_w) apply on the inlet boundary by using flux type "General inward flux" and salt flux (J_s) at the outlet of boundary by using flux type "External Convection" as shown in Fig. 5. Probes have been set to observe the estimation of the scalar quantity from a time-dependent simulation so as to measure evolution in the concentration of diluted species. A simulation with two cases is attempted in the software. In the first case, the reference frame is a moving mesh frame while the other is a fixed frame. The poroviscoelastic behaviour of hydrogel is considered as a moving mesh frame since the mesh is expanding, while transport of diluted species is considered in the fixed frame. Since the rate of swelling of the hydrogel is extremely high, there is a limitation with adopting the computational model as the model is based on the small displacement estimation. To address this issue, an arbitrary Lagrangian and Eulerian (ALE) methods are used. In the current work, the ALE method is utilized to estimate the evaluated position of hydrogel and the concentration profiles for each iteration. ALE is also known as a moving mesh method. The displacement of two independent variables u and w is applicable by prescribed mesh displacement.

The domain has been meshed with quad element, finer mesh size at the domain, and boundary layer properties at boundary applied to provide better resolution of diffusion and concentration gradients. The entire domain is divided into 741 elements with 27,555 degrees of freedom in total. Table 1 describes the domain element statistics.
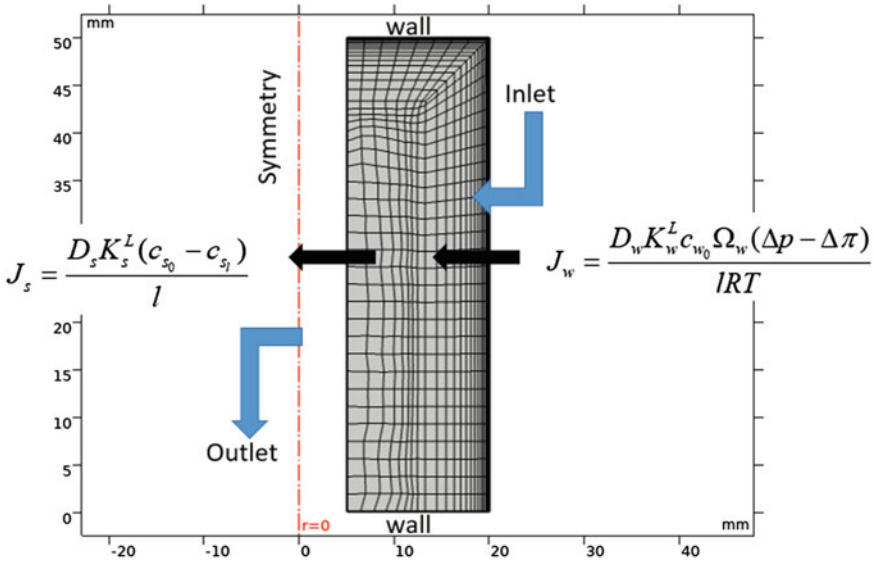
$$J_s = \frac{D_s K_s^L (c_{s_0} - c_{s_l})}{l}$$

$$J_w = \frac{D_w K_w^L c_{w_0} \Omega_w (\Delta p - \Delta \pi)}{lRT}$$

Fig. 5 Illustration of model boundary conditions in RO process

Table 1 Domain element statistics

Description	Value
Maximum element size	1.85 mm
Minimum element size	0.00625 mm
Curvature factor	0.25
Maximum element growth rate	1.25
Predefined size	Finer

3.3 Coupling Between Study 1 and Study 2

The coupling of two simulations is attempted in the software in such a way that one simulation's solution is working as a prior condition for the second one. The complete FEA simulation consists of two studies (study: 1 and 2), the range of simulation time for study: 1 is 0–5 h and for study: 2 is 5–20 h, with the time step of 0.01 reading was taken. The results have been achieved in both the studies with backward differentiation formula (BDF) with free time stepping method which is preferable for solving the time-dependent problem. The nonlinear to linear system of equations conversion is carried out using Newtonian iterations and solved by the direct solver MUMPS.

4   Results and Discussion

The results of the parametric free swelling and the diffusion across hydrogel membrane test are discussed in the present section I. In study: 1 the dry polymeric network is surrounded by water, as time passes the water diffuses into the network, and it results in swelling of hydrogel. And in study: 2 the swelled hydrogel is subjected to flux of diluted species. The geometry is meshed with fine quad elements and with the boundary layers sizing to enhance the resolution of the mesh in the places where the possibility of the steepest slopes of the variables is higher. The simulated outcomes are ensured that there is a mesh independency by consequently refining the mesh.

4.1   Free Swelling Simulation (Study: 1)

The swelling of the dry network of the polymer is the simplest feasible simulation. Equation 9 lists down the boundary conditions that formulate such simulation.

$$\forall \overline{X} \in \Gamma 2, \Gamma 3 : \left\{ \begin{array}{l} \mu_1 = \mu_1^{\text{ext}} \\ \bar{u} = \text{free} \end{array} \right\}; \forall \overline{X} \in \Gamma 4 : \left\{ \begin{array}{l} \bar{\nabla}\mu_1 = 0 \\ u_z = 0 \end{array} \right\} \forall \overline{X} \in \Gamma 1 : \left\{ \begin{array}{l} \bar{\nabla}\mu_1 = 0 \\ u_R = 0 \end{array} \right\}$$

(9)

Figure 6 is the model post meshing, where $\Gamma 2$ and $\Gamma 3$ are exposed to the pure water ($\mu_1 = \mu_1^{\text{ext}}$). These boundaries are unrestricted to deform and also displace. $\Gamma 4$ and $\Gamma 1$ are the boundaries that are the symmetric axis planes. Hence, it derives that there is no influx of water across the boundaries. The constraints are along the Z and R directions so that there is no displacement.

The proposed poroviscoelastic model has only four parameters G_1, G_2, D_1 and τ. The magnitude of each parameter was established as per [10], to achieve required water absorption and homogeneous deformations. G_1 denotes the elastic modulus of the hydrogel in the relaxed situation. This modulus significantly affects the quantum of water absorbed, the kinetics of the process, and total deformation. As the magnitude of G_1 is increased the gel gets stiffer and stiffer thereby causes less water absorption. At time ($t = 0$), the hydrogel is at its undeformed state. As the time passes from 0 to 5 h, and the system is moving towards the equilibrium so as to satisfy the boundary condition $\mu_1 = \mu_1^{\text{ext}}$ by absorbing water and swell, as shown in Fig. 7.

It has been found that the influence of the diffusion coefficient (D_1) on the water absorption is high. The relaxation time (τ) is the reduction of polymeric setup when water is absorbed. Higher value of τ denotes slower relaxation. This results in increased stiffness of the system for an extended period. This phenomenon thereby slower the absorption of the kinetics.

In order to gain the confidence on the solutions as obtained from the free swelling test, the derived solution of study: 1 is compared with poroviscoelastic model [10] simulated result as shown in Fig. 8 and found good correlation between them.
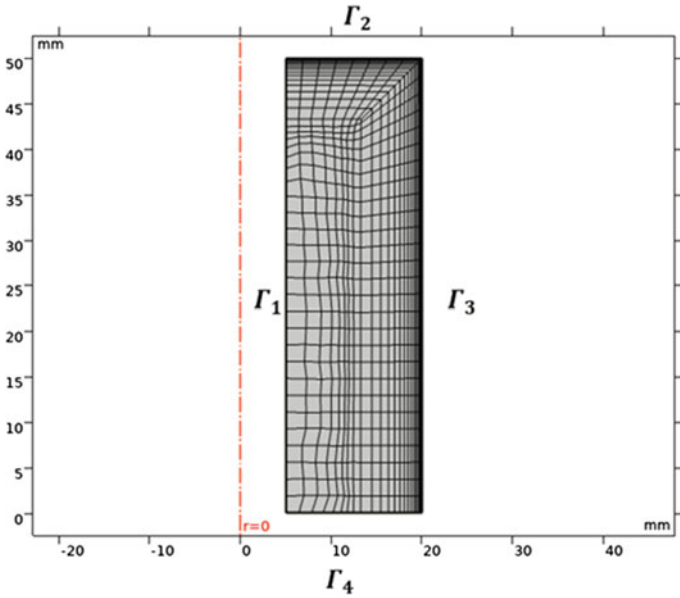
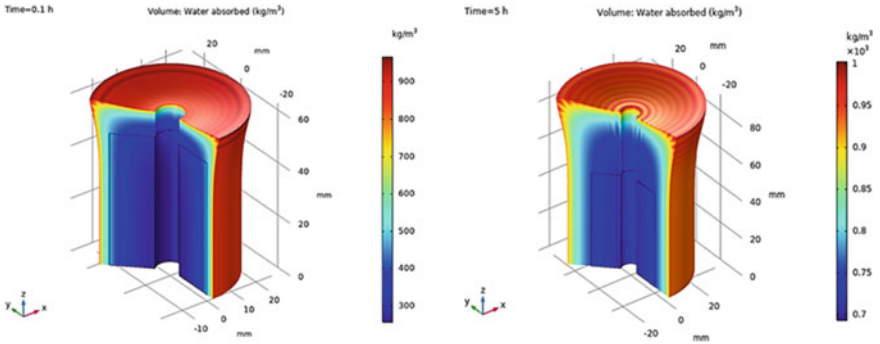**Fig. 6** Meshed domain indicating Γ as the domain boundaries

Fig. 7 Quantum of water absorbed and shape change during a swelling test

4.2 Transient Diffusion Across a Membrane Simulation (Study: 2)

Reverse osmosis trial was modelled by taking the swollen hydrogel as a membrane. The NaCl concentration is 35 g/l. Molar concentration of inlet water is calculated as 0.6 M, and respective osmotic pressure is also calculated using Van't Hoff's law as 30 bar. The value of diffusion coefficients (D_1), the distribution coefficients (K_2) and the permeability coefficients (P) of NaCl into hydrate hydrogel are taken count for
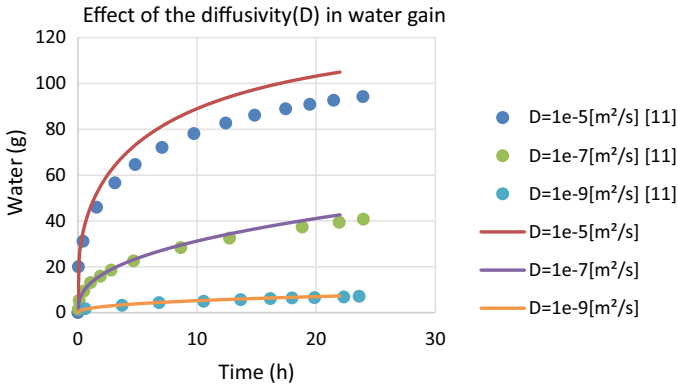
Fig. 8 Comparison between poroviscoelastic model [10] and current study

simulation, which are determined experimentally [21]. The flow of water with high chemical potential applies at the inlet boundary, and it diffuses into the membrane by means of Fick's diffusion law. Percentage of salt molecule diffusing into the membrane is too less as compared to water molecule due to the salt solubility into the membrane is lower.

Schema of the proposed desalination process via hydrogels is like as shown in (Fig. 9), the first dry gels are placed in pure water with concentration c_0 and gel is going to absorb the water and it will swell in the time interval 0–5 h, and then high-pressure flux of 0.6 molar concentrated water is imposed on the outer wall of swollen gel from the time interval 5–20 h.

The permeate flux of water is determined under the framework of SD model as reported in Fig. 10. It is reported that end of the simulation 120–130 ml (approx.) of water drain out of the membrane. According to SD model, the water flux through the membrane residues little up to the osmotic pressure of the salt solution. Later these surges as the stresses are applied.

Figure 11 shows the calculated salt rejection ratio using boundary probe, the capability to separate permeants as defined in Eq. 7. R denotes the capacity of the film to disperse salt out of the fed solution. It is also known as selectivity of the membrane, and the performance of a membrane is estimated based on its selectivity. In this simulation, it is seen that the average salt volume fraction reduces from 0.5 to 0.3 M and approaches a constant value. So it can be concluded that the salt rejection ratio of this film/membrane is 40%.

It can be observed that difference in the water concentration when it is diffusing from the feed side to permeate side as shown in Fig. 12. It is seen that the average salt volume fraction reduces from 0.5 to 0.3 M. This indicates the reverse osmosis is being well represented in Fig. 13. The proposed model was shown to be a valuable tool for predicting hydrogels' behaviour under a wide range of conditions and also allows for customization for many more applications.
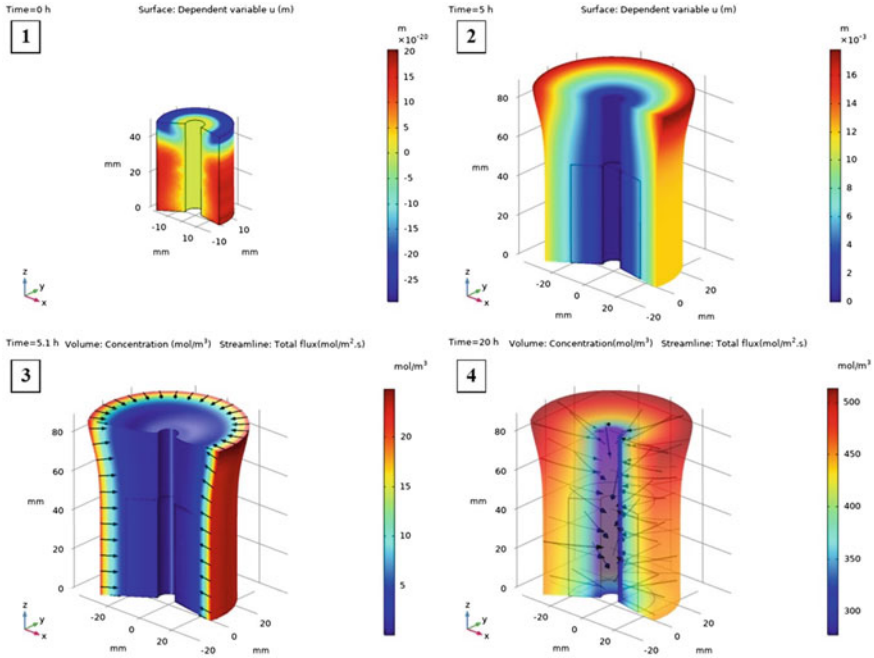
Fig. 9 Proposed RO process via swollen hydrogel **a** hydrogel at dry state @ $t = 0$ h, **b** free swelling of hydrogel after 5 h, **c** pressurized water flux imposed from surroundings @ $t = 5.1$ h, **d** total water flux out @ $t = 20$ h
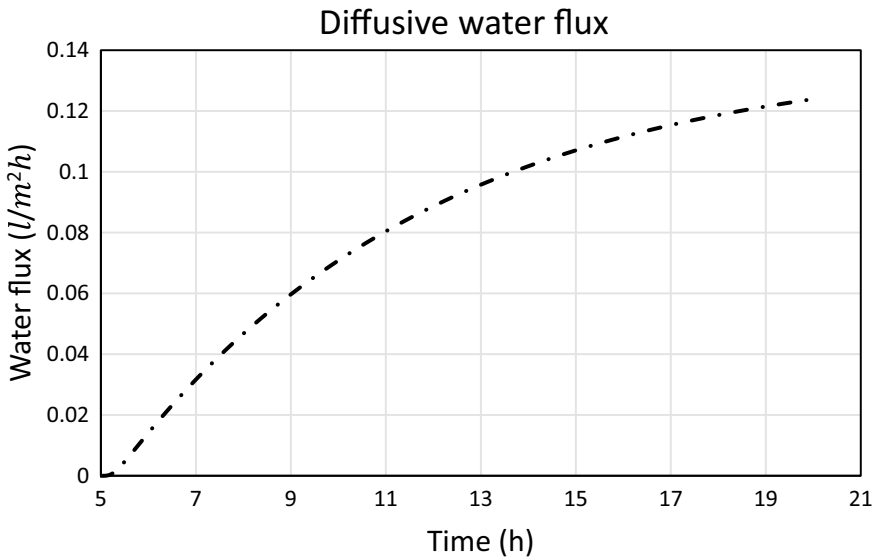

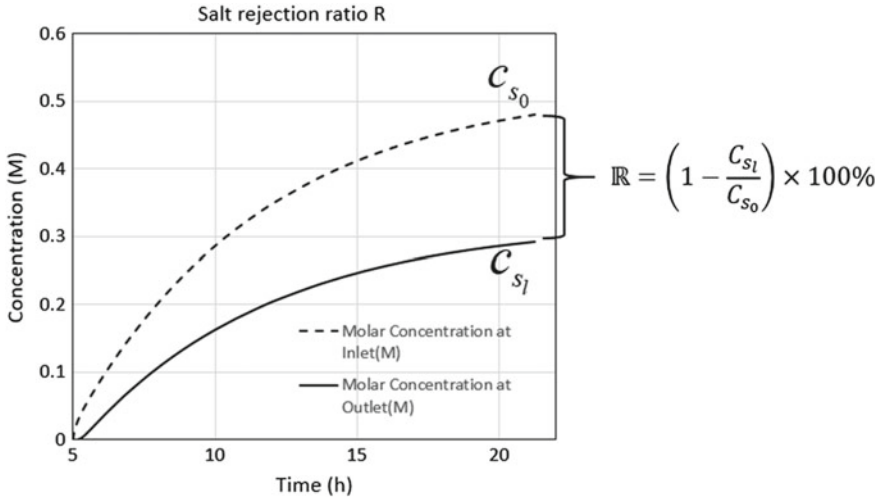**Fig. 10** Calculated water flux with respect to time from 5 to 20 h

$$R = \left(1 - \frac{C_{S_l}}{C_{S_0}}\right) \times 100\%$$

Fig. 11 Calculated salt rejection ratio using boundary probe
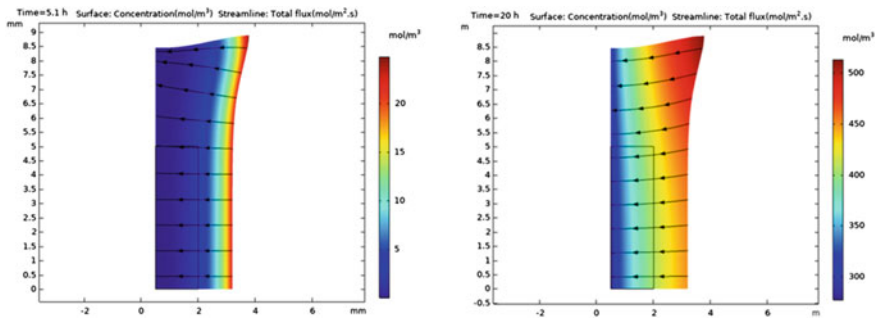
Fig. 12 Variation in water concentration with respect to time from $h = 5.1$–20 h
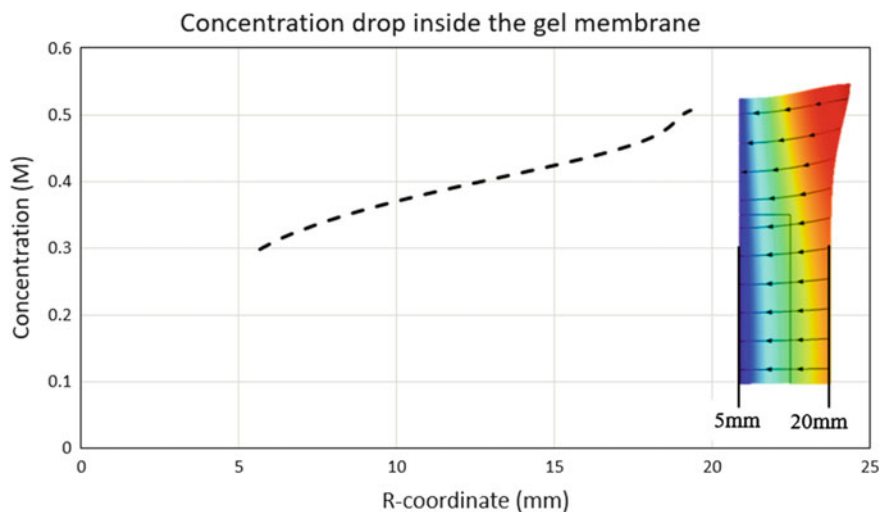
Fig. 13 Measurements of the water concentration gradients inside the gel membrane

5 Conclusion

The present work established that swollen hydrogels are one of the options to be considered for desalination purposes. Additionally, a parametric analysis has been done to estimate the overall significance of the model parameters on hydrogel's behaviour. A new model has been designed and simulated to mimic the behaviour of hydrogels as subjected to an external stimuli. Water has been considered as an external stimuli. The present work showed that the desalination ability of a hydrogel rests entirely on the configuration. As an example, the effective permeability of NaCl (salt) which is present in the hydrogel panels as how much salt is rejected from feed solution and the diffusivity of water inside the hydrogel allows to maximize the water flux from permeate side. The hydrogels have high ability to absorb water, water permeability, greater biocompatibility with low fouling potential making it suitable for desalination membrane. The meant schema is quite adaptable in designing and optimizing hydrogels in applications like bio-printings of the soft biological tissues.

References

1. Caccavo D, Vietri A, Lamberti G, Barba AA, Larsson A (2018) Modeling the mechanics and the transport phenomena in hydrogels, 1st edn Elsevier
2. Hogari FAK (1994) Advances in superabsorbent polymers. Washington (1994)
3. Matsuyama H, Teramoto M, Urano H (1997) Analysis of solute diffusion in poly(vinyl alcohol) hydrogel membrane. J Membr Sci 26(1):151–160
4. Kazanskii KS, Dubrovskii SA (1992) Chemistry and physics of 'agricultural' hydrogels. Adv Polym Sci 104:97–133 (Berlin, Heidelberg)

5. Masuda F (1994) Trends in the development of superabsorbent polymers for diapers. American Chemical Society, pp 88–98
6. Flory PJ, Rehner J (1943) Statistical mechanics of cross-linked polymer networks I. rubberlike elasticity. J Chem Phys 11(11):512–520
7. Ghantasala MK, Suthar KJ, Mancini DC (2010) Steady-state simulation of the chemo-electro-mechanical behaviour of hydrogels. Int J Model Simul 30(3):396–404
8. Lu K (2011) Modelling of multicomponent diffusion and swelling in protein gels. University of Canterbury, Dissertation
9. Höpfner J, Richter T, Kosovan P, Holm C, Wilhelm M (2013)
10. Caccavo D, Lamberti G (2017) PoroViscoElastic model to describe hydrogels behavior. Mater Sci Eng, C 76:102–113
11. Gurtin ME, Fried E, Anand L (2010) The mechanics and thermodynamics of continua. Cambridge University Press
12. Flory PJ, Rehner J (1943) Statistical mechanics of cross-linked polymer networks I. Rubberlike elasticity. J Chem Phys 11:512–520
13. Flory PJ, Rehner J (1943) Statistical mechanics of cross-linked polymer networks II Swelling. J Chem Phys 11(11):521–526
14. Lonsdale HK, Merten U, Riley RL (1965) Transport properties of cellulose acetate osmotic membranes. J Appl Polym Sci 9(4):1341–1362
15. Paul DR, Ebra-Lima OM (1970) Pressure-induced diffusion of organic liquids through highly swollen polymer membranes. J Appl Polym Sci 14(9):2201–2224
16. Rajagopal KR (2003) Diffusion through polymeric solids undergoing large deformations. Mater Sci Technol 19:1175–1180
17. Baek S, Srinivasa AR (2004) Diffusion of a fluid through an elastic solid undergoing large deformation. Int J Non-Linear Mech 39(2):201–218
18. Fernando PE, Souzab AC (2010) A theory for species migration in finitely strained solid with application to polymer network swelling. J Mech Phys Solids 58:515–529
19. Baker R (2012) Membrane technology and applications, 3rd edn. Wiley, Newark
20. Yasuda H, Lamaze CE, Ikenberry LD (1968) Permeability of solutes through hydrated polymer membranes. Die Makromolekulare Chemie 118:19–35
21. Caccavo D, Cascone S, Lamberti G, Barba AA, Larsson A (2016) Swellable hydrogel-based systems for controlled drug delivery. Smart Drug Delivery Syst (InTech)
22. Hinrichsen KO, Klemm E (2016) Chemical reaction engineering. Chem Eng Technol 39(11)
23. COMSOL Inc., COMSOL multiphysics reference manual (version 5.3a). Comsol

Experimental Analysis and Productivity Enhancement of Single Basin Solar Still by Utilizing Latent and Sensible Heat Storage Material

Vinay Thakur and **Nitin Kumar**

Abstract All living things have the fundamental need to consume safe drinking water on a daily basis; therefore, it is essential to have an understanding of the shortage of water and the primary freshwater supplies. With the rising levels of pollution caused by both industry and people, the amount of potable water that is available is coming under growing threat. The present work makes use of latent and sensible materials to maximize the distillate yield of a single basin solar still. Utilizing latent and sensible material enhances the production of distillates yield and overall performance of solar still. Latent material paraffin wax enhanced nocturnal distillates, while suspended wicks increased the rate of evaporation for daytime productivity. The experimental investigation utilizes 5,500 g of paraffin wax because it provides the highest cumulative efficiency. The overall productivity of paraffin wax and paraffin wax with suspended wicks increased by 27.65% and 30.12%, respectively. In a modified solar still, the overall maximized distillate yield was recorded as 4.24 kg/m^2 and the cumulative efficiency was 78.62%. The single component temperatures of solar still show significant changes in temperature throughout the day. It was determined that the utilization of wicks as a sensible material enhanced the evaporation rate and the quantity of distillate produced. 32.8 g of maximum distillates were obtained by using wicks with a length of three inches and a depth of 3 cm.

Keywords Single basin solar still · Thermal storage materials · Wicks and paraffin wax · Water depth · Productivity · Efficiency

1 Introduction

Insufficient freshwater supply is a global issue and all life forms need drinkable water, thus understanding how water is produced, distributed, and consumed is vital. Solar stills employ solar energy to produce freshwater more efficiently, cheaply, and

V. Thakur · N. Kumar (✉)
School of Core Engineering, Shoolini University, Solan, H.P 173212, India
e-mail: nksharma09@gmail.com

sustainably. As there is always room for improvement, many researchers investigated various methods to boost conventional solar still productivity. The transient solar still model with experimental data was validated by Cooper [1]. For single effect solar still, Valsaraj [2] improved the efficiency and productivity by varying the depth of water. Different materials were used by Nijmeh et al. [3] for conducting experimental work. Phadatare and Verma [4] showed that water depth plays important role in overall productivity enhancement. Further, Sandeep et al. [5] Patel and Kumar [6] Agrawal and Rana [7] carried out experiments and worked on water depth to achieve higher level of water productivity.

Several review papers were summarized based on the literature. Reviewing both active and passive solar stills, Katekar and Deshmukh [8] found a wide range of applications for each. When compared with other phase change materials, paraffin wax demonstrates its highest level of productivity, and the addition of nanoparticles to solar stills improved their thermal conductivity. The maximum efficiency 307.54% was achieved. The research conducted by Selvaraj and Natarajan [9] examined different solar stills as well as the numerous aspects that influenced performance and output. The design, operations, and weather parameters were reviewed to increase the scope of future development. Sivakumar and Ganapathy Sundaram [10] reviewed a number of methods that enhanced productivity. Numerous solar stills were investigated for their effects on a number of different parameters. Thakur et al. [11] reviewed different energy storage materials and found that paraffin wax shows maximum performance as compared to other materials.

The performance of solar still has been significantly improved by several modifications. Researchers have shown great output with the application of latent and sensible heat storage materials. Li [12] improved the performance for the purpose of determining the system's overall thermal efficiency, and general equations were utilized. The fact that various works make use of latent storage units demonstrates that these works can influence both the system and performance by employing a variety of different techniques. Kabeel et al. [13] used various phase change materials in their study to investigate various modifications and also to evaluate which phase change material was the most effective. Faegh and Shafii [14] improved distillate production rate. In addition, the usage of PCM resulted in an increase of the overall efficiency by 50%. The use of naturally available algal fibres was studied by Suraparaju et al. [15]. It was determined that the production of distillate yield decreased with the increase in pond fibres. The characteristics of materials that can store heat indefinitely were investigated by Yang et al. [16]. The influence of the nanoparticles on the nano-PCM was studied both theoretically and experimentally. For performance assessment, Essa et al. [17] conducted experimental work and introduced several modifications. Fixing the suspended trays and using a combination of nanoparticles and paraffin wax increased overall output. The research on the single-sloped basin type with selected the parameters that will be used to determine the results or conduct the experiment. The temperature of the distillate produced as well as the amount of heat transferred via convection and radiation were the various characteristics studied by Agrawal et al. [18].

The single slope solar still was investigated and put in a full day and night's work in preparation for the annual performance. The work in simulation was done in ANSYS FLUENT, and the conclusion was higher level of thermal efficiency as well as increased productivity at shallower depths given by Khare et al. [19]. According to the findings, yields were consistently higher at shallower water depths throughout the year. Also, the computation in the yearly and seasonal performance of the system in a variety of water depths was evaluated by Tiwari et al. [20]. The distillation process contains different parameters and considered the environmental, design, and operational parameters studied by Somanchi et al. [21]. The utilized jute cloth using a new approach, efficiency of solar stills was significantly increased by Sakthivel et al. [22]. The theoretical research was done to assess and compare the experimental findings. Murugavel et al. [23] used various materials that are capable of sensible heat storage with the amount of distillate yield. With the purpose of the investigation, the lower water depth was used. Muthu Saravanan et al. [24] stored heat in a modified solar still basin using Kanchey marbles. The redesigned solar still performed better. The utilization of nanoparticles by Kabeel et al. [25] increased evaporation by 41.3% and distillate output by 5.62 kg/m^2. Thakur et al. [26] found that solar stills need efficient materials. Nanoparticles and phase change materials were reviewed with improved solar still thermal conductivity. Chaichan and Kazem [27] found that heat transfer boosted distillate production by 60.53%. According to the findings of Badran [28], the weather more specifically the temperature and the wind has a direct impact on the production of yield. There was as much as a 51% increase in the still's overall productivity. The purpose of this work is to investigate the influence that heat-storage materials have on the solar still's capacity to produce more distillate while simultaneously increasing its overall efficiency.

2 Experimental Materials and Method

In the present work, many parameters were studied utilizing measuring instruments. Solar still having same geometric dimensions were fabricated and calibrated at Solan City, Himachal Pradesh, India, having latitude of 30.91°N. As latent and sensible heat storage materials, paraffin wax and suspended wicks were used. Using a pyranometer and thermocouples, the solar intensity and temperature of solar still components were measured. Wind speed was measured using an anemometer. The paraffin wax is encased in black-painted aluminium tubes to absorb maximum solar light and to prevent it from mixing with water. Suspended wicks were also used, and it is crucial to have a thorough awareness of the factors that can influence the performance of a solar still, and the depth of the water is also an important element in the creation of distillate output. Several groups of researchers came to the conclusion that lower water depths result in higher rates of productivity. In this study, depth of the water 3 cm was taken into consideration when designing the experimental approach also aluminium sheet was used for the fabrication of absorber basin as shown in Fig. 1.

Fig. 1 Photographic view of
aluminium sheet used in
solar still
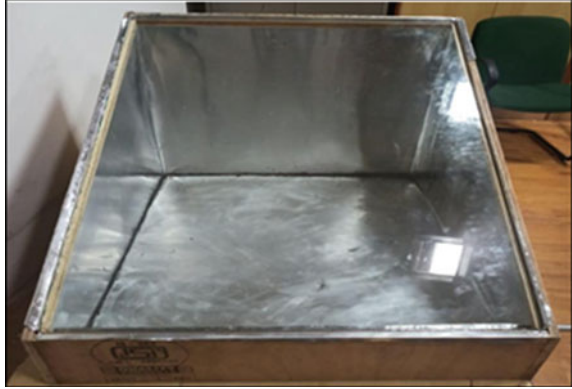
Plywood is utilized in several parts throughout the solar still in order to provide insulation as shown in Fig. 2. The required amount of water is poured into interior part of the still via the inlet placed at the rear of the solar still. A device called anemometer is used for obtaining wind speed. During the hours of morning to evening, the distillates were collected from both stills into plastic containers and weighed them using a digital machine. The overnight distillates were analysed the following morning, after collection took place between evening time to next day morning. It was determined by using a thermocouple for various places. Figure 3 shows the representation of working medium in conventional solar still. Two solar stills were fabricated and calibrated also paraffin wax, and suspended wicks were utilized to maximize the evaporation and nocturnal distillates. The basin tray of 0.75 m^2 at horizontal angle 30° with translucent glass covered the top basin. Black rubber lining in the basin improves solar radiation absorption. Rock wool insulated the solar still's bottom, sides, and back and water was placed inside the still, and window glass was used to cover it. The water in the basin has become warmer due to solar radiation, which has led to some of the water evaporating.

Fig. 2 Photographic view of
plywood used for insulation
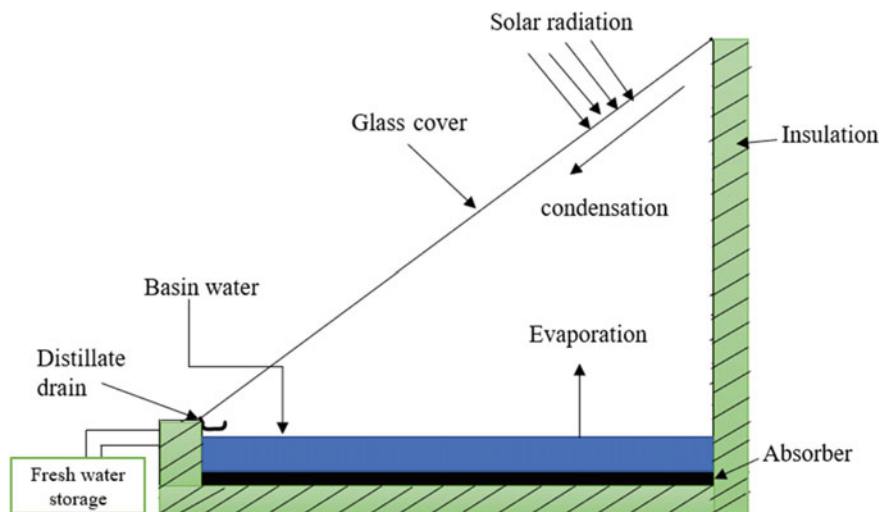
Fig. 3 Schematic diagram of conventional solar still

The use of silica gel and an M-seal between the glass cover and the frame of the still will ensure that no vapour escapes into the atmosphere from the basin of the still. The usage of silica gel and M-seal made all the parts completely watertight. The colour of the basin water is another critical element to consider; since the base still is the part that absorbs the most heat, it is also the part that gets the hottest. Convection and conduction are two processes that utilized inner temperature. The basin of a solar still is coloured black so that it can absorb all solar radiations. This causes the water in the basin to heat up, and the heat is then transferred to the base of the still, where it is channelled through an insulating material. Therefore, the introduction of external coloration could result in an increase in the performance. Latent and sensible material in modified still is shown in Fig. 4. This study focuses on solar stills efficiency, including the storage of latent and sensible heat. In order to enhance output and performance, paraffin wax was used. It helps to clarify the scope of the study and the basis for the current research.

3   Results and Discussion

Table 1 depicts the differences in conventional and modified solar still values. There is an increase in the solar still performance when the mass of latent material increased at 5500 g. When compared to conventional solar still, further increasing the amount caused the solar still's efficiency to decline as shown in Fig. 5. Hence, 5500 g of paraffin wax was used for experimental work. Due to paraffin wax's energy storage, the improved still's basin water temperature is lower in the morning. As solar intensity
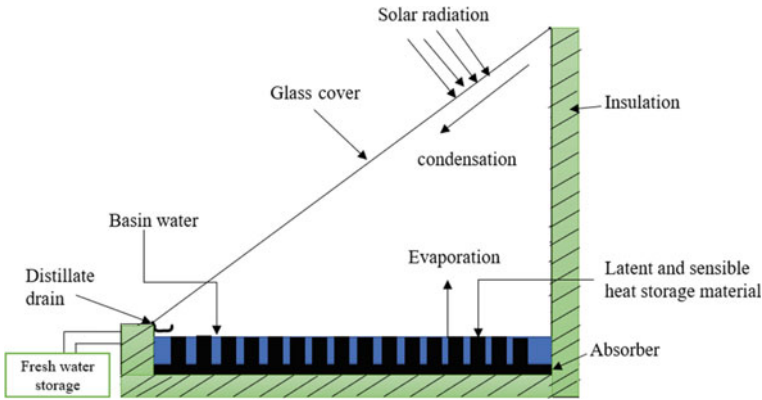
Fig. 4 Schematic diagram of modified solar still with heat storage materials

Table 1 Measuring values of modified and conventional solar still when mass of latent material increased

Mass of latent material (g)	Modified solar still (Cumulative efficiency %)	Conventional solar still (Cumulative efficiency %)
3000	62.82	47.40
5500	70.52	53.77
8000	65.84	49.85

peaks, the modified still's basin water temperature remained higher. The tendency of storing heat during day time by paraffin wax, resulted as improved night distillate production. The fluctuation in the weather parameters is shown in Fig. 6. Sensible material as different sizes of wicks was used as an experimental approach. These wicks improve the rate at which vapours evaporates inside the working solar still and enhance the performance of distillate production. This occurs by enhancing the evaporating surface area. Productivity of the distillate was measured using wicks of several sizes and then compared.

Figure 7 shows the fluctuation in conventional solar still component temperatures that remains varied throughout the daytime. The basin air temperature remains higher throughout the day but remains low at night time. Glass temperature remains higher till 12:30 pm because of more absorption of solar radiation by glass after that it remains lower in evening time. Using the temperature of the surrounding environment does not result in a bigger enhancement in performance. Solar radiation is another key factor that is considered while trying to increase the production of distillates. It has been determined that the output of the still improves with an increase in the sun radiation quantity that strikes it while it is operating. Distillate yield has a relationship that can be described as a direct proportion. It was discovered that a still with water flowing over its glass cover performed better than a typical still. The temperature difference between the water and the glass cover of a still determines its production.
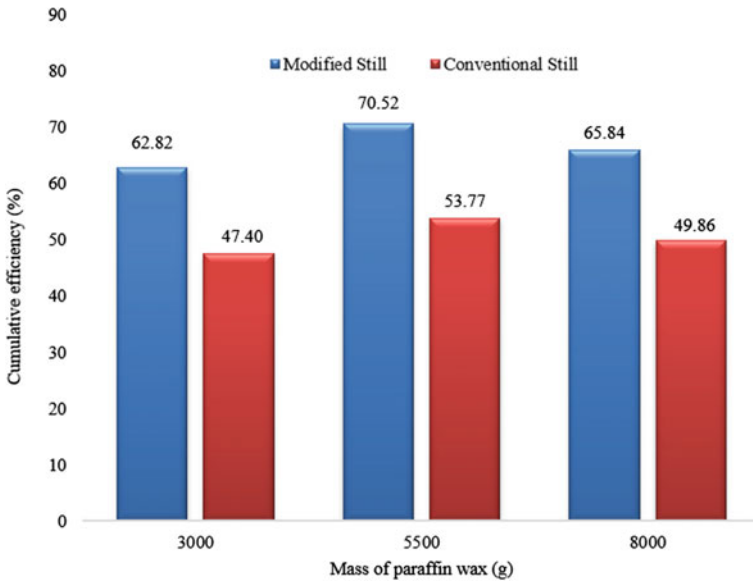
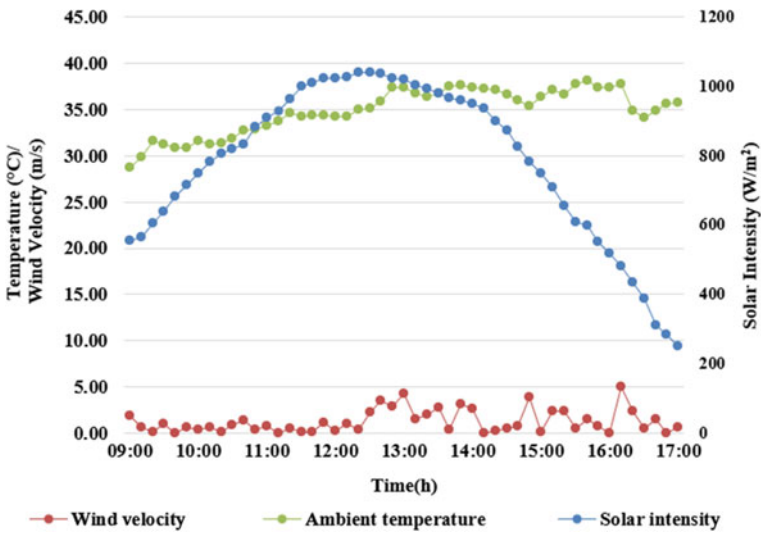**Fig. 5** Effect of mass of latent material to the efficiency of single basin solar still

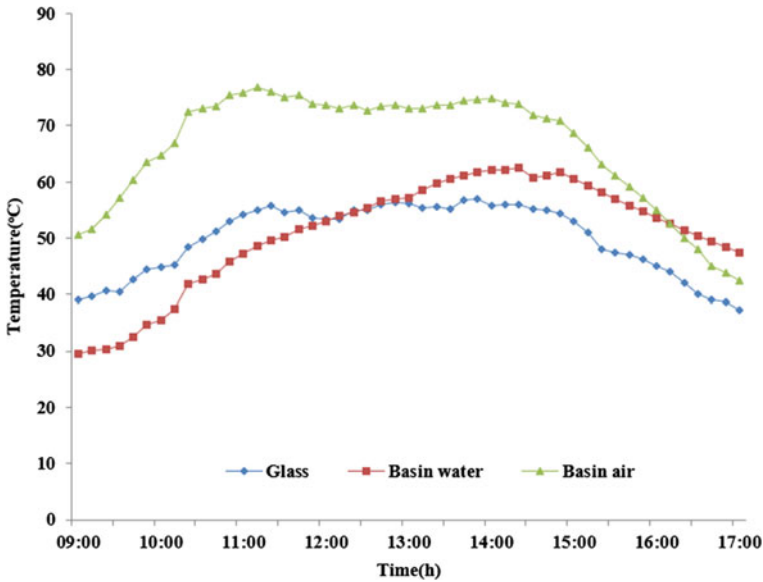**Fig. 6** Fluctuation in solar still weather parameters

Fig. 7 Fluctuation in conventional solar still component temperatures

Figure 8 shows the fluctuation in component temperatures varied from morning to evening time. The performance was studied by employing various materials. Glass temperature continues to be maximum because glass absorbs more energy in the morning. However, as the day progresses, paraffin wax begins to release the heat that it has stored. The temperature of paraffin wax tends to peak after maximum solar intensity, and it was below the basin water until 12:30 pm due to thermal inertia. After 12:30 pm, paraffin wax temperature stagnates and transfers latent heat to basin water, raising its temperature. Due to heat trapped in paraffin wax, basin water temperature dips below glass temperature, but rises as the day progresses.

The experimental work with suspended wicks and latent material was performed on month of May. Figure 6 shows the maximum value of solar intensity and observed in between 12:00 pm to 1:00 pm. Figure 9 shows the fluctuation of conventional and modified solar still component temperatures. The increase in the evaporation rate with suspended wicks and paraffin wax stored heat during daytime and released in evening and night time. Due to more area covered by suspended wicks, it takes more time to heat basin of modified solar still. Early morning solar intensity reduces distillate formation. Solar intensity increased until 1:30 pm, when both stills produced more distillate and decreases between 1:30 and 5 pm, reducing distillate production in both stills. Until 1:30 pm, modified and conventional stills produce nearly the same amount of distillate. After 1:30 pm, the distillate production was maximized in modified still because of stored heat inside the basin. The modified still's hot basin water increases its productivity by 80.73% at night and 3.42% during the day. Both stills have similar daytime productivity because paraffin wax stores energy and
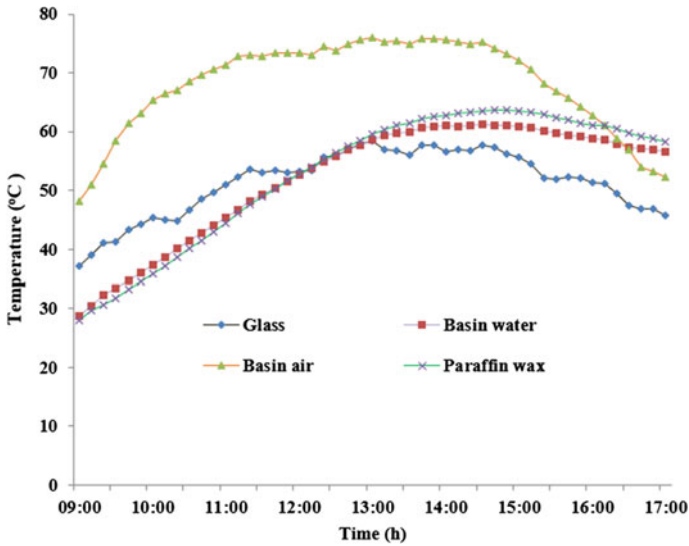
Fig. 8 Fluctuation in modified solar still component temperatures

releases it at night. Modified still was 27.65% more productive than conventional still. There are no additional components required for distillation. To obtain findings from an analysis, every parameter must be evaluated. Regarding incoming radiation, the effective rays are essential for water distillation. As the rate of evaporation, the passive still considers the productivity to be low. There will also be some leakage losses that may be accounted for when analysing the performance of the still.

The gain in day, night, and overall productivity is shown in Fig. 10. When paraffin wax was used, overall distillate production was 3.92 kg/m². Paraffin wax with suspended wicks enhances the overall distillate yield by 30.12% and overall distillate production was 4.24 kg/m². The maximum overall efficiency also improved by 78.62% for modified solar still. Figure 11 demonstrates how the temperature of the components changed over time. The most fundamental constituents were glass, air, and water from the basin. It was obvious that the air temperature in the basin continues to rise during the day and can reach up to 70–80 °C. However, as the sun goes down and night falls, the air inside the basin becomes warmer than the water temperature in the basin. The glass achieves a temperature of 55–60 °C. But by evening it has dropped below both the water and air temperatures of the basin.

Figure 12 demonstrates the output of distillate yield using wicks of 2 in. There was not much of a change in the production of distillate yield throughout the morning hours. However, when the temperature continued to rise throughout the day, a greater quantity of distillates was produced. Since there was less sun energy in the evening, there was a decrease in the amount of distillate produced. Figure 13 shows the output of the distillate yield when utilizing wicks that are 3 in. in length. The best results
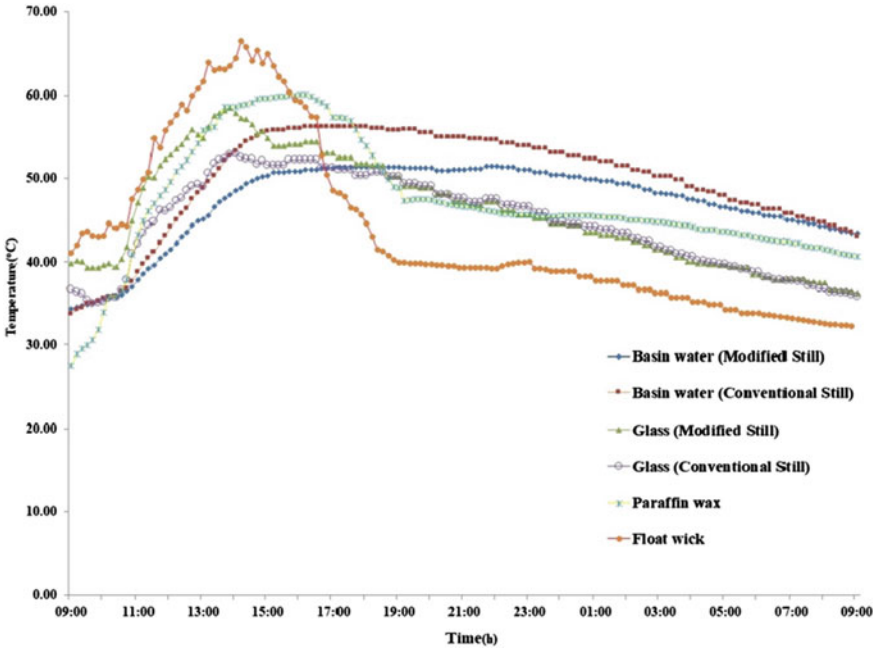
Fig. 9 Fluctuation in conventional and modified solar still component temperatures
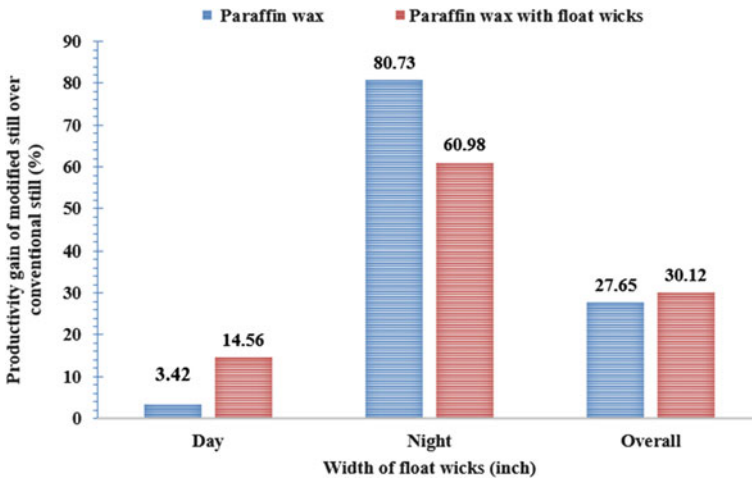

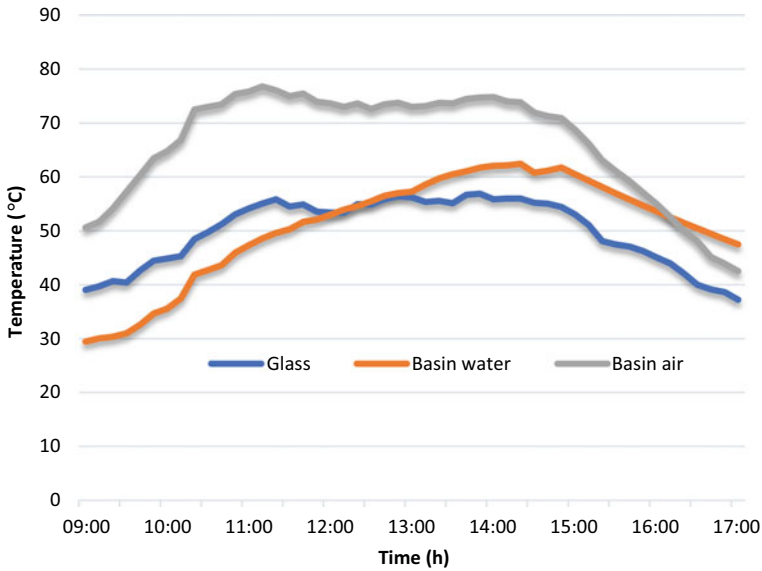**Fig. 10** Gain in the productivity with latent material and suspended wicks

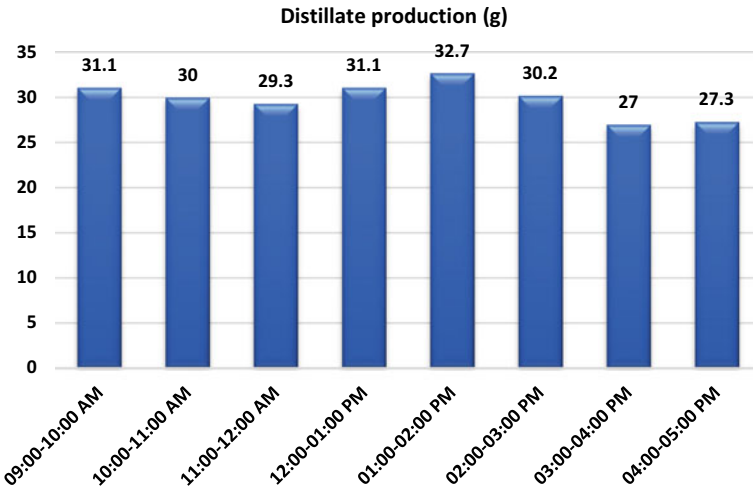**Fig. 11** Component temperatures of solar still

Fig. 12 Production of distillate yield with wicks (2 in.)

with the distillate were obtained between 1 and 2 in the afternoon. The production of distillates fluctuates during the day, and a yield of 32.8 g of distillate was obtained with sensible material.
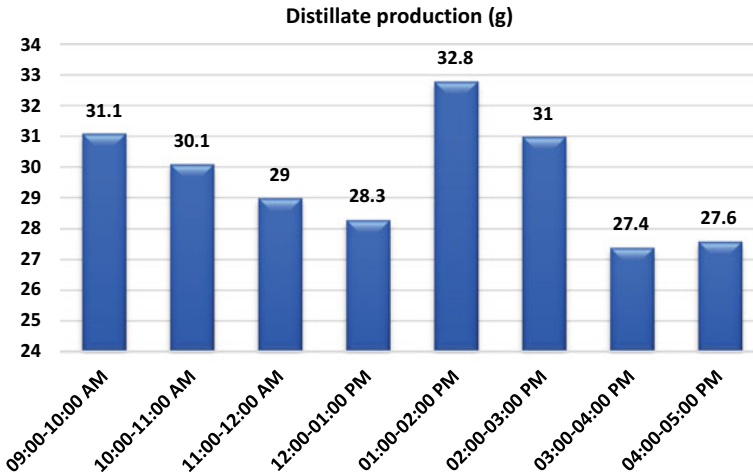
Distillate production (g)

Fig. 13 Production of distillate yield with wicks (3 in.)

4 Conclusion

The present work enhances the overall performance and daily distillate yield output. Thermal energy materials were studied and used in this study. For this purpose, paraffin wax enhanced the night productivity and suspended wicks improved daytime production of distillates. The use of paraffin wax with suspended wicks gives maximum overall productivity and efficiency. The findings of this study indicate that the utilization of materials leads to increase in the rate of evaporation. Wicks were investigated for their usage, and a number of component temperatures were measured.

- The use of paraffin wax enhanced the overall productivity by 27.65% and overall distillate yield was 3.92 kg/m^2.
- Paraffin wax with suspended wicks further enhanced the distillate yield as 4.24 kg/m^2 and enhanced the overall productivity by 30.12%.
- The maximum overall efficiency was improved by 78.62% for modified solar still.

It was also discovered that various natural fibres can be utilized to make further breakthroughs in the distillate production process.

References

1. Cooper PI (1973) Digital simulation of experimental solar still data. Solar Energ 14(4):451–468. https://doi.org/10.1016/0038-092X(73)90023-6

2. Valsaraj P (2002) An experimental study on solar distillation in a single slope basin still by surface heating the water mass. Renew Energ 25(4):607–612. https://doi.org/10.1016/S0960-1481(01)00094-5

3. Nijmeh S, Odeh S, Akash B (2005) Experimental and theoretical study of a single-basin solar sill in Jordan. Int commun heat mass Transf 32(3–4):565–572. https://doi.org/10.1016/j.icheatmasstransfer.2004.06.006

4. Phadatare MK, Verma SK (2007) Influence of water depth on internal heat and mass transfer in a plastic solar still. Desalination 217(1–3):267–275. https://doi.org/10.1016/j.desal.2007.03.006

5. Sandeep SK, Dwivedi VK (2015) Experimental study on modified single slope single basin active solar still. Desalination 367:69–75. https://doi.org/10.1016/j.desal.2015.03.031

6. Patel P, Kumar R (2016) Comparative performance evaluation of modified passive solar still using sensible heat storage material and increased frontal height. Procedia Technol 23:431–438. https://doi.org/10.1016/j.protcy.2016.03.047

7. Agrawal A, Rana RS (2018) Energy and exergy analysis of single slope single basin solar still in Indian condition: an experimental analysis. Mater Today: Proc 5(9):19656–19666. https://doi.org/10.1016/j.matpr.2018.06.328

8. Katekar VP, Deshmukh SS (2020) A review of the use of phase change materials on performance of solar stills. J Energ Storage 30:101398. https://doi.org/10.1016/j.est.2020.101398

9. Selvaraj K, Natarajan A (2018) Factors influencing the performance and productivity of solar stills-A review. Desalination 435:181–187. https://doi.org/10.1016/j.desal.2017.09.031

10. Sivakumar V, Sundaram EG (2013) Improvement techniques of solar still efficiency: A review. Renewable and Sustainable Energy Reviews, 28:246–264. https://doi.org/10.1016/j.rser.2013.07.037

11. Thakur V, Kumar N, Kumar S, Kumar N (2022) A brief review to improve the efficiency of solar still using efficient phase change materials. Mater Today: Proc 64:1295–1299. https://doi.org/10.1016/j.matpr.2022.04.119

12. Li G (2015) Energy and exergy performance assessments for latent heat thermal energy storage systems. Renew Sustain Energ Rev 51:926–954. https://doi.org/10.1016/j.rser.2015.06.052

13. Kabeel AE, El-Samadony YAF, El-Maghlany WM (2018) Comparative study on the solar still performance utilizing different PCM. Desalination 432:89–96. https://doi.org/10.1016/j.desal.2018.01.016

14. Faegh M, Shafii MB (2017) Experimental investigation of a solar still equipped with an external heat storage system using phase change materials and heat pipes. Desalination 409:128–135. https://doi.org/10.1016/j.desal.2017.01.023

15. Suraparaju SK, Dhanusuraman R, Natarajan SK (2021) Performance evaluation of single slope solar still with novel pond fibres. Process Saf Environ Protect 154:142–154. https://doi.org/10.1016/j.psep.2021.08.011

16. Yang R, Li D, Salazar SL, Rao Z, Arıcı M, Wei W (2021) Photothermal properties and photothermal conversion performance of nano-enhanced paraffin as a phase change thermal energy storage material. Solar Energy Materials and Solar Cells, 219, 110792. https://doi.org/10.1016/j.solmat.2020.110792

17. Essa FA et al (2020) "Wall-suspended trays inside stepped distiller with Al2O3/paraffin wax mixture and vapor suction: experimental implementation." J Energ Storage 32:102008. https://doi.org/10.1016/j.est.2020.102008

18. Agrawal A, Rana RS, Srivastava PK (2017) Heat transfer coefficients and productivity of a single slope single basin solar still in Indian climatic condition: Experimental and theoretical comparison. Resource-Efficient Technol 3(4):466–482. https://doi.org/10.1016/j.reffit.2017.05.003

19. Khare VR, Singh AP, Kumar H, Khatri R (2017) Modelling and performance enhancement of single slope solar still using CFD. Energy Procedia 109:447–455. https://doi.org/10.1016/j.egypro.2017.03.064

20. Tiwari AK, Tiwari GN (2007) Thermal modeling based on solar fraction and experimental study of the annual and seasonal performance of a single slope passive solar still: The effect of water depths. Desalination 207(1–3):184–204. https://doi.org/10.1016/j.desal.2006.07.011

21. Somanchi NS, Sagi SLS, Kumar TA, Kakarlamudi SPD, Parik A (2015) Modelling and analysis of single slope solar still at different water depth. Aquat Procedia 4:1477–1482. https://doi.org/10.1016/j.aqpro.2015.02.191

22. Sakthivel M, Shanmugasundaram S, Alwarsamy T (2010) An experimental study on a regenerative solar still with energy storage medium—Jute cloth. Desalination 264(1–2):24–31. https://doi.org/10.1016/j.desal.2010.06.074

23. Murugavel KK, Sivakumar S, Ahamed JR, Chockalingam KKSK, Srithar K (2010) Single basin double slope solar still with minimum basin depth and energy storing materials. Appl Energy 87(2):514–523. https://doi.org/10.1016/j.apenergy.2009.07.023

24. Saravanan NM, Rajakumar S, Moshi AAM (2021) Experimental investigation on the performance enhancement of single basin double slope solar still using kanchey marbles as sensible heat storage materials. Mater Today: Proc 39:1600–1604. https://doi.org/10.1016/j.matpr.2020.05.710

25. Kabeel AE, Sathyamurthy R, Manokar AM, Sharshir SW, Essa FA, Elshiekh AH (2020) Experimental study on tubular solar still using Graphene Oxide Nano particles in Phase Change Material (NPCM's) for fresh water production. J Energ Storage 28:101204. https://doi.org/10.1016/j.est.2020.101204

26. Thakur V, Dhindsa GS, Mittal MK, Sokhal GS (2019) Experimental investigation of basin type solar still having paraffin wax in the basin. Int J Mech Prod Eng Res Dev 9:958–965

27. Chaichan MT Kazem HA (2018) Single slope solar distillator productivity improvement using phase change material and Al2O3 nanoparticle. Solar Energy 164:370–381. https://doi.org/10.1016/j.solener.2018.02.049

28. Badran OO (2007) Experimental study of the enhancement parameters on a single slope solar still productivity. Desalination 209(1–3):136–143. https://doi.org/10.1016/j.desal.2007.04.022

Comprehensive Study on Wire Arc Additive Manufacturing (WAAM)

Saksham Chauhan and Andriya Narasimhulu

Abstract Wire arc additive manufacturing (WAAM) is presently growing as the major hub of research bodies throughout the universe. This is straightly noticeable in an enormous paper published recently pertaining to a myriad of distinct matters. Additive manufacturing is the quickest technique for the development of a product, and this is indicated by scientific industrial sections. It reinstated conventional ways in a few industrial circumstances by bringing down material utilisation. WAAM is much closer to welding in the process as it makes use of stratified deposition to design huge portions with less intricacy. Numerous experiments and estimates have evolved to ameliorate material properties concerning the remaining deformities like crackling and spattering. WAAM has acquired popularity as it has many benefits and very high efficiency. It increases the efficiency of the material and has a rate of deposition which is again very high and the lead time is shorter, the performance of the components is better, and the inventory cost is very low. This review is proposed to provide an appropriate summary of the field of WAAM. The inscribed matter in this review is embraced but not restricted to the materials. Various processes like monitoring, path planning, and modelling fall into the operations and techniques of WAAM. The alliance of detecting numerous authors into a consolidated form is the essence of this review. It is proposed to discover various fields in which the work is mislaid and in what ways the distinct topics can be manually integrated. A crucial estimation of introduced research along with welding research and a remarkable focus on additive manufacturing will accomplish this review.

Keywords Additive manufacturing · WAAM · Welding · Photopolymerisation · Stereolithography · Solidification · Microstructure

S. Chauhan · A. Narasimhulu (✉)
Netaji Subhas University of Technology, Delhi, India
e-mail: andriya@nsut.ac.in

1   Introduction

Scientists have spent years honing cutting-edge manufacturing techniques to produce a system that optimises the utilisation of resources like time and money. The term "additive manufacturing" describes a method of production in which a product is constructed by successively adding layers of material to get the required shape (AM) [1]. To achieve the required solid form, this technique involves layering on molten material in a progressive fashion. The aerospace and defence industries were the first to use this technique about 1988. Metals and polymers account for the vast majority of this technique's output. Wire arc additive manufacturing is now the most common method, but powder bed blend along with electron ray liquification is also good choice. Conventional manufacturing techniques fail because of the high volume of material wasted when starting with a huge block of metal to create the desired item. Due to the high cost of materials, the aerospace and defence sectors incur a loss. The aerospace industry has benefited greatly from the widespread use of carbon fibre reinforced parts due to its high strength-to-weight ratio. Titanium's similar surge in effort may be attributed to the metal's electrochemical affinity for carbon. Increasingly high prices due to increased demand have made the transition to AM production almost inevitable. AM has a terrible buying to flying ratio. As a flexible process, it excels at producing high-quality goods, and it can be used to a wide range of scenarios. That's why it's better than the industry norm for production. Some parts can be made with holes or a lattice pattern to reduce the overall weight and cost of making the product without affecting its mechanical energy or functionality. Such complexity would be challenging to grind from a single piece of conventional metal, but is entirely feasible using AM's stacked construction method [2].

1.1   Additive Manufacturing Process

Making the right choice among the AM processes is crucial for productive fabrication. The following are general standard methods that are available to satisfy AM mechanism being demonstrated in Fig. 1.

Binder jetting, which produces sheets of powder material plus a liquid ingredient called the binder for adhesion reasons, utilises a 3D printing head that travels along three conventional dimensions (x, y, and z). DED must be employed with almost all components, including metallic materials, ceramics, and polymers, no matter how heavy they are, to make the final parts. Before being put down in layers, solid wire, feedstock filaments, or filler metal must be melted with only an electric arc, laser, or electron beam. Wire arc additive manufacturing is a type of AM that is based on arc welding (WAAM). During material extrusion, polymers that have been spooled can be pushed through a heated nozzle or drawn into it. Melting materials also build up in layers, and these layers adhere together in the end either because of the way the temperature changes or because of chemical bonds. Powder bed fusion is
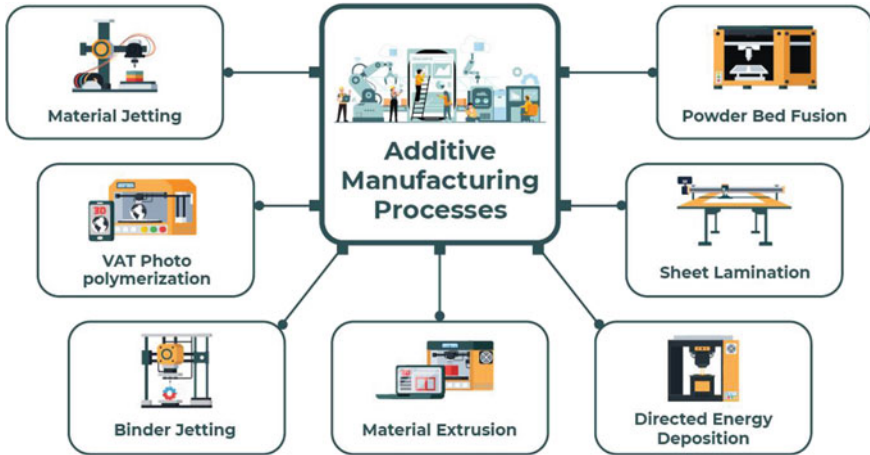
Fig. 1 Additive processes [3]

characterised by the production of molten or partly molten layers of material cleansed by blasting away superfluous powder. This idea is used in many AM techniques, such as Direct Metal Laser Melting (DMLM), Direct Metal Laser Sintering (DMLS), Electron Beam Melting (EBM), Selective Laser Sintering (SLS), and Selective Heat Sintering (SHS). Sheet lamination is simply the process of stacking thin layers of material to form a single 3D part. Laminated Object Manufacturing (LOM) and Ultrasonic Additive Manufacturing are two technologies that can be used for sheet lamination (UAM). Through vat polymerisation, a piece is made by making changes to a liquid epoxy photopolymer vat. Through mirrors, ultraviolet light cures layers of materials in a process called "photopolymerisation" [4].

Even if the aforementioned processes are applicable to AM, it may be categorised as one of three separate varieties of technology. Sintering is the initial method in which the powdered state of the substance to use for manufacturing is made hot to an absolute scales considerably beyond its liquefying stage in order to create detailed, high-resolution parts. The second method is called "complete melting," in which the powder content was using to make the portion completely disintegrated. Most of the time, this melting is with a laser. When a UV laser is ejected and pointed at photopolymer resin, it makes stuff that seems to be resilient to torque and therefore can handle temperatures for both ends of the scale. The third type of method is called stereolithography. To use these methods and technologies, you could print parts made of many different types of materials.

2   WAAM

The WAAM technique comes to be a sort of direct deposition of energy (DED) that employs the embracing of cord-feed as the primal matter or electric ray just as primary origin of energy. An electric curve, analogous to the one formed during the process of arc welding is produced when the workpiece as well as the electrodes are brought into contact with one another. In order to melting molten metal wire and transfer it into the created component, sufficient heat must be produced, which may be accomplished by combining a strong electrical currents with a substantial electric resistance that exists between both the workpiece and the electrode [5]. This approach is only applicable when using conductive substrates and electrodes. Figure 2 is an illustration of the WAAM method.

Because of the growing interest in this method, WAAM has emerged as a focus of vigorous investigation in recent years. When contrast to PBF alongside fine particles contingent DED, the WAAM method's rapid settling rate and cheap investment costs made it a more cost-effective solution for limited production quantity or bespoke products [6]. For instance, WAAM is capable of achieving depositing rates ranging about 10 kg per hour. This pace is significantly higher compared to powder-based techniques, which may produce no more than 600 grammes per hour [7]. In addition, as contrasted to EB, AM, or PBF, WAAM is capable of producing bigger parts since it does not need a vacuum system to eliminate flaws and oxidation, which seem to be two factors that restrict component size. Such new equipment pieces also contribute to a rise in costs [7]. Additionally, WAAM feedstock resources are available at a lower price. And its material consumption is indicated by the buy-to-fly (BTF) ratios conversely the quantity concerning feedstock utilising the number of materials
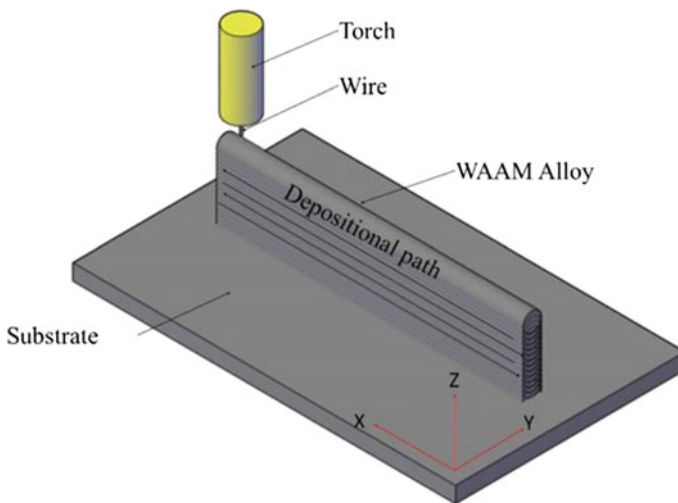

Fig. 2 WAAM method

enclosed by finished product, i.e., in greater comparison to EB, AM, or PB [6]. Lastly, WAAM utilises the electric ray similar to their heat origin, which may be employed in the surrounding ambience and outside of the compartment. The attributes make it possible for WAAM to conserve a substantial sum of money, particularly when it comes to costly materials like titanium [7].

On the other hand, WAAM has a few drawbacks that might make its adaption more difficult. The most significant drawback is something called residual stress (RS), which is a byproduct of thermal cycles that include local heating and cooling. High thermal gradients surrounding the heat source are responsible for the significant warming and cooling rates seen at various locations throughout the component [8]. These cause the component to expand and contract in a manner that is not consistent across its whole. Even when the heat source has been eliminated and also the item has cooled down, RS will still be present in the component. RS may have negative consequences on WAAM parts, including as distorting the component, causing it to delaminate, reducing its fatigue performance, and reducing its mechanical properties. An additional disadvantage is a microstructure that is produced as a consequence. When contrasted to the forging technique, the robustness and durability of WAAM components are inferior [6] ascribed to the existence of larger columniform granule. Since the curve in WAAM possess a diminish energy compactness relative to lasers conversely electron beams, the resulting temperature gradient is less extreme, allowing for the formation of these grains [6]. Finer grains are produced by temperature gradients that are higher. In order to achieve the same level of surface smoothness and layer thickness as a powder-based technique, WAAM needs much more machining than the latter [7].

3 Classification Contrary to WAAM Process

3.1 Gas Metal Arc Welding

Since the wire itself serves as the consumable electrode in GMAW, this welding technique is esteemed as one of the most versatile WAAM processes available. Additionally, as contrasted with GTAW and PAW, this welding process is capable of producing deposits at frequencies that are greater [8]. This approach, on the other hand, is prone to spill and arc inconsistency, both of which result in components of lesser quality. It is possible to make up for these deficiencies by using a few different strategies. Cold metal transfer (CMT) is a practice particularly which relies at an encumbered arc by immersing this same curve cable towards welding pool, which results in an elevated accumulation degree and minimal inserted heat [10]. The outcome of incorporating cold metal transfer (CMT) is demonstrated in GMAW AM of aluminium [9]. CMT is a method that relies on an encumbered arc by soaking the arc cord within welding hot tube [10]. CMT was coupled with various methods, such as pulsating the applied current, throughout the process. The use of these methods produced components that

had fewer pores, more grains that were equiaxed, welds that were oxidation transparent, and less spatter. In addition, [11] came to the conclusion that using CMT for high-temperature work tool steel avoids welding cracks, generates welds with more uniform layer width, and creates a product with a homogenous toughness profile, all of which contribute to an enhancement in the quality of component. Despite this, CMT is no more pertinent for welding Ti alloys by virtue of the existence of arc rambling, resulted in uneven weld areas [12].

3.2 *Gas Tungsten Arc Welding (GTAW)*

The electrode in GTAW is made of W strand, while another kind of wire serves as the material supply. In WAAM, GTAW is used widely, particularly for the purpose of titanium and aluminium welding. In comparison to GMAW, the benefits of GTAW provide a uniform layer structure, oxidation cleansing of the cathode, plus arc stability [13]. The fact that GTAW welders rely on an auxiliary wire feed that must be held in a specific position and inclination in relation to the electrode is an extra hurdle in comparison to the GMAW welders they are competing against [12].

3.3 *Plasma Arc Welding (PAW)*

PAW employs a non-comestible electrode. When contrast to GTAW, PAW has greater energy concentrations, superior arc stability, as well as a reduced quantity of inclusion, every one of which contributes to PAW's capability to achieve greater travel speeds while maintaining a superior quality part [14]. In addition, the pulsed PAW method, also known as PPAW, may be used to achieve reduced heat intake and better tensile clout, but it comes at the expense of poorer extension [15]. Nonetheless, because of the higher capital costs associated with the PAW process, it comes in at a higher price than GTAW and GMAW. In addition to this, PAW necessitates an external feed wire that is movable in relation to the electrode.

4 WAAM Apparatus

The potential application scope of WAAM systems is somewhat extensive; however, most of these systems may be classified as either autonomous or machine tool-based. These days, a wide variety of industrial machine tools and autonomous WAAM systems are accessible; in fact, these platforms are currently leading the market for fully integrated platforms and contain some capable manipulating systems as well as CAD/CAM software. In Fig. 3, a diagrammatic representation of the WAAM setup illustrates the many components that make it together. A WAAM equipment may

be formed from the combination of an arc welding source of power as well as any robotic prosthetic or manipulator that has three axes of movement. In a similar vein, there are numerous different power sources that are frequently employed however, the one that is appropriate relies mostly on the part that is being created as well as the material it is made of. It is possible to adapt a conventional robotic setup such that it may be utilised for the WAAM process. The most significant modifications made to the WAAM approach include equipping the turntable with an infinite spin, enhancing the software system, enhancing the thermal performance, and equipping the power supply with strong components so that it can withstand lengthy arc-on periods [16]. In the vast majority of WAAM systems, the articulating automaton serves as the mobility mechanism. In most cases, there are two different system options available, and each one is determined by the protective atmosphere. The initial one is made up of an enclosed space that has the capability of providing a very effective protective environment made of inert gas, similar to laser powder-based methods. However, it is not possible to make extremely big parts; therefore, this presents a significant size constraint. The second method wraps a conventional or custom-made shielding mechanisms around automatic welding arms or nozzles and positions it in such a manner as to achieve the greatest possible extent of a deposition while making use of a straight rail. Because of this, it is possible to successfully build large-scale assemblages and components [17].
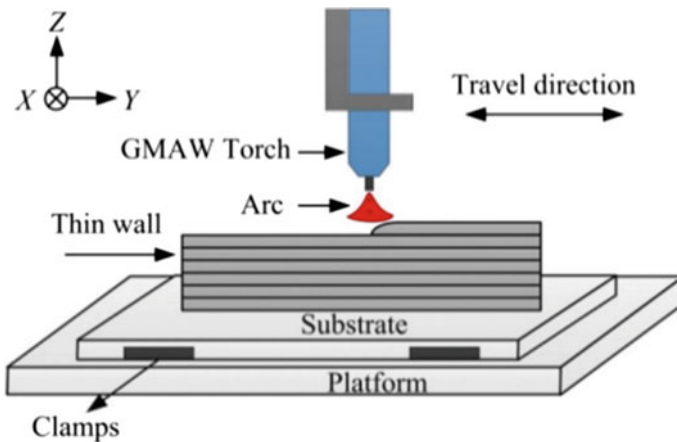
Fig. 3 WAAM setup [18]

5 Components Involved in the WAAM Manufacturing Process

The article targeted on the challenges that various researchers have encountered and explores the many metals and alloys that are utilised in the WAAM process. WAAM is able to make use of the material that is employed by traditional welding techniques. The feedstock is made available to be purchased in the marketplace in the shape of spools and in a wide variety of alloys. The different alloys utilised in the WAAM process are outlined below, along with the purposes for which they are best suited.

5.1 Titanium

WAAM technology has been used to study how titanium alloys can be used in different sectors. This is because titanium alloys are expensive, hard to work to, and have a high strength-to-weight ratio. Resolution and macroroughness (also known as waviness) are both about 0.5 mm when using WAAM for titanium alloys, and the deposition rate may vary anywhere from 0.75 to 2 kg/h. Consequently, the resulting metal layers are very thick; there is no requirement for the Hot Isostatic Pressing (HIPing) process, as well as the volume of the component is only restricted by the range of the manipulator [19]. WAAM-deposited deposited Ti-6Al-4 V has greater qualities then wrought alloy in terms of damage tolerance; in particular, its ability to withstand severe cyclic load is one order of magnitude better [20]. Despite this, the titanium alloy has significant anisotropy in terms of both its extension and its tensile strength. The rolling process results in strains in both the regular and cross-axes being created in the component [21, 22]. Last but not least, the sophisticated material possesses superior characteristics in comparison to the wrought alloy. It is demonstrated by the study that properties are independent just on coagulation circumstances; alternately, primarily dependent on the mechanical preparing which the item undergoes amid the accumulation [23].

5.2 Aluminium

Aluminium is perhaps the most appealing and affordable metal because of the unusual feature merger of outstanding corrosion opposition, elevated strength-to-weight ratio, and the flexibility to be united with unlike metals and non-metals. These characteristics allow Al to find extensive uses in a variety of industries, including transportation, electrical, and equipment, consumer items, engineering and construction, container and packaging, to mention just a few. Despite its extensive use, welding aluminium has proved difficult owing to its higher thermal expansion coefficient doubled coagulation drop relative to ferrous metals, extremely retentive oxide coating, and porosity

creation. The welding of aluminium is made more difficult by a phenomenon known as solidification cracking, which is directly connected to the composition of the alloy and indirectly relates to the quantity of eutectic that is present during solidification. In particular with aluminium–copper, aluminium–silicon, aluminium–magnesium, aluminium–lithium, and aluminium–magnesium–silicon alloys, fracture sensitivity rises in tandem with an increase in the alloy concentration until it reaches its maximum. Crack sensitivity is decreased when this threshold is exceeded due to the presence of extra eutectic supports in the backfilling of the crack (Table 1). Both alloy 2024 and alloy 7075 have a very high risk of solidification cracking. An illustration of solidification splitting in aluminium welding may be seen in Fig. 4. During welding, the volatile elements, like Mg, that are included in alloys of the 5xxx series (the primary alloying material), volatilise, which has a negative impact on the tensile qualities of the weld joint.

The upraised temperature in the heat-afflicted region (HAR) has a complicated impact. Recuperation, recrystallisation, grain expansion, precipitation dissolution, and/or reprecipitation are all possible outcomes for the heat-affected zone (HAZ), depending on how far it is from the heat source and the weld metal. It is possible for localised solidification cracking to take place whenever the temperature of a region that is close to a weld metal rises over the liquidus threshold of an alloy. Alloys in the series 6xxx and 7xxx suffer annihilation of tempering abrupted (Mg_2Si and $MgZn_2$, respectively), while alloys in the series 2xxx experience dissolution and reprecipitation (Al_2Cu), resulting in a decrease in overall strength. It is possible for partial dissolving and coarsening of the precipitate to take place in the area where the temperature won't go beyond solvus edge. These complexities have a negative

Table 1 Metals and their field of usage implementing WAAM

Applications	Alloys
Aerospace	Steel-based
Automotive	Ti-based, Ni-based
Marine	Al-based, Ni-based, bimetal
Corrosion R's	Al-based, steel
High temperature	Al-based, steel
Tools and moulds	Ti-based, Al-based, Ni-based, bimetal

Table 2 Compositional range for the binary system of aluminium that is both hot and short

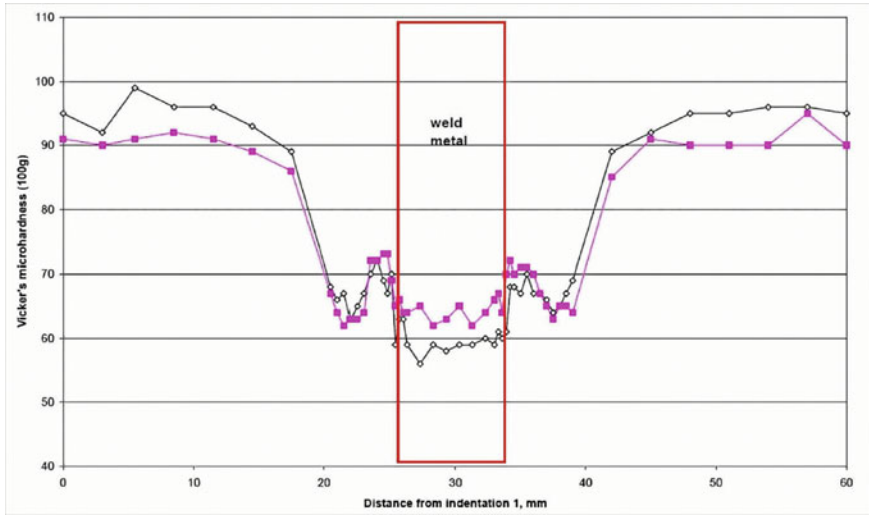| Alloy system	Hot short composition range (wt-%)
Al–Si	0.5–1.2
Al–Cu	2.0–4.0
Al–Mn	1.5–2.5
Al–Mg	0.5–2.5
Al–Zn	4.0–5.0
Al–Fe	1.0–1.5

Fig. 4 Microhardness alteration in the 6xxx series alloy over the weld when welded by MIG/MAG [24]

impact on the potency of the weld congregation, which, as shown in Fig. 4, fluctuates approximately along the centreline of the weld.

5.3 Stainless Steel

Because of its high ductility and resistant to corrosion, the WAAM processes is a subject of a growing extent of research projects. These researches attempt to produce stainless steel components. According to the findings of studies, WAAM has the potential to create stainless steel components that have favourable mechanical characteristics and microstructure [24]. When steel is welded or deposited, a composite form of austenite and ferrite may be observed, in spite of the experience that the microstructure of steel mostly consists of austenitic phase [25]. Both the heat cycle and the chemical properties of the stainless steel are significant elements that determine the phase fraction [26]. The quantity of ferrite in a component is mostly influenced by the pace at which it is cooled, and it is possible to get a weight percentage of up to thirty percent of ferrite [27, 28]. To successfully manufacture a controlled SS microstructure, it is essential to determine the appropriate process variables. Not only does fast cooling result in the development of limited austenite, in addition, it causes the precipitation of non-equilibrium nitrides [29]. Components have a trace of anisotropy, but with the right post-process heat treatment, this may be eliminated completely, and the final product can have qualities that are comparable to those of a product that was created in a normal manner. In the production of high-performance

alloy systems, WAAM-deposited stainless steel parts have also found a significant amount of use [26].

5.4 Additional Metals

Metals like bimetallic steel/Ni, steel/bronze, Mg alloys, aerospace (aggregate of Fe/ Al and Al/Ti), and automobile industries all have been the subject of research to investigate the possibility of employing WAAM [30]. Rather than working on the improvement and advancement of a process for the fabricating of functional components, the research focused primarily on determining the mechanical and microformation attribute about material, particularly for simple components with horizontal walls. This was done in lieu of focusing on the production of functional components.

6 Process Parameters

Controlling process parameters ensures stable, defect-free components. In a TIG-based WAAM system, critical factors affect bead's structure, abrasion, wetting inclination, melt via depth, microstructure, and oxidation values.

6.1 Wire Feeding Rate and Welding Speed

Setting the proportion of wire feeding speed to welding speed enables precise command over both the thickness and breadth of the layers that are produced [17]. When contrasted with using a single wire, the heat input generated by the dual-wire procedure is reduced, and the exterior morphology is improved. Both of these benefits occur while maintaining the same wire-feeding speed [31].

6.2 Heat Input

Because of the limited amount of heat input, the surface seems to be more even, and there is little risk of the weld pool overflowing and collapsing [32]. With higher heat inputs, it was found that the material had worse mechanical characteristics [33]. The mechanical anisotropy will decrease in response to lower heat input [34].

6.3 Travel Speed

When the travel speed is increased, the bead wideness, wetting inclination, melt-over extent all decrease. However, the bead thickness does not significantly alter throughout this process. There is speculation that there may be a reduction in the melt-through depth as a result of an increase in transit speed, which will lead to a reduced impact of heat input. Due to the increased travel speed, a little rise in the roughness of the bead may also be noted.

6.4 Distance Between the Beads

The degree to which the smoothness of a 1-d multipass architecture is impacted is mostly determined by the distance between the beads [35].

6.5 Voltage

When the voltage of the arc is raised, the thickness of the weld bead expands while the heights of the weld bead are smaller [36]. Controlling the voltage allows for further consistency in the breadth of structures with thin walls [37].

7 WAAM-Fabricated Component's Defect

WAAM manufacturing process is one that relies on welding, and it has also been observed that components may be manufactured in any form or size that is required. Because of this, anybody might be forgiven for assuming that the qualities of components will be compatible with the traditional welding technique. Stated statement, however, is not accurate due to the fact that its welding process will indeed be performed through for a variety of reasons, including various types of weld joining and weld cladding, among other things. We can clearly see the weld bead will be restricted to the majority of circumstances, if necessary, in case of casualness only a small number of weld beads would've been required to fulfil the requirements of the process. This is the case in nearly all of similar cases. The WAAM case, in particular when constructing components out of stainless steel, is wholly distinct due to the fact i.e., complete constituent is formed through layering the welding beads. It makes WAAM's case completely unique. In this particular instance, a great number of weld beads are required to be deposited, in particular in layers that correspond to the component that is being produced [38]. Because of this, the characteristics of the

weld beads can end up being different from those of standard welding. There is a significant chance that further flaws will be found in WAAM's produced components.

Although the significance of such weld flaws in WAAM elements is comparable to those of the welding procedures, it shall be acclaimed that it is extremely feasible to obtain a greater number of weld defects in this context due to the fact that a much greater number of weld beads are gathered together just to produce the final product. This is because the final element is formed by combining a large number of smaller weld beads. It is extremely difficult to achieve the reliability and quality aspects using products created using conventional techniques or typical AM procedures since the products generated by WAAM have faults. This makes it very difficult to fulfil the requirements. In light of this, it is highly advised to search for methods that might eliminate these faults throughout the process of fabricating metallic parts in WAAM [39]. The following is a list of the very few weld flaws which are most likely to occur in products that have been manufactured using WAAM. In addition, the weld flaws that manifest themselves throughout the WAAM production process are shown in Fig. 5.

- Porosity; High residual stress; Solidification cracking; Fatigue; Oxidation; Poor surface finish; Delamination; Deformation.
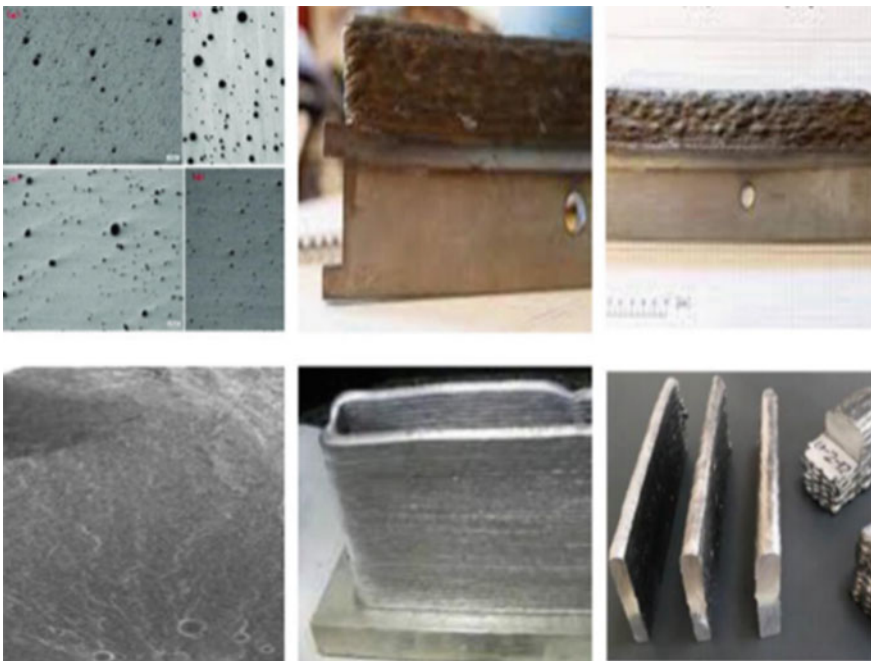
Fig. 5 Defects in WAAM components [40]

8 Methods to Reduce Defects in WAAM

8.1 Path Planning

When deciding on a particular strategy for route planning, it is very necessary to make certain that there will be an extremely limited number of arc extinguishing spots, since these locations are more likely to include flaws. On the other hand, one should try to avoid difficult paths and crossings wherever possible. Following the fabrication of the component, the component's outer surface must be machined in order to obtain a finished component. As a result, the harshness of the component's outermost layer is not as significant; however, the density of the component's internal systems plays a very significant role in determining the component's overall strength. In light of these observations, a number of authors have suggested a variety of approaches to the process of path planning, including raster [41], zigzag [42], contour [43], spiral [44, 45], fractal [46, 47], continuous [48], hybrid [49, 50], polygons [51], medial axis transformation [52], and adaptive medial [53].

It is very necessary to optimise the route of deposition in order to make a product that is free of defects. On the other hand, developing a route strategy and ensuring that it is optimised for each new shape may be a time-consuming process. In order to address the problem that was described, Michel et al. [54] developed a modular route planning approach. This requires the user to separate each layer into its own independent deposition section in order to construct a broad range of different complicated geometries. Jayaprakash et al. [55] created an intimate MATLAB's code to produce path planning among CAD model. Additionally, they implied that a model architecture would have complicated metallic structures with thin walls.

Metal may be stacked using unilateral/reciprocating piling. The accumulation of material in a single way might cause the structure to buckle and develop a hump [56, 57]. It is possible to get around this problem by using reciprocating stacking [58] or by changing the welding parameters at the wall's beginning and conclusion, such as welding I and travel speed [59]. In addition, a parallel accumulation is an option for speeding up the cycle time while cutting down on the amount of time spent waiting. Zhang et al. [59] made an observation that was quite similar to this one when they placed a tube-shaped prototype along a route that was not rotated. The authors discovered a substantial accumulation mistake at the beginning and the conclusion of their study, which may be remedied by switching to a rotational approach as the path method.

According to the findings of a number of studies, thermal buckling of the substrate may occur as a result of the build-up of heat; hence, a shift in the orientation of the substrate may be necessary to prevent this phenomenon.

After depositing a few layers, one may reach a stable state by adjusting the orientation of the substrate with respect to the lateral dimensions. This allows one to avoid oscillations [60, 61]. In a similar vein, Wu et al. [62] made some ideas that deformation of the substrate due to heat may be prevented by supplying low-power current is

applied to the highest levels while high-power current is applied to the lower levels. This would be done in order to achieve the desired effect.

8.2 Sensing and Control

Arc-based build-up and a longer cycle duration cause, WAAM is ideal for producing large components, although process stability and monitoring are critical. Studies have identified a variety of WAAM system sensing and control issues that might arise. Difficulties include wire twisting, wire feed position changes, geometrical inaccuracies, deposition flaws, and wire feeding system damage. The robotic arm twisted the cable may cause these issues. Zhang et al. [63] suggested a vision-based measurement approach to identify wire feeding position abnormalities to address the aforesaid issues. The programme estimates the wire's deflection angle in real time, allowing you to track changes. Passive infrared thermography by Cheng et al. [64] discovered weld bead form flaws in real time. AlexNet model was used to categorise the deposited molten layer profile as regular, deviation, flow, or hump. Based on current layer information, this system adjusts next layer depositing process variables. Other sensing equipment like a portable spectrometer [65] and microphone (acoustic signals) [66] were utilised to detect porosity problems and determine weld quality using algorithms for machine learning. JunXiong et al. said that controlling deposition form and size becomes increasingly challenging as the sum of levels raise [67]. The authors developed an adaptive control system that adjusts wire feed rate online to keep a consistent nozzle-to-top surface length and layer thickness in GMAW-based WAAM to address the aforesaid difficulties. A proportional, integral, and derivative (PID) closed-loop control adjusted wire feed rate and welding I to manage weld pool breadth. GTAW produces a uniform Inconel 718 profile [68]. Liu et al. [69] created an anticipating controller to regulate arc welding weld pool physics using machine vision to quantify length, breadth, and convexity. Xu et al. [70] presented a multi-sensor system to increase WAAM performance. Seven sensors have been included in this system in order to guide and assess various WAAM process parameters. These sensors include an infrared sensor for determining the layered temperature, an O2 concentration sensor and a gas flowmeter for the protecting gas, an arc V and I sensor in order to guide the warmth input, a wire feed speed sensor and a laser profilometer to keep track of the module's description while it is being deposited, and an arc V and I sensor to monitor the arc voltage.

Industry 4.0 and AI-based technologies, including cyber physical systems, IoT, big data, and cloud computing, may enhance WAAM systems. Big data, cloud computing, and IoT may support WAAM with CAD, route strategy, process improvement, and quality control [71] by reducing personnel and increasing data storage and processing capacity. WAAM uses neural network models or algorithms to forecast welding pool parameters and bead shape.

8.3   Maintaining Interpass Temperature

The interpass temp could be regarded as the temp at which the subsequent layer is accumulate. In WAAM, geometry of freshly deposited level is influenced by the one that came before it because the layer that came before it serves as the platform for the layer that comes after it. After layering of 20–25 layers, heat flow to the substrate gets poorer, and the amount of heat that is accumulated gradually rises. The collection of heat is something that may be kept to a minimum by including between the layer deposits, there is downtime. When this period of inactivity, accumulated layers will cool down as they will transmit heat to the surrounding environment. You may make sure that the desired interpass temperature is met by choosing an appropriate amount of downtime in between the interlayer deposits [72]. Because the rate of cooling also varies as the deposition process advances, a variable amount of idle time has to be supplied for each consecutive layer in order to maintain a consistent interpass temperature [73]. Montevecchi et al. came up with a novel method that is based on the finite element simulation to determine the varied amounts of down time with each succeeding layer [74]. An algorithm has been built for the purpose of this research that makes use of the simulated data in order to determine an exact amount of idle time for each layer. In addition, the authors verified the suggested method by carrying out the tests on just a test case components. In a similar manner, Geng and colleagues [75] created a conceptual method to improve the interpass temp and shown it by forming a wall made of 5A06 aluminium alloy. In this instance, the true temp at the arc marked site was analysed to the intended interpass temp, the alternative methods for material deposition—reciprocating motion, continuous movement, or delaying for following deposition—were chosen.

The total amount of time necessary to build the component will rise if idle time is allowed to pass between each layer. In their research, Va'zquez et al. [72] implemented a forced interpass cooling system by placing anvil chilled by liquid underneath the bottom plate. It was determined that controlled interpass cooling and just a pause period of one minute were necessary in order to achieve the desired mechanical characteristics. In addition, it has been stated that in order to attain the same mechanical qualities, a dwell period of nine minutes would have been necessary if the forced interpass cooling hadn't been done.

In a study somewhat similar to this one, Wu et al. [76] employing compressed air, the effects of strength interpass cooling in GTAW-WAAM were assessed CO_2 discovered an enhancement of the strength and hardness of Ti6Al4V.

There are just a few studies [77, 78] that employed the temperature of the substrate as a primary variable in order to investigate the thermal behaviour of WAAM. An experiment was carried out by B. Wu and colleagues [79], and the results showed that there was a difference in temperature between the substrate as well as the interpass temperature. This was especially true when the pause time duration between the layers was short. The researchers came to the conclusion that direct calculation of layer substrate temp using a non-contact measurement IR pyrometer may give data that is trustworthy and accurate.

When Chen Shen and colleagues [80] manufactured Fe3Al-based iron aluminide at a lowering interpass temp of 280 °C, they found that the initial several layers deposition towards the substrate had longitudinal fissures in them. The appearance of fractures is an indication that substantial residual stresses have been generated in the area close to the substrate. Because of this, it is very necessary to maintain an interpass temperature that is suitably high when depositing close to the substrate, particularly in situations where because the layer has a upraised heat conductivity. In addition, the author noticed an increment in yield strength and expansion in the centre region of the partition while interpass temp was raised.

Findings of many studies indicate that there is a significant need for the enhancement of mechanical specifications and microstructure; furthermore, the analysing of interpass temp may be a method that is capable of being utilised to successfully accomplish the aforementioned goals.

8.4 Porosity Reduction

Many research has shown that weld porosity is affected by variables including wire surface quality, purity of lead and base plate, weld criterion, duality, inert fumes, beacon leaning, etc. According to the available literature, porousness is the most pressing issue with aluminium AM since it drastically limits the mechanical behaviour of the elements. According to the research of Cong et al. [81], arc mode significantly affects the porosity of aluminium alloy.

As a consequence of its low heat generation and efficient oxide cleaning, CMT-PADV mode was able to effectively manage the porosity. It was claimed that around 150 micropores with a diameter of 50–100 lm were generated using the standard CMT mode. Micropores with a diameter of 10–15 lm were created in much lesser numbers using CMT-PADV mode. Microstructure of Al-6 Mg in pure CMT mode is constituted of average grain size with the normal size of 37 lm, as also found by Zhang et al. [74]. Averaging 30 lm in size, vaporised equiaxed granules were seen while operating in CMT + Pulse (CMTP) mode. In contrast, the equiaxed grain with a typical grain size of 20.6–28.5 lm was detected in the variable polarity (VP-CMT) mode, which is lower than the arc mode. The tubular dendrons were transformed into equated dendrons via the VPCMT arc/curve manner, which also reduced the grain size. The VPCMT mode strengthened the component to an uttermost tensile strength of 333 MPa, surpassing that of wrought alloy. The hardness of the manufactured specimen was adjacent to the authentic alloy, indicating that it might be commensurate with the cast aluminium blend components, as was the case when Yunpeng Nie et al. [82] created a slender partition of 4043 Al alloy having adjustable duality (CMT + ADV).

Existing research emphasises that vibration-assisted welding (VAW) procedures may reduce porosity and enhance the weld's mechanical properties [79]. The mechanical characteristics and related flaws in WAAM may be enhanced and reduced by using the vibration-assisted welding idea, as mentioned by Jose et al. [83]. In their

study on the impact of vibration on the microstructure and mechanical characteristics of Al–Mg blend during WAAM, Zhang et al. [84] found that grain refinement increases in tandem with the rate of vibration. Maximum tensile strength rose by 30 MPa, while average size of grains fell by 22.5% and porosity lowered from 6.66 to 1.52% due to vibration. Grain refining occurs as a result of the workpiece's vibration, which causes bending forces that break dendritic arms. The wire batch had a far larger impact on the area and magnitude of the porousness contrasted with the many aspects studied by Ryan et al. [85], who accumulated Al blend 2319 to examine the issue of distinct ways of CMT, lead batches, TS, WFS on porosity. Additionally, it was noted that the porosity really wasn't reliant on the voluminous content; rather, it was related to exterior polish, which impacts both the curve strength and the H composition. This was due to the fact that the surface finish influences the arc stability.

8.5   After-Process Heat Therapy

One of the best techniques to enhance WAAMed component mechanical characteristics and residual stresses is post-process heat treatment. Post accumulation heat therapy on WAAMed component granular size and mechanical characteristics has received little attention. High-pressure cold rolling may enhance WAAMed component mechanical qualities, but it inflates accumulation time, desired costly devices, and is challenging to employ with complicated configurations. Thus, a solution to enhance WAAMed component microstructure and mechanical characteristics is needed. When heated to 95 °C for 1 h and water quenched, Kim et al. [86] observed 25, 35, and 250% improvements in YS, UTS, and elongation. The specimens were formed through GMAW-accumulating low-C steel on austenitic steel to get a bimetal separation. Gao et al. [86] heat-treated a 9Cr steel wall and examined its microstructure and mechanical characteristics. According to martensitic structure, as-deposited toughness was good, however tempering temperature lowered UTS, YS, and toughness. Normalisation and tempering at 1323 and 1033 K improved strength and ductility. Gu et al. [87] used interfilm cold functioning and heat therapy after settling over 2219 Al blend. After interfilm rolling with 45 KN, the YS and UTS stopped at 244 and 314 MPa, subsequently, while after T6 heat treatment, they stopped at 305, 450 MPa. T6 heat therapy lowered the combining of the superfine granules and coarse granule area, element separateness, integration of intergranular and columnar granular area of AlSi7Mg0.6 [88]. Wang et al. [89] studied the microarrangements development of die steel H13 throughout WAAM and found anisotropic tensile features. Tensile ability became isotropic after 4 h of annealing at 83 °C. after action heat therapy varies on matter content and use. Because the after settling heat therapy has the potency to cause damage to the material, careful consideration must be given to both the material's composition and its intended uses.

8.6   Optimisation Techniques

To predict the bead configuration (bead's ht and thickness) accordance with settling specifications, a variety of techniques have been used, including the response surface method [90–92], factorial design [93], taguchi method [94–97], prediction of variance (ANOVA) [98], ANN [99] /the mixture of two distinct methods [100]. Response surface method (RSM) was utilised by Sarathchandra et al. [101] to examine the influence of weld I, standoff ht., weld agility on bead thickness and ht., insertion, and infusion. In another study, ANOVA was owned to investigate the impact of wire feed amount, Ag motion amount, travel agility, I, and bead size, shape, and roughness on the microstructure of Hastelloy X [102]. Artificial neural networks (ANNs) were modelled by Karmuhilan et al. [83] to predict bead shape based on the input variables. Additionally, the reverse model was created by the researcher to select weld parameters depending on required bead shape. Voltage with two stages, welding agility with three stages, feed estimate with three tiers was used as feed in aspects while both height and width were used as response variables for developing the ANN model. Full factorial experiment design was used for the trials. The inverted ANN type was planned to evaluate aided factors elicited from intended bead geometry. A forward ANN model was created to forecast bead geometries elicited from feed-in factors, while an inverted ANN type was designed to evaluate assisted factors generated from intended bead geometry. Nagesh et al. [100] used back-propagation NN to estimate the linkage among action factors, bead shape, Almeida et al. [50] used least square regression study to arbitrate the needed code of action criterion for the target partition thickness. It should be emphasised that the WAAM is a dynamic process because of many elements like fluctuating initial conditions and heat build-up, while the numerical models operate in an offline manner by utilising static training data. In order to assure the stability and correctness of WAAM, a real-time monitoring and assessment approach must be created. This technique would use real-time data, such as system temperature and weld bead geometry.

9   Summary

With WAAM as an affordable succeeding solution, the increasing market needs for aluminium goods, particularly high-strength alloys in the automotive and aerospace industries, might be met successfully. Variants of GMAW-based CMT have seen extensive use and study as a reliable WAAM of aluminium method. The use of interlayer rolling as well as the CMT-PADV technology significantly addressed the reduction of porosity, a significant problem hotly disputed in aluminium welding. Through a metallurgical lens, the study of weld pool behaviour and weld metal solidi-fication properties of heat-treatable and non-heat-treatable aluminium alloys for thin and thick structures may show to be a crucially constructive area of research. A significant gap in our understanding has been caused by the distortion and uneven

shrinkage that resulted from the unusual solidification behaviour of WAAM structure, as well as the residual stresses that this behaviour produced. Finding out more about the stress pattern in both closed and open loop constructions with various thicknesses would be intriguing. An important topic of research is the preservation of preheating and interpass temperatures as well as the relationship between heat build-up, residual stress generation, and mechanical characteristics. Unweldable aluminium alloys have shown strong WAAM capabilities, indicating the need to examine metallurgical features of WAAM solidification techniques. This discovery could make it necessary to redefine the term "weldability" or develop a new term for the "WAAMability" of alloys. Additionally, it is necessary to investigate if single-step forming may replace time-consuming interlayer rolling with aluminium alloys. Thus, weld deposition parameters, microstructure, defects, and mechanical qualities will determine the aluminium component's WAAM field maturity and integrity. Matching the mechanical characteristics of the WAAM product to those of the corresponding wrought goods, having no dimensional constraints on the product shape, having economic benefits, the necessity of relatively less sophisticated and less costly tools, and having simplicity in operation are the primary aspects that distinguish WAAM from methods such as superplastic forming, which were confined only up to the level of academic interest.

References

1. Ziolkowski M, Dyl T (2020) Possible applications of additive manufacturing technologies in shipbuilding: a review. Machines 8(4):84. https://doi.org/10.3390/machines8040084
2. Zocca A, Colombo P, Gomes CM, Günster J (2015) Additive manufacturing of ceramics: Issues, potentialities, and opportunities. J Am Ceram Soc 98(7):1983–2001. https://doi.org/10.1111/jace.13700
3. https://manufacturing.report/articles/which-additive-manufacturing-process-is-right-for-you
4. Gao W, Zhang Y, Ramanujan D, Ramani K, Chen Y, Williams CB et al (2015) The status, challenges, and future of additive manufacturing in engineering. Comput Aided Des 69:65–89. https://doi.org/10.1016/j.cad.2015.04.001
5. Hu J, Tsai HL (2007) Heat and mass transfer in gas metal arc welding. Part I: The arc. Int J Heat Mass Transf 50:833–846
6. Cunningham CR, Flynn JM, Shokrani A, Dhokia V, Newman ST (2018) Invited review article: strategies and processes for high quality wire arc additive manufacturing. Addit Manuf 22:672–686
7. Derekar KS (2018) A review of wire arc additive manufacturing and advances in wire arc additive manufacturing of aluminium. Mater Sci Technol (United Kingdom) 34:895–916
8. Williams SW, Martina F, Addison AC, Ding J, Pardal G, Colegrove P (2016) Wire + Arc additive manufacturing. Mater Sci Technol 32:641–647
9. Cong B, Ding J, Williams S (2015) Effect of arc mode in cold metal transfer process on porosity of additively manufactured Al-6.3%Cu alloy. Int J Adv Manuf Technol 76:1593–1606
10. Pickin CG, Young K (2006) Evaluation of cold metal transfer (CMT) process for welding aluminium alloy. Sci Technol Weld Join 11:583–585
11. Ali Y, Barnikol-Oettler S, Reimann J, Hildebrand J, Henckell P, Bergmann JP (2019) Wire arc additive manufacturing of hot work tool steel with CMT process. J Mater Process Technol 269:109–116

12. King WE, Barth HD, Castillo VM, Gallegos GF, Gibbs JW, Hahn DE, Kamath C, Rubenchik AM (2014) Observation of keyhole-mode laser melting in laser powder-bed fusion additive manufacturing. J Mater Process Technol 214:2915–2925
13. Geng H, Li J, Xiong J, Lin X, Zhang F (2017) Optimization of wire feed for GTAW based additive manufacturing. J Mater Process Technol 243:40–47
14. Martina F, Mehnen J, Williams SW, Colegrove P, Wang F (2012) Investigation of the benefits of plasma deposition for the additive layer manufacture of Ti-6Al-4V. J Mater Process Technol 212:1377–1386
15. Lin JJ, Lv YH, Liu YX, Xu BS, Sun Z, Li ZG, Wu YX (2016) Microstructural evolution and mechanical properties of Ti-6Al-4V wall deposited by pulsed plasma arc additive manufacturing. Mater Des 102:30–40
16. https://www.twi-global.com/technical-knowledge/job-knowledge/arc-basedadditive-manufacturing-137
17. Wua B, Pana Z, Dingb D, Cuiuria D, Lia H, Xuc J, Norrisha J (2018) J Manuf Proc 35:127–139
18. Determination of Surface Roughness in Wire and Arc Additive Manufacturing Based on Laser Vision Sensing
19. Manufacture of Complex Titanium Parts using Wire+Arc Additive ManufactureAdrian Addison, Jialuo Ding, Filomeno Martina, Helen Lockett, Stewart Williams Welding Engineering and Laser Processing Centre (WELPC), Cranfield University, Cranfield, MK43 0AL, United Kingdom Xiang Zhang, Faculty of Engineering and Computing, Coventry University, Coventry CV1 2JH,UK
20. Wang F, Williams S, Colegrove PA, Antonysamy A (2013) Metall Mat Trans A 44(2):968–977
21. Kurkin S, Anufriev V (1984) Weld Prod 31(10):32–34
22. Colegrove PA, Coules H, Fairman J, Martina F, Kashoob T, Mamash H, Cozzolino LD (2013) J Mater Process Technol 213(10):1782–1791
23. Martina F (2014) Investigation of methods to manipulate geometry, microstructure and mechanical properties in titanium large scale wire +Arc additive manufacturing PhD thesis, Cranfield University, UK, Cranfield, UK
24. Xu W, Gottos M, Roe M et al (2008) Impact tests on welded joints in 6000 series aluminium alloy extrusion for rail vehicles, Cambridge
25. Skiba T, Baufeld B, van der Biest O (2009) ISIJ Int 49(10):1588–1591
26. Washko SD, Agger G (1990) Wrought stainless steels. ASM Metals Handbook, 10th ed., Ohio: ASM International Handbook Committee, 841
27. Hosseini AV, Högström M, Hurtig K, Valiente Bermejo MA, Stridh L-E, Karlsson L (2019) Weld Worl 63(4):975–987. https://doi.org/10.1007/s40194-019-00735-y
28. Muthupandi V, Srinivasan PB, Seshadri SK, Sundaresan S (2003) Mater Sci Eng A 358:9
29. Vitek JM, David SA, Alexander DJ, Keiser JR, Nanstad RK (1991) Acta Metall Mater 39:503
30. Liao J (2001) ISIJ Int 41(5):460–467
31. Cong BQ, Su Y, Qi BJ (2016) Wire + arc additive manufacturing for aluminum alloy deposits. Aeros Manuf Technol 29–32:37
32. Wang S, Gu H, Wang W, Li C, Ren L, Wang Z et al (2019) Study on microstructural and mechanical properties of an Al–Cu–Sn alloy wall deposited by double-wirearc additive manufacturing process. Materials 13. https://doi.org/10.3390/ma13010073
33. Wang P, Zhang H, Zhu H, Li Q, Feng M (2021) Wire-arc additive manufacturing of AZ31 magnesium alloy fabricated by cold metal transfer heat source: processing, microstructure, and mechanical behavior. J Mater Process Technol 288:116895. https://doi.org/10.1016/j.jmatprotec.2020.116895
34. Lervåg M, Sørensen C, Robertstad A, Brønstad BM, Nyhus B, Eriksson M, et al (2020) Additive manufacturing with superduplex stainless steel wire by CMT process. Metals 10. https://doi.org/10.3390/met10020272
35. Wang S, Gu H, Wang W, Li C, Ren L, Wang Z et al (2020) The influence of heat input on the microstructure and properties of wire-arc-additive manufactured Al-Cu-Sn alloy deposits. Metals 10. https://doi.org/10.3390/met10010079

36. Bai JY, Wang JH, Lin SB (2016) Model for multi-beads overlapping calculation in GTA-additive manufacturing. J Mech Eng 52:97–102. https://doi.org/10.3901/JME.2016.10.097

37. Zhou LZ, Liu SH, Dong P (2006) Direct rapid manufacturing of metal parts besed on 3D welding. China Mech Eng 17

38. Abe T, Ji Kaneko HS (2020) Thermal sensing and heat input control for thin walled structure building based on numerical simulation for wire and arc additive manufacturing. Addit. Manuf 35. https://doi.org/10.1016/j.addma.2020.101357

39. Wu B, Pan Z, Ding D, Cuiuri D, Li H, Xu J et al (2018) A review of the wire arc additive manufacturing of metals: properties, defects and quality improvement. J Manuf Process 35:127–139. https://doi.org/10.1016/j.jmapro.2018.08.001

40. Sowrirajan M, Vijayan S, Arulraj M (2022) Welding based additive manufacturing: fundamentals. https://doi.org/10.5772/intechopen.104768

41. Bhatt PM, Kulkarni A, Kanyuck A, Malhan RK, Santos LS, Thakar S et al (2022) Automated process planning for conformal wire arc additive manufacturing. Int J Adv Manuf Technol 7:1–26. https://doi.org/10.1007/s00170-021-08391-7

42. Dunlavey MR (1983) Efficient polygon-filling algorithms for rasterdisplays. ACM Trans Graph 2:264–273. https://doi.org/10.1145/245.248

43. Rajan VT, Srinivasan V, Tarabanis KA (2001) The optimal zigzag direction for filling a two-dimensional region. Rapid Prototyp J 7:231–241. https://doi.org/10.1108/13552540110410431

44. Magee M, Seida S (1995) Path planning with offset curves for layered fabrication processes. J Manuf Syst 14:1995

45. Wang H, Jang P, Stori JA (2005) A metric-based approach to two dimensional (2D) tool-path optimization for high-speed machining. J Manuf Sci Eng Trans ASME 127:33–48. https://doi.org/10.1115/1.1830492

46. Ren F, Sun Y, Guo D (2009) Combined reparameterization-based spiral toolpath generation for five-axis sculptured surface machining. Int J Adv Manuf Technol 40:760–768. https://doi.org/10.1007/s00170-008-1385-9

47. Chiu WK, Yeung YC, Yu KM (2006) Toolpath generation for layer manufacturing of fractal objects. Rapid Prototyp J 12:214–221. https://doi.org/10.1108/13552540610682723

48. Wasser T, Jayal AD, Pistor C (1999) Implementation and evaluation of novel buildstyles in fused deposition modeling (FDM). Solid Free Fabr Proc 1999:95–102

49. Dwivedi R, Kovacevic R (2004) Automated torch path planning using polygon subdivision for solid freeform fabrication based on welding. J Manuf Syst 23:278–291. https://doi.org/10.1016/S0278-6125(04)80040-2

50. Ding D, Pan Z, Cuiuri D, Li H (2014) A tool-path generation strategy for wire and arc additive manufacturing. Int J Adv Manuf Technol 73:173–183. https://doi.org/10.1007/s00170-014-5808-5

51. Jin GQ, Li WD, Gao L (2013) An adaptive process planning approach of rapid prototyping and manufacturing. Robot Comput Integr Manuf 29:23–38. https://doi.org/10.1016/j.rcim.2012.07.001

52. Ding D, Pan Z, Cuiuri D, Li H (2015) A practical path planning methodology for wire and arc additive manufacturing of thin-walled structures. Robot Comput Integr Manuf 34:8–19. https://doi.org/10.1016/j.rcim.2015.01.003

53. Ding D, Pan Z, Cuiuri D, Li H, Larkin N (2016) Adaptive path planning for wire-feed additive manufacturing using medial axis transformation. J Clean Prod 133:942–952. https://doi.org/10.1016/j.jclepro.2016.06.036

54. Ding D, Pan Z, Cuiuri D, Li H, Van Duin S, Larkin N (2016) Bead modelling and implementation of adaptive MAT path in wire and arc additive manufacturing. Robot Comput Integr Manuf 39:32–42. https://doi.org/10.1016/j.rcim.2015.12.004

55. Michel M, Lockett H, Ding J, Martina F, Marinelli G, Williams S (2019) A modular path planning solution for wire + arc additive manufacturing. Robot Comput Integr Manuf 60:1–11. https://doi.org/10.1016/j.rcim.2019.05.009

56. Panchagnula JS, Simhambhatla S (2018) Manufacture of complex thin-walled metallic objects using weld-deposition based additive manufacturing. Robot Comput Integr Manuf 49:194–203. https://doi.org/10.1016/j.rcim.2017.06.003

57. Ye D, Wu D, Hua X, Xu C, Wu Y (2017) Using the multi-wire GMAW processes for controlling the formation of humping. Weld World 61:649–658. https://doi.org/10.1007/s40194-017-0458-5

58. Nguyen TC, Weckman DC, Johnson DA, Kerr HW (2005) The humping phenomenon during high speed gas metal arc welding. Sci Technol Weld Join 10:447–459. https://doi.org/10.1179/174329305X44134

59. Anzalone G, Zhang C, Wijnen B, Sanders P, Pearce J et al (2013) A Low-cost open-source metal 3-D printer. IEEE Access, IEEE 1:803–810. https://doi.org/10.1109/ACCESS.2013.2293018.hal-02119701

60. Zhang M, Chen Y, Li P, Male AT (2003) Weld deposition-based rapid prototyping: a preliminary study. J Mater Process Technol 135:347–357. https://doi.org/10.1016/S0924-0136(02)00867-1

61. Graf M, Halsig A, Hofer K, Awiszus B, Mayr P (2018) Thermo-mechanical modelling of wire-arc additive manufacturing (WAAM) of semi-finished products, Metals (Basel). https://doi.org/10.3390/met8121009

62. Yehorov Y, da Silva LJ, Scotti A (2019) Balancing WAAM production costs and wall surface quality through parameter selection: a case study of an al-Mg5 alloy multilayer-non-oscillated single PassWall. J Manuf Mater Process. https://doi.org/10.3390/jmmp3020032

63. Wu W, Xue J, Wang L, Zhang Z, Hu Y, Dong C (2019) Forming process, microstructure, and mechanical properties of thin-walled 316L stainless steel using speed-cold-welding additive manufacturing. Metals (Basel). https://doi.org/10.3390/met9010109

64. Zhan Q, Liang Y, Ding J, Williams S (2017) A wire deflectiondetection method based on image processing in wire + arc additive manufacturing. Int J Adv Manuf Technol 89:755–763. https://doi.org/10.1007/s00170-016-9106-2

65. Chen X, Zhang H, Hu J, Xiao Y (2019) A passive on-line defect detection method for wire and arc additive manufacturing based on infrared thermography. Solid Free Fabr 2019 Proc 30th Annu Int Solid Free Fabr Symp - An Addit Manuf Conf SFF (2019):1497–1510

66. Huang Y, Wu D, Zhang Z, Chen H, Chen S (2017) EMD-based pulsed TIG welding process porosity defect detection and defect diagnosis using GA-SVM. J Mater Process Technol 239:92–102. https://doi.org/10.1016/j.jmatprotec.2016.07.015

67. Sumesh KR, Mohandas K, Babu RS (2015) Use of machine learning algorithms for weld quality monitoring using acoustic Signature. Procedia Comput Sci 50:316–322. https://doi.org/10.1016/j.procs.2015.04.042

68. Xiong J, Zhang G (2014) Adaptive control of deposited height in GMAW-based layer additive manufacturing. J Mater Process Technol 214:962–968. https://doi.org/10.1016/j.jmatprotec.2013.11.014

69. Smith JS, Balfour C (2005) Real-time top-face vision based control of weld pool size. Ind Rob 32:334–340. https://doi.org/10.1108/01439910510600209

70. Liu YK, Zhang YM (2013) Control of 3D weld pool surface. Control Eng Pract 21:1469–1480. https://doi.org/10.1016/j.conengprac.2013.06.019

71. Xu F, Madhaven N, Dhokia V, McAndrew AR, Colegrove PA, Williams S et al (2016) Multi-sensor system for wire-fed additive manufacture of titanium alloys. In: 26th International conference on flexible automation and intelligent manufacturing (FAIM 2016) 2016: Article in Press.

72. Xia C, Pan Z, Polden J, Li H, Xu Y, Chen S et al (2020) A review on wire arc additive manufacturing: monitoring, control and a framework of automated system. J Manuf Syst 57:31–45. https://doi.org/10.1016/j.jmsy.2020.08.008

73. Vazquez L, Rodrıguez N, Rodrıguez I, Alberdi, E, Alvarez P (2020) Influence of Interpass cooling conditions on microstructure and tensile properties of Ti-6Al-4V parts manufactured by WAAM, Weld. World, 64:1377–1388. https://doi.org/10.1007/s40194-020-00921-3

74. Zhao H, Zhang G, Yin Z, Wu L (2013) Effects of interpass idle time on thermal stresses in multipass multilayer weld-based rapid prototyping. J Manuf Sci Eng Trans ASME 135:1–7. https://doi.org/10.1115/1.4023363

75. Montevecchi F, Venturini G, Grossi N, Scippa A, Campatelli G (2018) Idle time selection for wire-arc additive manufacturing: a finite element-based technique. Addit Manuf 21:479–486. https://doi.org/10.1016/j.addma.2018.01.007

76. Geng H, Li J, Xiong J, Lin X (2017) Optimisation of interpass temperature and heat input for wire and arc additive manufacturing 5A06 aluminium alloy. Sci Technol Weld Join 22:472–483. https://doi.org/10.1080/13621718.2016.1259031

77. Wu B, Pan Z, Ding D, Cuiuri D, Li H, Fei Z (2018) The effects of forced interpass cooling on the material properties of wire arc additively manufactured Ti6Al4V alloy. J Mater Process Technol 258:97–105. https://doi.org/10.1016/j.jmatprotec.2018.03.024

78. Ding J, Colegrove P, Mehnen J, Ganguly S, Almeida PMS, Wang F et al (2011) Thermo-mechanical analysis of wire and arc additive layer manufacturing process on large multi-layer parts. Comput Mater Sci 50:3315–3322. https://doi.org/10.1016/j.commatsci.2011.06.023

79. Denlinger ER, Heigel JC, Michaleris P, Palmer TA (2015) Effect of inter-layer dwell time on distortion and residual stress in additive manufacturing of titanium and nickel alloys. J Mater Process Technol 215:123–131. https://doi.org/10.1016/j.jmatprotec.2014.07.030

80. Ingram E, Golan O, Haj-Ali R, Eliaz N (2019) The effect of localized vibration during welding on the microstructure and mechanical behavior of steel welds. Materials (Basel). https://doi.org/10.3390/ma12162553

81. Shen C, Pan Z, Cuiuri D, Ding D, Li H (2017) Influences of deposition current and interpass temperature to the fe3al-based iron aluminide fabricated using wire-arc additive manufacturing process. Int J Adv Manuf Technol 88:2009–2018. https://doi.org/10.1007/s00170-016-8935-3

82. Cong B, Ding J, Williams S (2015) Effect of arc mode in cold metal transfer process on porosity of additively manufactured Al-6 3 % Cu alloy. Int J Adv Manuf Technol. https://doi.org/10.1007/s00170-014-6346-x

83. Nie Y, Zhang P, Wu X, Li G, Yan H, Yu Z (2018) Rapid prototyping of 4043 al-alloy parts by cold metal transfer. Sci Technol Weld Join 23:527–535. https://doi.org/10.1080/13621718.2018.1438236

84. Jose MJ, Kumar SS, Sharma A (2016) Vibration assisted welding and their influence on quality of welds. Sci Technol Weld Join 21:243–258. https://doi.org/10.1179/1362171815Y.0000000088

85. Zhang C, Gao M, Zeng X (2019) Workpiece vibration augmented wire arc additive manufacturing of high strength aluminum alloy. J Mater Process Technol 271:85–92. https://doi.org/10.1016/j.jmatprotec.2019.03.028

86. Ryan EM, Sabin TJ, Watts JF, Whiting MJ (2018) The influence of build parameters and wire batch on porosity of wire and arc additive manufactured aluminium alloy 2319. J Mater Process Technol 262:577–584. https://doi.org/10.1016/j.jmatprotec.2018.07.030

87. Gao C, Chen X, Chen X, Su C (2019) Microstructure and mechanical properties of as-deposited and heat-treated additive manufactured 9Cr steel. Mater Sci Technol (United Kingdom) 35:2234–2242. https://doi.org/10.1080/02670836.2019.1668603

88. Gu J, Ding J, Williams SW, Gu H, Bai J, Zhai Y et al (2016) The strengthening effect of inter-layer cold working and post-deposition heat treatment on the additively manufactured Al-6.3Cu alloy, Mater Sci Eng A, 651:18–26. https://doi.org/10.1016/j.msea.2015.10.101

89. Yang Q, Xia C, Deng Y, Li X, Wang H (2019) Microstructure and mechanical properties of AlSi7Mg0.6 Aluminum alloy fabricated by wire and arc additive manufacturing based on cold Metal transfer (WAAM-CMT), Materials (Basel). https://doi.org/10.3390/ma12162525

90. Wang T, Zhang Y, Wu Z, Shi C (2018) Microstructure and properties of die steel fabricated by WAAM using H13 wire. Vacuum 149:185–189. https://doi.org/10.1016/j.vacuum.2017.12.034

91. Kim D, Rhee S, Park H (2002) Modelling and optimization of a GMA welding process by genetic algorithm and response surface methodology. Int J Prod Res 40:1699–1711. https://doi.org/10.1080/00207540110119964

92. Gunaraj V, Murugan N (2000) Prediction and optimization of weld bead volume for the submerged arc process - Part 2. Weld J (Miami, Fla) 79:331
93. Gunaraj V, Murugan N (1999) Application of response surface methodology for predicting weld bead quality in submerged arc welding of pipes. J Mater Process Technol 88:266–275. https://doi.org/10.1016/S0924-0136(98)00405-1
94. Srimath N, Murugan N (2012) Development of mathematical models for prediction of weld bead geometry in cladding mild steel valve seat rings by PTAW. Proc Eng 38:15–20. https://doi.org/10.1016/j.proeng.2012.06.003
95. Choteborsky R, Rusul AH, Navratilova M, Hrabe P (2010) Effects of welding process parameters on the geometry and dilution of the bead in the automatic surfacing. Conf Proceeding - 4th Int Conf TAE 2010 Trends Agric Eng 2010, 41:244–247
96. Rao PS, Gupta OP, Murty SSN, Rao ABK (2009) Effect of process parameters and mathematical model for the prediction of bead geometry in pulsed GMA Welding. Int J Adv Manuf Technol 45:496–505. https://doi.org/10.1007/s00170-009-1991-1
97. Tarng YS, Yang WH (1998) Optimisation of the Weld Bead Geometry in Gas Tungsten Arc Welding by the Taguchi Method. Int J Adv Manuf Technol 14:549–554. https://doi.org/10.1007/BF01301698
98. Dinovitzer M, Chen X, Laliberte J, Huang X, Frei H (2019) Effect of wire and arc additive manufacturing (WAAM) process parameters on bead geometry and microstructure. Addit Manuf 26:138–146. https://doi.org/10.1016/j.addma.2018.12.013
99. Tarng YS, Juang SC, Chang CH (2002) The use of grey-based taguchi methods to determine submerged arc welding process parameters in hardfacing. J Mater Process Technol 128:1–6. https://doi.org/10.1016/S0924-0136(01)01261-4
100. Nagesh DS, Datta GL (2002) Prediction of weld bead geometry and penetration in shielded metal-arc welding using artificial neural networks. J Mater Process Technol 123:303–312. https://doi.org/10.1016/S0924-0136(02)00101-2
101. Tarng YS, Yang WH, Juang SC (2000) Use of fuzzy logic in the taguchi method for the optimization of the submerged arc welding process. Int J Adv Manuf Technol 16:688–694. https://doi.org/10.1007/s001700070040
102. Sarathchandra DT, Davidson MJ, Visvanathan G (2020) Parameters effect on SS304 beads deposited by wire arc additive manufacturing. Mater Manuf Process 00:1–7. https://doi.org/10.1080/10426914.2020.1743852

An Experimental Study to Probe Defect Formation and Failure Mode in Dissimilar Spot Joints

Suraj Prasad ⓘ **, Swagat Dwibedi** ⓘ **, and Abhilash Purohit** ⓘ

Abstract Expulsion is a familiar occurrence in the resistance spot welding process, which deteriorates the weld quality. Among various parameters, applied pressure significantly impacts in the expulsion of molten metal, which is undesirable. To understand the influence of electrode pressure on joint strength and mode of failure, thin sheets of Ti-6Al-4 V and SS316L are welded together in overlapped conditions using the RSW process at varying electrode pressure of 3, 4, 5, and 6 kg/cm^2, keeping other parameters constant. Further, joint strength and mode of failure are investigated. The results showed that with an increase in electrode pressure to an optimum value, i.e., 3–5 kg/cm^2, the strength of the weld joint is enhanced. In contrast, increasing electrode pressure beyond the optimum value leads to the expulsion of material, which restricts the nugget growth, leading to a reduction in joint strength.

Keywords Electrode pressure · Ti-SS · Tensile-shear strength · IF failure mode · Expulsion defect

1 Introduction

The evolution in the manufacturing field has focused on developing novel welding methods, and the necessity of joints in numerous operating conditions has given rise to the joining of dissimilar materials [1]. In the joining of dissimilar materials, several

S. Prasad
Department of Metallurgical and Materials Engineering, Indian Institute of Technology Patna, Bihta, Bihar 801106, India

S. Dwibedi (✉)
Department of Mechanical Engineering, Indian Institute of Technology Guwahati, Guwahati, Assam 781039, India
e-mail: swagatsudhadwibedi@gmail.com; swagatsudhadwibedi@yahoo.com

A. Purohit
Department of Mechanical Engineering, Synergy Institute of Engineering and Technology, Dhenkanal, Odisha 759001, India

problems arise, like the formation of unwanted second phases, variations in chemical composition, choosing suitable filler materials, and differences in thermophysical properties [2]. However, the dissimilar welding of titanium alloys and stainless steels facilitates exceptional mechanical properties, corrosion resistance, and lightweight numerous dissimilar metal combinations. Hence, it has gained considerable attention in the nuclear, chemical, and cryogenic sectors [3]. Stainless steel (SS) is substantially used in contrast to iron and carbon steel due to its excellent weldability, corrosion and thermal resistance, and ease of fabrication [4, 5]. Austenite and ferrite phases make SS316L one of the most appealing austenitic stainless steels (ASSs). Due to the lower pct. of carbon, carbide formation is also reduced in the grain boundaries [6].

On the other side, titanium and its alloys have been among the prominent engineering alloys in industrial usage [7]. Owing to excellent strength, low density, and greater thermal quality, Ti-6Al-4 V is extensively used in aerospace applications [8]. Since titanium alloys are expensive and stainless steel is economical, joining the two materials helps eliminate the components' cost and weight and simultaneously incorporates the advantages of both parent materials [9]. Ti-6Al-4 V also has a great affinity towards gases like nitrogen, oxygen, and hydrogen, which complicates using traditional welding process and eventually results in unfavourable effects on the weld strength. RSW can be employed as it enables precise generation of heat in constricted region, thereby limiting premature failure [10]. RSW is an essential and widely used joining process in automotive industries due to its low cost, robustness to part tolerance, low skill requirement, and easy automation. Therefore, RSW is the preferred method to join sheet metals for beverage containers, automotive, kitchen utensils, and spare parts [11].

Mansor et al. [6] experimentally determined the significance of electrode force in deciding the weld quality. Dwibedi et al. [12] examined the impact of weld time on the nugget size, strength, and failure mode of the spot weldments. The authors reported that increased weld time to a certain optimum level increases the strength and nugget size. However, Valaee-Tale et al. [13] reported that with the increase in electrode force, the nugget diameter tends to increase to a particular maximum value, which reduces after that reduces. Pouranvari et al. reported that the expulsion in spot welds could decrease energy-absorbing capacity [14]. Expulsion often leads to reduction in weld thickness and void in the weld centre, resulting in severe deterioration of joint strength, which is highly undesirable.

From the above discussion, it is clear that optimising the weld input variable is crucial to obtain high-quality joint strength. Hence, this work is mainly concerned with determining the impact of electrode pressure on the joint quality. Further, the joint strength using tensile-shear testing, macrostructure, and failure behaviour is also investigated.
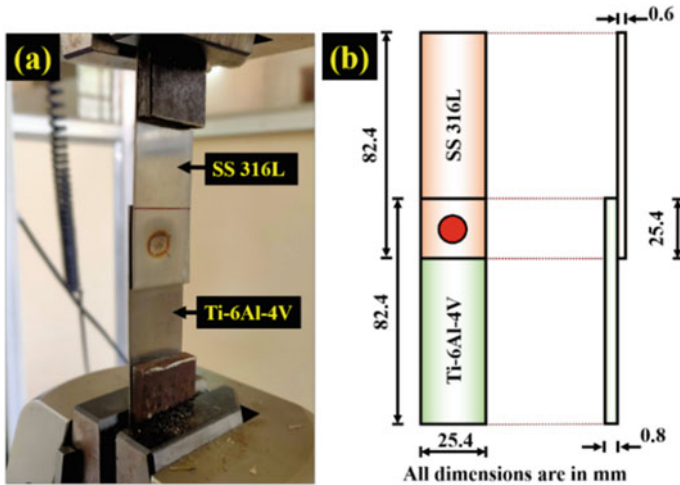
Fig. 1 **a** Spot weldment in lap configuration and **b** schematic of the welded specimen

2 Experimental Procedure

2.1 Materials and Methodology

In this study, sheets of Ti-6Al-4 V and SS316L with dissimilar thicknesses are selected as RSW specimens. SS316L sheets with dimensions 82.4 × 25.3 × 0.6 mm and Ti-6Al-4 V of dimensions 82.4 × 25.3 × 0.8 mm are selected to form the joint in lap configuration. Before carrying out the experiments, the materials were polished and cleaned eliminate any contaminated layers in the samples. The weld specimens are welded in a lap configuration with an overlapped length of 25.4 mm. Figure 1 depicts the specimen and its layout welded by the RSW process.

2.2 Welding Process

RSW process is used to carry out the experiments. Figure 2 depicts the schematic diagram of the RSW setup. The setup includes a compressor, electrode, paddle, pressure gauge, and electronic control. The RSW setup is controlled pneumatically and comprises a water-cooling system to cool the overall setup. The setup has the flexibility to change the parameters like electrode pressure, weld current, and time. The joining of the specimens is conducted in ambient conditions. During the process, the electrode pressure was controlled and measured continuously.
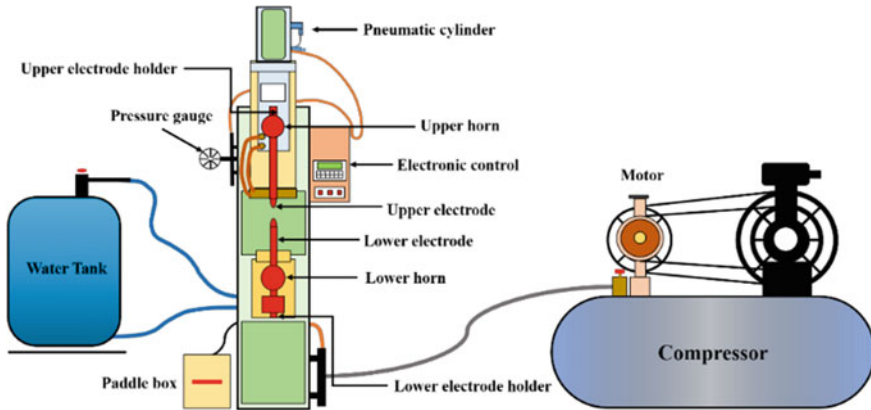
Fig. 2 Schematic of overall experimental RSW setup

Table 1 Process parameters employed for RSW experimentation

Sample no	S1	S2	S3	S4
Electrode pressure (kg/cm^2)	3	4	5	6
Current 7.8 kA, T_{squeeze}, T_{weld}, T_{hold}, T_{off} ~ 30 cycles				

2.3 Process Parameters

In the present study, to determine the effect of electrode pressure on the weldments, the electrode pressure was kept variable, keeping all other parameters unchanged. Here, the electrode pressure (E_p) (kg/cm^2) is varied from 3 to 6 during the experimentation. Table 1 shows the process parameters considered during the RSW welding. Post welding, the joints were tested by UTM to scrutinise the strength of the specimens, which determines the weld joint quality. The sample S1, S2, S3, and S4 denotes the sample being welded at different values of electrode pressure.

3 Results and Discussion

3.1 Tensile-Shear Test

Tensile-shear strength is one of the most critical parameters that signify the weld joint strength. Apart from tensile-shear strength, the tests are conducted to determine the load-bearing capacity (LBC) and fracture mode. The tests are performed using Universal Testing Machine (INSTRON) under ambient conditions with a speed

Fig. 3 RSW joints fabricated at different process parameters (S1, S2, S3, and S4)

(crosshead) of 1 mm/min. The specimens welded using the RSW process are shown in Fig. 3.

The influence of E_p on the tensile-shear load is summarised in Fig. 4. The graph outlines the sample processed at increasing E_p from S1 to S3 shows the peak tensile-shear load increase from 1.05 to 3.06 kN. However, with a further rise in electrode pressure to S4, the peak load reduced drastically from 3.06 to 1.65 kN. The increase in peak load with an increase in electrode pressure from S1 to S3 is attributed mainly to the rise in weld nugget diameter. This increment in the nugget area restricts the shear failure. However, the decrease in peak load in the sample processed at 6 kg/cm^2 electrode pressure may result from molten metal expulsion from the weld zone. As a result of an increase in electrode force, nugget growth is restricted, leading to a substantial reduction in the maximal tensile-shear load value. This occurs when the liquid nugget force on solid containment equals or exceeds the effective electrode force.

3.2 Mode of Failure Analysis

The maximum load is determined using a load–displacement plot. Upon analysing the fracture surface from the macrographs, the failure mode of the specimen is detected. The spot weld joints generally fail in different ways: pullout failure (PF), interfacial failure (IF), and partial-IF (PIF). The fracture mode relies on the least force required for failure. The shear stress between the sheets and its interface is the dominant force for the IF failure mode, whereas tensile force around the nugget boundary is the decisive force for the PF fracture mode. When the weld nugget is small, the necking is caused when the shear stress approaches a threshold value before tensile stress.
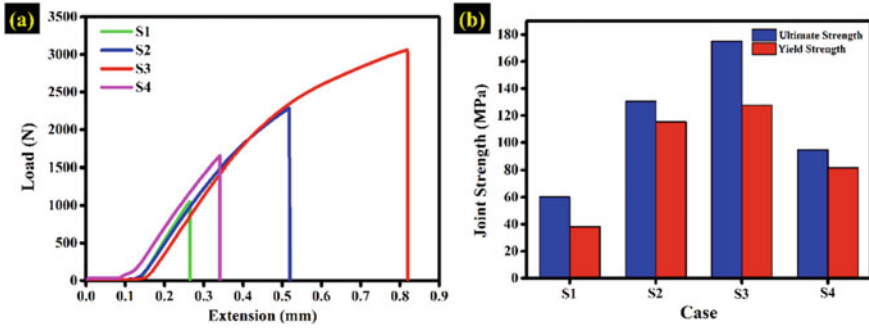
Fig. 4 **a** Applied load-extension curve obtained through tensile-shear test and **b** joint strength obtained in various cases

Thus, the IF failure mode is more likely; nonetheless, beyond the critical weld nugget PF mode is expected. The mode of failure can have a significant effect on LBC and energy absorption capability. In this study, only interfacial failure occurs in the weld samples. The reason attributed for the interfacial failure is due to the use of low E_p. Also, the evolution of Ti-Fe IMC in the fusion zone region provides brittle and hard behaviour, which leads to interfacial failure and lowers the LBC of the weld joint. Figure 5 depicts the interfacial mode of failure obtained in the experiment.
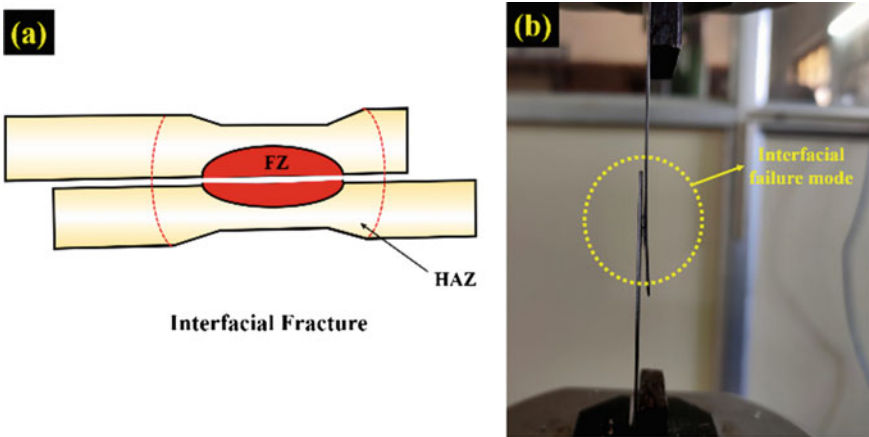
Fig. 5 **a** Schematic diagram of interfacial failure and **b** photograph of failed specimen (S1) obtained during experimentation

3.3 Defect Formation

The expulsion phenomenon occurs during spot welding when molten metal is ejected from the weld zone, reducing the weld strength of the joint. This might happen on the faying surface or at the electrode/workpiece contact region. The ejection that occurs at the contact between the workpiece and the electrode influences the surface quality as well as the longevity of the electrode but has little effect on the weld strength. However, expulsion occurring at faying layers involves the loss of molten metal and is undesirable. During welding, the pressure exerted by the molten metal causes it to exert force on its surrounding solid. Valaee-Tale et al. [13] reported expulsion results when the stress at the sheet interface exceeds the material's yield stress. When the diameter of the nugget remains small, the resultant force remains lower than the electrode force, which results in interface compressive stress in the sheet and prevents expulsion. However, when the diameter of nugget increases, the nugget force becomes more than the electrode force, and the stress becomes tensile, exceeding the material's yield strength and leading to the expulsion of the molten metal. Figure 6 presents the images of the failure modes of four different samples obtained from tensile tests. The four samples produce interfacial failure (IF) mode to complete tear around weld nugget and HAZ. With the increase in electrode pressure from 3 to 4 kg/cm^2, the weld nugget diameter increases, increasing the tensile-shear force, which eventually requires higher energy for the rupture of welded sheets. Although the failure is interfacial, it achieved the highest strength of 174.98 MPa at 5 kg/cm^2 of electrode pressure.
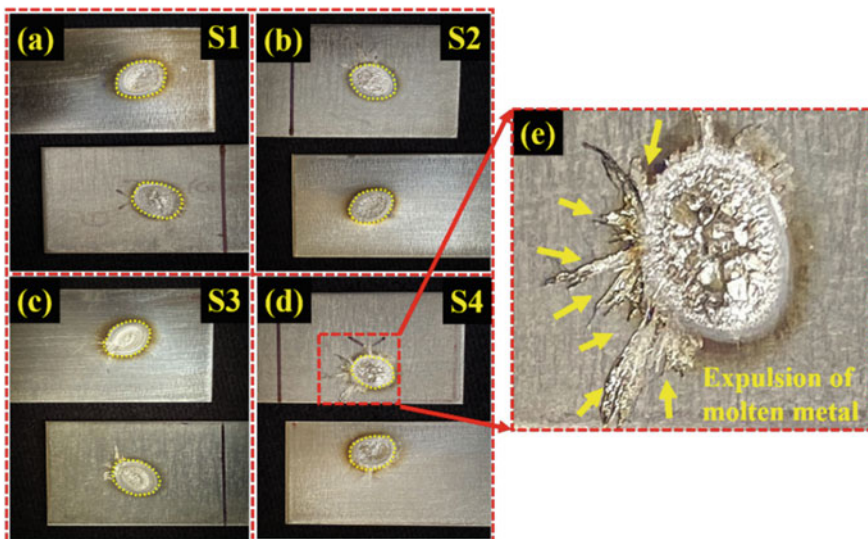
Fig. 6 **a–d** Fracture surface of weldments at different welding conditions, and **e** molten metal expulsion from the weld nugget for S4 case

4 Conclusion

This study successfully accessed the dissimilar spot welding of 0.6 mm thick SS316L and 0.8 mm thick Ti-6Al-4 V. The subsequent conclusions can be deduced from this present work:

1. Joint strength is found to be increasing with electrode pressure for sample S1, S2, and S3. Beyond the optimum electrode pressure (S3-5 kg/cm^2), further increase causes a reduction in strength due to the expulsion of metal, which restricts the growth of nugget and decreasing the load-bearing capacity.
2. The fracture analysis of the failed tensile-shear specimen is attributed to interfacial mode of failure at all values of electrode pressure. This failure behaviour can be related to the development of the Ti-Fe IMC in the fusion zone, which decreases the LBC of the joint and leads to failure via crack propagation through the weld zone.
3. It can be deduced that the electrode pressure is a significant parameter that induces expulsion during welding and is crucial to optimise as it shows detrimental effects on the workpiece.

References

1. Naik SR, Gadad GM, Hebbale AM (2021) Joining of dissimilar metals using microwave hybrid heating and Tungsten Inert Gas welding—a review. Mater Today Proc 46:2635–2640. https://doi.org/10.1016/j.matpr.2021.02.322
2. Dwibedi S, Bag S (2021) Development of micro-plasma arc welding system for different thickness dissimilar austenitic stainless steels. J Inst Eng India Ser C. 102:657–671. https://doi.org/10.1007/s40032-021-00696-6
3. Astarita A, Curioni M, Squillace A, Zhou X, Bellucci F, Thompson GE, Beamish KA (2015) Corrosion behaviour of stainless steel-titanium alloy linear friction welded joints: galvanic coupling: corrosion of stainless steel-titanium alloy welds. Mater Corros 66:111–117. https://doi.org/10.1002/maco.201307476
4. Dwibedi S, Jain NK (2016) Investigation on autogenous joining of stainless steel sheets of different thickness using micro Plasma Transferred Arc (μ-PTA) process. http://dspace.iiti.ac.in:8080/xmlui/handle/123456789/329
5. Dwibedi S, Jain NK, Pathak S (2018) Investigations on joining of stainless steel tailored blanks by μ-PTA process. Mater Manuf Process 33:1851–1863. https://doi.org/10.1080/10426914.2018.1476766
6. Mansor MSM, Yusof F, Ariga T, Miyashita Y (2018) Microstructure and mechanical properties of micro-resistance spot welding between stainless steel 316L and Ti-6Al-4V. Int J Adv Manuf Technol 96:2567–2581. https://doi.org/10.1007/s00170-018-1688-4
7. Kaya Y, Kahraman N (2012) The effects of electrode force, welding current and welding time on the resistance spot weldability of pure titanium. Int J Adv Manuf Technol 60:127–134. https://doi.org/10.1007/s00170-011-3604-z
8. Vigraman T, Ravindran D, Narayanasamy R (2012) Effect of phase transformation and intermetallic compounds on the microstructure and tensile strength properties of diffusion-bonded joints between Ti–6Al–4V and AISI 304L. Mater Des 1980–2015(36):714–727. https://doi.org/10.1016/j.matdes.2011.12.024

9. Wang T, Zhang B, Feng J (2014) Influences of different filler metals on electron beam welding of titanium alloy to stainless steel. Trans Nonferrous Met Soc China 24:108–114. https://doi.org/10.1016/S1003-6326(14)63034-X
10. Kumar B, Dwibedi S, Bag S, Mahapatra M, Gupta R (2022) A comparative study on microstructural and mechanical behaviour of spot welded Ti-6Al-4V alloy in as-welded and solution treated condition. Adv Mater Process Technol 8:2637–2651 https://doi.org/10.1080/2374068X.2021.1934648
11. Kumar B, Maharana BR, Sahu AK, Dwibedi S, Jena A, Das S, Prasad S (2022) Influence of squeeze time on fracture mode of SS304 spot weldments. In: Natarajan, S.K., Prakash, R., Sankaranarayanasamy, K. (eds) Recent Advances in Manufacturing, Automation, Design and Energy Technologies. Lecture Notes in Mechanical Engineering. Springer, Singapore. https://doi.org/10.1007/978-981-16-4222-7_36
12. Dwibedi S, Kumar B, Bhoi SR, Tripathy SR, Pattanaik S, Prasad S, Behera R (2020) To investigate the influence of weld time on joint characteristics of Hastelloy X weldments fabricated by RSW process. Mater Today Proc 26:2763–2769. https://doi.org/10.1016/j.matpr.2020.02.576
13. Valaee-Tale M, Sheikhi M, Mazaheri Y, Malek Ghaini F, Usefifar GR (2020) Criterion for predicting expulsion in resistance spot welding of steel sheets. J Mater Process Technol 275:116329. https://doi.org/10.1016/j.jmatprotec.2019.116329
14. Pouranvari M, Abedi A, Marashi P, Goodarzi M (2008) Effect of expulsion on peak load and energy absorption of low carbon steel resistance spot welds. Sci Technol Weld Join 13:39–43. https://doi.org/10.1179/174329307X249342

Finite Element Simulation of Tunnel Defect in Friction Stir Welding of Pure Copper: Effect of Tool Geometry

Debtanay Das[ID], Swarup Bag[ID], and Sukhomay Pal[ID]

Abstract The current work describes the development of a numerical model to accurately predict the occurrence of various defects during FSW of pure copper using thermomechanical responses. The developed numerical model examines the effect of varying tool dimensions on thermomechanical responses and defect formation. The tool traverse and rotation speed are kept constant at 30 mm/min and 1200 rpm. The shoulder diameter is varied between 14 and 28 mm. The 14 mm tool produces an imperfect weld with surface and sub-surface tunnel defects, whereas the 18 mm tool eliminates the surface tunnel defect. An increase of the shoulder diameter to 28 mm further reduces the extent of sub-surface tunnel defect. The increase in the shoulder diameter eliminates the surface tunnel and reduces the height of the sub-surface tunnel by about 50%. Significant material velocity, strain rate, and temperature on the retreating side (RS) produces the sub-surface tunnel defect on the advancing side (AS). The model can predict the initiation and advancement of the tunnel defect along the welding length. The velocity profile indicates that the material is equally distributed between the AS and RS behind the tool at the conclusion of the dwell stage. Alternatively, the material deposition becomes unequal between the AS and RS as the tool starts traversing. The tool–workpiece interface observes less stress and alternatively high strain, strain rate, and velocity distribution compared to the rest of the workpiece.

Keywords CEL · FSW · Surface and sub-surface defect

1 Introduction

Copper alloys find application in various industries due to their good thermal and electrical properties for fabricating heat exchangers, tubing, valves, and chemical equipment [1]. Defect-free joint by the different fusion welding techniques of Cu is

D. Das (✉) · S. Bag · S. Pal

Department of Mechanical Engineering, Indian Institute of Technology Guwahati, Assam, India

e-mail: debtanay@iitg.ac.in

tough to achieve due to high melting point and thermal conductivity, and presence of oxygen in the base material. This leads to severe embrittlement and porosity of the welded joints [2]. Due to its low heat input, less weld distortion, and better welding performance, the FSW process is becoming a preferred choice for the welding of Cu [3]. The vital process parameters influencing the FSW are the tool traverse and rotational speed, tilt angle, plunge depth, shoulder, and probe design and dimension [4, 5]. The rotation and traverse speed moderation influence the heat input to the weld plate [6]. The heat input significantly controls the joint quality and the microstructure of the welded sample [7]. The rotational speed investigated for welding the Cu alloys in the published literature ranges between 1000 and 1600 rpm and traverse speed between 30 and 150 mm/min [8, 9]. Besides the tool traverse and rotation speed, the heat input significantly depends on the tool shoulder (TS) and probe geometry. As most of the heat generated during FSW relies on the frictional heating, the total heat generated during the process is a function of the tool geometry [10, 11]. The tool probe is responsible for the material plasticization at the stir zone (SZ) and the weld quality. Different tool profiles are already investigated in the published literature [12, 13].

The experimental investigation of any manufacturing process provides an accurate result. However, the initial cost incurred due to the material and equipments required and the time expenditure are very high. Simultaneously, the numerical model for any process can significantly reduce the cost involved in the design and development of the process. Various numerical models are already developed that are able to predict the different thermomechanical responses and also the defects associated with FSW of aluminum alloys [14–16]. Sahlot et al. [1] developed a CFD-based 3D heat transfer model to study the heat transfer variation observed in the Cu during welding. An ALE-based model is described to investigate the Cu-FSW as well as to predict the hardness distribution in the welded sample [17]. The experimental validation indicates a near-accurate hardness value prediction by the developed model. The published literature describes various numerical models for the hybrid FSW of Cu, dissimilar FSW of Cu, and cooling-assisted FSW of Cu based on the Lagrangian and CFD approaches [18, 19]. The industrial acceptance of any manufacturing process depends on microstructural changes and mechanical strength evaluations. The prediction of defects and resistance to failure of the welded sample is equally important. The fracture resistance of dissimilar Al-Cu FSW was investigated by Aliha et al. [20].

Despite a significant number of published literatures focusing on the FSW process, the influence of varying tool geometry on the Cu-FSW is not explored. Moreover, there is a lack of a numerical model for Cu-FSW based on the CEL technique to visualize the surface and sub-surface phenomena during the process. The current work targets to fill this research gap to develop the whole process model. The numerical model using CEL approach predicts not only the transient distortion field on the workpiece domain, but also captures the surface phenomena for a large deformation process incorporating tool–material interaction of FSW process. The developed model is used to understand the influence of varying the shoulder diameter (SD),

on the various thermomechanical responses of the Cu-FSW. Moreover, the model is also used to predict the evolution of various defects during FSW.

2 Numerical Model

The CEL method is employed in the analysis of the FSW process, where the tool is represented as a Lagrangian domain and the workpiece as an Eulerian domain. Figure 1 illustrates the schematic of the solution domain utilized in this study. Further information about the numerical modeling approach can be found elsewhere [21].

The mass, momentum, and energy conservation equations during welding are given as [22]

$$\frac{\partial \rho}{\partial t} + \nabla \cdot (\rho v) = 0 \tag{1}$$

$$\rho \left(\frac{\partial v}{\partial t} + \nabla \cdot (v \otimes v) \right) = \nabla \cdot \sigma + \rho g \tag{2}$$

$$\rho C_p \left(\frac{\partial T}{\partial t} + v \cdot \nabla T \right) = \nabla \cdot (k \nabla T) + \nabla \cdot (\sigma \cdot v) + \dot{Q} \tag{3}$$

where ρ, v, σ, g, C_p, k, T, $\dot{Q}$ are the density, material velocity, Cauchy stress tensor, gravity constant, specific heat capacity, thermal conductivity, absolute temperature, and volumetric heat generation rate, respectively. The Lagrangian conservation equations are first converted to the Eulerian conservation equation. The general conservation form of the Eulerian form is given as [23]

$$\frac{\partial \phi}{\partial t} + \nabla \cdot \mathbf{\Phi}(\phi, v, x, t) = S \tag{4}$$

Fig. 1 Representation of various material, void, and tool domains along with mechanical boundary conditions imposed on the developed CEL model
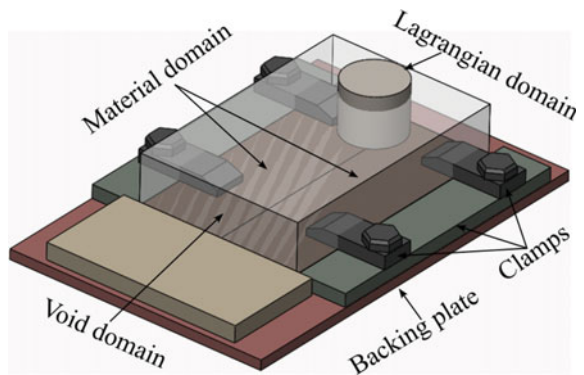
The operator splitting is used to split the Lagrangian and the Eulerian terms as given by

$$\frac{\partial \phi}{\partial t} = S \tag{5}$$

$$\frac{\partial \phi}{\partial t} + \nabla \cdot \mathbf{\Phi}(\phi, v, x, t) = 0 \tag{6}$$

where ϕ, $\mathbf{\Phi}$, and S are the arbitrary solution variable, flux function, and the source term.

The heat generation in FSW is due to both the frictional heating and heat generated due to material plasticization. The current model incorporates the effect of both heating approaches. The FSW tool has three surfaces in contact with the workpiece during welding, i.e., the TS, tool probe, and the tool probe root surface. The heat generated due to frictional heating by these three surfaces is given by [24, 25]

$$Q_{\text{shouler}} = \int\limits_{0}^{2\pi} \int\limits_{R_{\text{probe}}}^{R_{\text{shoulder}}} \omega \tau_{\text{contact}} r^2 \mathrm{d}r \mathrm{d}\theta \tag{7}$$

$$Q_{\text{probe}} = \int\limits_{0}^{2\pi} \int\limits_{0}^{H_{\text{probe}}} \omega \tau_{\text{contact}} r^2 \mathrm{d}r \mathrm{d}\theta \tag{8}$$

$$Q_{\text{pr}} = \int\limits_{0}^{2\pi} \int\limits_{0}^{R_{\text{probe}}} \omega \tau_{\text{contact}} r^2 \mathrm{d}r \mathrm{d}\theta \tag{9}$$

where ω is the rotational velocity, τ_{contact} is the contact shear stress, R_{probe} is the tool probe radius, and R_{shoulder} is the TS radius. The heat generated due to the material plastic deformation due to the tool–workpiece (TW) interaction is given by [26, 27]

$$Q_{\text{plas}} = \beta \bar{\sigma} \dot{\bar{\varepsilon}} \tag{10}$$

where β, $\bar{\sigma}$ and $\dot{\bar{\varepsilon}}$ are the conversion coefficient from plastic deformation to thermal heat, the equivalent stress, and the equivalent plastic straining rate.

To capture the influence of temperature, strain, and strain rate on flow stresses, the Johnson–Cook (JC) material model and damage models are employed [28]. These models provide a characterization of the material behavior, allowing for an accurate representation of the response under different loading conditions. The JC material constants for pure Cu are provided in the literature [29]. Figure 2 presents the material properties for the workpiece domain used in the current model.
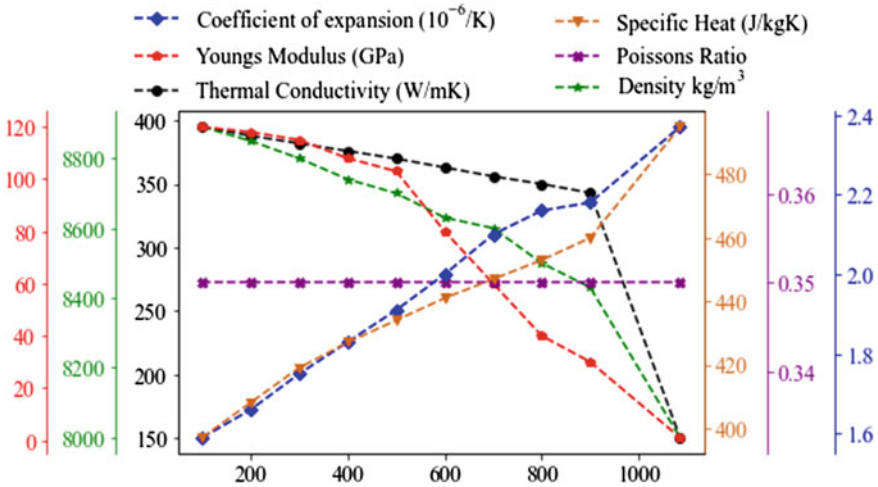
Fig. 2 Temperature-dependent material properties of pure Cu [30]

3 Result and Discussion

The current work predicts the welding of two Cu plates of thickness 100 mm ×
50 mm × 4 mm. A conventional FSW tool having a cylindrical probe with 4 mm
diameter is employed to weld the plates, whereas the SD is varied between 14 mm
and 28 mm. To investigate the consequence of varying the SD on the formation of
various surface and sub-surface defects, a constant welding parameter of 30 mm/min
and 1200 rpm are considered. Any form of tool tilt is not considered in the current
model. The tool is fabricated using the H-13 tool steel material.

Figure 3 illustrates the difference in the surface morphology with the change in the
tool SD. The increase in the SD primarily improves the heat generation, and thus, the
material flow. As the SD increases from 14 mm to 28 mm, the highest temperature on
the workpiece increases from 851 °C to 1018 °C. Simultaneously, the surface tunnel
defect is clearly visible with the SD of 14 mm and 18 mm (Fig. 3a, b). However, the
surface tunnel diminishes with the further increase in the SD to 24 mm and 28 mm
(Fig. 3c, d). The esteemed literature previously investigated and established that
the optimum SD to plate thickness (T) ratio is 3.5 for Al and Mg alloys [31, 32].
However, the same trend is not followed for the Cu-FSW, as seen in Fig. 3. A higher
thermal conductivity of Cu than the Al and Mg will dissipate heat to other areas of the
plate leading to the need for a bigger SD to generate sufficient heat to minimize the
defect formation. Therefore, the higher thermal conductivity and diffusivity could be
a possible reason for the deviation of the established 3.5 SD to T ratio for the FSW
of Cu.

Figure 4 shows the cross section of the welded sample with the tool of different
SD. The increase in the SD leads to the reduction of the defects in the welded
sample. As the welding is performed with an SD of 14 mm, the heat generation is
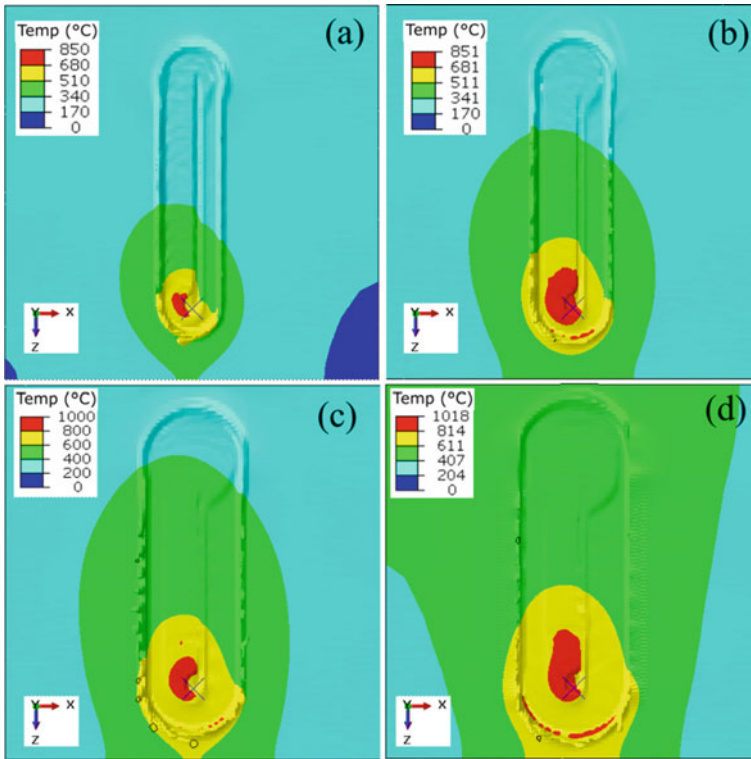
Fig. 3 Surface appearance during FSW of pure Cu with SD as **a** 14, **b** 18, **c** 24, and **d** 28 mm

less than optimum, i.e., less than 80% of the melting point temperature, leading to insufficient plasticization. The same is responsible for the formation of the tunnel defects (Fig. 4a). On increasing the SD to 18 mm and 24 mm, initially, the surface tunnel defect is completely eliminated and successively, the dimension of the sub-surface tunnel defect is also reduced as shown in Fig. 4b, and c. As the SD is further increased to 28 mm in Fig. 4d, the height of the sub-surface tunnel defect reduces by half, whereas the width of the defect also observes a reduction. The better plasticization of the material with increased SD is responsible for the reduction in defect formation. The further increase of the SD is restricted as the highest temperature observed with the SD of 28 mm case is a little over 90% of the base material melting point, and a further increase in the SD may lead to the excessive heating of the material. Therefore, the SD range between 24 mm and 28 mm can be considered the optimum SD window for Cu-FSW. Figure 5a depicts the material movement at the TW interface at the completion of plunge stage. The concentration of the velocity line just behind the tool probe indicates that the material is rotated about the tool and deposited behind it. The material deposition is uniform between the advancing side (AS) and the retreating side (RS) at the completion of the dwell stage. However, as the tool starts traversing, the material is pushed forward and splits between the AS
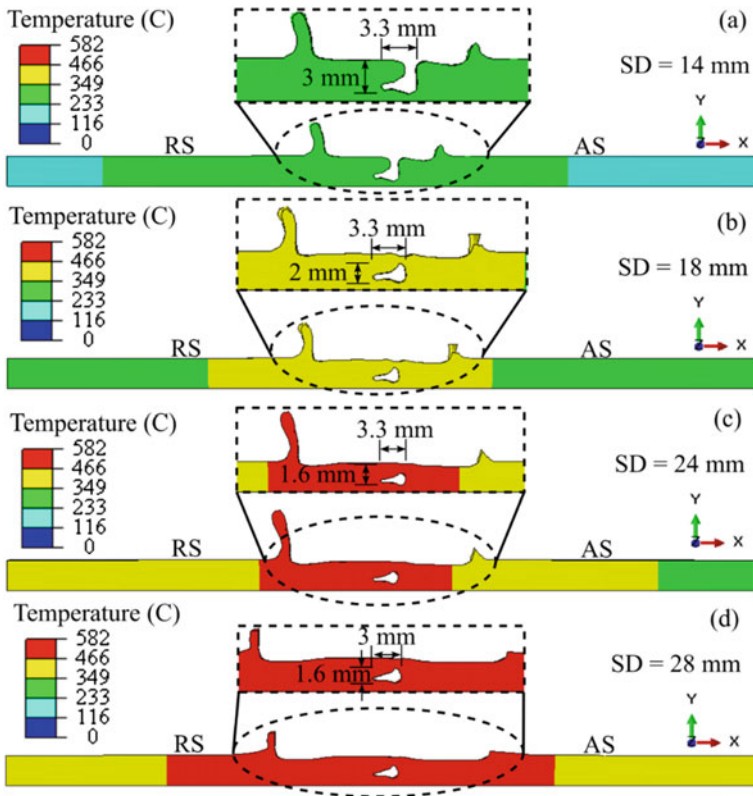
Fig. 4 Traverse cross-sectional appearance during FSW of pure Cu with SD as **a** 14, **b** 18, **c** 24, and **d** 28 mm

and RS causing the flash formation (Fig. 5b). Moreover, the velocity line around the tool probe is more directed toward the RS, compared to the AS. There is a significant drop in material velocity between Fig. 5a and b. The significantly low-temperature material in front of the traversing tool offers more resistance to material plasticization and movement and can lead to a reduction in material velocity. Figure 6 shows the front view (Fig. 6a) and the top view (Fig. 6b) of the traverse cross-sectional cut plane at the middle of the workpiece. The sub-surface velocity profile of the material also indicates a more dedicated material flow toward the RS than the AS. The material is rotated around the tool and is deposited toward the RS, thus filling the void left behind by the traversing tool on the RS. However, such material flow is not observed toward the AS (Fig. 6). This can be a possible explanation for the formation of the sub-surface tunnel defect toward the AS as shown in Fig. 4.

Figure 7 highlights the initiation and the evolution of the tunnel defect throughout the welding length. The cut-plane is considered in the longitudinal direction at the middle of the workpiece. The total duration to complete the welding is 120 s. Toward the completion of the dwell stage, we observe a proper temperature distribution along
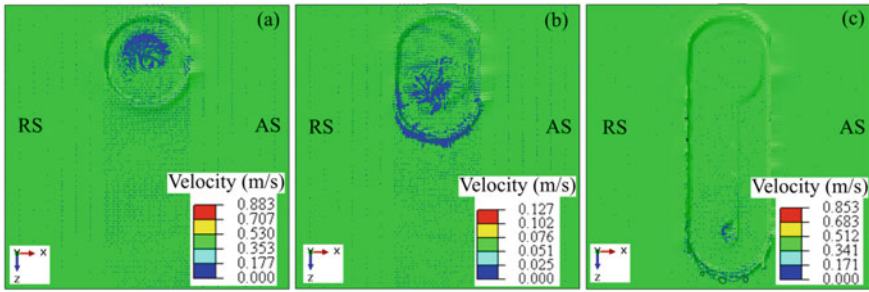
Fig. 5 Velocity distribution on the top surface of the solution domain at **a** 0 s, **b** 24 s, **c** 120 s with an SD of 28 mm, 30 mm/min, and 1200 rpm
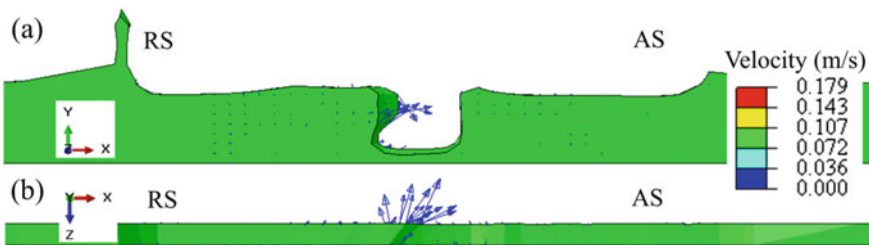
Fig. 6 Velocity distribution at the center plane of the workpiece with an SD of 28 mm **a** side view and **b** top view for the tool moving at 30 mm/min and 1200 rpm

the thickness of the workpiece, and a small amount of material is pushed out due to the tool plunge action (Fig. 7a). Initially, the tunnel defect is not observed with the progress of tool and it initiates after about 24 s as shown in Fig. 7b. The prediction of the exit hole is shown in Fig. 7c. As more material is ejected from the workpiece domain due to the tool action, there is a scarcity of material to fill the void left behind the traversing tool. This leads to the tunnel defect formation that continues for the remainder of the weld length, as shown in Fig. 7c. Figure 8 illustrates the temperature and the von Mises stress distribution on the workpiece at the end of each of the plunge, dwell, and the linear stages. During the plunge stage, the tool probe is primarily in contact with the workpiece, while the shoulder has marginal interaction with the workpiece. Therefore, the heat generation is limited to 644 °C (Fig. 8a). Simultaneously, the stress developed on the body is about 486.2 MPa (Fig. 8d). As the TS is in proper contact with the workpiece throughout the complete duration of the dwell stage, the heat generation on the workpiece is significantly higher, and the maximum temperature reaches about 984°C (Fig. 8b). Since the rise in temperature leads to more plasticization and easy flow of the material, the stress value at the completion of the dwell stage reduces significantly to 382.6 MPa as shown in Fig. 8e. A similar tendency of rise in workpiece temperature and reduction in the stress also continues to the linear stage. However, the change in the temperature
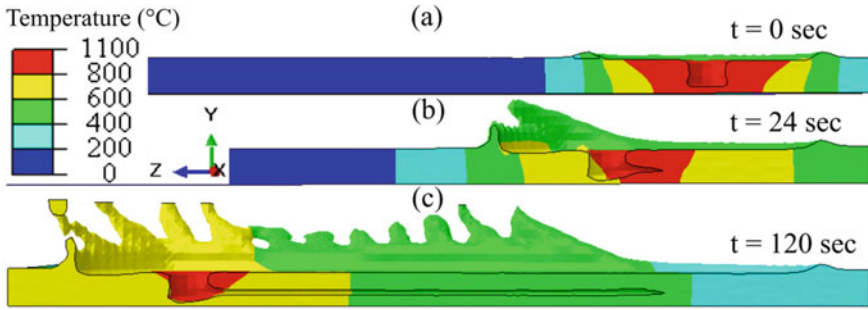
Fig. 7 Progress in the tunnel defect evolution along the longitudinal cross section with 30 mm/min and 1200 rpm at **a** 0 s, **b** 24 s, and **c** 120 s with an SD of 28 mm
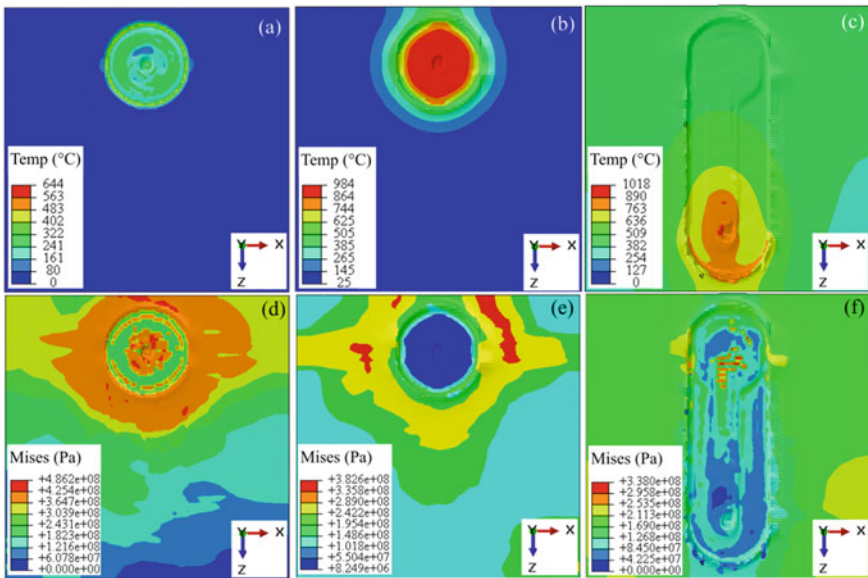
Fig. 8 Progress in the von Mises stress progression at **a** plunge end, **b** dwell end, **c** linear end; and temperature distribution at **d** plunge end, **e** dwell end, **f** linear end with an SD of 28 mm at 30 mm/min and 1200 rpm

and stress value between the end of the dwell and linear stages is marginal at about 34 °C and 44.6 MPa as shown in Fig. 8c and f.

Figure 9 presents the temperature, stress, equivalent plastic strain, plastic strain, velocity and strain rate distribution along cross section of the workpiece at partial completion of welding. The said analysis is performed to ascertain the capability of the developed model to provide in-process thermomechanical responses. Figure 9a represents the traverse line along which the thermomechanical responses are predicted. Typically, a higher temperature is observed on the AS of the FSW.
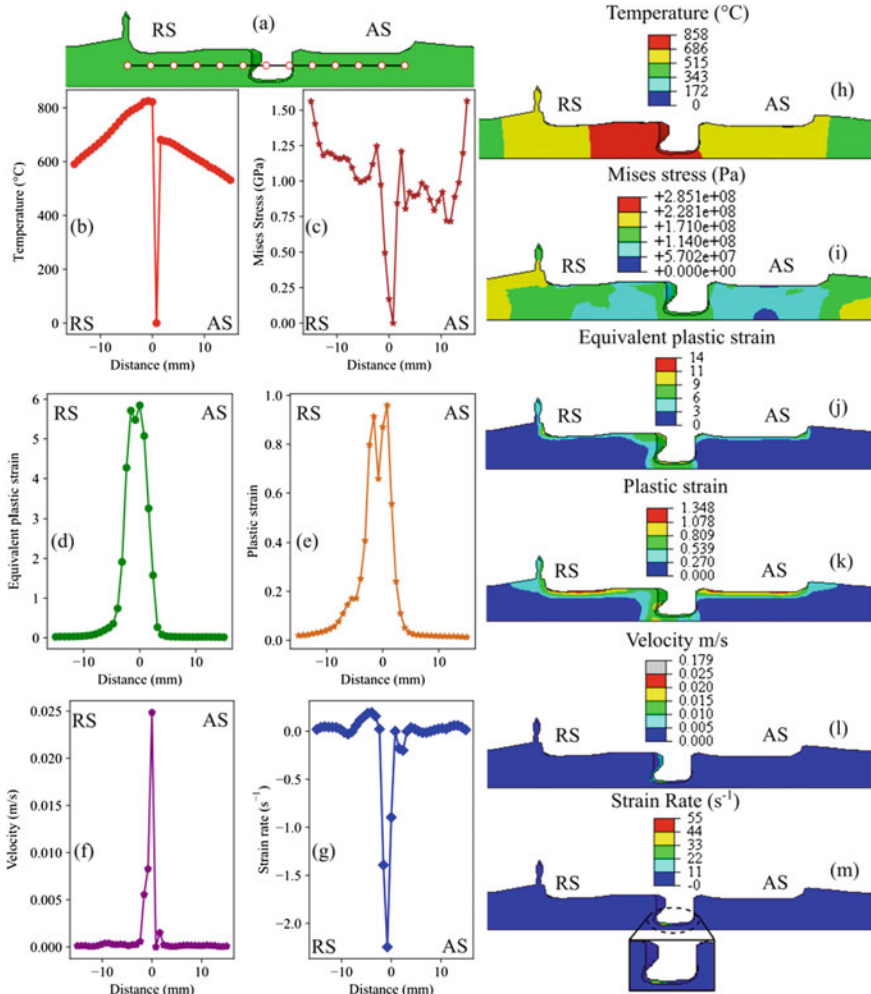
Fig. 9 **a** Schematic representation of the line of inspection at the center plane passing through the centroid, **b** temperature, **c** von Mises stress, **d** equivalent plastic strain, **e** plastic strain, **f** velocity, **g** strain rate distribution along the line shown in **a**; contour plot at the completion of half of the welding for **h** temperature, **i** von Mises stress, **j** equivalent plastic strain, **k** plastic strain, **l** velocity, **m** strain rate distribution

However, in the current instance, a higher temperature value is predicted on the RS (Fig. 9b, h). The absence of material behind the tool leads to the generation of the tunnel defect on the AS (Fig. 4), leading to lower heat generation on the AS. The difference in the maximum temperature next to the tool probe region between the AS and RS is about 150 °C. The von Mises stress distribution is presented in Fig. 9c, i. The lower stress value is observed near the tool probe. As the distance from the weld centerline increases, the temperature reduces while the stress increases. This

occurs due to the resistance presented by the less heated material to the material being pushed due to the action of the tool. Figure 9d, e present the equivalent plastic strain and plastic strain distribution, whereas Fig. 9i, j present the contour plot for the equivalent plastic strain and plastic strain. The strain distribution clearly indicates that material straining primarily occurs where the TS and the probe are in contact with the workpiece. The maximum strain is observed at the TW interface. As one move in the depth direction and traverse direction, i.e., away from the weld centerline, there is a significant decrease of the strain distribution. The material plasticization occurs at the TW interface; therefore, the material just beyond the interface exhibits strain distribution. However, as one moves away from the interface, the strain distribution becomes minimal. Moreover, a higher strain value is observed on the RS, indicating a higher straining of material on the RS. A similar tendency is observed with the velocity distribution at the TW interface. A significantly higher velocity is observed on the RS than the AS. This ensures that more material is pushed toward the RS resulting in the absence of the sub-surface tunnel defect toward the RS. The strain rate distribution is presented in Fig. 9g, m. The highest strain rate is observed at the TW interface at the RS. The negative value of the strain indicates a compressive nature. Moreover, the highest strain rate region coincides with the highest velocity region. This indicates the material being deposited behind the tool due to the action of the tool is being compressed into the SZ.

4 Conclusions

The current work primarily focuses on developing a model that can predict the various defects during Cu-FSW. Only the effect of SD on weld quality was investigated for the current work and can be further broadened to incorporate the effect of other parameters, such as the probe size, design, and tilt angle. The subsequent deductions made from the current investigation are:

- The 14 mm tool produces a significantly defective weld with both the surface and sub-surface tunnel defect, whereas the 18 mm tool eliminates the surface tunnel defect.
- Increasing the shoulder diameter to 28 mm eliminates the surface tunnel defect and further reduces the sub-surface tunnel defect.
- The change in the shoulder diameter can alone eliminate the formation of the surface tunnel and reduce the height of the sub-surface tunnel defect by about 50%.
- The model can predict any temporal or spatial distribution of temperature, stress, strain, strain rate, velocity, surface tunnel defect, and sub-surface tunnel defect during FSW. Hence, it can be considered as a whole process model.
- During FSW of pure Cu, the highest temperature, von Mises stress, equivalent plastic strain, plastic strain, velocity, and strain rate distribution are observed to be about 800 °C, 125 MPa, 6, 1, 25 mm/s, and 2.5 s^{-1}, respectively.

References

1. Sahlot P, Singh AK, Badheka VJ, Arora A (2019) Friction stir welding of copper: numerical modeling and validation. Trans Indian Inst Met 72:1339–1347
2. Lin JW, Chang HC, Wu MH (2014) Comparison of mechanical properties of pure copper welded using friction stir welding and tungsten inert gas welding. J Manuf Process 16:296–304
3. Lee WB, Jung SB (2004) The joint properties of copper by friction stir welding. Mater Lett 58:1041–1046
4. Mishra RS, Ma ZY (2005) Friction stir welding and processing. Mater Sci Eng R Rep 50:1–78
5. Zhang Z, Zhang HW (2009) Numerical studies on controlling of process parameters in friction stir welding. J Mater Process Technol 209:241–270
6. Xue P, Xie GM, Xiao BL, Ma ZY, Geng L (2010) Effect of heat input conditions on microstructure and mechanical properties of friction-stir-welded pure copper. Metall Mater Trans A Phys Metall Mater Sci 41:2010–2021
7. Shen JJ, Liu HJ, Cui F (2010) Effect of welding speed on microstructure and mechanical properties of friction stir welded copper. Mater Des 31:3937–3942
8. Sakthivel T, Mukhopadhyay J (2007) Microstructure and mechanical properties of friction stir welded copper. J Mater Sci 42:8126–8129
9. Farrokhi H, Heidarzadeh A, Saeid T (2013) Frictions stir welding of copper under different welding parameters and media. Sci Technol Weld Join 18:697–702
10. Arora A, De A, Debroy T (2011) Toward optimum friction stir welding tool shoulder diameter. Scr Mater 64:9–12
11. Mehta M, Arora A, De A, Debroy T (2011) Tool geometry for friction stir welding - Optimum shoulder diameter. Metall Mater Trans A Phys Metall Mater Sci 42:2716–2722
12. Khodaverdizadeh H, Heidarzadeh A, Saeid T (2013) Effect of tool pin profile on microstructure and mechanical properties of friction stir welded pure copper joints. Mater Des 45:265–270
13. Kumar A, Raju LS (2012) Influence of tool pin profiles on friction stir welding of copper. Mater Manuf Process 27:1414–1418
14. Akbari M, Ezzati M, Asadi P (2022) Investigation of the effect of tool probe profile on reinforced particles distribution using experimental and CEL approaches. Int J Light Mater Manuf 5:213–223
15. Das D, Bag S, Pal S (2021) Investigating surface defect by tool-material interaction in friction stir welding using coupled Eulerian-Lagrangian approach. Manuf Lett 30:23–26
16. Al-Badour F, Merah N, Shuaib A, Bazoune A (2014) Thermo-mechanical finite element model of friction stir welding of dissimilar alloys. Int J Adv Manuf Technol 72:607–617
17. Pashazadeh H, Masoumi A, Teimournezhad J (2013) Numerical modelling for the hardness evaluation of friction stir welded copper metals. Mater Des 49:913–921
18. Patel NP, Parlikar P, Singh Dhari R, Mehta K, Pandya M (2019) Numerical modelling on cooling assisted friction stir welding of dissimilar Al-Cu joint. J Manuf Process 47:98–109
19. Gotawala N, Shrivastava A (2020) Analysis of material distribution in dissimilar friction stir welded joints of Al 1050 and copper. J Manuf Process 57:725–736
20. Aliha MRM, Kalantari MH, Ghoreishi SMN, Torabi AR, Etesam S (2019) Mixed mode I/II crack growth investigation for bi-metal FSW aluminum alloy AA7075-T6/pure copper joints. Theor Appl Fract Mech 103:102243
21. Das D, Bag S, Pal S, Ruhul Amin M (2020) Prediction of surface profile in friction stir welding using coupled eulerian and lagrangian method. In: ASME international mechanical engineering congress and exposition, proceedings (IMECE). p V011T11A035. ASME

22. Akbari M, Asadi P, Behnagh RA (2021) Modeling of material flow in dissimilar friction stir lap welding of aluminum and brass using coupled Eulerian and Lagrangian method. Int J Adv Manuf Technol 113:721–734
23. Ragab M, Liu H, Yang GJ, Ahmed MMZ (2021) Friction stir welding of 1Cr11Ni2W2MoV martensitic stainless steel: numerical simulation based on coupled Eulerian Lagrangian approach supported with experimental work. Appl Sci 11:1–18
24. Neto DM, Neto P (2013) Numerical modeling of friction stir welding process: a literature review. Int J Adv Manuf Technol 65:115–126
25. Das D, Bag S, Pal S, Ruhul Amin M (2021) A finite element model for the prediction of chip formation and surface morphology in friction stir welding process. J Manuf Sci Eng 144:041015
26. Wen Q, Li WY, Gao YJ, Yang J, Wang FF (2019) Numerical simulation and experimental investigation of band patterns in bobbin tool friction stir welding of aluminum alloy. Int J Adv Manuf Technol 100:2679–2687
27. Das D, Bag S, Pal S, Sharma A (2023) Material Defects in friction stir welding through thermos—mechanical simulation : dissimilar materials with tool wear consideration. Materials (Basel). 16:301 (2023)
28. Das D, Bag S, Pal S (2021) A finite element model for surface and volumetric defects in the FSW process using a coupled Eulerian-Lagrangian approach. Sci Technol Weld Join 26:412–419
29. Liu H, Zhang J, Xu X, Qi Y, Liu Z, Zhao W (2019) Effects of dislocation density evolution on mechanical behavior of OFHC copper during high-speed machining. Materials (Basel) 12:1–18
30. Zhang X, Li L, Pan T, Chen Y, Zhang Y, Li W, Liou F (2020) Additive manufacturing of copper-tool steel dissimilar joining: experimental characterization and thermal modeling. Mater Charact 170:110692
31. Malarvizhi S, Balasubramanian V (2012) Influences of tool shoulder diameter to plate thickness ratio (D/T) on stir zone formation and tensile properties of friction stir welded dissimilar joints of AA6061 aluminum-AZ31B magnesium alloys. Mater Des 40:453–460
32. Sevvel P, Jaiganesh V (2015) Effect of tool shoulder diameter to plate thickness ratio on mechanical properties and nugget zone characteristics during FSW of dissimilar mg alloys. Trans Indian Inst Met 68:41–46

Modelling Temperature Distribution in Multi-track Multi-layer Selective Laser Melted Parts: A Finite Element Approach

Anuj Kumar and Mukul Shukla

Abstract Selective laser melting (SLM) is an additive manufacturing (AM) process suited for printing three-dimensional metallic components. Throughout the SLM process, the thermal characteristics are crucial in ensuring the build quality of the print. Therefore, it becomes essential to determine the temperature distribution of the SLMed parts. Experimental approaches to address this issue are capital and time intensive. Numerical modelling studies for temperature distribution generally simulate single tracks, which cannot be extrapolated for the whole SLMed part. In this study, the multi-track, multi-layer SLM builds of IN718 were simulated using a three-dimensional finite element model. The temperature-dependent material properties were considered in modelling, and the laser scanning beam was described as a moving volumetric heat source. The temperature distribution on printed layers was evaluated, after which thermal profiles from simulated layers were extracted, and the permissible limit exercise was performed to identify potential hotspots. The predicted thermal history can also be used to optimise SLM process parameters. Further, the effects of scan strategy (layer start and rotation angle) on the temperature distribution were studied. It is evident from the results that the layer rotation angle affects the thermal history as the length of the scan vector changes depending upon the scan strategy used in a layer. This modelling approach can be utilised to further develop the microstructure evolution based on the simulated thermal history for SLMed parts.

Keywords Additive manufacturing · IN718 · Selective laser melting · Thermal history

A. Kumar · M. Shukla (✉)
Department of Mechanical Engineering, Motilal Nehru National Institute of Technology Allahabad, Prayagraj, India
e-mail: mukulshukla@mnnit.ac.in

M. Shukla
Department of Mechanical and Industrial Engineering Technology, University of Johannesburg, Johannesburg, South Africa

1 Introduction

Metal additive manufacturing also known as MAM demonstrated remarkable ability in the fabrication of metal objects with complex geometry [1]. The geometric versatility of MAM stems from the layer-by-layer scanning of a heat source, which generally melts the metal powder or wires [2]. Among the different MAM processes flourishing, selective laser melting (SLM) offers advantages in developing fully dense, near-net-shape metallic parts [3]. The high-energy laser scans the previously placed powder layer, melting the powder particles beneath the beam, which leads to the creation of a melt pool [4]. A fine track of solid metal is developed as the laser beam travels, and by repeating these scans, the entire part is fabricated [5].

Nickel-based superalloys have become more prevalent in pivotal industries like aerospace, marine, and nuclear [6]. Due to its potential to retain its high strength at elevated temperatures, Inconel 718 (IN718) has gained acceptance in many applications [7]. SLM fabrication of IN718 components has addressed many of the challenges associated with conventional manufacturing methods [8]. However, the challenge regarding the process-induced defects, microstructure, and property relationships with process parameters and dimensional accuracy is still there for SLMed parts [9].

One viable approach for limiting or eliminating SLM defects and achieving higher build quality is to determine the temperature of melt pool during printing and control it accordingly. Further, the resulting microstructure and properties of SLMed parts are strongly influenced by temperature distribution, as it governs the solidification characteristics and grain growth [10]. The thermal history is also shown to have a strong effect on melt pool geometry and hence the dimensional accuracy of the SLMed parts [11]. Temperature distribution is also used in residual stress evaluation, grain growth estimation, and process parameter optimisation, in addition to assessing and limiting defects [12]. Thus, it is evident that temperature distribution plays an important role in realising defect free SLM builds, and therefore, an efficient framework is desired that can predict temperature distribution with a given set of process parameter condition. Several researchers incorporated different frameworks to obtain temperature profiles using experimental, analytical, and numerical approaches [13].

In the experimental domain, researchers started to monitor thermal history with the help of various sensors to observe in situ control of build quality [14]. Incorporating various monitoring sensors into the SLM setup and analysing the generated data is both costly and time intensive [15]. Therefore, developing rapid and cost-effective numerical modelling approaches to predict temperature distribution is so critical in the context of SLM.

Various multiscale modelling frameworks are also developed to study the temperature distribution in SLM builds [16]. These numerical models seem to be reliable to predict the thermal history in SLM because they also reveal the underlying physics of the process [17]. Studies using numerical modelling techniques for various combinations of process parameters on various material systems are documented in the literature [18, 19]. A numerical model with a Gaussian heat source is developed for a
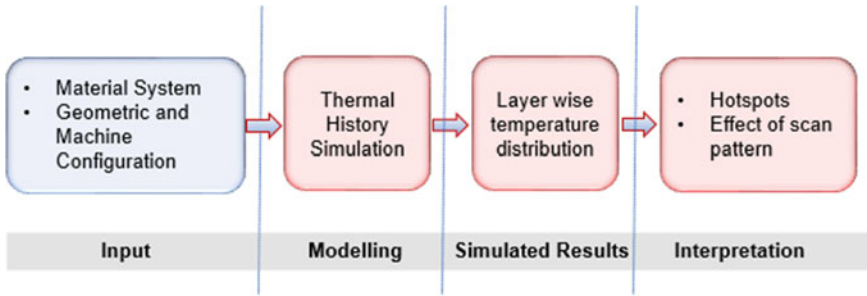
Fig. 1 Modelling framework used in the study

single bead print to predict the effect of important process conditions on SLM build [20]. In another study, a thermal simulation model is employed to assess the influence of scan speed on the developed solidification characteristics in the SLM parts [21]. The thermal model is useful to predict the temperature distribution as well as to develop the linkage between process parameters and the developed thermal history [22]. Zhao [23] used a FEM-based numerical model to foresee the residual stresses based on the thermal history during the printing of titanium alloy. Tan [24] proposed a thermo-microstructural model to determine the temperature history and grain growth for various SLM process parameters.

It is evident from the literature that several studies have been conducted on predicting the thermal history as a signature for various outcomes, including grain growth, distortion, residual stress, and quality control. But the point-wise temperature distribution or nodal thermal history is not yet fully explored by numerical modelling, and hence there is a need for an efficient approach to model temperature distribution in SLM builds. In this study, the multi-track, multi-layer SLM builds of IN718 were simulated using a three-dimensional FEM model. The temperature distribution on printed layers was evaluated, after which thermal profiles from simulated layers were extracted and the permissible limit exercise was performed to identify potential hotspots. Additionally, the impact of the layer rotation angle or scan pattern on the simulated thermal history was investigated. Figure 1 depicts the framework employed in the study.

2   Material and Methods

For thermal analysis, some physical assumptions related to the SLM process were taken into account. The physical characteristics of the powder particles were homogeneous, and the powder bed was regarded as a continuous media. The numerical modelling takes into account the material's temperature-dependent thermophysical properties. The convective heat transfer coefficient for the powder bed was assumed

to be constant. The material data for IN718 with thermophysical properties was taken from the ANSYS mechanical engineering data source.

2.1 Governing Equations

Various key SLM process parameters such as laser power (P), scanning speed (v), hatch spacing (h), and layer thickness (t) are related to laser energy density (E_d) as:

$$E_d = \frac{P}{v.t.h} \text{J/mm}^3 \tag{1}$$

The partial differential equation for the transient heat transfer satisfied by the temporal and spatial distribution of the temperature field is given by [25]:

$$\rho c \frac{\partial T}{\partial t} = \frac{\partial}{\partial x}\left(k\frac{\partial T}{\partial x}\right) + \frac{\partial}{\partial y}\left(k\frac{\partial T}{\partial y}\right) + \frac{\partial}{\partial z}\left(k\frac{\partial T}{\partial z}\right) + Q \tag{2}$$

where T is the temperature, t is the interaction time, and ρ, c, k are material density, heat capacity, and thermal conductivity, respectively. Q represents the volumetric heat generation.

The initial state of the temperature distribution can be written as-

$$T(x, y, z, t)_{t=o} = T_0 \tag{3}$$

where T_0 is the ambient temperature. The following is a representation of the natural boundary condition with energy balance:

$$k\frac{\partial T}{\partial z} + h(T - T_0) + \sigma\varepsilon(T^4 - T_0^4) = Q \tag{4}$$

where h is the coefficient of convective heat transfer, ε is the emissivity of the surface, and σ represent the Stefan–Boltzmann constant.

It was assumed that the surface heat flux distribution throughout the powder bed follows a Gaussian distribution and is expressed by [26]

$$Q_0 = \frac{32AP}{\pi D^2}\exp\left(\Delta\frac{2r^2}{D^2}\right) \tag{5}$$

where A, P, and D represent the energy absorption coefficient, laser power, effective laser spot diameter. Further, r represents the radial distance between a point on the powder bed and laser spot.

2.2 Thermal History Simulation

The thermal history in the SLM builds was simulated by generating elemental temperature distributions on individual layers of the build. In this approach, results from a coaxial average sensor were simulated, comprising the temperature distribution for an arbitrary layer within the build with a given material system and process parameter combination. A simulated map of the instantaneous temperatures was generated within a circular field of view centred around the laser at the top surface of the build. Temperatures were averaged over the field of view radius, which was defined by the sensor radius, an input parameter. The average temperature will generally decrease as the sensor radius is increased since the thermal gradients are strongest in the melt pool vicinity.

First, a 3 mm cube was designed using 3D CAD modelling software, Ansys SpaceClaim, and imported into the numerical simulation module. The designed cube and considered layer for temperature distribution are shown in Fig. 2. Then a thermal model was employed with all the input process parameters given in Table 1. Sensor radius of 0.2 mm and the layer at 2 mm height from the bottom was considered for temperature distribution modelling.

To further study the influence of the scan pattern or layer rotation angle, three adjacent layers, starting from the bottom layer, were simulated. As the layer start angle and layer rotation angle are 57° and 67°, the first three layers have starting angles of 57°, 124°, and 181°, respectively. The centre point on the individual layer
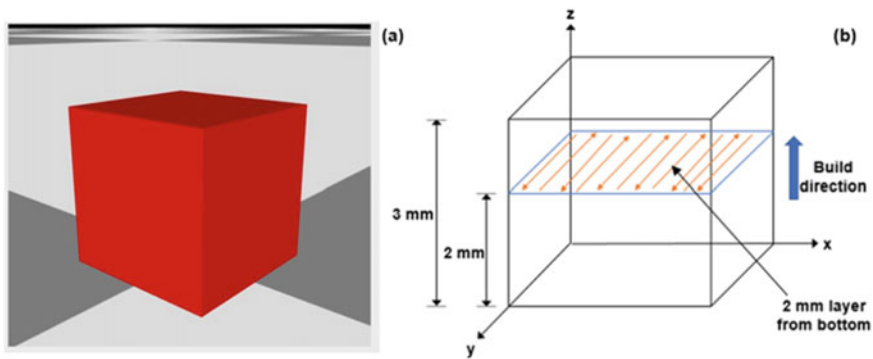
Fig. 2 Representation of **a** 3 mm cube and **b** the layer at 2 mm from the bottom considered for the temperature distribution

Table 1 Process parameters used for thermal simulation

Laser power (W)	Scan speed (mm/s)	Layer thickness (μm)	Hatch spacing (μm)	Base plate temperature (°C)	Laser spot size (μm)	Layer start/ rotation angle (°)
200	900	30	120	80	100	57/67
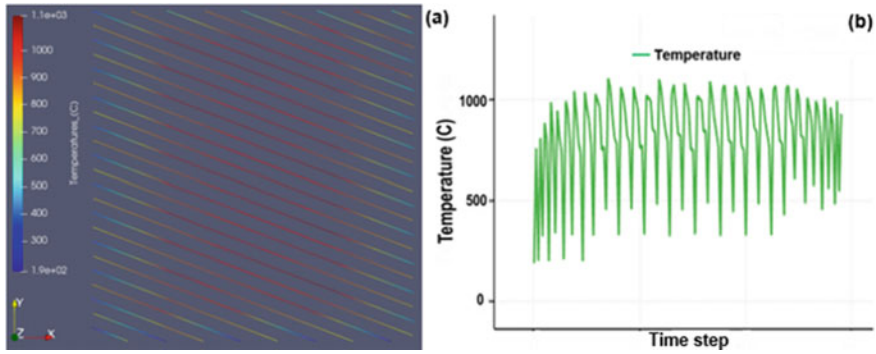
Fig. 3 Representation of **a** thermal history and **b** variation of temperature with time during print

was considered for the comparison, and the temperature at that point is taken as T_{point}. Moreover, the maximum temperature on each individual layer (T_{max}) was also used to compare the thermal history of these layers. The individual layer results and comparative study are discussed in the next section.

3   Results and Discussions

3.1   Thermal History

By analysing the output visualisation toolkit files, the temperature distribution on the printed layer was predicted. The temperature distribution outputs for a layer at 2 mm from the bottom are shown in Fig. 3. Figure 3a depicts the temperature distribution over the whole layer, whereas Fig. 3b shows the fluctuations in the temperature as the layer is printed.

Further, domains from the individual layer were extracted, and the permissible limit exercise was performed to find out the potential hotspots. The extracted domain from the layer at 2.0 mm height from the base is shown in Fig. 4, along with spots where the local temperature surpasses 1050 °C.

3.2   Effect of the Scan Pattern on the Thermal History

Individual layer results from three adjacent layers starting from the bottom layer are shown in Table 2. The temperature at the centre point of the layers (T_{point}) is increasing as the next layer is printed. T_{point} for the first layer is 988.5 °C, whereas for second layer it is significantly increased to 1049.3 °C (Figs. 5 and 6). This is due to the additional heating provided by the previously deposited layer. Similarly,
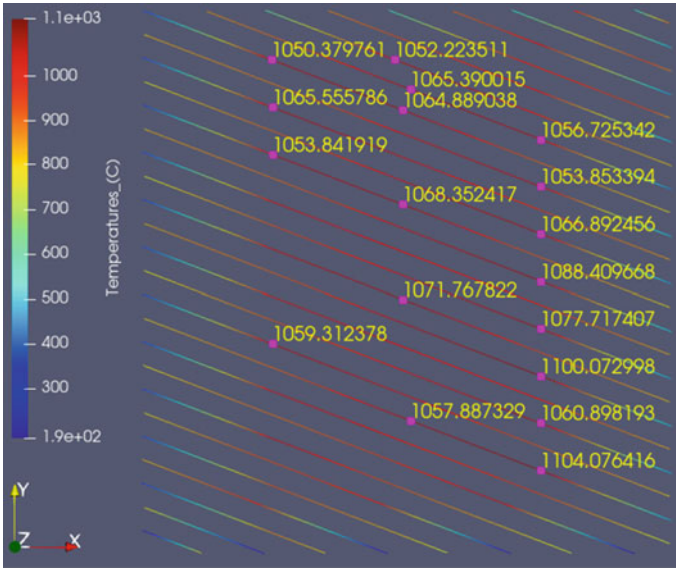
Fig. 4 2 mm layer from the bottom showing hotspots where local temperature exceeds 1050 °C

Table 2 Effect of scan pattern on thermal history

Layer	Layer start angle (°)	T_{point} (°C)	T_{max} (°C)
1	57	988.5	1066.1
2	124	1049.3	1119.5
3	191	1077.8	1127.3
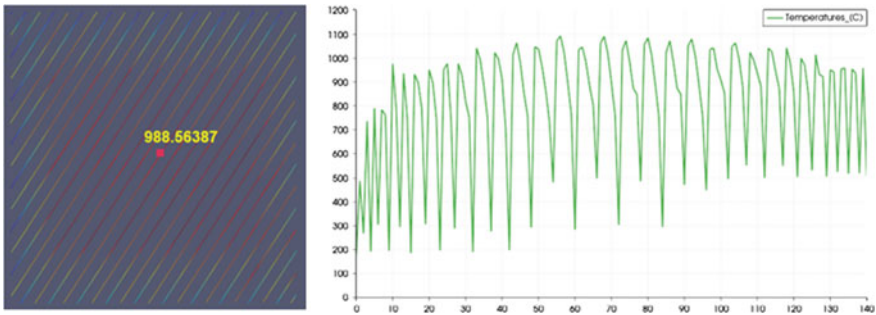
Fig. 5 Temperature distribution on the first layer from base with T_{point}

the temperature of the third layer is increased to 1077.8 °C (Fig. 7). The thermal impact of the residual heat from deposited layers can also be seen in the maximum temperature (T_{max}), which is also increasing as second and third layers are printed.
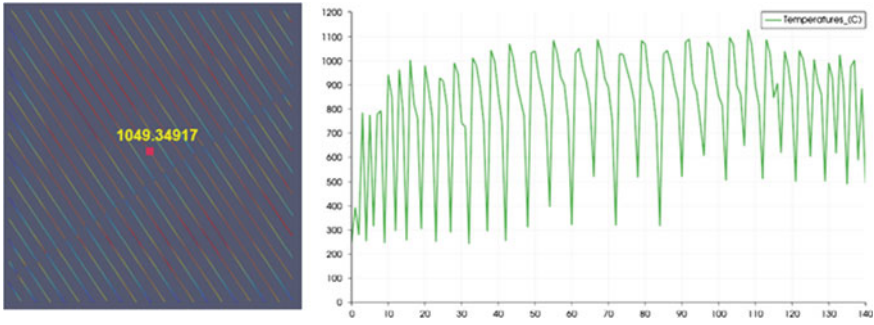
Fig. 6 Temperature distribution on the second layer from with T_{point}
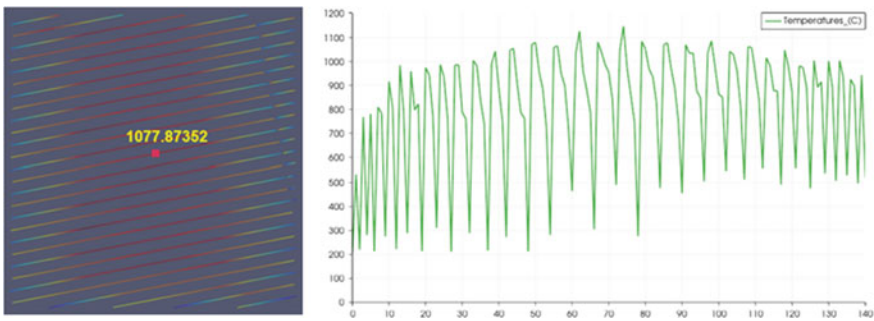
Fig. 7 Temperature distribution on the third layer from base with T_{point}

The individual layer scans show how the layer rotation angle alters the number of tracks on a layer and also the length of an individual track. It demonstrates that any arbitrary point on the layer experiences a significantly different temperature history depending on the layer start and rotation angles. The effects of this altered temperature distribution can be seen in the developed residual stresses and distortion, but these outcomes are not in the scope of current study.

4 Conclusion

In this work, a numerical modelling approach was employed to study the temperature distribution in multi-track, multi-layer SLMed IN718. The simulated thermal history, corresponding to SLM process parameters, was further utilised in conducting permissible limit exercise and potential hotspots identification. These hotspots where the local temperature exceeds the permissible limit can be attributed to the potential process-induced defects commonly found in SLMed parts. Hence, this thermal history simulation can be utilised prior to the actual printing of SLMed parts to assess

the temperature distribution and hotspots and optimise the SLM input parameters accordingly. Further, the effect of the scan pattern was also analysed by considering the temperature at the centre point and the maximum temperatures of individual adjacent layers. The different thermal histories in these layers are attributed to residual heat from previous layers and a change in the length of scan vectors due to different layer start and rotation angles.

References

1. Bandyopadhyay A, Heer B (2018) Additive manufacturing of multi-material structures. Mater Sci Eng R Rep 129(17):1–16
2. Yusuf SM, Cutler S, Gao N (2019) The impact of metal additive manufacturing on the aerospace industry. Metals 9:1286
3. Sefene EM (2022) State-of-the-art of selective laser melting process: a comprehensive review. J Manuf Syst 63:250–274
4. Kumar S, Maity SR, Patnaik L (2021) Mechanical and scratch behaviour of TiAlN coated and 3D printed H13 tool steel. Adv Mater Proc Technol 8(2):337–351
5. Frazier WE (2014) Metal additive manufacturing: a review. J Mater Eng Perform 23:1917–1928
6. Teixeira O, Silva FJG, Atzeni E (2021) Residual stresses and heat treatments of Inconel 718 parts manufactured via metal laser beam powder bed fusion: an overview. Int J Adv Manuf Technol 113:3139–3162
7. Lambarri J, Leunda J, Garcia-Navas V, Soriano C, Sanz C (2013) Microstructural and tensile characterization of Inconel 718 laser coatings for aeronautic components. Opt Lasers Eng 51(7):813–821
8. Wang X, Gong X, Chou K (2017) Review on powder-bed laser additive manufacturing of Inconel 718 parts. Proc Inst Mech Eng Part B: J Eng Manuf 231(11):1890–1903
9. Jaber H, Kovacs T, Janos K (2022) Investigating the impact of a selective laser melting process on Ti6Al4V alloy hybrid powders with spherical and irregular shapes. Adv Mater Proc Technol 8(1):715–731
10. Gao S, Yan X, Chang C, Aubry E, Liu M, Liao H, Fenineche N (2021) Effect of laser energy density on surface morphology, microstructure, and magnetic properties of selective laser melted Fe-3wt.% Si Alloys. J Mater Eng Perform 30(7):5020–5030
11. Dilip JJS, Zhang S, Teng C, Zeng K, Robinson C, Pal D, Stucker B (2017) Influence of processing parameters on the evolution of melt pool, porosity, and microstructures in Ti-6Al-4V alloy parts fabricated by selective laser melting. Prog Additive Manuf 2:157–167
12. Zhang X, Mao B, Mushongera L, Kundin J, Liao Y (2021) Laser powder bed fusion of titanium aluminides: an investigation on site-specific microstructure evolution mechanism. Mater Des 201:109501
13. Spears TG, Gold SA (2016) In-process sensing in selective laser melting (SLM) additive manufacturing. Integrating Mater Manuf Innovat 5:16–40
14. Shrestha S, Chou K (2018) Single track scanning experiment in laser powder bed fusion process. Proced Manuf 26:857–864
15. Scime L, Beuth JL (2019) Melt pool geometry and morphology variability for the Inconel 718 alloy in a laser powder bed fusion additive manufacturing process. Addit Manuf 29:100830
16. Khairallah SA, Anderson AT (2014) Mesoscopic simulation model of selective laser melting of stainless-steel powder. J Mater Process Technol 214:2627–2636
17. Khairallah SA, Anderson AT, Rubenchik A, King WE (2016) Laser powder-bed fusion additive manufacturing: physics of complex melt flow and formation mechanisms of pores, spatter, and denudation zones. Acta Mater 108:36–45

18. Wang N, Shen J, Hu S, Liang Y (2020) Numerical analysis of the TIG arc preheating effect in CMT based cladding of Inconel 625. Eng Res Express 2(1):015030
19. Jelvani S, Razavi RS, Barekat M, Dehnavi M (2020) Empirical-statistical modelling and prediction of geometric characteristics for laser-aided direct metal deposition of Inconel 718 superalloy. Met Mater Int 26(5):668–681
20. Patil RB, Yadava V (2007) Finite element analysis of temperature distribution in single metallic powder layer during metal laser sintering. Int J Mach Tools Manuf 47(7):1069–1080
21. Gusarov AV, Yadroitsev I, Bertrand P, Smurov I (2007) Heat transfer modelling and stability analysis of selective laser melting. Appl Surf Sci 254(4):975–979
22. Arisoy YM, Criales LE, Ozel T (2019) Modelling and simulation of thermal field and solidification in laser powder bed fusion of nickel alloy IN625. Opt Laser Technol 109:278–292
23. Zhao X, Iyer A, Promoppatum P, Yao SC (2017) Numerical modelling of the thermal behaviour and residual stress in the direct metal laser sintering process of titanium alloy products. Addit Manuf 14:126–136
24. Tan P, Shen F, Li B, Zhou K (2019) A thermo-metallurgical-mechanical model for selective laser melting of Ti6Al4V. Mater Des 168:107642
25. Li Y, Gu D (2014) Parametric analysis of thermal behaviour during selective laser melting additive manufacturing of aluminium alloy powder. Mater Des 63:856–867
26. Yin J, Zhu H, Ke L, Lei W, Dai C, Zuo D (2012) Simulation of temperature distribution in single metallic powder layer for laser micro-sintering. Comput Mater Sci 53(1):333–339

Correction to: Development of a Payload-Dropping Quadcopter Using Landing Gears with Electronic Servo

E. M. Maheshwar, R. Ibrahim, and K. K. Nithiyanantham

Correction to:
Chapter 17 in: P. Tambe et al. (eds.), *Advances in Mechanical Engineering and Material Science*, **Lecture Notes in Mechanical Engineering,**
https://doi.org/10.1007/978-981-99-5613-5_17

The original version of this book was inadvertently published with an error in the first name of E. M. Maheshwar and spelling of R. Ibrahim, which have now been corrected. The book has been updated with the changes.

The updated version of this chapter can be found at
https://doi.org/10.1007/978-981-99-5613-5_17

Author Index

Subject Index

A

Additive manufacturing, 281–283, 331
Artificial roughness, 33–35, 40, 44
Assistive robot, 120–123, 125, 130
Augmentation techniques, 228
Autonomous mobile robot, 235

B

Ball picking mechanism, 238, 243, 245–247
Blended Wing Body (BWB), 152
Boiler, 1–14
Brinkman number, 57, 60, 62
Bubble growth, 97, 99, 100

C

Carrageenan, 97, 99, 100, 102, 103, 105
CEL, 318, 319
Chili fruit, 187–190, 192, 194
Circulating Fluidized Bed Combustion (CFBC), 1, 3–19
Computational Fluid Dynamic (CFD), 33, 35, 37, 44, 158, 318
Couette flow, 57, 58, 66
Crack growth, 133–137, 139, 142–148

D

Decryption, 107–109, 111, 116, 117
Deep learning, 173, 175–178, 181–184, 241
DeltaEC, 69, 75, 79, 80, 82, 83
Desalination, 249, 251, 261, 264

Design, 1, 3–8, 12, 14, 33, 44, 48, 53, 69, 71, 73–76, 78–80, 98, 99, 110, 120, 121, 135, 141, 151, 152, 155, 156, 158, 160, 175, 197, 198, 209, 211, 213, 214, 223, 228, 235–238, 242, 244, 245, 247, 249, 281, 299, 318, 327
Double layer micro-perforated panel absorber, 160
3D Location model, 189

E

Efficiency, 1–5, 7, 8, 12, 13, 15, 16, 19, 34, 86, 98, 99, 107, 151, 152, 158, 200, 215, 217, 219, 222, 245, 246, 267–269, 271–273, 275, 278, 281
Electric vehicle battery pack, 181, 185
Electrode pressure, 307–311, 313, 314
Emissions, 1, 2, 4, 7, 11–14, 19, 47–49
Encryption, 107, 109, 111–114, 116, 117, 180
End of life, 175

F

Femur bone, 197, 200, 201
Film condensation, 23, 24
Finite element analysis, 136, 138, 140, 159, 160, 198, 200
Fracture mechanics, 135, 136, 199
FSW, 317–323, 325, 327